TUDelft

Delft University of Technology

Magnetic Energy Transfer in Roads

Prasanth, Venugopal

Important note
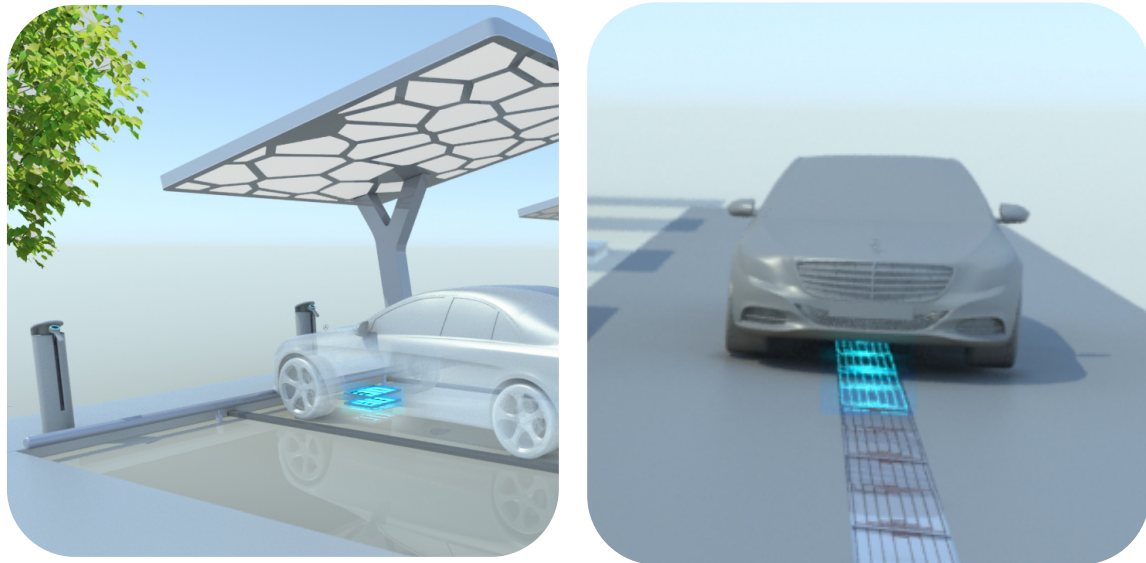To cite this publication, please use the final published version (if applicable).
Please check the document version above.

Magnetic Energy Transfer in Roads
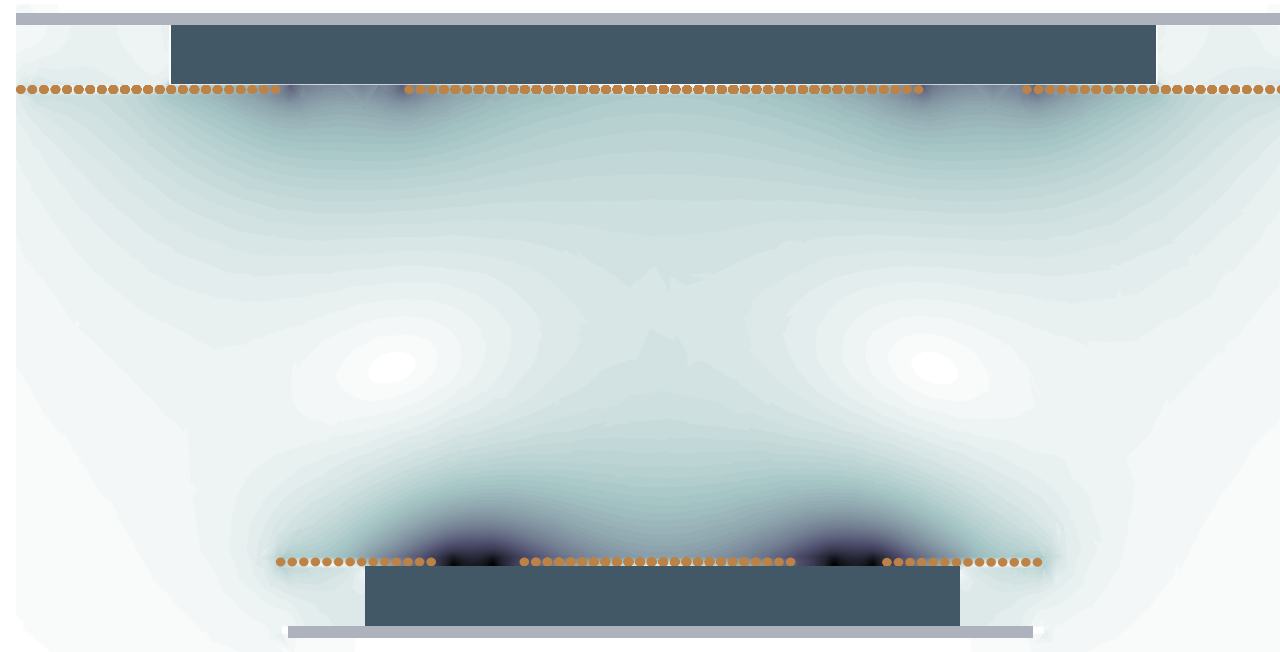
Prasanth Venugopal

About the author

Prasanth Venugopal was born in Salem, India, on April 7, 1989. He received his Bachelor's degree in Electrical and Electronics Engineering (B. Tech, *silver medal*) from Amrita Vishwa Vidyapeetham University, Tamil Nadu, India, in 2010. He graduated with an MSc. degree (*cum laude*) in Electrical Power Engineering at the Delft University of Technology (TU Delft), the Netherlands in 2012. His study was partially financed by a JN TATA scholarship. His MSc. thesis, "Wireless Power Transfer for E-Mobility" was awarded a *Ufd Cofely Energy Efficiency Award* in 2013. After a brief stint as a researcher in the EPP group, TU Delft, he continued with his Ph.D. (Dec 2012 - Dec 2016) in the DC Systems Energy Conversion and Storage group at the faculty of Electrical Engineering, Mathematics and Computer Science. He joined Qualcomm Halo, Munich as a Senior Electrical Engineer from November 2016.

Magnetic Energy Transfer in Roads

Prasanth Venugopal

Magnetic Energy Transfer in Roads

Proefschrift

ter verkrijging van de graad van doctor
aan de Technische Universiteit Delft,
op gezag van de Rector Magnificus prof. ir. T.H.J.J. van der Hagen;
voorzitter van het College voor Promoties,
in het openbaar te verdedigen op
Vrijdag 4 mei 2018 om 10:00 uur

door

Prasanth VENUGOPAL

elektrotechnisch ingenieur,
Technische Universiteit Delft, Nederland,
geboren te Salem, India

This dissertation has been approved by the promotor:
  promotor: Prof. dr. P. Bauer and
  promotor: Prof. dr. J.A. Ferreira

Composition of the doctoral committee:
  Rector magnificus,   Chairperson
  promotor: Prof. dr. P. Bauer
  promotor: Prof. dr. J.A. Ferreira

Independent members:
  Prof. dr. ir. A.H.M. Smets   Technische Universiteit Delft, the Netherlands
  Prof. dr. E. Lomonova   Technische Universiteit Eindhoven, the Netherlands
  Prof. dr. ir. H.E.J.G. Schlangen Technische Universiteit Delft, the Netherlands
  Prof. dr. ir. A.V.D. Bossche   Universiteit Ghent, Belgium

Other members:
  Dr.ir. H. Polinder   Technische Universiteit Delft, the Netherlands

Acknowledgements

This book is dedicated to my late grand parents - Bhageerathy Kovilamma, M.T.G. Nedungadi, K.M.V. Pandalai and Saraswathy Kovilamma.

Contents

Summary

This thesis deals with the modelling and application of magnetic fields in roads. The backbone technology being inductive power transfer (IPT) for electric vehicles. The magnetics for energy transfer in vehicles, can be adapted for heating steel fibres in roads, referred to as self-healing and modelling this is a second aspect of this thesis.

The first sections of this thesis is dedicated to an overview of modelling techniques for coil design of IPT systems using both analytical and semi-analytical tools. A detailed literature review of techniques is followed by a comparison highlighting the strengths and weakness of techniques in terms of ease of use, computational efficiency, application to material interfaces etc. Analytical modelling of single and multi-coil configurations of IPT systems is carried out subsequently. The theory of partial inductance is used to model these geometries, to assess the impact of system parameters such as coupling, power transferred and magnetic efficiency with shapes of couplers and misalignment. Next, the problem of misalignment is highlighted by considering a distributed IPT system. The analytical modelling and experimental analysis of misalignment - lateral and longitudinal is performed. Edge effect is observed and experimentally validated.

The second part of this thesis is dedicated to a multi-objective optimization based on the results of the developed analytical model. The goal being the development of a prototype IPT system for powering light EVs. The double rectangular (DR) coupler is chosen as the geometry for power transfer. Several geometry parameters - turns, ferrites (number, dimensions), gap between ferrites etc. are considered as design variables. Efficiency, area related power density and weight are considered as the optimization targets. Pareto fronts are developed and a particle is chosen for the development of a prototype. An experimental set-up is built consisting of a 85 kHz inverter, compensated charge-pads, rectifier and resistive load. The inverter is based on SiC MOSFETS and SiC Schottky anti-parallel diodes, the rectifier made from the same diodes. Phase shift control of the inverter legs is used to control power flow. An experimental analysis to validate the magnetic models is also developed.

The third part of this thesis deals with system level economic analysis of IPT technology. A case study of bus fleet is considered and a generic methodology is developed to determine driving range as a function of mass and frontal area of the EV. The economic analysis is performed also identifying the trade-offs between road coverage of IPT, efficiency and battery size. Finally, the thesis culminates with a vision toward a future highway. Such a highway is expected to undergo a functional upgrade to handle electrification of transportation. This evolves around the integration of IPT systems, with low maintenance inductive healing asphalt roadways and renewable energy generation. The modelling challenges to such an integration is studied both using simulations and experiments. A case study for sizing renewable energy in a highway (A12) in the Netherlands using IPT is detailed.

uw Samenvatting

Dit proefschrift behandelt het modelleren en toepassen van magnetische velden in wegen. Met hierin als technologische ruggengraat de inductieve energieoverdracht (IPT) voor het opladen van elektrische voertuigen. De magnetische eigenschappen voor energieoverdracht in voertuigen kunnen ook worden toegepast voor het verwarmen van staalvezels in wegen. Deze eigenschappen worden ook wel aangeduid als 'self-healing' en 'modellering' en worden behandelt in het tweede aspect van dit proefschrift.

De eerste sectie van dit proefschrift heeft betrekking op een overzicht van modelleertechnieken voor het ontwerpen van spoelen van IPT-systemen door het gebruiken van zowel analytische als semi-analytische hulpmiddelen. Een gedetailleerde literatuur evaluatie van de technologie wordt gevolgd door een vergelijking tussen de sterke en zwakke punten van de technologie op basis eigenschappen zoals gebruiksgemak, reken efficiëntie, toepassing op materiaal interfaces enzovoorts.

Achteraf is een analytische modellering uitgevoerd van enkele en meervoudige spoel configuraties van IPT-systemen. De theorie van 'gedeeltelijke inductie' is gebruikt voor het modelleren van geometrieën om de impact van systeemparameters te beoordelen op eigenschappen zoals koppeling, vermogensoverdracht en magnetische efficiëntie door koppelingen en uitlijnfouten. Vervolgens wordt het probleem geanalyseerd van verkeerde uitlijning in IPT-systemen. De analytische modellering en experimentele analyse van foutieve uitlijning wordt lateraal en longitudinaal uitgevoerd. Randeffecten worden waargenomen en experimenteel gevalideerd.

Het tweede deel van dit proefschrift is gewijd aan multi-objectieve optimalisatie op basis van de resultaten van het ontwikkelde analytische model. Het doel is de ontwikkeling van een prototype van het IPT-systeem voor het aansturen van lichte EV's. De dubbele rechthoekige (DR) koppeling is hiervoor de gekozen geometrie voor energie overdracht. Verschillende geometrie parameters zoals aantal windingen, ferrieten (aantal en dimensies), de afstand tussen ferrieten enzovoorts, worden beschouwd als ontwerpvariabelen. Efficiëntie, gebied gerelateerde vermogensdichtheid en gewicht worden beschouwd als optimalisatie doelen. Pareto fronten worden ontwikkeld en een deeltje wordt gekozen voor de ontwikkeling van een prototype. Een experimentele set-up is gebouwd bestaande uit een 85 kHz omvormer, gecompenseerde lading-pads, gelijkrichter en resistieve belasting. De omvormer is gebaseerd op SiC MOSFETS en SiC Schottky anti-parallelle diodes, de rectifier is gemaakt van dezelfde diodes. Met fase verschuivings besturing van de poten van de omvormer wordt de stroomsterkte geregeld. Ook is een experimentele analyse ontwikkeld om de magnetische modellen te valideren.

Het derde deel van dit proefschrift behandelt de economische analyse van IPT-technologie op systeemniveau. Een case study van een busvloot ontwikkelt een generieke methode om

de te behalen rij afstand te bepalen als functie van de massa en het frontale oppervlak van het voertuig. De economische analyse identificeert ook de wisselwerking tussen de weg bedekking van IPT systemen, efficientie en de grootte van de batterij. Het proefschrift sluit af met een visie van de snelweg van de toekomst. Zo'n snelweg zal naar verwachting een functionele upgrade ondergaan om elektrisch opladen van het transport aan te kunnen. Deze evolueert rond de integratie van IPT-systemen, inductief te herstellen asfaltwegen en hernieuwbare energieopwekking. De modellering is uitgedaagd om deze integratie te bestuderen, zowel met behulp van simulaties als ook met experimenten. Een dergelijke case study voor integratie van hernieuwbare energie op een snelweg (A12) in Nederland met behulp van IPT is gedetailleerd uitgevoerd.

Glossary

BR   basic restrictions
BS   Biot-Savart's law
DR/Circ double rectangle/circle
EM   electromagnetic
EV   electric vehicle
FE(M) finite element (method/model)
FOM   figure of merit
GMD   geometric mean distance
ICNIRP International Commission on Non-Ionizing Radiation
IEEE   Institute of Electrical and Electronics Engineers
IHA   inductive healing asphalt
IPT   inductive power transfer
ITF   international transport forum
KNMI Koninklijk Nederlands Meteorologisch Instituut
LMNZ longitudinal mu-near-zero
MNZ   mu-near-zero
MPE   maximum permissible exposure
NI   Neummann's integral
ORNL Oak Ridge National Laboratory
PCB   printed circuit board
PDE   partial differential equation
PEEC partial element equivalent circuit
PI   partial inductance
PM   permanent magnet (machine)
PP   parallel-parallel
PS   parallel-series
PSO   particle swarm optimization
Quad quadrature
RFID radio-frequency identification
SAE   Society of Automotive Engineers
SAR   specific absorption rate
SCT   Schwarz Christoffel transformation
SP   series-parallel

SS   series-series
TI   theory of images
TNO   Nederlandse Organisatie voor Toegepast Natuurwetenschappelijk Onderzoek
u.p.f   unity power factor
VA   volt-ampere
VLF/LF/UHF very low frequency/low frequency/ultra high frequeny
VRM   variable reluctance machine (motor)
WEVC wireless electric vehicle charging

Introduction

Traditional utilization of fossil fuels propelled the industrialization of world and created an era of economic and human prosperity. However, the fact that fossil fuels are getting depleted at a very fast rate and its impact on the environment - global warming, climate change, pollution and resulting ecological destruction demands a shift to alternative modes of energy generation and utilization [1]. According to ITF (International Transport Forum) 2010 statistics, transportation accounted for 23% of the total CO_2 emissions and 30% of OECD CO_2 emissions [2]. Also, it is reported to account for about 15% of the total GHG emissions. Thus, an urgent transition to a cleaner alternative is imperative to create a sustainable planet for future generations.

Electrification of road transportation is becoming an important step toward solving the problems of anthropogenic climate change as well as for controlling pollution. The development of Electric Vehicles (EVs) as a transitory technology that has a low carbon footprint is plagued with challenges including limited driving range, limited battery size, high cost and lack of charging infrastructure. Also, galvanic/conductive charging which is the most straightforward replacement to gasoline stations, pose the risk of electrocution at unfavorable weather due to handling. Hence, decoupling the EV users from the mode of charging led to development of contactless/wireless power transfer.

Inductive Power Transfer (IPT) is a mode of wireless power transfer where magnetic fields act as the energy carrier medium. Encouraging developments in the field of IPT for both stationary and on-road dynamic powering is expected to help alleviate the problems of range extension and user-charger decoupling. Another persuasive development in future roadway technology is the concept of self-healing roads that use induction healing to remove the potholes in roads. This thesis is centred around the utilization of magnetic fields as a source of energy transfer in EVs in the road and for inductive healing of low maintenance self-healing asphalt.

Magnetic fields that emanate from a charge-pad or coil carrying alternating currents are also

alternating in nature. This fluctuating magnetic field when inductively coupled to another charge-pad can create power transfer. Alternatively, conductive materials placed close to an alternating field can create eddy currents through them resulting in heating of the same. These two effects of magnetic fields - electrical energy transfer and eddy current heating are the basis of inductive power transfer and inductive heating/healing. A combination of these roadway electrification technologies that will see independent implementation in the future, can pose coexistence roadblocks during integration. This thesis also bridges this gap by modelling and finding interdependencies that pose challenges and proposes viable alternatives for all technologies to be combined together. These two applications of magnetic fields are introduced in Section 1.1 and Section 1.4.

1.1 Magnetic Fields for Power Transfer of EVs - State of Art

There are three developments in the electromagnetic power transfer for EV charging. They are stationary charging, semi-dynamic charging and on-road/dynamic charging. In case of stationary/static charging, parking lots can be upgraded to charge EVs with the comfort of not plugging in any charging cables. Static wireless charging is expected to improve the charging experience by preventing hazards due to tripping on the cable or even electrocution. Such systems can be buried or flush-mount, thereby not affecting the façade of a city and being safe from vandalism and unfavourable weather conditions [3]. Practical examples of stationary charging include bus based wireless electric vehicle charging systems (WEVC). Such systems have helped in reducing the weight of on-board batteries and have improved efficiency. For eg: Condutix-Wamplfler's WEVC in buses at Torino, Geneo and s'Hertogenbosch in the Netherlands [4]. Efficiencies of more than 90% are reported at 60, 120 or 180 kW [4]. WAVE IPT, a spin-off from Utah State University is working on 50 kW IPT systems achieving more than 90 % efficiency [5]. They are expecting to install IPT systems with 250 kW charging [5]. OLEV, a spin-off from Korean Advanced Institute of Science and Technology (KAIST) developed a third generation of wireless power transfer in with a power transfer efficiency of 83% at a 20-cm air gap [3].

Companies like Witricity, Qualcomm Halo, Conductix-Wampfler, Bombardier, Momentum Dynamics, HEVO Power etc. are building market ready charge-pads for electric vehicles charging using IPT systems [3], [12]. Witricity that started out of Massachusetts Institute of Technology, have developed systems that deliver $91 - 93\%$ efficiency at 11 kW power transfer [13]. HaloIPT that started out as a spin-off from the University of Auckland, works extensively in a patented "Double D"magnetic structure for power transfer [3], [14]. Qualcomm acquired Halo in 2011 and they are involved in developing systems from 3.3 kW to 20 kW with $> 90\%$ efficiency [14].

Semi-dynamic charging can be useful to deliver energy back to battery during an opportune stop moment during a trip or during slow moving instances eg: stop lights, taxi-ranks etc [7]. This is a hybrid situation between fully static EVs and being fully dynamic. They are

expected to be installed in the roads in the mid-term future as more EVs populate the road. In published work, it is shown that the on-road wireless charging can be used to power the EVs at stop lights in a semi-dynamic fashion in [8].

Dynamic charging is the concept of charging the battery of EV or even using it for traction when the vehicle is in motion. This is usually achieved by having sectional IPT systems/ repeated charge-pads on the road. An example of dynamic charging IPT systems on the road as demonstrated at Oak Ridge National Laboratory (ORNL) is shown in Fig. 1.1. Dynamic charging can enhance battery life by charging with small packets of energy while nullifying range anxiety in long trips caused due to limited battery size. Dynamic charging as researched in [9], concludes that for an EV with a battery of 24 kWh, 500 km range can be achieved by IPT system of 25 kW with 40% road coverage. In a related study in California, the combination of dynamic and static charging is shown as cost effective compared to gasoline vehicles fuelled at $2.50 and $4 per gallon [10].

Figure 1.1: Repeated circular charge-pads for the in-motion dynamic charging of EVs as demonstrated at ORNL [11].

1.1.1 Systems for Inductive Power Transfer

Inductive Power Transfer involves the transfer of power from a coil to another displaced over an air-gap. The operating principle involves the generation of an alternating magnetic field from an ac supply (*Ampere's law*). Such an alternating field when linked with another coil induces an emf (*Faraday-Lenz law of induction*). The disadvantage of an incipient large air-gap is the large reluctance it adds to the magnetic path. Thus, compensating capacitors are added to both the coils which are then tuned to resonance so as to nullify the reactive

power [17]. This technology that eliminates wired power transfer is called Wireless Power Transfer. A typical IPT system integrated to an EV is shown in Fig. 1.2.
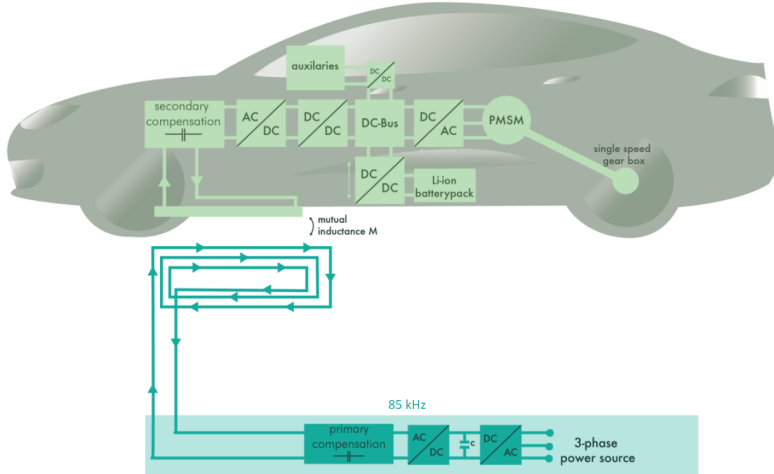
Figure 1.2: A typical IPT system with a 3-phase power source that drives an EV with a PMSM machine. Different configurations can have a 1-phase ac, 3-phase ac or even a dc power input source. Also, depending on the EV, the e-Powertrain is subjected to change.

IPT has a number of advantages such as elimination of messy cords, reduced wear and tear and hence the maintenance requirement, increased reliability, ability to be used in dangerous and difficult terrains such as explosive environments, underwater power delivery due to the non-contact nature of magnetic fields, massive reduction of battery size and range extension in case of electric vehicles (EVs) [18], [19]. There are a number of essential system requirements for an IPT system, they are [20]:

- *Coil magnetics*: A pair of coils that can transfer power from the ground to EV. Usually, a coil based on copper, ferrites (field shaping) and magnetic shield (Al) forms the charge pad (concentrated IPT system) or it can be in the form of long tracks for distributed IPT systems.

- *Power inverter*, where ac is generated in the VLF $(3 - 30 \text{ kHz})$/LF $(30 - 300 \text{ kHz})$ frequency range with embedded primary power-control.

- *Energy Management*, typically consisting of a dc/dc converter with control so as to perform secondary power-control to the vehicle battery.

Near-field inductively coupled systems consist of two coils separated from each other by an air gap with the magnetic flux created by the exciting coil/primary inducing an emf onto the

pickup/secondary. Conventionally, such an air-cored transformer results in low efficiency and low power transfer due to the large leakage fields associated with both the primary and secondary. Typically, the coupling coefficient of such transformers are low ($k = 0.01$–0.5, loosely coupled), while iron-core transformers operate at close to unity (tightly coupled) [18]. Now, when the entire system is made to resonate, these problems can be circumvented. This is done by connecting capacitors suitably (either in series or parallel or a combination) to both the primary and secondary, with the entire system operating at a single resonant frequency.

1.1.2 Compensation in IPT Systems

An uncompensated IPT System transfers energy between two loosely coupled coils, the primary inductor of inductance L_1 and the secondary, L_2 and as shown in Fig. 1.3. The mutual inductance between the primary inductor and the secondary inductor is M.
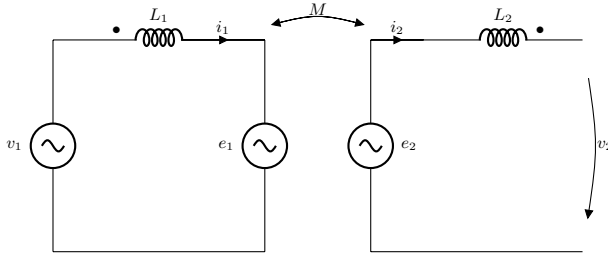
Figure 1.3: Equivalent Circuit of a loosely coupled coil-pair

The emf induced in the secondary coil due to primary current i_1 when excited by an alternating current of frequency ω is given by

$$e_2 = j\omega M i_1 \tag{1.1}$$

and the emf induced onto the primary coil due the secondary current i_2 is

$$e_1 = j\omega M i_2 \tag{1.2}$$

The large reluctance associated with the air-gap in loosely coupled coils results in poor efficiency and large leakage reactance. It is hence necessary to perform reactive power compensation by adding capacitors to the primary and secondary coils. This system of double-resonating coils acts as a band-pass filter effectively allowing only power at resonant frequency to be transferred to load at high efficiency.

Depending on the connection of the capacitors to the coils there are four basic compensation strategies: Series - Series (SS), Series - Parallel (SP), Parallel - Series (PS) and Parallel - Parallel

(PP) as shown in Figure 1.4. The source voltage is denoted by v_1 and the load is ideally represented as R_L. The transmitting side inductances and capacitances are denoted by L_1 and C_1 respectively while the receiving side parameters are L_2 and C_2 respectively. R_1 and R_2 are the winding resistances of the two coils. M is the mutual inductance between the primary and secondary inductors.

(a) SS Compensation Topology

(b) SP Compensation Topology

(c) PS Compensation Topology

(d) PP Compensation Topology
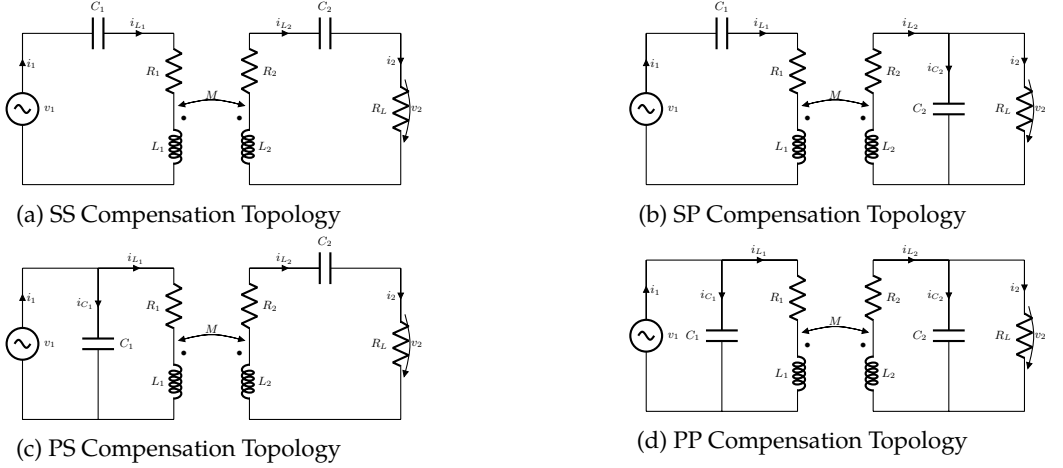
Figure 1.4: Basic IPT compensation topologies

To determine the compensation capacitance values, the secondary capacitance, C_2, is designed to resonate with the secondary inductance, L_2. This ensures that the power delivery to the load via the secondary circuit is maximized. Finally, primary capacitance, C_1, is chosen so as to nullify the reflected reactive loading of the primary coil. In ideal conditions, this would imply both maximum active power delivery and operation at u.p.f.

The secondary compensation C_2, for all the compensation topologies is given by:

$$C_2 = \frac{1}{\omega_0^2 L_2} \tag{1.3}$$

where ω_0 is the resonant frequency of the IPT system. To calculate primary compensation, C_1, the total impedance, Z of Figure 1.4 needs to be calculated for all topologies as reflected to the primary side. C_1 is then determined by nullifying the imaginary part of Z_1 to zero. The source voltage, v_1, can therefore be represented by:

$$v_1 = i_1 Z_T \tag{1.4}$$

The impedance of the receiver side is calculated as a lumped impedance, Z_2 as represented

as

$$Z_2 = \begin{cases} R_2 + j\left(\omega L_2 - \dfrac{1}{\omega C_2}\right) + R_L & \text{secondary series compensation} \\[3mm] R_2 + j\omega L_2 + \dfrac{R_L}{1 + j\omega C_2 R_L} & \text{secondary parallel compensation} \end{cases} \tag{1.5}$$

1.1.3 Designing the primary compensation

The primary compensation capacitance, C_1, is designed by equating the reactance of Z_T for the respective topology to zero. This ensure both high power factor and also maximum power transfer. The expressions for C_1, determined using (1.5) and total impedance are tabulated in Table 1.1. The winding resistances of the primary and secondary coils are neglected as they are usually small.

Table 1.1: Derivation of Primary compensation

Type	C_1
SS	$\dfrac{1}{\omega_0^2 L_1}$
SP	$\dfrac{1}{\omega_0^2 \left(L_1 - \dfrac{M^2}{L_2}\right)}$
PS	$\dfrac{L_1}{\omega_0^2 L_1^2 + \left(\dfrac{\omega_0^2 M^2}{R_L}\right)^2}$
PP	$\dfrac{L_1 - \dfrac{M^2}{L_2}}{\omega_0^2 \left(L_1 - \dfrac{M^2}{L_2}\right)^2 + \left(\dfrac{R_L M^2}{L_2^2}\right)^2}$

From the expressions of C_1 tabulated in Table 1.1, it can be observed that C_1 is load independent in the SS and SP topologies. However, there is a load dependence in the primary parallel topologies. Hence, load variations can result in detuning in parallel primary topologies and hence are not considered in this thesis. Also, the SS topology is the only one wherein C_1 is independent of the mutual inductance, M, between the primary and the

secondary. In addition, for distributed IPT systems, where a track feeds multiple pick-up circuits, the primary series topologies offer the advantage that impact of loading/unloading on tuning variations is minimal. Literature also includes work on LCL compensation and LCC compensation [20], [21] . These topologies have the advantage that distributed elements can share the VA. However, the multiple roots of their characteristic impedance implies that a variable frequency system can make the system operate in an unstable operating point [21].

1.2 System Performance Measures

Two useful systems parameters that can be defined for IPT systems is the power transferred and the magnetic efficiency of the system. The system parameters will be derived in the following paragraphs. The maximum voltage that can be induced onto a pick-up is referred to as open circuit voltage. From (1.1), open circuited voltage v_{oc}, of the coupled system is given by:

$$v_{oc} = j\omega M i_1 \tag{1.6}$$

The maximum current that can be sourced by a pick-up is referred to as short circuit current, i_{sc}, is given as follows:

$$i_{sc} = \frac{v_{oc}}{j\omega L_2} = \frac{M i_1}{L_2} \tag{1.7}$$

The uncompensated power transferred to the load is related to v_{oc} and i_{sc} is referred to as P_{su}. It represents the maximum VA rating of the pick-up

$$P_{su} = v_{oc} i_{sc} = \frac{\omega M^2 i_1^2}{L_2} \tag{1.8}$$

Now, the output power, P_o, can be calculated, by ignoring power dissipation in the winding of the pick-up as follows:

$$P_o = \frac{v_2^2}{R_L}$$
$$= \frac{e_2^2}{R_L}$$
$$= \frac{(\omega M i_1)^2}{R_L} \tag{1.9}$$
$$= \left(\frac{\omega M^2 i_1^2}{L_2}\right)\left(\frac{\omega L_2}{R_L}\right)$$
$$P_o = \frac{\omega M^2 i_1^2}{L_2} Q_{2,L} \tag{1.10}$$

From (1.8) and (1.10)

$$P_o = P_{su}Q_{2,L} \tag{1.11}$$

Where, $Q_{2,L}$ is the loaded quality factor of the tuned secondary, $Q_{2,L} = \dfrac{\omega L_2}{R_2 + R_L} \approx \dfrac{\omega L_2}{R_L}$ as $R_L \gg R_2$. It is important to consider the distinction that the quality factor of the coil (native/intrinsic quality factor) is defined considering the winding resistance as $Q_2 = \dfrac{\omega L_2}{R_2}$.

Another, alternative way of writing the output power equation (1.11) [20] is

$$
\begin{aligned}
P_o &= \frac{\omega M^2 i_1^2}{L_2}Q_{2,L} \\
&= \omega L_1 i_1 \times i_1 \times \frac{M^2}{L_1 L_2} \times Q_{2,L} \\
&= v_1 i_1 k^2 Q_{2,L}
\end{aligned}
\tag{1.12}
$$

The output power in (1.12), suggests that the IPT system scales the input VA by the square of coupling and loaded quality factor of the secondary. This further exemplifies the effect of a magnetic design which enhances the power exponentially. The effect of frequency is contained with the voltage expression of the primary indicating that the frequency can increases the power transfer until maximum VA limit is reached. For a given frequency, the NI product of the magnetics can be increased so as to enhance power transfer until maximum VA rating is hit.

The output power equations are derived here for a series tuned pick-up, but they are conserved for a parallel tuned pick-up with the difference that loaded quality factor is given as $Q_{2,L} = \dfrac{R_2 + R_L}{\omega L_2}$.

Power losses occur in the magnetics in copper losses and eddy losses (skin and proximity) in the coil resistances, iron losses in the ferrites and eddy losses in Al shield. Also, in the compensation network, ESR of the capacitors result in power losses. Finally, the semiconductors used in the various power conversion stages of IPT systems also contribute to inefficiency.

From (1.5) and further analysis, assuming that the resonant angular frequency is ω_0, the magnetic efficiency, η_{SS}, of a SS IPT topology is given by

$$
\begin{aligned}
\eta_{mag} &= \frac{i_2^2 R_L}{i_1^2 R_1 + i_2^2 R_2 + i_2^2 R_L} \\
\eta_{mag} &= \frac{R_L}{(R_L + R_2)\left(1 + R_1 \frac{(R_2 + R_L)}{\omega_0^2 M^2}\right)}
\end{aligned}
\tag{1.13}
$$

It is evident that the efficiency increases with decrease in resistance of charge-pads. Also, η_{mag} increases with an increase in $(\omega_0 M)$. In order to maximize the power transfer efficiency, a figure of merit (FOM) has been derived for IPT systems in [22] as

$$FOM = kQ \tag{1.14}$$

where k is the coupling coefficient, $k = M/\sqrt{L_1 L_2}$ and $Q = \sqrt{Q_1 Q_2}$. $Q_1 = (\omega L_1)/R_1$ and $Q_2 = (\omega L_2)/R_2$ are the intrinsic quality factors of the primary and secondary coils. This FOM is used for optimization of IPT magnetics and emphasises that the efficiency of an IPT system can be maximised with $(\omega_0 M)$ and/or reduction in the series resistances of the charge-pads.

1.3   Features of IPT Charge-pad

IPT charge pads particularly for EV charging applications have a number of distinct features and they are discussed below:

- **Charge-pad nomenclature**
  A number of different classifications of charge pads are presented in literature. This section covers some important distinctions.

  Lumped IPT systems usually employ a concentrated coil in a charge-pad design. However, distributed IPT systems consist of a large track that can power one or more pick-ups. As expected, lumped systems have higher coupling (typically $0.1 < k < 0.5$) than distributed systems (typically $k < 0.1$).

  Single sided-charge pads have magnetic flux that is restricted to a plane above the charge-pad. However, in case of a double-sided charge-pad, magnetic flux path is also present below the charge-pad. Double-sided pads create undesirable leakage flux that doesn't couple with a pick-up. Hence, a polarised charge-pad is usually considered in IPT systems.

  A multi-coil (segmented) charge-pad is composed of multiple single coils that usually run currents in opposite direction ($\phi = 180°$). This creates a flux pattern (horizontal flux) that is directionally oriented from one coil to the other. Such a charge-pad is also called as a polarised charge-pad. A quadrature coil is one that runs a current in quadrature ($\phi = 90°$) such that the flux from it doesn't couple with the flux from a non-quadrature coil in its vicinity.

- **Misalignment tolerant design**
  IPT systems for EV charging need tolerance to alignment for charging at required power levels at high efficiency. Misalignment tolerant IPT designs are of importance for applications including material handling involving distributed IPT systems (long wires/tracks). Also, for stationary EV charging (typically ± 100 mm) and dynamic

powering of EVs using lumped charge-pads, misalignment tolerance is an important criterion. This work studies the effect of misalignment and also performs magnetic modelling of its effect using coil shapes.

- **Electromagnetic safety**
  The leakage fields that permeate the space around the charge-pad can impact both the health of a living entity in close proximity. It can also result in unwanted heating of foreign objects that are closeby. Different regulating bodies have published standards for limiting exposure - ICNIRP (International Commission on Non-Ionizing Radiation Protection), IEEE etc. The frequency dependence of these limits for time-varying alternating fields is set as a limit for optimization in this thesis. However, circuitry and control strategies for foreign object detection and living object protection is beyond the scope of this thesis.

- **Interoperability**
  For a new technology like IPT for EVs to be developed where there exists a large number of design variants including magnetic topology, frequency of operation, power levels, z-gaps and safety related detection circuitry, standards are required to create consensus on several dimensions. The SAE (Society of Automotive Engineers) is working on an upcoming standard J2954. A small band of frequency around 85 kHz ($81.39 - 90$ kHz) is being allocated for light EV IPT wireless charging for four power classes ($3.7, 7.7, 11, 22$ kW) [23]. It is expected that in the future different designs for charge-pads will be interoperable with each other, leading to seamless power delivery between asymmetrical charge-pads

- **Power density of charge-pads**
  Compact charge-pads are the demand of EV manufacturers. Thus, optimization of magnetics keeping power-density as high, while reducing weight of the charge-pad is an important requirement in practical systems.

1.4   Magnetic Fields for Self-Healing Roads

Typically roads are made of porous asphalt concrete in the Netherlands. Porous asphalt concrete has advantages over dense graded asphalt concrete with respect to noise reduction and water drainage. However the porous structure does not benefit from the durability of asphalt and will cause premature raveling of the road [24]. Asphalt concrete is a self-healing material [25]. Micro cracks are formed in the material when it is exposed to a sufficiently large stress or strain. The self-healing (molecular rearrangement) process will start after the load that generated the damage has been removed.
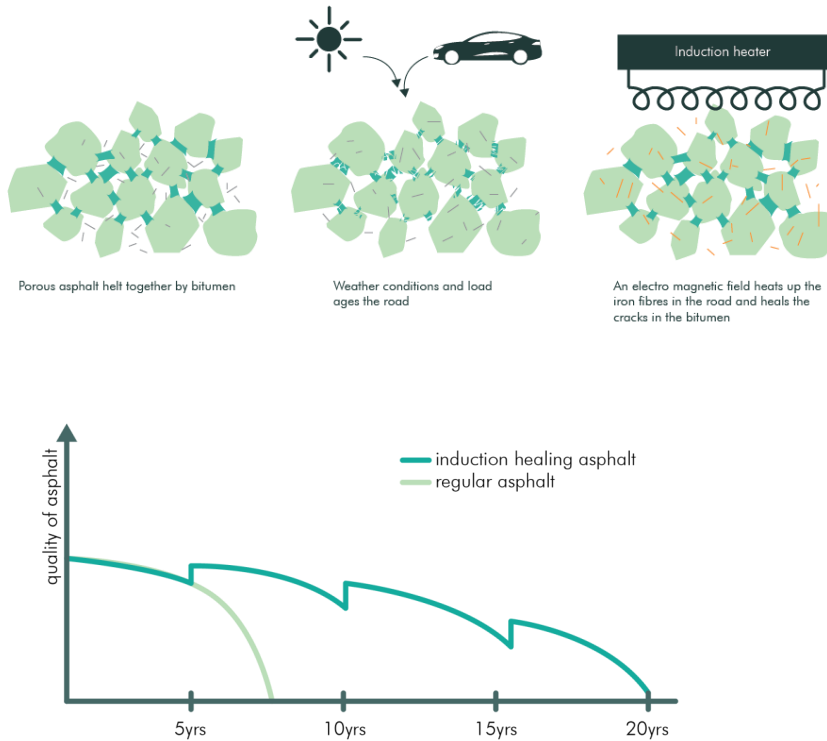
Figure 1.5: The process of induction heating of self-healing roads and the resulting increase in life span of the roads.

The heating can be done using different methods, but induction heating is preferred over other methods because it does not contaminate the asphalt, can provide a good distribution of the heating power inside the asphalt and it is possible to properly control the amount of heat generated [27]. For the asphalt to be heated by means of induction it first needs to be conductive. Thus, eddy currents are induced in the asphalt by mixing additives in the asphalt, like graphite or steel wool. Asphalt which is treated with such additives is referred to as inductive healing asphalt (IHA). The most effective form of IHA researched in [28] consists of an equal distribution of 3.2, 6.4, and 9.5 mm of grade 00 steel wool. This porous asphalt concrete when heated to 85 °C and rested for a period of 3 to 6 hours could recover 70 % to 85 % of their original strength [28]. A description of induction heating for self-healing is indicated in Fig. 1.5.

1.4.1 Research Question

Transportation based on EVs powered by clean electricity can become feasible if the cost of EV comes down drastically. A major burden for EV acceptance is the large battery size which adds cost, volume and weight to the vehicle. Magnetic energy transfer using IPT offers a reliable alternative by pumping small packets of energy from the road to EV while driving, which can then be used for charging the battery and/or for the propulsion drive train. In addition, a barrier to this development is the burden of infrastructure that has been designed to be applied to ICE based vehicles.

A novel technology for upgrading the road infrastructure is the low maintenance self-healing roads. These twin applications of magnetic fields in conjuncture with renewable energy utilization is expected to hasten the roadway transition to EVs in a smooth manner. However, each individual technology as a standalone development is usually being researched analysed and improved. Thus, a combination of these technologies can pose integration challenges due to interdependencies and this thesis tries to model them and also propose viable solutions to combine them. In this context, the following question forms the basis of this research thesis:

How to model and apply magnetic fields in the future roads to make energy transfer and low maintenance roads a reality?

While this is a broad objective, this thesis does try to understand and open doors of several issues specific to magnetics in a future roadway where several technologies will amalgamate. It is meant to serve as a mature treatment of inductive energy transfer and as an opening into the area of combined inductive energy/healing roadways. The background of the field of inductive healing asphalt is material sciences. The electrical engineering treatment of this subject and the multi-disciplinary nature of this objective means that some results are being used to optimize materials in a quest for better performance.

It is difficult to predict if these technologies will certainly be implemented in the future. However, some attempt has been made to understand the benefits of their combination and also to bridge the gap between research and industrial implementation also by raising genuine cautions and suggesting viable alternatives.

Thesis Objectives

The following are the main goals of this thesis as summarized from the research question:

- Identify, classify and evaluate analytical and semi-analytical techniques for magnetic energy transfer charge-pads.

- Make a classification using a selected analytical technique of several coupler shapes and use performance based figures of merit to identify misalignment-tolerant couplers.

- Mathematically model, classify and perform experiments on the effect of magnetic fields due to misalignment.

- Perform a multi-objective optimization to select a particle that fulfils the application selected and perform experiments on a lab-scale demonstrator for energy transfer using magnetic fields. In addition, perform validation of magnetic models developed.

- Study the economic implications of inductive power transfer systems.

- Model the losses in inductive healing asphalt and propose an integrated technology roadway combining magnetic fields for energy transfer, healing and renewable energy utilization.

1.4.2   Thesis Outline

The objective of this thesis is in the modelling and application of magnetic fields in the road for power transfer using IPT and for healing potholes using induction heating. IPT being the backbone technology, this thesis develops a fundamental analytical model to describe the effect of shapes of couplers on the system performance during energy transfer. An important scientific contribution being the development of analytical models for single-coil IPT air-cored couplers and their extension to multi-coil couplers. Based on this initial shape optimization, the chosen coupler is then used to perform a detailed optimization. An important problem that affects systems that transfer magnetic fields as the energy source is that of misalignment, this problem has been mathematically analysed, experimented and classified as lateral and longitudinal. Misalignment impacts power transfer and edge effects are exacerbated in applications involving distributed IPT systems.

Any engineering problem where several targets need to be met would mean that an optimization is necessary to establish trade-offs. Multi-objective optimization based on Particle Swarm Optimization (PSO) is used in this thesis to perform an efficiency (η), weight (w) and area-power density (α) pareto analysis of a 1kW prototype IPT system. The power electronic system is designed with wide-bandgap devices to perform operational testing. Finally, two highway based case studies, one involving the technical challenges in integrating the various technologies for future roadways and another involving the economic feasibility of IPT systems is carried out.

The various chapters that are part of this thesis are visualised in Fig. 1.6 and listed below:

- **Chapter 2 : Analytical and Semi-Analytical Techniques for Coil Design of IPT Systems - An Overview**
  A historical approach of outlining significant milestones in the area of inductance and mutual inductance computations is carried out in this chapter. The extraction of magnetic parameters is classified as field evaluation techniques and their analysis as circuit evaluation techniques. Field evaluation has been considered with general magnetic problems and problems involving different media in focus. Applications of field
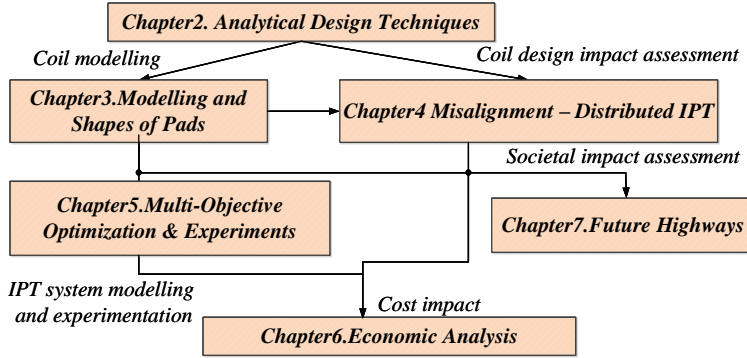
Figure 1.6: Interdependencies and flow of various chapters in the thesis.

evaluation techniques considered are Biot-Savart Law, Neumann's integral, Schwarz-Christoffel mapping, Partial Inductance and Method of Images. Circuit evaluation techniques involving both electric circuit and magnetic circuits are presented.

- **Chapter 3 : Analytical Modelling and Study of Shapes for IPT Systems**
  The focus of this chapter is to apply electromagnetic analysis in order to compute inductances and mutual inductances and extract the coupling from the same. Neumann's integral is a powerful technique so as to calculate these parameters. The computation has been carried out for air-cored coils considering a number of coil shapes in mind. The concept of linearity is explored to extend the discussion to multi-coil geometries. The results obtained can be used for comparing various coil shapes for utilization in IPT applications. This step yields a coil shape that is subsequently used for a detailed optimization.

- **Chapter 4 : Study of Misalignment in Sectional IPT Systems**
  This chapter deals with distributed IPT systems. Specifically, it deals with variation of mutual inductance referred to as misalignment. Biot-Savart's law is used to perform analytical computation of mutual inductance subjected to both x-directional and y-directional misalignment. These misalignment characteristics are referred to as lateral and longitudinal misalignment. Conventional sectional tracks are subjected to unsymmetrical misalignment at their ends. This is as a result of edge effect and is experimentally verified and a design that offsets this problem is suggested.

- **Chapter 5 : Multi-Objective Optimisation and Experimental Analysis of a DR IPT System for Light EVs**
  This chapter looks into the 3-D magnetic evaluation of IPT systems. The various materials present in an IPT charge pad- copper coils, ferrites for field shaping and Al shield are considered in this study. The multi-objective optimization of a DR charge-pad for a 1kW IPT system keeping targets of maximizing efficiency and area-power

density, while minimizing weight $(\eta - \alpha - w)$. A lab scale prototype is built and experimented using a SiC H bridge inverter.

- **Chapter 6 : Economic Analysis of IPT Systems : A Case Study**
  This chapter considers the economic implications of IPT systems particularly with regard to a bus fleet. A generic methodology is described to determine the driving range of any EV with variable gross mass and frontal area. A dynamic power consumption model is developed for the EV, also exploring the trade-offs between percentage road coverage, transport efficiency and change in on-board storage with economics as the backbone.

- **Chapter 7 : Challenges and Interdependencies of Future Sustainable Roads**
  Road based technologies like electric vehicles (EVs), driving range enhancing contactless charging, lifetime time enhancing self-healing roads and in-situ energy generating elements are considered in this chapter. The technical challenges of integrating different emerging on-road technologies are analytically and experimentally researched. Finally, case study of a future highway and with these technologies are considered as an example.

Analytical and Semi-Analytical Techniques for Coil Design of IPT Systems - An Overview

The rising applications in the field of Inductive Power Transfer prompts a look at various analytical tools to perform magnetic design. This chapter aims to classify, evaluate and apply different analytical techniques for magnetic modelling of inductively coupled air-cored power transfer systems. To model such a system, magnetic parameters - L, M, k etc. need to be computed and this is referred to as field evaluation. Next, the circuit modelling techniques to evaluate efficiency, losses and power transfer include both electric circuit and magnetic circuit analysis. An application example of self-inductance by analytical computations is considered and validated using FEM simulations and by performing experiments. Modelling challenges for multi-coil design is elaborated, discussing leakage constraints and an IPT design methodology.

Based on

- V. Prasanth, P. Bauer, J. A. Ferreira, and H. Polinder, "Review of analytical methods to extract magnetic parameters of an inductively coupled circuit," in *IEEE PELS Emerging Technologies: Wireless Power (WoW)*, 2015, pp. 1–8; and

- V. Prasanth, P. Bauer, J. A. Ferreira, and H. Polinder, "Analytical and Semi-Analytical Techniques for Modelling the Magnetics of Air-Cored IPT Systems," in *IEEE Transactions on Industrial Applications*, 2017, (Submitted).

2.1 Introduction

Magnetically coupled coils transfer energy by means of an alternating magnetic field between a source and load that are not placed in contact. This technique of wireless or contactless energy transfer that relies on induction is also referred to as Inductive Power Transfer (IPT) [18], [29]. Wireless inductive power can be propagated over a short distance as well as over large distances in vacuum or in a media. In case of far-field applications, electromagnetic waves propagate in an omnidirectional manner with the transmitter and receiver designated as an antenna [30]. Here, power can be transferred to distances several times the dimensions of the antenna [30]. Typical examples of this technique include UHF RFID [30] and Microwave Power Transfer in Space Solar Power [31].

In case of near-field IPT systems, energy is transferred to short distances which is typically an order of the dimension of coil [32]. Whether far-field or near-field, wireless IPT operates on Tesla's concept of tuned resonances for both transmitter and receiver [32], resulting in nullification of reactive power demand and enhancing the active power flow to the load.

To model a system of magnetically coupled coils, a preliminary assessment is presented in [33]. The field parameters (magnetic field intensities, magnetic flux densities, self and mutual inductances, coupling coefficients) are calculated as a first step in the magnetic modelling. The analytical techniques that can be used to evaluate these field parameters are classified as field modelling techniques. Once the field model is described, circuit parameters such as currents, voltages, power, energy and efficiency need to be computed. This can be carried out by using the circuit modelling techniques. The field and circuit modelling techniques are classified in Fig. 2.1. The various analytical techniques applied have been derived from first principles.
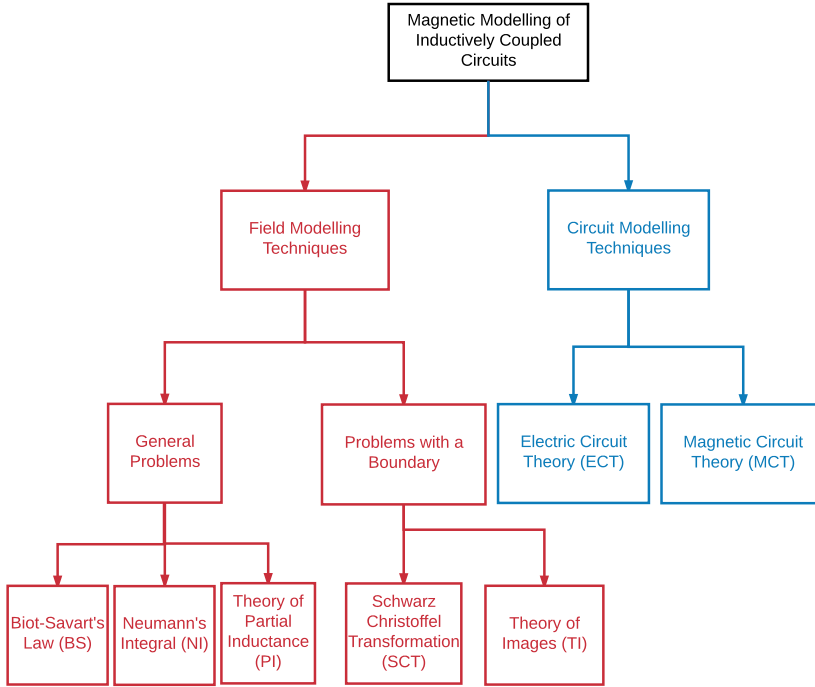
Figure 2.1: Field and circuit modelling techniques of magnetic problems based on electromagnetic analytical and semi-analytical techniques.

2.2 Background History

The two distinct branches of magnetism and electricity merged into unison with the discovery by Ørsted that electric currents create magnetism in 1820. With Ampère's (1826) discovery of the attraction of electric conductors and Faraday's experiments (1831) subsequently leading to the understanding of magnetic fields as lines of force, there was an increased focus in the field of electromagnetism. Both these along with Gauss's law on magnetism and electricity were presented mathematically by Maxwell (1873) in his seminal work – "A treatise on Electricity and Magnetism" and henceforth these equations were referred to as Maxwell's equations [34]. Induction coils, influenced by the work of Faraday, Henry and Page, were first developed by Callan (1836) who used dc from a galvanic cell through an interrupter (Callan's repeater) to produce rate of change of magnetic flux and demonstrated induction between coils [35], [37]. They are shown in Fig. 2.2. Following this, a number of induction coils were developed including that of Ruhmkorff [35]. The first transformer was invented by Zipernowski, Blâthy and Déri (ZBD Transformer) and patented in 1885. Following this, Westinghouse and Stanley improved the design made it

Figure 2.2: Callan's induction coils, produced sparks upto 15 inches (38.1 cm) and helped Callan recognize that induction depended on the rate of interrupting the circuit. This achievement was unchallenged till 1890 [35], [36].

possible to manufacture the same in a commercially viable and easy manner in the United States [37]. Westinghouse also had firm faith in the applications of alternating current and obtained exclusive rights to Nikola Tesla's patents for the polyphase system of alternating current (1888) [38]. In the period between $1890 - 1910$, Tesla experimented with resonant coils, referred to popularly as Tesla Coils and even unsuccessfully tried sending power in space leading to the eventual decommissioning of the famous Wardenclyff Tower in 1917 [39].

Since the time of Ørsted, inductance has played an important role so as to quantify the magnetic fields associated with the flow of electric currents. Inductances of circular geometries classically have been addressed by Kirchhoff, Rayleigh, Lorentz, Maxwell [41] etc. From the early 1900s, published works including those of Butterworth who studied the self and mutual inductance of various coils and also studied eddy currents and skin effect [42], [43]. A large bibliography of references covering inductances are available in Hak's "Eisenlose Drosselspulen" (1938) and Grover's "Inductance Calculations" (1946) [44]. Wheeler (1958) treated a pair of coaxial and coplanar spherical coils as an antenna and also studied its self-resonance [45]. Grover's tabulation method involving calculating GMD (Geometric Mean Distance) as defined by Maxwell is used rather extensively even today [46]. However, zeroth and first order calculations are only considered accurate with loosely coupled coils and short coils considered inaccurate $[35] - [38]$. Also, GMD being approximate and only valid for infinitely long structures makes the tabulation method inaccurate for finite length computations [47]. In case of physical measurements of mutual inductance, Campbell working at the National Physical Laboratory (1907) made the measurement standard for both inductances and mutual inductances [48]. It was made of two layers of coils, 75 turns each and made of bare wires in the form of a helix that served as the primary and wound over marble. The marble was cylindrical of 30 cm diameter. The secondary consists of 488
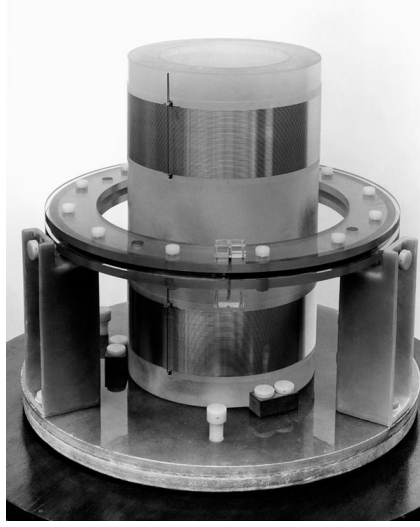
Figure 2.3: Campbell's mutual inductance standard [40]. It still serves as the primary standard in many metrology laboratories across the world.

turns in a $1\ cm^2$ section with the nominal value of mutual inductance close to 10 mH [49]. Such a standard is shown in Fig. 2.3. Over the years, mutual inductance computations are made using either the Campbell calculable mutual inductor method [42] $-$[44] or by using the bridge methods such as Campbell Bridge, Foster Bridge [50], [51] etc.

2.3 Generalized n-Coupled Coil System

It is useful to think of a multi-coil system so as to define and evaluate its magnetic parameters. A three coil system $(n = 3)$ and its flux linkage is represented in Fig. 2.4. When a pure sinusoidal voltage is applied to coil 1, according to Faraday's law the induced emf, e_1 is related to the time-rate of change of magnetic flux linkage, ψ_1 as [52].

$$e_1 = \frac{d\psi_1}{dt} = \frac{d}{dt} \iint\limits_{S_1} \overrightarrow{\mathbf{B_1}} \cdot d\overrightarrow{\mathbf{S}} = \frac{d}{dt} \oint\limits_{C_1} \overrightarrow{\mathbf{A_1}} \cdot d\overrightarrow{\mathbf{l}} = \frac{d\left(L_1 i_1\right)}{dt} \tag{2.1}$$

In the above equation, S_1 is the surface enclosed by the wire, $d\overrightarrow{\mathbf{S}}$ is an elementary surface, C_1 is the contour along the length of the wire in the direction of current flow and $d\overrightarrow{\mathbf{l}}$ is its elementary length. Now, when the other two coils are brought closer, the current
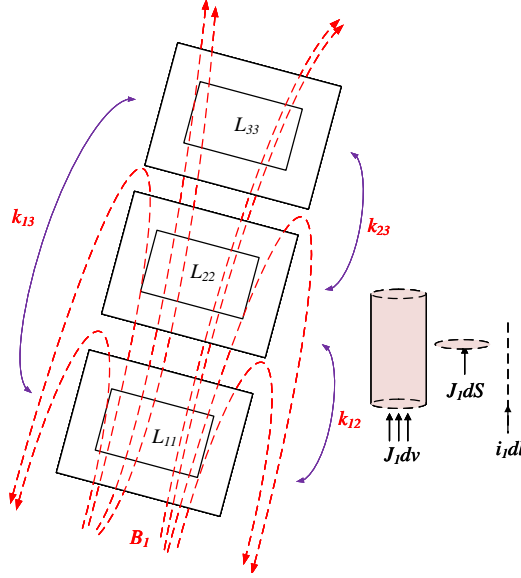
Figure 2.4: Flux linkage in a three coil system. An excitation current in the circuit applied to coil 1 can be quantitatively represented in terms of a volume density (Jdv) or surface density (JdS) or a median line current (idl). Also, the magnetic vector potential due to current i_n in n^{th} coil is 'A_n' that results in a flux density 'B_n'. The flux lines due to exciting current in the coil 1 acting independently is shown in the above figure and the coupling between the coils are represented as k_{12}, k_{13} and k_{23}.

flowing through one of them can induce a voltage onto the other. This ability to transfer energy between magnetically coupled coils is measured with mutual inductance. For a linear circuit, the total energy stored in the magnetic field U_m can be written in terms of the self-inductance ($L_{mm}, m = 1 - 3$) and mutual inductances ($L_{mn}, m \neq n$) as

$$U_m = \frac{1}{2}L_{11}i_1^2 + \frac{1}{2}L_{22}i_2^2 + \frac{1}{2}L_{33}i_3^2 + L_{12}i_1i_2 + L_{23}i_2i_3 + L_{13}i_1i_3 \qquad (2.2)$$

Now, the total voltage in coil 1 is given as

$$v_1 = i_1R_1 + L_{11}\frac{di_1}{dt} + L_{12}\frac{di_2}{dt} + L_{13}\frac{di_3}{dt} \qquad (2.3)$$

Or, the induced voltage in the primary inductor is given by

$$e_1 = L_{11}\frac{di_1}{dt} + L_{12}\frac{di_2}{dt} + L_{13}\frac{di_3}{dt} \tag{2.4}$$

Here, L_{11} is the self-inductance of coil 1 and L_{12}, L_{13} are the mutual inductance between coil 1 & coil 2 and coil 1 & coil 3 respectively. They are mathematically defined in terms of magnetic flux densities as

$$L_{11} = \frac{1}{i_1} \iint\limits_{S_1} \overrightarrow{\mathbf{B_1}} \cdot d\overrightarrow{\mathbf{S}}$$

$$L_{12} = \frac{1}{i_1} \iint\limits_{S_2} \overrightarrow{\mathbf{B_1}} \cdot d\overrightarrow{\mathbf{S}} = \frac{1}{i_2} \iint\limits_{S_1} \overrightarrow{\mathbf{B_2}} \cdot d\overrightarrow{\mathbf{S}} \tag{2.5}$$

$$L_{13} = \frac{1}{i_1} \iint\limits_{S_3} \overrightarrow{\mathbf{B_1}} \cdot d\overrightarrow{\mathbf{S}} = \frac{1}{i_3} \iint\limits_{S_1} \overrightarrow{\mathbf{B_3}} \cdot d\overrightarrow{\mathbf{S}}$$

For a general case, the induced emf in the nth coil can be written as

$$e_n = L_{n1}\frac{di_1}{dt} + L_{n2}\frac{di_2}{dt} + ... + L_{nn}\frac{di_n}{dt} \tag{2.6}$$

For a system of $n-$coupled windings, the coupling coefficient between the ith coil and j^{th} coil can be defined as

$$k_{ij} = \frac{M_{ij}}{\sqrt{L_i L_j}} \tag{2.7}$$

Finally, the voltage equation for the system can be written as

$$
\begin{bmatrix} v_1 \\ v_2 \\ \vdots \\ v_n \end{bmatrix} =
\begin{bmatrix} R_1 & 0 & \cdots & 0 \\ 0 & R_2 & \cdots & 0 \\ \vdots & \vdots & \vdots & \vdots \\ 0 & 0 & \cdots & R_n \end{bmatrix}
\begin{bmatrix} i_1 \\ i_2 \\ \vdots \\ i_n \end{bmatrix} +
\begin{bmatrix} L_{11} & L_{12} & \cdots & L_{1n} \\ L_{21} & L_{22} & \cdots & L_{2n} \\ \vdots & \vdots & \vdots & \vdots \\ L_{n1} & L_{n2} & \cdots & L_{nn} \end{bmatrix}
\begin{bmatrix} \frac{di_1}{dt} \\ \frac{di_2}{dt} \\ \vdots \\ \frac{di_n}{dt} \end{bmatrix}
$$

$$
=
\begin{bmatrix} R_1 & 0 & \cdots & 0 \\ 0 & R_2 & \cdots & 0 \\ \vdots & \vdots & \vdots & \vdots \\ 0 & 0 & \cdots & R_n \end{bmatrix}
\begin{bmatrix} i_1 \\ i_2 \\ \vdots \\ i_n \end{bmatrix} +
\begin{bmatrix} L_{11} & k_{21}\sqrt{(L_1 L_2)} & \cdots & k_{1n}\sqrt{(L_1 L_n)} \\ k_{12}\sqrt{(L_1 L_2)} & L_{22} & \cdots & k_{2n}\sqrt{(L_2 L_n)} \\ \vdots & \vdots & \vdots & \vdots \\ k_{1n}\sqrt{(L_1 L_n)} & k_{2n}\sqrt{(L_2 L_n)} & \cdots & L_{nn} \end{bmatrix}
\begin{bmatrix} \frac{di_1}{dt} \\ \frac{di_2}{dt} \\ \vdots \\ \frac{di_n}{dt} \end{bmatrix}
\tag{2.8}
$$

2.4 Analytical and Semi-Analytical Methods to Evaluate Magnetic Parameters

Electromagnetic problems can be solved for inductive parameters analytically by starting with field extractions from Maxwell's equations. In case of analytical techniques, exact solutions are derived by solving the PDEs. However, analytical techniques can be applied only to certain class of problems due to complexity of calculations. While in case of numerical techniques, numerically approximate steps are performed to arrive at a solution to an electromagnetic problem. The accuracy of such solutions depends on the modelling - discretization and computational resource available. Semi-analytical techniques combine both analytical and numerical solutions to a problem.

2.4.1 Field Modelling Techniques

Field modelling techniques form the first step in magnetic modelling. Here, the field parameters are evaluated using the magnetic field definitions and inductance definitions presented in Section 2.3 and can be further used to calculate coupling.

Application of Biot-Savart law
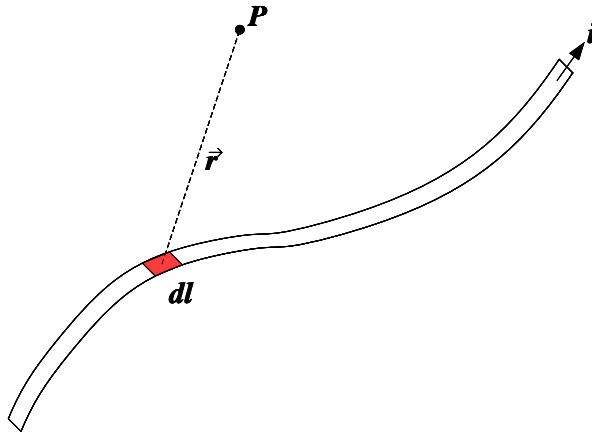
Figure 2.5: Application of Biot-Savart law at a point P due to current element $id\,\overrightarrow{\mathbf{l}}$. The flux density at any point is perpendicular to both the current element and the position vector of that point.

The flux density $d\overrightarrow{\mathbf{B}}$ at any point due to a current element $id\overrightarrow{\mathbf{l}}$ and displaced by $\overrightarrow{\mathbf{r}}$ with the unit vector along its direction, $\hat{\mathbf{r}}$ is given by applying Biot-Savart law as shown in Fig. 2.5. This vector is perpendicular to both $d\overrightarrow{\mathbf{l}}$ as well as $\overrightarrow{\mathbf{r}}$.

$$d\overrightarrow{\mathbf{B}} = \frac{\mu_0}{4\pi}\frac{id\overrightarrow{\mathbf{l}}\times\hat{\mathbf{r}}}{r^2} \tag{2.9}$$

By applying the principle of superposition, the flux density can be obtained as a line integral in the direction of conventional current along the contour C.

$$\overrightarrow{\mathbf{B}} = \frac{\mu_0}{4\pi}\int_C \frac{id\overrightarrow{\mathbf{l}}\times\hat{\mathbf{r}}}{r^2} \tag{2.10}$$

Now, this flux density can be used to calculate the self and mutual inductance by defining the magnetic flux linkages of coil 1 (ψ_1) and that linking coil 2 due to current in coil 1 (ψ_{12}) as

$$L_1 = \frac{\psi_1}{i_1} = \frac{1}{i_1}\iint_{S_1}\overrightarrow{\mathbf{B_1}}\cdot d\overrightarrow{\mathbf{S}}$$
$$L_{12} = M = \frac{\psi_{12}}{i_1} = \frac{1}{i_1}\iint_{S_2}\overrightarrow{\mathbf{B_1}}\cdot d\overrightarrow{\mathbf{S}} \tag{2.11}$$

The coupling can then be obtained from (2.7). Closed form expression for various shapes are presented in [53], [54]. In published work, code that takes the complex geometry as a combination of circular loops, helix and straight lines are presented in [55]. For an analytical expression of a rectangular cross sectional wire using elliptical integrals, the work in [56] presents a detailed analysis. The inductances of air-gap generators is presented in [57]. In [58], the analytical expressions for curved conductors are derived. Also, as an extension to the work, in [59], rectangular busbars and annular arc-shaped conductors are analysed. Analytical results for both self and mutual inductances are presented in the form of complete elliptical integrals of the first and second kind and by use of *Heuman's Lambda* function in [47]. Also, in the field of Inductive Power Transfer (IPT) that is seeing a flurry of applications utilizing loosely coupled coils, coils with circular and square geometries are compared using Biot-Savart law in [60]. Finally, in case of distributed IPT systems for on-road dynamic power transfer, a coil misalignment model and the concept of edge effect is introduced in [17].
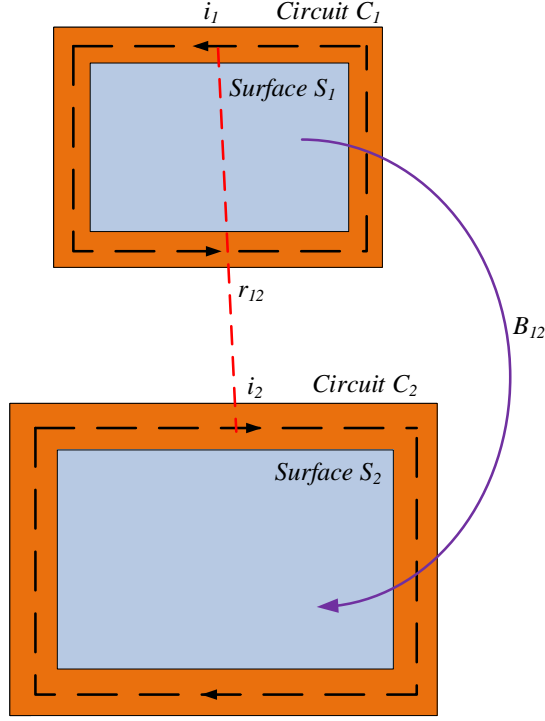
Figure 2.6: Defining the Neumann integral by considering two current loops with the contours (C_1, C_2) along the boundary of any surface (S_1, S_2) [61].

Application of Neumann's integral

To derive the Neumann's integral equation, consider two circuit loops C_1 and C_2, with current i_1 flowing through C_1 as shown in Fig. 2.6. This current creates a potential in C_2 which in turn runs a current i_2 through C_2. In such a case, the mutual inductance L_{12} of the first coil can be written from (2.5) in terms of the magnetic vector potential, $\overrightarrow{\mathbf{A}}$ as

$$M = L_{12} = \frac{\psi_{12}}{i_1} = \frac{1}{i_1} \iint_{S_2} \overrightarrow{\mathbf{B_1}} \cdot d\overrightarrow{\mathbf{S}} = \frac{1}{i_1} \oint_{C_2} \overrightarrow{\mathbf{A_1}} \cdot d\overrightarrow{\mathbf{l_2}} \qquad (2.12)$$

Since $\overrightarrow{\mathbf{A_1}}$ is created due to i_1 flowing through C_1, the flux linkage in circuit C_2 is given by defining $\overrightarrow{\mathbf{r_{12}}}$ as the distance between the current elements in C_1 and in C_2 as

$$A_1 = \frac{\mu_0}{4\pi} \oint_{c_1} \frac{i_1 \overrightarrow{d\mathbf{l_1}}}{r_{12}} \tag{2.13}$$

Now, the mutual inductance between the two loops can be written as [44], [61]

$$M = L_{12} = \frac{\psi_{12}}{i_1} = \frac{\mu_0}{4\pi} \oint_{c_1} \oint_{c_2} \frac{\overrightarrow{d\mathbf{l_1}} \cdot \overrightarrow{d\mathbf{l_2}}}{r_{12}} \tag{2.14}$$

Hence, the mutual inductance is dependent on the geometry of the two coils as well as the permeability of the media containing them. Also, the integral in (2.14) is order independent and hence proves the symmetrical nature of L_{12} and L_{21} ($L_{12} = L_{21}$) for a linear magnetic system of coils. On the other hand, the self-inductance of C_1 in Fig. 2.6 can be obtained by evaluating the double integral in (2.14) with contours C_1 and $C_{1'}$ such that C_1 is along the interior edge of the wire and $C_{1'}$ is along the filamentary current along the center of the wire [44].

$$L_{11} = \frac{\psi_1}{i_1} = \frac{\mu_0}{4\pi} \oint_{c_1} \oint_{c_{1'}} \frac{\overrightarrow{d\mathbf{l_1}} \cdot \overrightarrow{d\mathbf{l_{1'}}}}{r_{11'}} \tag{2.15}$$

This integral has been solved for linear conductors in [54], [62]. This techniques has been applied to calculate inductances of spiral geometries [63], end winding leakage inductance [64], [65], partial mutual inductance of on-chip interconnects [66], in planar PCB mutual inductance calculations [67], in magnetic resonant coupling [68] among many others.

Application of Partial Inductance

A powerful tool to compute the magnetic parameters of complicated geometry is that of the method of partial inductances. This technique as conceptualized through the works of Grover [44] , Kaden [69] and Ruehli [70] on PEEC (Partial Element Equivalent Circuit) involves the consideration of inductances of sections of a closed loop of wire which on summing up gives the total inductance of the closed circuit. The form of such an inductance is based on (2.15) and is written as a summation of self and mutual partial-inductances given by

$$L_{11} = \frac{\psi_1}{i_1} = \frac{1}{i_1} \oint_{C_2} \overrightarrow{\mathbf{A_1}} \cdot \overrightarrow{d\mathbf{l_2}} = \frac{1}{i_1} \iint_{S_2} \overrightarrow{\mathbf{B_1}} \cdot \overrightarrow{d\mathbf{S}} = \frac{1}{i_1} \left[\sum_{i=1}^{n} \oint_{C_i} \overrightarrow{\mathbf{A_i}} \cdot \overrightarrow{d\,\mathbf{l}} \right] \tag{2.16}$$

According to [61], the self partial inductance of the ith loop is given as $L_{pi} = \frac{1}{i_1} \oint_{C_i} \overrightarrow{\mathbf{A_i}} \cdot \overrightarrow{d\,\mathbf{l}}$ and is physically defined as the ratio of magnetic flux through a surface bounded by infinity
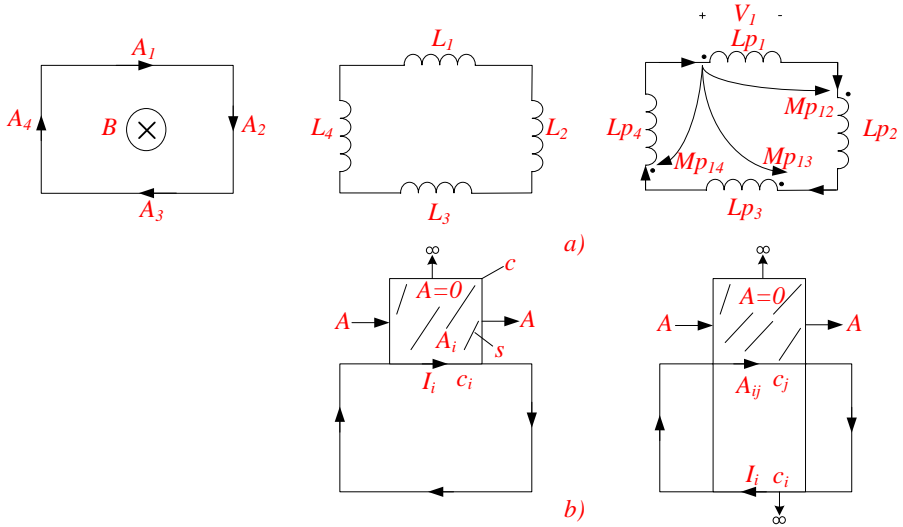
Figure 2.7: a) A rectangular loop with the self partial inductances and the mutual partial inductances defined b) The physical definitions of self and mutual partial inductances by considering a contour extending to infinity enclosing a surface where the flux is considered [61].

and the conductor itself to the current through the segment. Also, the mutual partial inductance between two current carrying segments (of same or different conductors) is defined in [61] as the ratio of that magnetic flux created by the first segment that links the surface bounded between the second conductor and infinity. The definition of partial inductances (self and mutual) is shown in case of a rectangular conductor as in Fig. 2.7. The mutual partial inductance is given as

$$M_{pij} = \frac{1}{i_i} \oint_{C_i} \overrightarrow{\mathbf{A_{ij}}} \cdot d\overrightarrow{\mathbf{l}} = \frac{\mu_0}{4\pi} \oint_{c_i} \oint_{c_j} \frac{d\overrightarrow{\mathbf{l_1}} \cdot d\overrightarrow{\mathbf{l_2}}}{r_{12}} \tag{2.17}$$

It is possible to construct both self and mutual inductance matrices from (2.16) and (2.17) and extract coupling from (2.7). This has been investigated in [71]. Partial Inductances are used to analyze signal integrity caused due to parasitic in PCB tracks [72]. They have also been used in RFID studies where self-inductances are separately computed using PEEC and magnetic coupling is obtained using a filamentary mutual inductance computation [73]. Analytical integration and quadrature formula has been used to find the equivalent

inductance and resistance matrices of a three-dimensional multiconductor structure in [74].

Application of Conformal Mapping - Schwarz-Christoffel Transformation

Conformal mapping can be applied to magnetic problems having boundary between different materials. It involves transformation of a contour bounded domain into a relatively simple polygon in a complex plane such as rectangle, triangle etc. The theory of S-C mapping is stated as reproduced from [75]. *Let P be the interior of a polygon Γ having n vertices $w_1, w_2...w_n$, and the interior angles $\alpha_{1\pi}, \alpha_{2\pi}...\alpha_{n\pi}$, in counterclockwise order. Let f be any conformal map from the upper half-plane H+ to P with $f(\infty) = w_n$. Then,*

$$w = f(z) = A + C \int_{z_0}^{z} \prod_{k=1}^{n-1} (\zeta - z_k)^{\alpha_k - 1} \, d\zeta \qquad (2.18)$$

For some complex constants A and C, where $w_k = f(z_k)$ for $k = 1, 2, \cdots n - 1$.

Here, $z = x + jy$ and $w = u + jv$ are complex numbers in the $z-$ and $w-$planes, respectively. The transformation is indicated in Fig. 2.8. The transformation $w = f(z)$ is conformal at a point only if $f(z)$ is analytical there. Thus, the *Cauchy-Riemann Conditions* need to be satisfied by $f(z)$ [76].
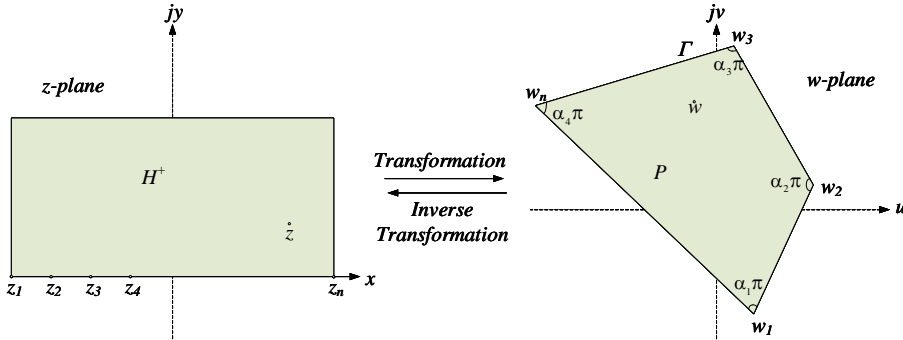
Figure 2.8: The $z-$plane and $w-$plane of the S-C mapping theorem with the upper half-plane $H+$ mapped to the interior P, of a four sided polygon, Γ. Variations of this formula can map different canonical domains (triangle, rectangle, disk, strip etc.) to a polygon [75].

Cauchy Riemann Conditions   If the stream function or the field-lines function is given by $\zeta(x, y)$ and the potential function that is orthogonal to the stream function is given by $\phi(x, y)$. In the $z-$plane, both these functions satisfy the Laplace's equation.

$$\nabla^2\phi = \frac{\partial^2\phi}{\partial x} + \frac{\partial^2\phi}{\partial y} = 0$$
$$\nabla^2\zeta = \frac{\partial^2\zeta}{\partial x} + \frac{\partial^2\zeta}{\partial y} = 0$$

(2.19)

The *Cauchy Riemann Conditions* that must necessarily be satisfied for a function to be analytical with the real and imaginary parts of $w(z)$ given as

$$\frac{\partial\zeta}{\partial x} = \frac{\partial\phi}{\partial y}$$
$$\frac{\partial\zeta}{\partial y} = -\frac{\partial\phi}{\partial x}$$

(2.20)

This mapping being conformal preserves the angle between curves although the transformed curves in the w-plane may have no resemblance to the original curve. In the context of electro-magnetics, the orthogonality between the fields and potential is maintained and the calculated energy in the transformed plane is the same as that in the original plane. To calculate the magnetic coupling by using S-C technique, the following steps are involved:

1. Obtaining the parameters z_k which are the prevertices in the $z-$plane as the magnetic system forms the polygon in the $w-$plane. In other words, the inverse transformation needs to be applied to convert the points in the target polygon back to the canonical domain. This is also called the "parameter problem" transforming the geometry to that of a parallel plate capacitor, so as to enable the simple computation of the capacitance transformation [77].

2. Performing the S-C Transformation. Analytical computation is easy for a maximum of three vertices. For more vertices, Numerical evaluation only yields viable results.

3. Utilization of capacitance-reluctance analogy as given by [78]

$$\mathcal{R} = \frac{l}{\mu A} = \frac{\epsilon}{\mu C}$$

(2.21)

4. Obtaining coupling by calculating the inductances using reluctance and the mutual inductance with any other previously described method.

A limitation of this method is that it can be applied to only 2D problems, usually with infinite permeability of core [79]. In [76], inductances of 2D magnetic cores are solved analytically using the technique presented in [80]. An extension of this method has been considered in [78] to calculate 3D air-gap reluctances, by considering two 2D planes, thereby accounting for all three spatial dimensions. In the area of electromagnetic field analysis of electric machines, a number of research papers have been presented. In [81], a surface PM motor has been analysed. In [77], an 8/8 VRM is analysed and compared with the solutions from FEA. In [82], an actuator has been designed based on the transformation. Other machine topologies include: Tubular PM actuator [83], Inset and surface-mounted PM machines [84], Flux-switching PM machines [85], Linear switched flux PM machines [86] etc.

Application of Method of Images

Lord Kelvin first introduced the 'Method of Images' to solve electrostatic problems with a boundary between two media in 1848 [87]. He showed that in front of a conducting sheet, the field of an electric charge can be represented as a summation of the field of the original charge and a charge located at the position of its mirror image. Maxwell further extended this treatment to all combinations of conducting spheres and planes in his treatise [87]. This theory has been extended to electromagnetic fields and some of the earliest work in this domain is attributed to Dr. G.F.C. Searle [88]. The problem of Searle as described by Hague is reproduced in Fig. 2.9 [88].

The problem in Fig. 2.9 can be simplified into a general problem statement involving two media with different permeability as shown in Fig. 2.10. To derive the conditions for applying the method of images, i is the current of a wire whose optical image at Y is carrying a virtual current of mi (flowing opposite to i) considering the entire region has a single media of permeability μ_1.

In such a situation, the magnetic flux density at P which is originally a point in the interface between the two media is given by Biot-Savart Law as

$$\overrightarrow{\mathbf{B_i}} = \frac{\mu_1 i}{2\pi r} \, , \overrightarrow{\mathbf{B_{mi}}} = \frac{\mu_1 mi}{2\pi r} \tag{2.22}$$

The resultant normal component of flux density, $\overrightarrow{\mathbf{B_{(1p,n)}}}$ and tangential component, $\overrightarrow{\mathbf{H_{(1p,t)}}}$ of the field at point P can be written for the condition in Fig. 2.10 as

$$\overrightarrow{\mathbf{B_{1p,n}}} = \overrightarrow{\mathbf{B_i}} \cos\theta + \overrightarrow{\mathbf{B_{mi}}} \cos\theta = \frac{\mu_1 i}{2\pi r}(1+m)\cos\theta$$

$$\overrightarrow{\mathbf{H_{1p,t}}} = \frac{i}{2\pi r}(1-m)\sin\theta \tag{2.23}$$
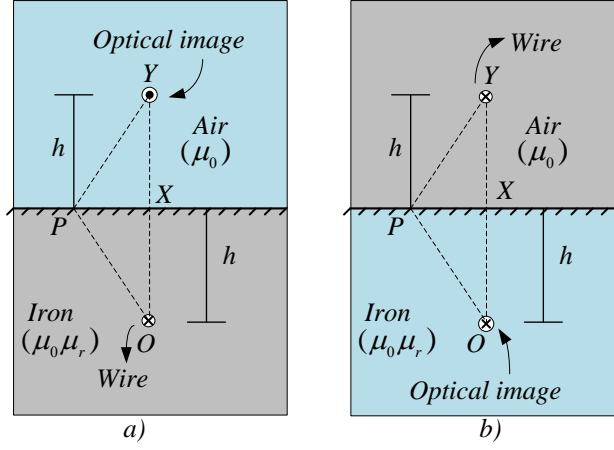
Figure 2.9: Theory of images applied to an electromagnetic problem involving coils embedded in iron of permeability (μ_0, μ_r) as in a) and for coils outside a block of iron as in b) [88].

Now, considering the whole region of permeability μ_2 and assuming that a current $(1 + n)i$ is flowing at the point O (taken in the same direction of mi). Then,

$$
\begin{aligned}
\overrightarrow{\mathbf{B_{2p,n}}} &= \frac{\mu_2 i}{2\pi r}(1 + n)\cos\theta \\
\overrightarrow{\mathbf{H_{2p,t}}} &= \frac{i}{2\pi r}(1 + n)\sin\theta
\end{aligned}
\tag{2.24}
$$

Finally, considering the inter-facial boundary conditions,

$$
\overrightarrow{\mathbf{B_{1p,n}}} = \overrightarrow{\mathbf{B_{2p,n}}} , \overrightarrow{\mathbf{H_{1p,t}}} = \overrightarrow{\mathbf{H_{2p,t}}}
\tag{2.25}
$$

We can relate the image currents as a function of permeability as

$$
m = \frac{\mu_2 - \mu_1}{\mu_2 + \mu_1} , n = \frac{\mu_1 - \mu_2}{\mu_2 + \mu_1}
\tag{2.26}
$$

Finally, the solution to Searle's problem in Fig. 2.9 a) can be summed up for iron with relative permeability (μ) and air (1). If the entire media is made up of iron, the magnetic field at P
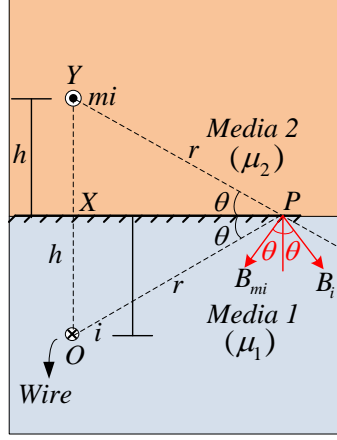
Figure 2.10: Electromagnetic image for the solution to the Searle's problem, considering generalized parameters for both the media [89].

is due to i at O and $-\left(\frac{\mu-1}{\mu+1} \times i\right)$ (note that the sign change is because the image current is in the opposite direction) at Y. Now, if the entire media is air, the field is due to current $\left(\frac{2\mu}{\mu+1} \times i\right)$ at O. In case of Fig. 2.9 b), with wire in air and image in iron, if air fills the entire domain, the magnetic field at P is due to i at O and $\left(\frac{\mu-1}{\mu+1} \times i\right)$ (Here, the image current is in the same direction of the current in the wire). Also, when iron fills the entire media, the field is due to current $\left(\frac{2}{\mu+1} \times i\right)$ at Y. An alternative derivation of the image currents using Poisson's equation is presented in [90]. The method of images has been applied to end-winding fields in [91]. The leakage inductances of low frequency transformers have been investigated in [92].

The various features and comparisons of the different field evaluation techniques is presented in Table 2.1.

Lumped electric circuits evolved with the historical work of Park [94], Kron [95], Schwinger [96] among others who generalized the work of Ohm, Henry, Faraday and Kirchoff [97]. The validity of these circuits is restricted to those problems in electromagnetics where the wavelength of the fields, λ is large compared to the dimensions of the apparatus, $l(\lambda \gg l)$ [97]. Historically, the development of circuit theory was independent and preceded in development to that of Maxwell's equations [97]. However, Maxwell's equations will yield the circuit equations when the length condition is applied as an approximation [97], [98].

Table 2.1: Comparison of field evaluation techniques

Technique	Features
Biot-Savart's Law	1. Straight forward procedure and is simple for simple geometries like circular coils, rectangle etc [54]. 2. For complicated geometries, elliptical integrals need to be solved [56]. 3. Can take into high frequency (HF) effects like current crowding (skin effect, proximity effect) by using a current-density formulation. 4. Needs boundary conditions to solve problems with interfaces.
Neumann's Integral	1. Assumed that current flows in thin filamentary circuits [44]. 2. The expressions formed are easier to integrate due to use of $\vec{A}$. 3. It is difficult to include HF effects and it is difficult for complicated geometries. 4. Needs boundary conditions to solve problems with interfaces.
Theory of Partial Inductance	1. Assumptions of filamentary current holds here. 2. The expressions formed are easier to integrate due to use of $\vec{A}$ as well as summation. 3. It is difficult to include HF effects. 4. It can handle complicated geometry by resolving various sections and calculating the various partial inductances [70]. 5. Needs boundary conditions to solve problems with interfaces.
Method of Images	1. Mostly suitable for sources close to boundary, compared to thickness of other material [79]. 2. Takes into account finite permeability of different materials. 3. For complex boundaries, infinite number of images need to be present [79]. 4. This technique is suited for interfaces.
Schwarz Christoffel Transformation	1. Limited to 2D problems [79]. 2. Usually considers infinite permeability of cores. 3. Can't determine the field in the material which is replaced by images [93]. 4. Numerical computational issues like more computation time for complicated problems, crowding, elongation [93]. 5. This technique can handle boundaries directly.

The electrical circuit description of a system of two magnetically coupled coils by considering the mutual inductance ($M = L_{12} = L_{21}$). In such a case, the circuit that represents these equations can be modelled as in Fig. 2.11.

However, the electric circuit theory description based on the mutual inductance has limita-
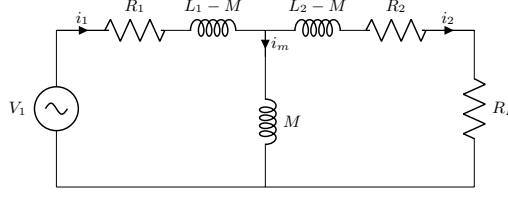
Figure 2.11: Electrical circuit description of a pair of mutually coupled coils with primary inductance L_1 and secondary inductance L_2, with mutual inductance M, connected to a resistive load, R_L .

tion due to the fact that the model doesn't take into account the number of turns i.e., it is not a physical model [99]. A physical model for magnetically coupled coils is that of the Steinmetz exact equivalent circuit, where turns ratio is reflected onto the mutual inductance, yielding the magnetizing inductance. Such a physical circuit is shown in Fig. 2.12.
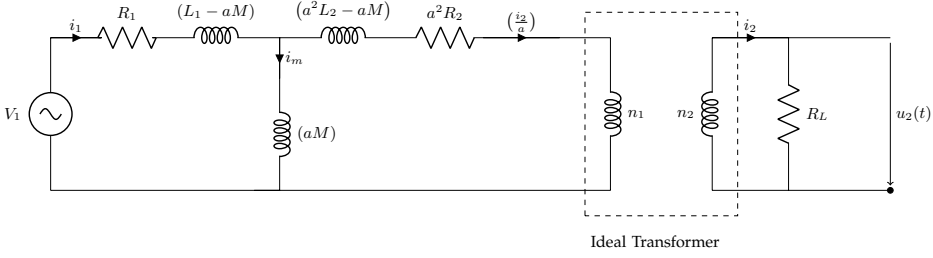
Figure 2.12: Electrical circuit description of a primary transposed transformer with turns ratio $a = \left(\frac{n_1}{n_2}\right)$. The primary has inductance L_1, carries current i_1 and secondary, L_2 and i_2. The mutual inductance of the circuit is M, connected to a resistive load, R_L .

In case of magnetic circuits, they are the topological dual of electric circuits. The principle of topological duality as shown by Cauer (1934) was extended between the electric circuit and magnetic circuit by Cherry (1948) and further improved by Slemon (1953) [100], [101]. The magnetic equivalent circuit has been modelled traditionally with reluctance models [102]. However, the reluctance-resistance analogy has a number of limitations [103], [104]:

1. Magnetic reluctances due to the resistance analogy seem to dissipate power, while in reality magnetic components store energy.

2. This technique is limited to planar networks. In case of nonplanar networks that contain crossovers, this procedure is not valid. This is easily ascertained from elementary graph theory as such networks don't have duals. In magnetics, any magnetic component with more than three windings is nonplanar with all couplings considered.

3. Modelling energy dissipation in the core material with inductors is less intuitive.

4. In case of a generalized electrical, mechanical or hydraulic system, the product of flow (through variable's) and effort variable's (across) is power. However, in case of the traditional magnetic circuit, it is energy and hence loses the consistency as illustrated below:

$$[v \times i] = V \times A = W \tag{2.27}$$
$$[\mathcal{F} \times \phi] = A \times Wb = J \tag{2.28}$$

5. Non-linear magnetics generate differential-algebraic equations (DAE) which can't be solved using ordinary differential equation (ODE) solvers.

6. For closely coupled magnetic interfaces, the equations are stiff.

Thus, an alternative representation to solve the aforesaid problems resulted in the permeance-capacitance analogy as proposed by Buntenbach in the late 1960's [103], [105]. Through the work of Blanken [106] and Hamill [104], [107] it has seen a recent resurgence of interest. Here, the network is modelled in terms of permeances with the effort variable, the rate-of-change of magnetic flux ($\dot{\phi}$). This would fix power as the product of the effort and flow variables. The relationships between magnetic and electric parameters that model this behaviour is listed in Table 2.2.

Table 2.2: Analogy between electric circuits and magnetic circuits based on permeance model

Magnetic circuit			Electric circuit		
parameter	symbol	unit	parameter	symbol	unit
MMF	$\mathcal{F}$	A	Voltage	v	V
Rate of change of flux	$\dot{\phi}$	V	Current	i	A
Permeance	$\wp$	H	Capacitance	C	F
Flux	$\phi = \int \dot{\phi} dt$	Wb	Charge	$q = \int i dt$	C
Permeability	$\mu = \mu_0 \mu_r$	H/m	Permittivity	$\epsilon = \epsilon_0 \epsilon_r$	F/m
Power	$P = \mathcal{F}\dot{\phi}$	W	Power	$P = vi$	W
Energy	$E = \int \mathcal{F} d\phi$	J	Energy	$E = \int vidt$	J

In the resulting model, in order to link the electric and magnetic circuits based on the permeance model, the gyrator-capacitor network is used [107]. A gyrator is an ideal two-port circuit element that operates like a 'dualizer' [107]. In other words, it reflects the dual of an impedance from one port to the other. If G is the gyration resistance, the $v - i$ characteristic of the gyrator is given in the form below

The sign convention used in the above equation is different from that used in two-port networks, however it is considered to be useful in this network particularly for energy

considerations [107]. The MEC based on the gyrator-capacitor network is shown from the traditional reluctance model in Fig. 2.13.
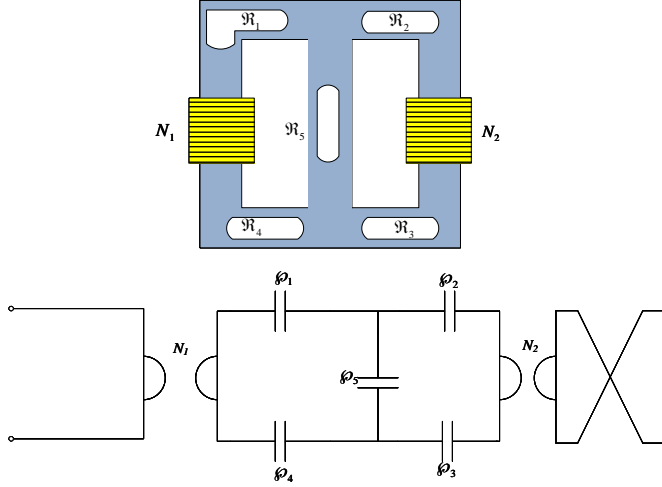
Figure 2.13: a) Magnetic circuit of a leaky two winding transformer b) Gyrator-capacitor model of the two winding transformer [104].

In recent literature, this model has also been expanded by addition of a resistance term so as to model the core losses, making it the Gyrator Re-Cap model that models the core losses using the resistances [108], [109]. This brought about a fast and revolutionary core modelling tool. Subsequently, a number of work revolves around integrated magnetics. In [110], the model is used to characterize the magnetic fields in a toroid with gap. In [111], to model the non-linearity of the magnetic core. This model has been further simplified with the removal of the gyrator as proposed in [112], calling it the capacitive modelling approach and used subsequently in [113], [114]. These models have also been used in designing the magnetics of a magnetic arm-switch technique for operating inverters both in parallel and series for current and voltage correction [115]. An integrated PPIBC (primary parallel isolated boost converter) is designed using this model in [116].

2.5   Electromagnetic Standards for Safety and Shielding Techniques

A complete design of magnetics of IPT systems must also consider constraints imposed by electromagnetic fields around coils. The leakage fields that permeate the space around

inductive power coils are a source of both electromagnetic noise for nearby electronic devices as well as a health hazard for humans and animals. A number of regulating bodies throughout the world are involved in establishing codes that regulate the exposure to harmful fields, efficient utilization of the electromagnetic spectrum as well as limiting EMC (electromagnetic compatibility) [117]. Regulations for wireless power transfer (both near and far-field) are dependent on frequency of the spectrum and signalling method (in-band or out-of-band, uni or bi-directional) [117]. For workers exposed to EM leakage fields (upto 300 GHz) as well as for the general public, safety guidelines are presented by the International Commission on Non-Ionizing Radiation Protection − ICNIRP 1998 [118] and 2010 [119]. Also, the Institute for Electrical and Electronics Engineers (IEEE C95.1-2005) [120] provides a set of guidelines for exposure limits. The frequency dependent parameters used to quantify the EM effects include maximum field strengths - electric and magnetic and densities, maximum contact current, specific absorption rate (SAR) of energy etc. The ICNIRP guidelines from 1998 to 2010 have undergone changes particularly in the low frequency time-varying electric and magnetic field are due to [121]:

- A replacement of induced current density by induced internal electric field due to sufficient experimental and published data with this metric.

- Computer simulations based on detailed anatomical human models than simple geometrical models for dosimetry.

Thus, the reference levels in ICNIRP 2010, due to improved modelling, results in revised magnetic field limits to be less conservative while electric fields (bearing exceptions) remain largely unchanged [121]. Reference levels for occupational exposure and that of general public to spatial averages of electric and magnetic fields from ICNIRP 2010 is presented in Table 2.3. It is generally observed that the guidelines become stringent for higher frequencies. Also, the corresponding levels from the IEEE standards are presented in Table 2.4.

Table 2.3: Health exposure limits for electric and magnetic fields as prescribed by ICNIRP 2010 [119]

	Occupational Exposure			General Public Exposure		
Freq range (Hz)	E (kVm^{-1})	H (Am^{-1})	B (T)	E (kVm^{-1})	H (Am^{-1})	B (T)
3k - 10M	1.7×10^{-1}	80	1×10^{-4}	8.3×10^{-2}	21	2.7×10^{-5}

The standards from IEEE define Basic Restrictions (BR) as well as Maximum Permissible Exposure (MPE). The basic restrictions consider the safety risk factors and are expressed depending on the frequency range as *in-situ* electric field (3 kHz to 5 MHz), specific absorption rate (100 kHz to 3 GHz), or incident power density (3 GHz to 300 GHz). More specific permissible limits to head, limbs, torso etc. are also defined and tabulated in [120], with f being frequency in kHz.

Table 2.4: IEEE MPE and BR for whole body and localised exposure [120]

Freq.	Condition	Parameter	General Public	Control Group
3 kHz- 100 kHz	Whole body exposure	MPE E(rms) (V/m)	614	1842
	Both feet	MPE RMS induced current (mA)	$0.90f$	$2f$
	Each foot	MPE RMS induced current (mA)	$0.45f$	$1f$
	Grasp contact	MPE RMS induced current (mA)	N.A.	$1f$
	Touch contact	MPE RMS induced current (mA)	$0.167f$	$0.5f$
100 kHz- 3 GHz	Whole body exposure	BR SAR (W/kg)	0.08	0.4
	Localized exposure	BR SAR peak-spatial avg (W/kg)	2	10
	Localized exposure	BR SAR Extremities (W/kg)	4	20

2.5.1 Shielding Techniques

Shielding refers to the process of cancellation or complete nullification of unintended EMF that are present in a certain region of space. It is enough in many applications to reduce the EMF below levels prescribed by the standards and regulations. Shielding achieved without expediting additional energy sources is referred to as passive shielding. Active shielding involves additional circuitry so as to reduce/nullify the EMF. Passive shielding can be achieved by utilizing soft magnetic materials (eg: ferrite with high permeability and low conductivity typically $\mu_r > 1000$ and $\sigma << 100$ S/m) that guide and confine the flux through them and shape it in such a manner that leakage fields are minimized [122]. In a coupled coil system, this technique can also improve mutual inductance and hence power transferred and efficiency of power transfer (due to reduced leakage losses). However, hysteresis losses in the magnetic material which depends on the frequency and magnitude of the field can create losses [122]. Another type of passive shielding (metallic) involves the nullification of EMF due to the creation of *eddy currents* on a metallic surface (eg: Aluminium, Copper etc.) as per *Faraday-Lenz* law. This magnetic field opposes the original field and results in reduction of leakage fields. The efficacy of this method is also limited by frequency and hence thickness of the metallic conductor must be greater than the skin depth. Novel research in material engineering focused on enhancing coupling of Inductive Power Transfer systems using metamaterials also report that mu-near-zero (MNZ) metamaterials and longitudinal mu-near-zero metamaterials (LMNZ) have enhanced shielding effects as absorber and field reflector respectively [123]. In the future, it is expected that metamaterials will be used in the design of high-coupling coils as well as for EMI/EMC shielding. The different types of passive and active shielding is illustrated in Fig. 2.14.
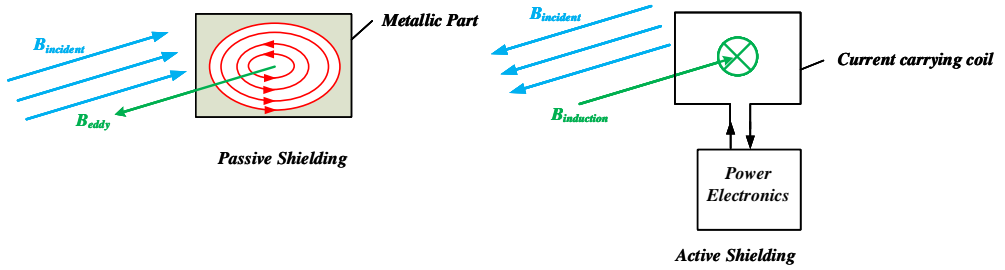
Figure 2.14: The different types of shielding - passive eddy current based metallic shielding and active shielding based on power electronics circuitry.

2.6   Design of Inductive Power Transfer Systems

The starting point of a design methodology for any application of inductively powered systems involves the understanding of system specifications. This incorporates system requirements such as output power, frequency, dimensions, weight, air-gap length, input voltage (current) etc. Since varied applications have different specifications, the result of magnetic design for each set of specification is a novel magnetic system. An observable trend in IPT systems in general, is a push for higher frequencies, realising high power-densities and at high efficiency. At VLF $(3-30)$ kHz, ferrite based IPT systems with aluminium shields (for making the flux uni-directional) that achieve high coupling and power transfer are observed in literature. The applications are mainly in charging electric vehicles, induction cooking and mining operations [124]. However, transferring high power at high frequency results in increased switching losses in the semiconductor devices, high ac losses in the coils and high dielectric losses in the capacitor. Hence, low power applications (RFID, consumer electronics etc.) are typically operated at much higher frequencies, $(10's - 100's)$ MHz and air-cored coils are often used as the coupler (to nullify high frequency core losses in ferrites) [33]. The choice of high frequency power transfer results in high power density (due to reduced passive component sizes) with an improvement in transient response [125].

A detailed design methodology for IPT systems is presented in Fig. 2.15. For designing the magnetics of such a system, the first step involves making a choice of the various materials and functionalities that need to be present in the system - conductors, magnetic flux channelling and shielding. Conductors such as copper *litz* wire, foil conductors etc. carry the current, the magnetic flux of which is channelled by high permeability materials like ferrite $\mu_r > 1000$. The magnetic leakages at undesirable positions in space are shielded by magnetic shields. Any analytical technique can be used to estimate the magnetic parameters of such a system. Often in IPT systems, several magnetic designs can achieve a desired power transfer and hence it is essential to enlist the various constraints that need to be met

Inputs
- *Output Power*
- *Frequency*
- *Dimensions & Size*
- *Weight*
- *Air gap length*
- *Input voltage/current etc.*

Economic analysis and Technology assessment
1. Costing of coils and converters
2. Societal (safety) and technology impact on enivronment

Magnetic Design
Coil Shapes
(eg: circular, rectangular etc.)
Choice of materials
1. Conductor
(eg: copper litz wire, copper wire, foil conductors etc.)
2. Flux channelling materials
(eg: ferrites, steel, iron etc.)
3. Flux shielding materials
(Passive eg: aluminium, copper etc. Active eg: switched mode converter)
4. Electric and magnetic circuit analysis and thermal analysis

More refined inputs for redesign

Power Electronics Optimization
1. Maximize efficiency, power density
2. Optimize weight and volume
3. EMC impact and safety

Redesign coils by considering all design options

Redesign power electronics considering all design options

Magnetic Optimization
1. Maximize magnetic coupling (k)
2. Minimize coupling gradient (gradk$_x$, gradk$_y$, gradk$_z$)
3. Minimize EMF (leakages)
ICNIRP standards
4. Minimize materials in the pads
5. Coil magnetics loss analysis
Eddy current losses (Skin and Proximity) in coil
Eddy current losses and Hysteresis Losses in materials

Power Electronics Design
1. Primary/track power electronics
(ac grid: rectifier, PFC, inverter, EMI filter
dc grid: dc/dc converter, EMI inverter)
2. Resonant compensation design
(SS,SP,PS,PP,LCL, LCC, LC ladder.)
3. Pickup power electronics
(rectifier, filter and dc/dc converter)
4. Electric and magnetic circuit analysis and thermal analysis

Figure 2.15: Design methodology for IPT systems incorporating the magnetic design, magnetic optimization followed by design and optimization of power electonics. A feedback from the output of power electronics optimization can input further refinement in magnetic design with an economic model and impact assessment as the final step.

to pick an effective design. Several constraints including maximum bounds on geometric dimensions, weight, volume, magnetic efficiency, cost etc. can be identified and a multi-objective optimization can be performed to choose a certain geometry that performs well within the defined bounds. In some applications such as EVs, misalignment tolerance for

stationary charging (atleast ± 10 cm from centre) as well as maximum leakage tolerances from ICNIRP/IEEE are constraints. While meeting the leakage constraints, it is possible at high leakage fields that passive/active shielding might be necessary. The frequency dependent losses in the magnetics such as eddy current losses - skin and proximity in the conductors etc. all contribute to inefficiency and temperature rise in the coils. Thus, coupling to a thermal model can yield requirements for cooling if necessary. A detailed thermal model is presented in [126].

The power electronics design including the primary side rectifier, inverter and EMI filter design (if operated from ac grid) then follows through the compensation strategies. Each compensation strategy can yield a voltage/current sourced primary/secondary. Hence, passive components such as an additional inductor to yield a current source to a parallel resonant topology is important (LCL compensation). Often, square wave switching PWM is used and varying the frequency to achieve soft switching is an important target to yield low losses during inverter switching. The pickup stage often includes a rectifier and a dc/dc converter which feeds power into the battery for various applications. The power electronics can be further optimized keeping efficiency, power density and costs as objectives [127]. A feedback loop also considering outputs of the power electronics that influence the magnetic design for eg: having an integrated magnetic charge-pad and power converter so as to further improve power density by having a shared cooling stage yields a compact IPT system. Finally, the designed system must also perform well interms of both economic considerations as well as the impact of technology to the environment and safety of people. The design cycle is completed with such an economic analysis and environmental assessment of technology.

2.7 Discussion

In this chapter, review of magnetic modelling of loosely coupled air-cored coils to aid the design of IPT system is considered. The magnetic parameters of the system have been defined and the analytical and semi-analytical techniques for magnetics modelling are classified as field and circuit modelling techniques respectively. An effective coil design follows through the two techniques.

Field modelling techniques considered for general problems are applicable to all coils. However, boundary conditions need to be applied at the interface of different materials. For general problems, Biot-Savart's law and Neumman's integral are considered keeping the calculation of the mutual inductance and magnetic coupling between circuits in mind. Theory of partial inductance can be used to model the inductances of complicated geometries by breaking the structures into appropriate sections. In case of problems with a boundary, conformal mapping and method of images provide valuable insight.

Circuit modelling techniques include both electric circuit and magnetic circuit analysis.

Circuit theory translates the electromagnetic phenomena in action from magnetic fields to currents, voltages and their derivatives. Traditional circuit theory has limitations which have been considered and some adaptations such as the Gyrator-Capacitor model of magnetic circuits which better model the magnetics has been considered. Any coil design technique that is resorted to must also finally respect the limitations imposed by EM fields that permeate the space nearby. The limitations are dependent on frequency and a number of standards including IEEE and ICNIRP-1998 and 2010 have been discussed. Shielding techniques are introduced and elaborated. The problem of field leakage is exacerbated by demands of high power transfer at higher frequencies where the constraints are more stringent. However, developments in fast-switching wide-bandgap semiconductors and meta-materials for shielding are expected to push this technology further. Finally, a design methodology taking into consideration a multi-objective design and optimization oriented magnetics and power electronics design is undertaken in this work.

Analytical Modelling and Study of Shapes for IPT Systems

To study the effect of shapes on magnetic fields due to air-cored coils- the theory of partial inductances is detailed in this chapter. The self & mutual inductance, coupling computation of air-cored coils is carried out here. A multi-turn sectional inductance matrix is considered for the evaluation. Air gap, turns and dimensions are considered in the derivation and its evaluation. In this context, a number of basic shapes such as rectangle, circular, square etc. can be compared and the result can be evaluated so as to determine the parameters of various geometries. A combination of simple shapes lead to multi-coil pads. This chapter proposes an extension to a multi-coil system of coils using the principle of linearity. The multi-coil geometries analyzed include double rectangular (DR), double circular (DCirc) along with a coil in quadrature (Quad). This analysis forms the basis for a shape evaluation of magnetic fields and is the basis of further optimization.

Based on

- V. Prasanth, P. Bauer and J. A. Ferreira, "A sectional matrix method for IPT coil shape optimization," in *International Conference on Power Electronics and ECCE Asia (ICPE-ECCE Asia)*, 2015, pp. 1684–1691.

- V. Prasanth, S. Bandyopadhyay, P. Bauer and J. A. Ferreira, "Analysis and comparison of multi-coil inductive power transfer systems," in *Power Electronics and Motion Control Conference (PEMC) Varna*, 2016, pp. 993–999.

- V. Prasanth, S. Bandyopadhyay, P. Bauer and J. A. Ferreira, "A generic matrix method to model the magnetics of multi-coil ipt systems," in *Energies*, 2017.

3.1   Introduction

In literature, coil optimization and magnetic parameter estimation (L_1, L_2, M, k) are performed relying on EM field solvers and/or combining with evolutionary algorithms [128], [20]-[130]. In other work, numerical techniques (solving look-up tables (book of Grover [131]), solving Bessel functions [132], solving elliptical integrals [133]) and PEEC solvers [134]-[137] are used to achieve the same. In the book of Grover, there is available closed-form expressions for self-inductance of a number of polygonal shapes. However, all the equations are developed for a single-turn inductor which exclude the effect of the air-gap and the resulting reduction in fill factor. In a previous work [17], analytical study of $2D$ misalignment of rectangular conductors has been carried out. The results could be extended to $3D$ by considering two $2D$ planes. However, an analytical coil design technique has not been considered. In this chapter, this gap for coil design is bridged by proposing a sectional self-inductance matrix for multi-turn inductors with the effect of air-gap and hence fill factor in the equations. Closed form expressions of L and M are derived and the analytical computation of k is carried out. The calculations can be easily implemented and thereby reduces the dependence on expensive FEM and PEEC software.

The developed equations are used in the design and optimization of shapes of transmitter and receiver that is to be used for IPT systems in EV applications. This chapter deals with the electromagnetic analysis and design of these coils of various shapes.

3.2   Partial Inductances-Single Turn Rectangular Charge-Pad

Assuming currents to be in line filaments (neglecting eddy current losses) and that the effects of retardation (radiation) are neglected, the mutual inductance L_{12} of a coupled circuit can be written as [138]

$$L_{12} = \frac{\lambda_2}{i_1} = \frac{\mu_0}{4\pi} \times \oint_{c_1} \oint_{c_2} \frac{\overrightarrow{d\mathbf{l_1}}.\overrightarrow{d\mathbf{l_2}}}{r_{12}} \tag{3.1}$$

In (3.1), c_1 is the contour along the median line of the current carrying conductor of the primary while c_2 is the contour of median line of the secondary/pickup, with r_{12} as the distance between corresponding current elements. The self-inductance of a coil can be written in the same manner, except that the contours are along the median line and the inner edge of the wire. For a first consideration, it is useful to think of a single turn rectangular coil as in Fig. 3.1. A rectangular structure can be split into four sections $(dl_{1'}, dl_{2'}, ..dl_{4'})$, each of which refer to conductors in the top, bottom, left and right respectively In such a case, (3.1) can be written in terms of the various sections of the coil as
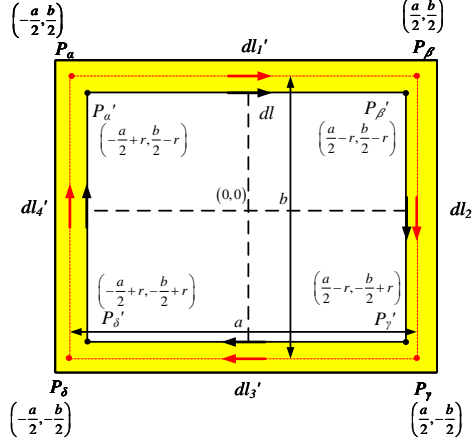
Figure 3.1: Definition of the contour of the elementary inner edge of a single turn rectangular coil dl and the various sections of the contour of the elementary line along the centre of the wire $(dl_{1'}, dl_{2'}, ..dl_{4'})$. For further evaluation, the contour of dl can be split at the top, right, bottom and left sections as $(dl_1, dl_2, ..dl_4)$.

$$L_e = \frac{\mu_0}{4\pi} \times \left[\oint_{l_{1'}} \oint_{l_1} \frac{\overrightarrow{dl_{1'}}.\overrightarrow{dl_1}}{r_{1'1}} + \oint_{l_{2'}} \oint_{l_1} \frac{\overrightarrow{dl_{2'}}.\overrightarrow{dl_1}}{r_{2'1}} + \oint_{l_{3'}} \oint_{l_1} \frac{\overrightarrow{dl_{3'}}.\overrightarrow{dl_1}}{r_{3'1}} + \oint_{l_{4'}} \oint_{l_1} \frac{\overrightarrow{dl_{4'}}.\overrightarrow{dl_1}}{r_{4'1}} \right]$$
(3.2)

This can be written as a matrix in the form where the rows represent the section of the conductor that carriers the current (section of the contour of the centre) and columns represent the section on which the inductance contribution is considered. Each element of the matrix is a partial inductance (self partial inductance $(i = j)$ and mutual partial inductance $(i \neq j)$).

$$M = \frac{\mu_0}{4\pi} \times \begin{bmatrix} \oint_{l_{1'}} \oint_{l_1} \frac{\overrightarrow{dl_{1'}}.\overrightarrow{dl_1}}{r_{1'1}} & \oint_{l_{1'}} \oint_{l_2} \frac{\overrightarrow{dl_{1'}}.\overrightarrow{dl_2}}{r_{1'2}} & \cdots & \oint_{l_{1'}} \oint_{l_4} \frac{\overrightarrow{dl_{1'}}.\overrightarrow{dl_4}}{r_{1'4}} \\[2em] \oint_{l_{2'}} \oint_{l_1} \frac{\overrightarrow{dl_{2'}}.\overrightarrow{dl_1}}{r_{2'1}} & \oint_{l_{2'}} \oint_{l_2} \frac{\overrightarrow{dl_{2'}}.\overrightarrow{dl_2}}{r_{2'2}} & \cdots & \oint_{l_{2'}} \oint_{l_4} \frac{\overrightarrow{dl_{2'}}.\overrightarrow{dl_4}}{r_{2'4}} \\[2em] \oint_{l_{3'}} \oint_{l_1} \frac{\overrightarrow{dl_{3'}}.\overrightarrow{dl_1}}{r_{3'1}} & \oint_{l_{3'}} \oint_{l_2} \frac{\overrightarrow{dl_{3'}}.\overrightarrow{dl_2}}{r_{3'2}} & \cdots & \oint_{l_{3'}} \oint_{l_4} \frac{\overrightarrow{dl_{3'}}.\overrightarrow{dl_4}}{r_{3'4}} \\[2em] \oint_{l_{4'}} \oint_{l_1} \frac{\overrightarrow{dl_{4'}}.\overrightarrow{dl_1}}{r_{4'1}} & \oint_{l_{4'}} \oint_{l_2} \frac{\overrightarrow{dl_{4'}}.\overrightarrow{dl_2}}{r_{4'2}} & \cdots & \oint_{l_{4'}} \oint_{l_4} \frac{\overrightarrow{dl_{4'}}.\overrightarrow{dl_4}}{r_{4'4}} \end{bmatrix}$$
(3.3)

The net external self-inductance can be written as

$$L_e = \sum_{i=1}^{4} \sum_{j=1}^{4} L_{ij} \tag{3.4}$$

The orthogonality of the vector dot product makes the odd-even $L(i,j)$ and even-odd $L(i,j)$ pair of terms in the matrix of L_{ij} to vanish to zero. For eg: $(\vec{dl_1}. \vec{dl_2} = dx_1 \hat{i}. dy \hat{j} = 0)$.

$$L_{ijlk} = \begin{bmatrix} L_{11} & 0 & L_{13} & 0 \\ 0 & L_{22} & 0 & L_{24} \\ L_{31} & 0 & L_{33} & 0 \\ 0 & L_{42} & 0 & L_{44} \end{bmatrix} \tag{3.5}$$

Thus, the total external self-inductance can be written in terms of $L_a = L_{11} = L_{33}, L_b = L_{22} = L_{44}, M_a = L_{13} = L_{31}, M_b = L_{24} = L_{42}$ as

$$L_e = 2(L_a + L_b - M_a - M_b) \tag{3.6}$$

Where, the self-partial inductances $(L_a, L_b = L_{(a=b)})$ are given by

$$L_a = \frac{\mu_0}{4\pi} \times \left[\int_{-\frac{a}{2}+r}^{\frac{a}{2}-r} dx_1 \int_{-\frac{a}{2}}^{\frac{a}{2}} \frac{dx_2}{\sqrt{(x_2 - x_1)^2 + r^2}} \right]$$

$$L_a = (a-r) \ln \left| \frac{a - r + \sqrt{r^2 + (a-r)^2}}{-a + r + \sqrt{r^2 + (-a+r)^2}} \right| + r \ln \left| \frac{-r + \sqrt{2}r}{r + \sqrt{2}r} \right| \tag{3.7}$$

$$+ 2\sqrt{2}r - \sqrt{(r^2 + (a-r)^2)} - \sqrt{(r^2 + (-a+r)^2)}$$

Also, the mutual partial inductances $(M_a, M_b = M_{(a=b)})$ are given as

$$M_a = \frac{\mu_0}{4\pi} \times \left[\int_{-\frac{a}{2}+r}^{\frac{a}{2}-r} dx_3 \int_{-\frac{a}{2}}^{\frac{a}{2}} \frac{dx_2}{\sqrt{(x_2 - x_3)^2 + (b-r)^2}} \right] \tag{3.8}$$

3.3   Partial Inductance due to Arbitrary Current Segments

To further expand the theory to two arbitrarily place current carrying segments as shown in Fig. 3.2. The displacement vectors of the two segments are $\vec{l_1}$ and $\vec{l_2}$
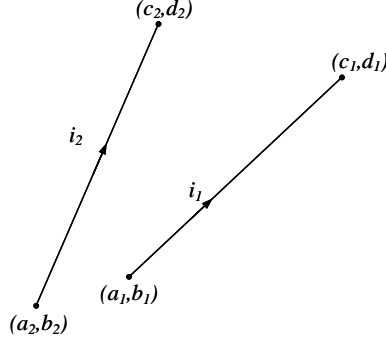
Figure 3.2: Two arbitrary current carrying segments in the xy plane.

They are represented using the slope-intercept formulae as:

$$y_1 = m_1 x_1 + c_1 \tag{3.9}$$

$$y_2 = m_2 x_2 + c_2 \tag{3.10}$$

Where, the slopes and intercepts with $(i = 1, 2)$ are written as

$$m_i = \frac{d_i - b_i}{c_i - a_i}$$
$$c_i = \frac{b_i (c_i - a_i) - a_i (d_i - b_i)}{c_i - a_i} \tag{3.11}$$

The Neumann's integral for the inductance contribution is given as

$$L_{12} = \frac{\lambda_2}{i_1} = \frac{\mu_0}{4\pi} \oint_{c_1} \oint_{c_2} \frac{\vec{dl_1}.\vec{dl_2}}{r_{12}} \tag{3.12}$$

Now, the line segments can be written as

$$\vec{l_1} = m_1 \vec{x_1} + c_1 \tag{3.13}$$

$$\vec{l_2} = m_2 \vec{x_2} + c_2 \tag{3.14}$$

Now, the vector dot product can be further written as

$$\vec{dl_1}.\vec{dl_2} = m_1 m_2 dx_1 dx_2 \tag{3.15}$$

Also, the displacement vector between the line segments is written as

$$r_{12} = \sqrt{(x_2 - x_1)^2 + (m_1 x_1 - m_2 x_2 + k_1 - k_2)^2} \tag{3.16}$$

Finally, the inductance contribution can be written as

$$L_{12} = \frac{\lambda_2}{i_1} = \frac{\mu_0}{4\pi} \int_{x_1=a_1}^{c_1} \int_{x_2=a_2}^{c_2} \frac{(1+m_1 m_2)dx_1 dx_2}{\sqrt{(x_2-x_1)^2 + (m_1 x_1 - m_2 x_2 + k_1 - k_2)^2}} \qquad (3.17)$$

The equation (3.17) is useful to characterize angular couplers for eg: triangular couplers.

3.4 Multi-Turn Charge-Pad

The analysis of the total inductance of a multi-turn rectangular coil is performed also considering the air-gap between the turns. Consider the per-turn inductance written as L_{ijlk} which represents the partial inductance contribution due to current flowing through i^{th} turn, j^{th} section on the lth turn, k^{th} section. In such a case, it is important to derive the expressions of the mutual partial inductances considering that the dimensions of the coil change with corresponding change in number of turns. It is useful to list the vertices of the extremes of the contour along the center of the wire as well as along the inner edge of the wire for the Nth winding. A multi-turn inductor is shown in Fig. 3.3.
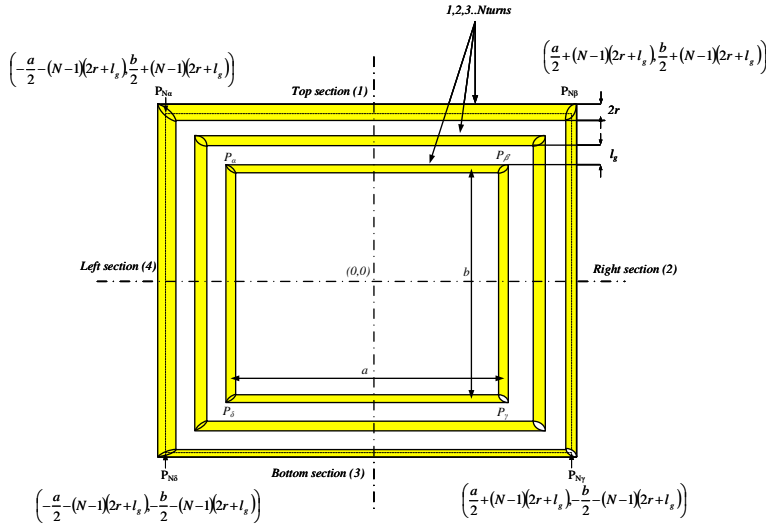
Figure 3.3: A multi turn inductor with dimensions defined from the centre of a wire of circular section with radius r and wound in a manner such that air gap is uniform (l_g) and the center contour of the wire has vertices $P_\alpha = (-a/2, b/2), P_\beta = (a/2, b/2), P_\gamma = (a/2, -b/2), P_\delta = (-a/2, -b/2)$.

The vertices along the inner edge can be written as

$$P_{N\alpha} = \left[-\frac{a}{2} - (N-1)(2r+l_g), \frac{b}{2} + (N-1)(2r+l_g) \right]$$

$$P_{N\beta} = \left[\frac{a}{2} + (N-1)(2r+l_g), \frac{b}{2} + (N-1)(2r+l_g) \right]$$

$$P_{N\gamma} = \left[\frac{a}{2} + (N-1)(2r+l_g), -\frac{b}{2} - (N-1)(2r+l_g) \right] \quad (3.18)$$

$$P_{N\delta} = \left[-\frac{a}{2} - (N-1)(2r+l_g), -\frac{b}{2} + (N-1)(2r+l_g) \right]$$

The vertices along the middle edge can be written as

$$P_{N\alpha i} = \left[\left(-\frac{a}{2} + r \right) - (N-1)(2r+l_g), \left(\frac{b}{2} - r \right) + (N-1)(2r+l_g) \right]$$

$$P_{N\beta i} = \left[\left(\frac{a}{2} - r \right) + (N-1)(2r+l_g), \left(\frac{b}{2} - r \right) + (N-1)(2r+l_g) \right]$$

$$P_{N\gamma i} = \left[\left(\frac{a}{2} - r \right) + (N-1)(2r+l_g), \left(-\frac{b}{2} + r \right) - (N-1)(2r+l_g) \right] \quad (3.19)$$

$$P_{N\delta i} = \left[\left(-\frac{a}{2} + r \right) - (N-1)(2r+l_g), \left(-\frac{b}{2} + r \right) - (N-1)(2r+l_g) \right]$$

The partial self-inductance of the Nth turn (due to the 1st section) can be derived as

$$L_{N1N1} = \frac{\mu_0}{4\pi} \times \left[\int_{k_1}^{k_2} dx_1 \int_{\alpha}^{\beta} \frac{dx_2}{\sqrt{(x_2 - x_1)^2 + r^2}} \right] \quad (3.20)$$

Where,

$$k_1 = \left(-\frac{a}{2} + r \right) - (N-1)(2r+l_g), \, k_2 = \left(\frac{a}{2} - r \right) + (N-1)(2r+l_g)$$

$$\alpha = -\frac{a}{2} - (N-1)(2r+l_g), \, \beta = \frac{a}{2} + (N-1)(2r+l_g) \quad (3.21)$$

The result of such an integration is

$$\frac{\mu_0}{4\pi} \times [I(C = \beta) - I(C = \alpha)] \quad (3.22)$$

Where,

$$I(C) = \sqrt{r^2 + (C - k_2)^2} - \sqrt{r^2 + (C - k_1)^2} + \ln \left| \frac{\left(\sqrt{r^2 + (C - k_1)^2} + (C - k_1) \right)^{(C-k_1)}}{\left(\sqrt{r^2 + (C - k_2)^2} + (C - k_2) \right)^{(C-k_2)}} \right|$$

(3.23)

The per-turn self-inductance matrix can be written as

$$L_{ijlk} = \frac{\mu_0}{4\pi} \times \begin{bmatrix} \sum_{i=1}^{N}\sum_{l=1}^{N} L_{i1l1} & 0 & -\sum_{i=1}^{N}\sum_{l=1}^{N} L_{i1l3} & 0 \\ 0 & \sum_{i=1}^{N}\sum_{l=1}^{N} L_{i2l2} & 0 & -\sum_{i=1}^{N}\sum_{l=1}^{N} L_{i2l4} \\ -\sum_{i=1}^{N}\sum_{l=1}^{N} L_{i3l1} & 0 & \sum_{i=1}^{N}\sum_{l=1}^{N} L_{i3l3} & 0 \\ 0 & -\sum_{i=1}^{N}\sum_{l=1}^{N} L_{i4l2} & 0 & \sum_{i=1}^{N}\sum_{l=1}^{N} L_{i4l4} \end{bmatrix}$$

(3.24)

The diagonal terms in the above matrix are the sectional partial self-inductance and the off-diagonal terms are the sectional partial mutual inductance. Note that the signs of sectional self-inductance are positive and sectional partial mutual inductance are negative for rectangular structures. The summation terms can be evaluated by calculating some general matrices like L_{N1k1}, L_{N1k3}. The inductance contributions of L_{N2k2}, L_{N2k4} can be obtained by inverting $a \times b$ in the previous set of general expressions. The net external self-inductance can then be written as

$$L_e = \sum_{i=1}^{N}\sum_{j=1}^{4}\sum_{l=1}^{N}\sum_{k=1}^{4} L_{ijlk}$$

(3.25)

This can also be extended to a number of polygonal shapes. For eg: In case of a triangle, the sectional mutual inductance matrix can be written generally as in (3.26). However if sections are orthogonal as in a right angled triangle, the orthogonal sections contribute to no partial inductance terms.

$$L_{ijlk} = \frac{\mu_0}{4\pi} \times \begin{bmatrix} \sum_{i=1}^{N}\sum_{l=1}^{N} L_{i1l1} & \sum_{i=1}^{N}\sum_{l=1}^{N} L_{i1l2} & \sum_{i=1}^{N}\sum_{l=1}^{N} L_{i1l3} \\ \sum_{i=1}^{N}\sum_{l=1}^{N} L_{i2l1} & \sum_{i=1}^{N}\sum_{l=1}^{N} L_{i2l2} & \sum_{i=1}^{N}\sum_{l=1}^{N} L_{i2l3} \\ \sum_{i=1}^{N}\sum_{l=1}^{N} L_{i3l1} & \sum_{i=1}^{N}\sum_{l=1}^{N} L_{i3l2} & \sum_{i=1}^{N}\sum_{l=1}^{N} L_{i3l3} \end{bmatrix} \tag{3.26}$$

3.4.1 Sectional Partial Inductances

The sectional partial self-inductance is defined as the sum of the partial self and partial mutual inductance contributions of current in a particular section on the same section on all possible turns. The sectional partial mutual self-inductance is defined as the sum of the partial mutual inductance contributions of current in a particular section on a different section for all combinations of possible turns. Following the previous procedures, the partial self-inductance due to current in the Nth turn first section on the kth turn first section is given by

$$L_{N1k1} = \frac{\mu_0}{4\pi} \times \left[\int_{k_1}^{k_2} dx_1 \int_{\alpha}^{\beta} \frac{dx_2}{\sqrt{(x_2 - x_1)^2 + (r + (N-k)(2r + l_g))^2}} \right]$$

Symbols:

$$k_1 = \left(-\frac{a}{2} + r\right) - (k-1)(2r + l_g), \; k_2 = \left(\frac{a}{2} - r\right) + (k-1)(2r + l_g)$$

$$\alpha = -\frac{a}{2} - (N-1)(2r + l_g), \; \beta = \frac{a}{2} + (N-1)(2r + l_g)$$

$\tag{3.27}$

The result of this integration is the same as (3.22) with $I(C)$ defined as

$$I(C) = \sqrt{(r + (N-k)(2r + l_g))^2 + (C - k_2)^2}$$
$$-\sqrt{(r + (N-k)(2r + l_g))^2 + (C - k_1)^2}$$
$$+\ln \left| \frac{\left(\sqrt{(r + (N-k)(2r + l_g))^2 + (C - k_1)^2} + (C - k_1)\right)^{(C-k_1)}}{\left(\sqrt{(r + (N-k)(2r + l_g))^2 + (C - k_2)^2} + (C - k_2)\right)^{(C-k_2)}} \right| \tag{3.28}$$

Similarly, the partial mutual self-inductance can be written as

$$L_{N1k3} = \frac{\mu_0}{4\pi} \times \left[\int_{k_1}^{k_2} dx_1 \int_{\alpha}^{\beta} \frac{dx_2}{\sqrt{(x_2 - x_1)^2 + ((b - r) + (2r + l_g)(N + k - 2))^2}} \right]$$

Symbols: (3.29)

$$k_1 = \left(-\frac{a}{2} + r\right) - (k-1)(2r + l_g), \, k_2 = \left(\frac{a}{2} - r\right) + (k-1)(2r + l_g)$$

$$\alpha = -\frac{a}{2} - (N-1)(2r + l_g), \, \beta = \frac{a}{2} + (N-1)(2r + l_g)$$

Again, the result of this integration is the same as (3.22) with $I(C)$ defined as

$$I(C) = \sqrt{((N + k - 2)(2r + l_g) + (b - r))^2 + (C - k_2)^2}$$
$$- \sqrt{((N + k - 2)(2r + l_g) + (b - r))^2 + (C - k_1)^2}$$
$$+ \ln \left| \frac{\left(\sqrt{((N + k - 2)(2r + l_g) + (b - r))^2 + (C - k_1)^2} + (C - k_1)\right)^{(C - k_1)}}{\left(\sqrt{((N + k - 2)(2r + l_g) + (b - r))^2 + (C - k_2)^2} + (C - k_2)\right)^{(C - k_2)}} \right|$$

(3.30)

3.5   Mutual Inductance between Rectangular Coils

A simple description of the mutual inductance scenario of a single turn primary and a single turn secondary is depicted in Fig. 3.4. As an extension of the theory previously developed, the mutual inductance for a multi-turn and/or multi-layer rectangular coil can be written in terms of the contributions due to current flowing through i^{th} turn, j^{th} section of the primary on the lth turn, k^{th} section on the secondary. The sectional mutual inductance matrix can be written as

$$M_{ijlk} = \frac{\mu_0}{4\pi} \times \begin{bmatrix} \sum\limits_{i=1}^{N}\sum\limits_{l=1}^{N} M_{i1l1} & 0 & -\sum\limits_{i=1}^{N}\sum\limits_{l=1}^{N} M_{i1l3} & 0 \\ 0 & \sum\limits_{i=1}^{N}\sum\limits_{l=1}^{N} M_{i2l2} & 0 & -\sum\limits_{i=1}^{N}\sum\limits_{l=1}^{N} M_{i2l4} \\ -\sum\limits_{i=1}^{N}\sum\limits_{l=1}^{N} M_{i3l1} & 0 & \sum\limits_{i=1}^{N}\sum\limits_{l=1}^{N} M_{i3l3} & 0 \\ 0 & -\sum\limits_{i=1}^{N}\sum\limits_{l=1}^{N} M_{i4l2} & 0 & \sum\limits_{i=1}^{N}\sum\limits_{l=1}^{N} M_{i4l4} \end{bmatrix}$$

(3.31)
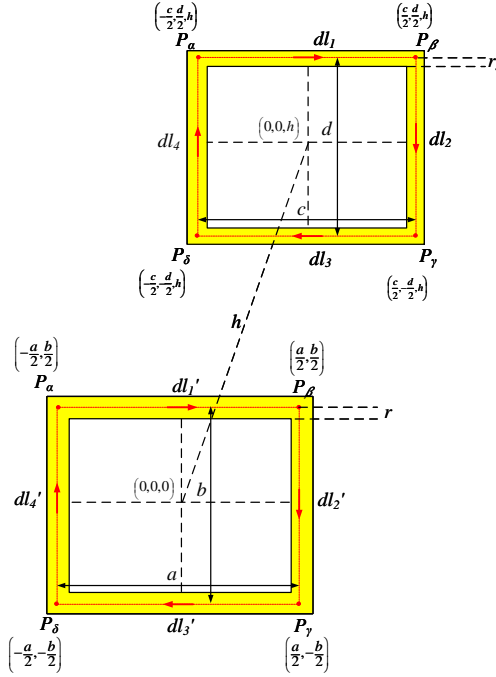
Figure 3.4: Mutual inductance between a general single turn primary and a single turn secondary. The length and breadth of the primary are (a, b) while that of the secondary are (c, d). The vertical displacement between the primary and secondary is h.
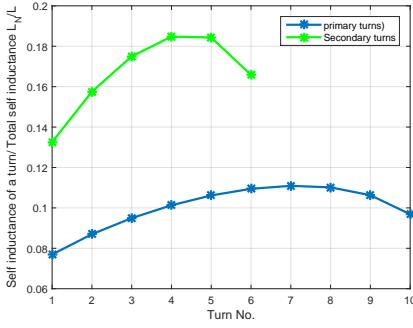
Figure 3.5: Normalized self-inductance of a rectangular primary $(a \times b)$ of radius r and secondary $(c \times d)$ of radius r_s as a function of each turn of the corresponding primary and secondary as defined in Table 3.1.
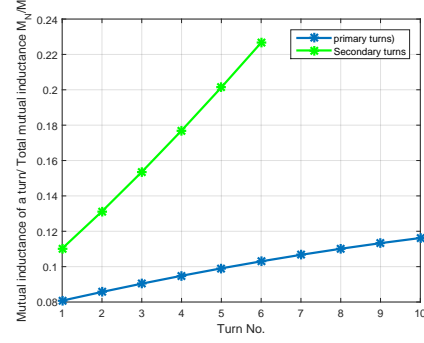
Figure 3.6: Normalized mutual inductance of a rectangular primary $(a \times b)$ of radius r and secondary $(c \times d)$ of radius r_s as a function of each turn of the corresponding primary and secondary as defined in Table 3.1.

3.6 Analytical Computations

The generality of this theory developed makes it possible to analyse rectangular shapes of variable turns, air-gaps and sectional lengths. In the analysis, the dimensions of coils used in the primary and secondary are listed in Table 3.1.

Table 3.1: The dimensions of the primary and secondary rectangular coils for analysis

a	b	c	d	r	r_s	h	N_1	N_2
10 cm	15 cm	5 cm	8 cm	1 mm	1 mm	13.3 cm	10	6

The normalized self-inductance of the rectangular coils as in Fig. 3.5, suggests that the intermediate turns contribute better to self-inductance than smaller and larger turns.

Thus, the distributed leakage picture of the coils, in terms of the per-turn contributions to self-inductance and leakage can be extracted based on the information presented. Also, the trends of normalized mutual inductance as in Fig. 3.6 suggests that the larger turns contribute more to the coupling and hence the mutual inductance.

The distribution of leakages as indicated in Fig. 3.7 shows that there is a high contribution to overall leakage for intermediate turns.

For a dimensionally large primary $(a \times b)$ compared to the secondary, as in Fig. 3.8, the effect
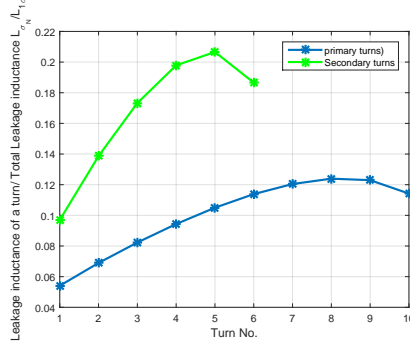
Figure 3.7: Normalized leakage inductance of a rectangular primary $(a \times b)$ of radius r and secondary $(c \times d)$ of radius r_s as a function of each turn of the corresponding primary and secondary as defined in Table 3.1.
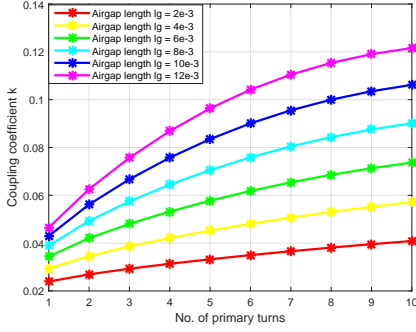
Figure 3.8: Coupling coefficient with variable primary turns for different air-gaps l_g with a secondary fixed as $(c \times d)$ as defined in Table 3.1.
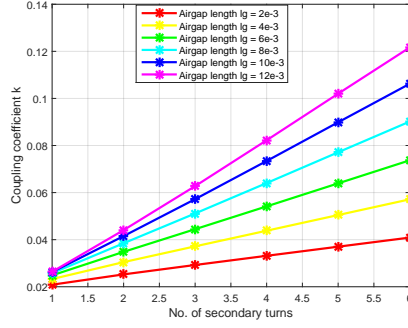
Figure 3.9: Coupling coefficient as a function of secondary turns for variable air-gaps l_g with a primary fixed as $(a \times b)$ as defined in Table 3.1.

that turns has on the coupling is exponential while the effect of increasing the secondary turns for a dimensionally small secondary $(c \times d)$ is less drastic-linear as in Fig. 3.9.

3.7   Circular Coils

In the case of a circular coil, the application of Neumman's integral as in (3.1), the two contours c_1 and c_2 represent the contour of current filaments assumed to be in the middle of primary and secondary. However, in case of self-inductance, the same equation can

be used with the two contours taken as the mid-current and inner edge contour of the same conductor. Now, consider the case of a misaligned circular coil pair, such a coil pair is indicated in Fig. 3.10. The inner radius of the ith turn of the primary and j^{th} turn of
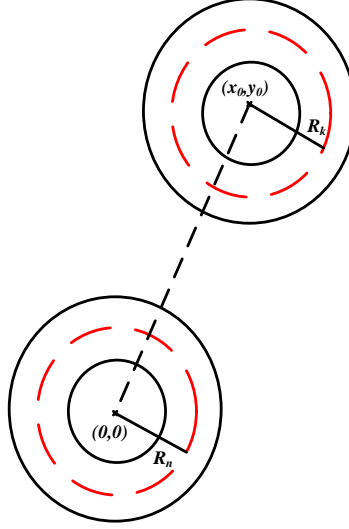
Figure 3.10: A coupled circular coil system with primary having $i = 1, 2..., n$ turns and the secondary having $j = 1, 2..., k$ turns, the radii of the mid current contour of the nth primary turn and k^{th} secondary turn are R_n and R_k.

secondary are $R_i = R_p + (i - 1)(2r + l_g)$, $R_j = R_s + (j - 1)(2r + l_g)$ respectively. In such a case, the partial mutual inductance is written in terms of azimuths, ϕ_i and ϕ_j of the respective coils as

$$M_{ij} = \frac{\mu_0}{4\pi} \times \left[\int_{\phi_i=0}^{2\pi} \int_{\phi_j=0}^{2\pi} I d\phi_i d\phi_j \right] \tag{3.32}$$

Where I, R_i, R_j are defined as

$$I = \frac{R_i R_j \sin \phi_i \sin \phi_j + R_i R_j \cos \phi_i \cos \phi_j}{\sqrt{(R_i \cos \phi_i - (x_0 + R_j \cos \phi_j))^2 + (R_i \sin \phi_i - (y_0 + R_j \sin \phi_j))^2}} \tag{3.33}$$

The final mutual inductance can be defined for primary having $'n'$ turns and secondary with $'k'$ turns as

$$M = \sum_{i=1}^{n} \sum_{j=1}^{k} L_{ij} \tag{3.34}$$

The self-inductances can be extracted similarly from (3.34) by defining the radius of of the middle edge and the inner edge of each turn. Also, in case of an IPT system based on multiple coils, the magnetic and resistive parameters can be evaluated from (3.37).

3.8   Extension to Multi-Coil Charge Pads

Consider a linear magnetic system excited by a pure sinusoidal (non-harmonic) voltage consisting of a primary and pickup composed of several segmented coils as shown in Fig. 3.11. The coils can be individually connected serially or in parallel to compose the multi-coil charge-pad. Let the primary be composed of $'n'$ coils, $(1, 2, ..n)$ and pickup with $'m-n'$ coils, $(n+1, n+2, ..m, (m > n))$. Consequently, the voltage matrix, $[V]$ for all the coils can be written as a in terms of currents, $[i]$ and time-derivative of currents, $\left[\frac{di}{dt}\right]$
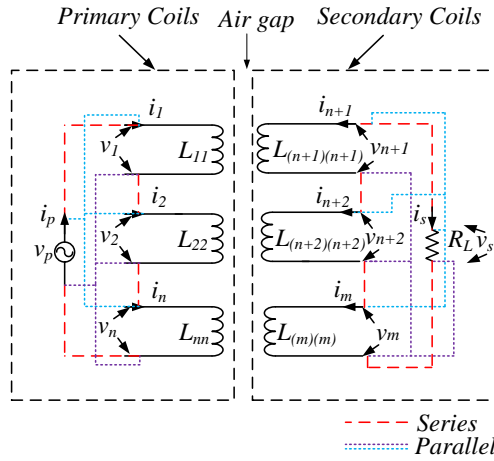
Figure 3.11: Defining a IPT system with primary and secondary composed of multiple coils with self-inductances as $(L_{ij}, i = j)$ and mutual inductances as $(L_{ij}, i \neq j)$.

$$[V] = [L] \times \left[\frac{di}{dt}\right] + [R] \times [i] \tag{3.35}$$

Where the matrices are defined as

$$[V] = \begin{bmatrix} v_1 \\ v_2 \\ \vdots \\ v_n \\ v_{n+1} \\ v_{n+2} \\ \vdots \\ v_m \end{bmatrix} \quad \left[\frac{di}{dt}\right] = [i'] = \begin{bmatrix} i'_1 \\ i'_2 \\ \vdots \\ i'_n \\ i'_{n+1} \\ i'_{n+2} \\ \vdots \\ i'_m \end{bmatrix} \quad [i] = \begin{bmatrix} i_1 \\ i_2 \\ \vdots \\ i_n \\ i_{n+1} \\ i_{n+2} \\ \vdots \\ i_m \end{bmatrix} \quad [R] = \begin{bmatrix} R_1 & 0 & 0 & 0 & 0 & 0 & 0 & 0 \\ 0 & R_2 & 0 & 0 & 0 & 0 & 0 & 0 \\ \vdots & \vdots & \vdots & \vdots & \vdots & \vdots & \vdots & \vdots \\ 0 & 0 & 0 & 0 & 0 & 0 & 0 & R_8 \end{bmatrix}$$

$$[L] = \begin{bmatrix} L_{11} & L_{12} & \cdots & L_{1n} & L_{1(n+1)} & L_{1(n+2)} & \cdots & L_{1(m)} \\ L_{21} & L_{22} & \cdots & L_{2n} & L_{2(n+1)} & L_{2(n+2)} & \cdots & L_{2(m)} \\ \vdots & \vdots & \vdots & \vdots & \vdots & \vdots & \vdots & \vdots \\ L_{n1} & L_{n2} & \cdots & L_{nn} & L_{n(n+1)} & L_{n(n+2)} & \cdots & L_{n(m)} \\ L_{(n+1)1} & L_{(n+1)2} & \cdots & L_{(n+1)n} & 0 & 0 & 0 & 0 \\ L_{(n+2)1} & L_{(n+2)2} & \cdots & L_{(n+2)n} & 0 & 0 & 0 & 0 \\ \vdots & \vdots & \vdots & \vdots & 0 & 0 & 0 & 0 \\ L_{m1} & L_{m2} & \cdots & L_{mn} & 0 & 0 & 0 & 0 \end{bmatrix} \quad (3.36)$$

The series and parallel combination can now be decomposed from this multi-coil combination. In case of a series connected set of coils, $i_p = i_1 = i_2 \cdots = i_n$ and $i_s = i_{n+1} = i_{n+2} \cdots = i_m$. Also, in case of the parallel set of coils, $i_p = i_1 + i_2 \cdots + i_n$ and $i_s = i_{n+1} + i_{n+2} \cdots + i_m$. After such a transformation, it becomes easy to reduce such a system of parallel or series coils into a single coil-pair. In such a system, for both series and parallel system of coils, it can be easy to prove that

$$\begin{bmatrix} \sum_{i=1}^{n} v_i \\ \sum_{j=n+1}^{m} v_j \end{bmatrix} = \begin{bmatrix} \sum_{i=1}^{n}\sum_{j=1}^{n} L_{ij} & \sum_{i=1}^{n}\sum_{j=n+1}^{m} L_{ij} \\ \sum_{j=n+1}^{m}\sum_{i=1}^{n} L_{ij} & \sum_{j=n+1}^{m}\sum_{i=n+1}^{m} L_{ij} \end{bmatrix} \times \begin{bmatrix} i_p' \\ i_s' \end{bmatrix} + \begin{bmatrix} \sum_{i=1}^{n} R_i & 0 \\ 0 & \sum_{j=n+1}^{m} R_j \end{bmatrix} \times \begin{bmatrix} i_p \\ i_s \end{bmatrix}$$

$$(3.37)$$

The Equation (3.37) indicates that it is possible to convert a linear magnetic system with multi-coil into a system of a single coil pair by calculating the individual contributions. Such a equivalent coil system is shown in Fig. 3.12. Such a transposition makes it easy to analytically model multi-coil linear magnetic systems by using the principles of single coils already developed previously.
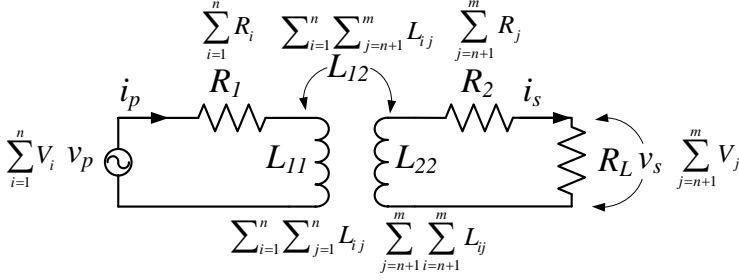
Figure 3.12: Equivalent single coil pair for a system of coils with $(1, 2..n)$ coils in the primary and $(n + 1, n + 2..m)$ coils in the pickup.

3.9   Validation of Analytical Model

To validate the analytical models that are developed in previous sections, FEM simulation and experimentation are carried out. Circular and rectangular shapes are compared. The physical properties of the coils are tabulated in Table 3.2. To show the efficacy of analytical expressions, a reduced fill factor was employed for rectangular coils by maintaining an air-gap of 0.6 cm between the turns.

Table 3.2: Properties of the compared circular and rectangular coils

Type of coil	a (cm)	b (cm)	l_g (cm)	N (turns)
Rectangular ($R1$)	4	2	0.6	9
Rectangular ($R2$)	6	4	0.6	15
Circular (C)	inner diameter = 5.5 cm			14
litz wire used	600×0.071 mm, 2.1 mm dia overall			

The constructed coils are shown in Fig. 3.13. The measurements, analysis and simulations are carried out at variable z-gaps between the coils and also at several misaligned positions. The z-gaps are simulated at 3, 5, 7 and 9 cms of coil displacements in the z-direction, taking vertical misalignment in consideration. In case of lateral misalignment, perfect alignment, 75%, 50% and 25% alignments are chosen along x-axis. The results along y-axis for symmetrical shapes follows the same trend as the x-axis and hence are not considered.

Measurements are made by using Agilent 4294A impedance analyser. The mutual inductances are extracted from self-inductances by carrying out a constructive and destructive flux measurement by connecting the coils serially from one end to the other and then swapping
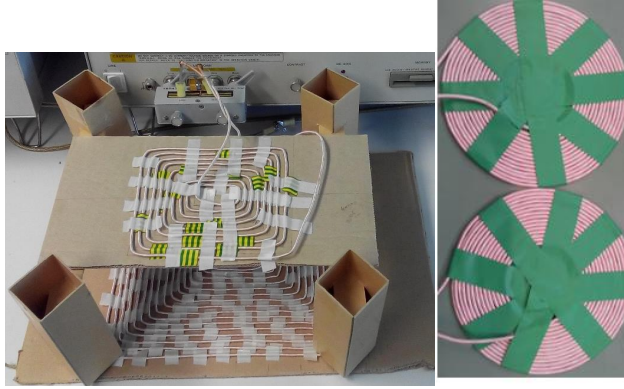
Figure 3.13: Experimental comparison of rectangular and circular coils with parameters as tabulated in Table 3.2.

one of the ends (L_{const}, L_{des}). The expressions used for extracting the mutual inductance and coupling are

$$M = \frac{L_{const} - L_{des}}{4} \tag{3.38}$$

$$k = \frac{M}{\sqrt{L_1 L_2}} \tag{3.39}$$

The analytical expressions for circular coils are calculated from (2.12) − (3.34). Also, for rectangular coils, (3.20) − (3.31) are computed. MATLAB scripts are written separately for each of the computation and a software tool for self, mutual and coupling computations is developed for air-cored coils. A comparison of coupling obtained analytically and by making measurements for circular coils is presented in Fig. 3.14.

The results show a large degree of agreement between the analytical expressions and the measured results. Mismatch in the results are due to the dimensional tolerances of *litz* wire in the experiments (unlike a solid conductor used in the analysis) that are not considered in the analytical expressions. Some instrumental accuracy limitations also add to this error. The trends lines match while there is an increasing error at large z-gaps (upto 30%). This is caused due to the inaccuracy in the estimation of rather small mutual inductance at larger offsets, the error of which is more pronounced.

FEM models were created and simulated so as to perform numerical evaluation of the coils considered. The FEM models developed are presented in Fig. 3.15.

The coupling and self-inductances of circular and rectangular coils are compared analytically, using FEM simulations and experimentation. The results are presented in Fig. 3.16, the
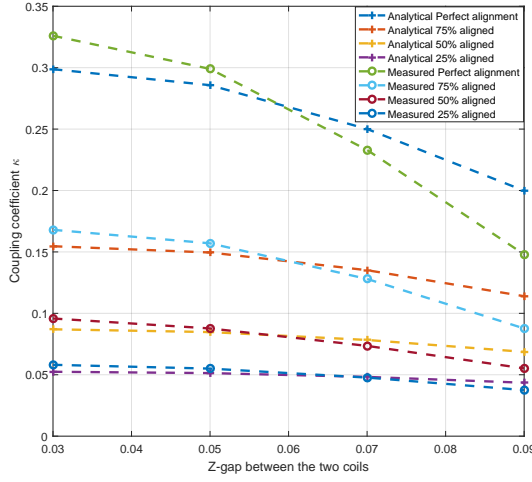
Figure 3.14: The analytical and experimental comparison of coupling coefficient of circular coils with z-gaps of 3, 5, 7 and 9 cms with coils of parameters as tabulated in Table 3.2.
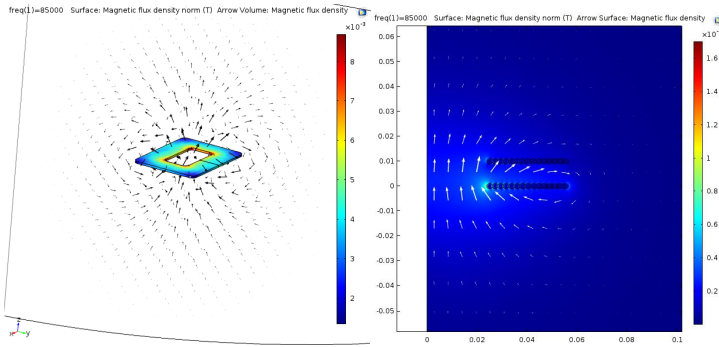
Figure 3.15: FEM simulation models of the rectangular coil (top-left), circular coil (top-right) and the rectangular coil (bottom) couple. The rectangular coils are modelled in a $3D$ domain while the circular coils due to their rotational symmetry are modelled in the $2D$ domain.

coupling being recorded at perfect alignment and variable z-gaps while self-inductances measured for all variable shapes. All measurements show the same trend and there is a close match between analytical observations, FEM simulations and measurements.

Figure 3.16: Coupling coefficient of rectangular pads at various z-gaps and self-inductances of air-cored charge pads of various shapes. The coupling is measured at various z-gaps at the best aligned point. The parameters of the coils are as presented in Table 3.2.

3.10   Shape and Performance of Air Couplers

The effect of shapes in IPT systems can be analysed for air-cored couplers based on the mathematical analysis that has been derived previously. To make such a comparison, a few performance parameters are considered. They are the open circuit voltage v_{oc}, short circuit current i_{sc}, maximum output power, S_{max} and maximum efficiency, η_{max}. Open circuit voltage is the maximum voltage that the IPT system can source and short circuit current is the maximum current that the same can deliver.

For a coupled charge-pad, if L_1 and L_2 are the self-inductances of the two couplers with 'M'' as the mutual inductance and operated at angular frequency ω, creating current i_1 through the primary, the open-circuit voltage is defined as $v_{oc} = j\omega M i_1$ and during short-circuit if i_{sc} is the current flowing in the pickup, $i_{sc} = \dfrac{v_{oc}}{j\omega L_2} = \dfrac{M i_1}{L_2}$. Now, the maximum output power is defined in terms of loaded quality factor of pickup, $Q_{2L} = (\omega \times L_2)/(R_L + R_2)$, where R_L is the load resistance and R_2 is the ac-resistance of the pickup charge-pad as

$$S_{max} = v_{oc} \times i_{sc} = \frac{(i_1^2 M^2 Q_{(2,L)}\omega)}{L_2} \tag{3.40}$$

The above equation quantifies the maximum output power that such an air-cored coupler can source. Also, the maximum efficiency of IPT systems have been derived independent of

compensation applied and load present in terms of native quality factors of the primary (Q_1) and pickup (Q_2) as [139]

$$\eta_{max} = \frac{k\sqrt{Q_1 Q_2}}{2 + k\sqrt{Q_1 Q_2}} \tag{3.41}$$

These parameters have been used to compare a number of differently shaped air-cored charge-pads. All shapes considered have been analysed keeping area conserved. This way, generalizations of the behaviour of fields and hence coupling, power transferred and other parameters are possible. Several analysis were also carried out keeping perimeter conserved and multi-turns with similar results. In addition, these results also correspond and can be generalized to charge-pads with flux-enhancing materials such as Ferrite. This as enhanced coupling is obtained by placing Ferrites along the natural direction of flux lines. Hence, the basic tendency of the shape in terms of coupling and its gradient is similar in all IPT applications. The compared shapes are listed in Table 3.3. All considered shapes have been simulated with a one turn coil and a z-gap of 1 cm. This so that the effect of shapes are more enhanced.

Table 3.3: Physical parameters of various coil shapes used in the air-cored coupler.

Considered Shape	Parameters
Rectangle dim.(mm)	650×400
Square dim.(mm)	509.9×509.9
Circle rad.(mm)	287.6
Double Circle (DCirc) dim.(mm)	203.4
Double Rectangle (DR) symmetric dim.(mm)	459.6×282.8
Double Rectangle + Quadrature symmetric dim.(mm) (DR+Quad)	375.3×230.9
Area (m^2)	0.2600

The multi-coil shapes are composed of multiple symmetric coils that are placed close to each other with the coils carrying currents in opposite direction. The mutual inductance and coupling of these charge-pads are obtained by analyzing (3.37) and using the mathematical analysis of single coils. A study of coupling by misaligning the coils along x-direction (lateral displacement) is presented in Figure 3.17.

It can be inferred that circle and four sided shapes differ in the tolerance to coupling variations when subjected to lateral misalignment. The coupling of rectangular and square coils tend to decay gradually, while the circular shape sees a more sharper drop with misalignment. Circular shape due to the fact that it has the highest area for a given perimeter among closed shapes, has the highest coupling at the best aligned point. The double coils also share the same feature but with a larger extension of the power profile. It is important to note that in this analysis, since area is kept conserved, the perimeter varies between the shapes and hence it is important to keep trends in mind, rather than absolute values. Null-coupling points in DR and DCirc coils, occur at positions where a pick-up coil is
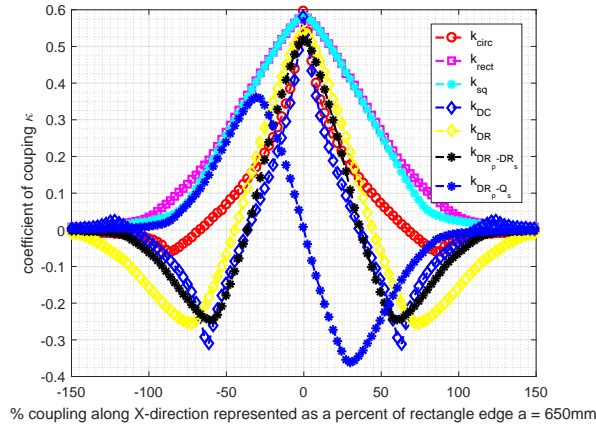
Figure 3.17: Coupling coefficients of single and multi-coil shapes with x-directional misalignment of coils in Table 3.3.

confronted with opposing flux of equal magnitude from the primary charge-pad. Among the double coils, the DCirc geometry has greater best-aligned coupling than that of DR geometry. However, the misalignment profile for DR coils is broader than that of DCirc coils and hence it is well suited to applications where larger misalignment behaviour is expected, for eg: EVs. When such an analysis was broadened to include the behaviour of a DR primary and a DR Quad pick-up, the Quad picking up flux emanating from a DR primary behaves best at the misaligned points, while is the worst at the best-aligned point. On the contrary, the DR pick-up behaves complementary to the Quad pick-up with a DR primary.

Power transferred to the pick-up is evaluated from (3.40). The uncompensated power calculated when subjected to lateral misalignment is shown in Figure 3.18. Among single coils, the circular coil has a sharp misalignment band while the four sided shapes have greater tolerance. The double shapes follow the features of their single equivalents, with the difference that there is a misalignment point when a single coil among both the primary and pick-up receives power. This creates two more zones of power transfer apart from the best aligned point. In these points, the power is reduced to $< 25\%$ as the pick-up voltage is reduced to half, which in turn halves the pick-up current. However, these double shapes suffer from a no-power zone created at the null coupling points. These null power points can be eliminated by using a quadrature coil, the coupling of which is complementary to the main coils and hence an addition of power from the quadrature coils removes these null zones. It is important to note that in an actual implementation, the magnitudes of these curves will depend on the number of turns of each coil, materials present, the source characteristic - voltage/current, resonant behaviour etc.

The maximum efficiency as presented in (3.41) has dependence on quality factor which
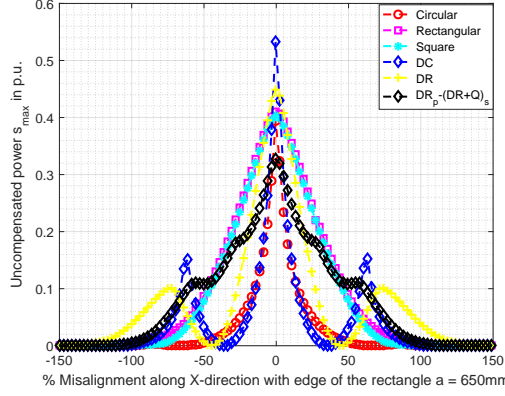
Figure 3.18: Uncompensated power analysed on the basis of a unit current flowing through various shapes of single turn and equal area as indicated in Table 3.3. The misalignment is considered along x-direction.

in-turn depend on the ac resistances of the coils. The ac-resistances for the *litz* wire used is extracted from a tabulation technique as presented in [140]. The calculated ac resistance factor including both skin and proximity effects for *litz* wire indicated in Table 3.2 is $\dfrac{R_{ac}}{R_{dc}} = 1.029$. The result of maximum efficiency computation when subjected to variable coupling during misalignment is shown in Figure 3.19. This plot represents the theoretical maximum efficiency that can be expected at various misaligned points for various shapes. The efficiency values floor at the power null points as expected.
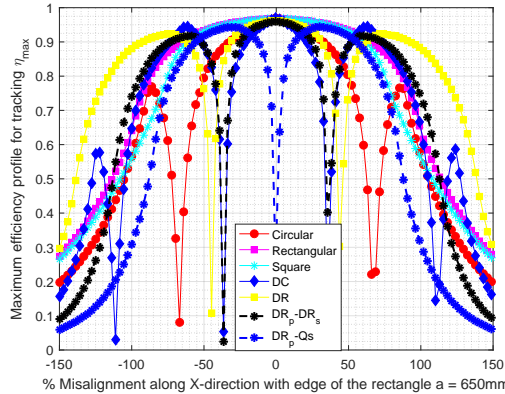
Figure 3.19: Maximum efficiency tracking of single and multi-coil shapes with x-directional misalignment of coils in Table 3.3. Each curve envelops the contour of peak expectation of efficiency analysed from (3.41)

3.11   Conclusion

In this chapter, a generic analytical tool that is useful to model the magnetics of single and multi coil geometries is developed. The analytical equations developed can be extended to polygonal shapes and can be used to model n-multi coil geometries as well. The analytical expressions have the strength that they are computational efficient eg: computation of inductances and coupling of a single turn rectangular charge-pad takes 0.653 s (2.2 GHz Intel i3-processor and 4 GB RAM). In case of FEM analysis, each individual calculation takes several seconds. This difference gets exaggerated for multi-coil IPT systems and analytical formulation yields accurate and fast results. This is a first step in magnetic design, wherein the fundamental magnetics can be evaluated.

Such an analytical approach can yield the variation in magnetic parameters due to coupler geometry. Now, different applications of IPT systems can have different objectives: minimization of gradient of coupling in highly misalignment tolerant EV IPT systems $min(\frac{\partial k}{\partial x}, \frac{\partial k}{\partial y})$, elimination of power null points in power sensitive applications ($P_{x,y} \neq 0$). Thus, different strategies can be evolved based on the spatial variation of coupling, efficiency and/or power transfer. This chapter can empower this decision making before going in for a detailed multi-objective optimization after fixing a geometry suited to the application.

However, a limitation that this approach has is that the principle of superposition holds for linear magnetic systems. Thus, non-linearities in the system such as saturation are neglected in the study. This is a valid assumption for air-cored geometries and hence the study yields good results. However, interfaces of different materials in high power IPT systems such as ferrites and shielding materials (aluminium) need to respect boundary conditions to compute magnetic parameters. Thus, the equations need to be adapted for boundaries and this extension is beyond the scope of this chapter. In related work, an analytical LCL filter design where interfaces are modelled by using method of images is presented in [141]. Image method can be applied to the analysis in this chapter to model parameters of couplers with several material interfaces. Additionally, the effect of frequency on inductances (due to eddy currents) is not considered in this chapter.

A detailed numerical optimization based on the inputs from this study so as to optimize ferrite, aluminium and other materials that may be present in charge-pads is the next step. Such a FEM optimisation is considered in Chapter 5. Some useful results obtained from the analysis are:

1. The analysis, compared with FEM and experiments have a good match. Almost all observations have an error less than 10%. This is acceptable for magnetic analysis.

2. The coupling of single coils are such that circular coils have the best coupling at the well-aligned point and the four sided coils have a larger misalignment tolerant band. Thus, rectangular coils can be used for more misalignment tolerant designs and circular for well-aligned applications.

3. The coupling behaviour of multi-coil geometries follow the trend of single-coil shapes but have null-coupling points. By designing a quadrature coil located between the mid points of the single-coils, flux can be captured at the null-coupling points.

4. The quadrature and double rectangle pickup have complementary coupling-misalignment behaviour. At the best aligned point, the quadrature coil picks up no flux and at a misalignment point (null-coupling) of double rectangle pickup, the quadrature coil picks up maximum flux.

5. The double rectangular and double circular shapes can effectively extend the range of power transfer to larger misaligned positions. The addition of quadrature coil to the pickup can remove null-coupling points from the power profile. This is a good solution for constant power applications, with optimized magnetics.

6. The total enclosed area of the shapes has been kept constant to make a fair comparison. However, it is possible to influence the turns in the quadrature coils in double rectangle quadrature pads and this impacts the peaks obtained in the misalignment points.

Study of Misalignment in IPT Systems

This chapter looks into the problem of misalignment in distributed IPT systems. The idea of varying mutual inductance longitudinally referred to as longitudinal misalignment is introduced here. The analytical expressions for both lateral and longitudinal misalignment are derived. Experimental validation of the theory developed is also performed. In case of conventional rectangular coils, the vertical sections are not symmetrical. This was observed in the mutual inductance profile experimentally and the concept of "Edge Effect" was introduced to explain the same. An inductor with symmetrical ends was constructed to tackle this problem.

Based on

- V. Prasanth and P. Bauer, "Distributed ipt systems for dynamic powering :Misalignment analysis," *IEEE Transactions on Industrial Electronics*, vol. 61, no. 11, pp. 6013–6021, Nov 2014. and

- V. Prasanth and P. Bauer, "Study of misalignment for On Road Charging," in *IEEE Transportation Electrification Conference and Expo (ITEC)*, 2013, pp. 1-8.

4.1 Introduction

In this chapter, the power of analytical expressions is used to study the effect of misalignment in distributed IPT systems. Distributed IPT systems consists of long tracks which is energized by a power inverter. Typically, the tracks don't have ferrites or use minimal ferrites.

Distributed IPT systems are typically applied in the fields of monorails, automatically guided vehicles (AGV) and also in polyphase IPT systems for road transport. The distributed systems for monorails typically have a pick-up that is in close proximity to the track and in some cases surround the track. Several pick-up designs of monorail based distributed IPT system are present in literature. Examples include E-shaped pick-up, S shaped pick-up, coaxial pick-up [144].

AGV based IPT systems unlike monorails have more freedom to move and hence the pick-up is not in close proximity to the primary. Here, different pick-ups have been researched, including flat pick-up, flat-E pick-up etc [144]. A geometry that is considered for utilization in such systems is shown in Fig. 4.1.

Long rectangular loop based primary and the magnetic fields

a)

Cross-sectional view of pickup/secondary placed on top of the primary

b)
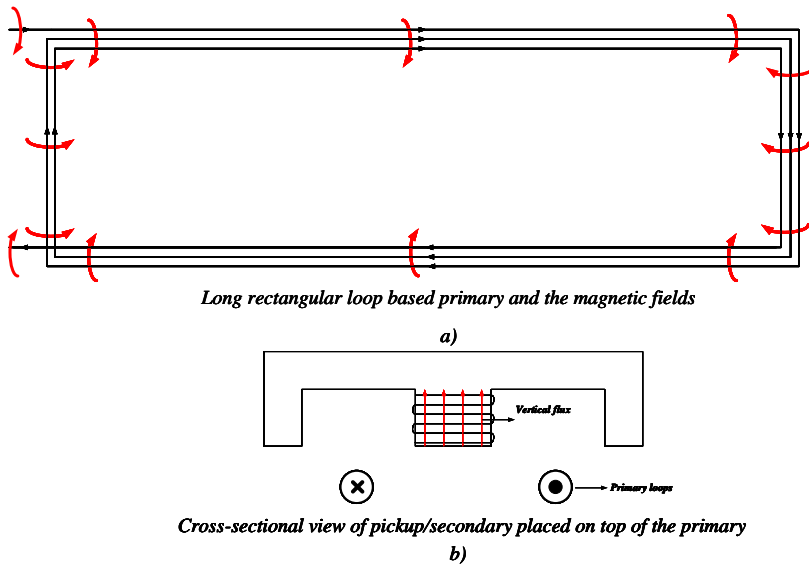
Figure 4.1: a) Typical loops that form the primary of distributed inductive power transfer systems b) Magnetic system consisting of an E core as pick-up typically used in AGV systems.

4.2 Analytical Computation of Misalignment

Misalignment, in case of a bipolar distributed IPT system as shown in Fig. 4.1, can be approximated by considering the primary as a system of two parallel conductors. Consider these two parallel conductors carrying the same current, i, but in opposite directions (bipolar) as shown diagrammatically in Fig. 4.2. The length of each conductor is taken as $2L$, with O and O' being the midpoint. The coordinates of the origin O is $(0, 0)$.
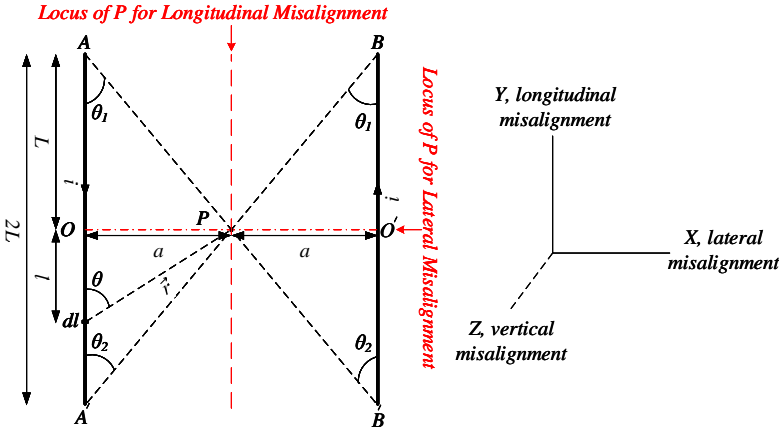
Figure 4.2: Calculating the flux density at a point P which is at the midpoint of the symmetrical conductors of length $2L$ and located symmetrically at the midpoint of the lateral displacement of $2a$ between the conductors in the XY plane.

4.2.1 Perfect Alignment at the Center of the Loop

Let there be a point P as in Fig. 4.2, at a distance a from either conductor. This situation is similar to the well aligned primary of the IPT system, when the pick-up (represented by P) is in the middle of the loop. It will be proved in this section that the flux density B due to these conductors for the locus of P along the lateral and longitudinal axis will vary as a function of the angles it subtends at the two extreme ends of each conductor (θ_1, θ_2).

The flux density at any point due to a current element $id\overrightarrow{l}$ and displaced by $\overrightarrow{r}$ with the unit vector along its direction, $\hat{r}$ is given by applying Biot-Savart law as in (2.9).

Now, in the situation in Fig. 4.2, by the principle of superposition applied to the point P by considering AA' and BB' separately as:

$$\overrightarrow{\mathbf{B}} = \overrightarrow{\mathbf{B}}_{AA'} + \overrightarrow{\mathbf{B}}_{BB'} \tag{4.1}$$

It is easy to ascertain that the flux densities add each other in between the conductors as the currents are in the opposite direction. Now, consider the conductor AA'

$$d\overrightarrow{\mathbf{B}}_{AA'} = \frac{\mu_0}{4\pi} \frac{id\overrightarrow{\mathbf{l}} \times \hat{\mathbf{r}}}{r^2} \tag{4.2}$$

Consider the following transformations, $a = r\sin\theta$ and $l = a\cot\theta$. Thus,

$$d\overrightarrow{\mathbf{B}}_{AA'} = \frac{\mu_0 i}{4\pi} \times \frac{-(a\csc^2\theta d\theta)\sin\theta}{(a\csc\theta)^2} \tag{4.3}$$

Finally, it can be obtained that

$$\overrightarrow{\mathbf{B}}_{AA'} = -\frac{\mu_0 i}{4\pi a} \times \int_{-\theta_1}^{\theta_2} \sin\theta d\theta = \frac{\mu_0 i}{4\pi a}(\cos\theta_2 + cos\theta_1) \tag{4.4}$$

As a result of the symmetry of point P, with the y coordinate at the midpoint, $-\theta_1 = \theta_2 = \alpha$

$$\overrightarrow{\mathbf{B}}_{AA'} = \frac{\mu_0 i}{2\pi a} \times \cos\alpha = \frac{\mu_0 i}{2\pi a}\frac{L}{\sqrt{(L^2 + a^2)}} \tag{4.5}$$

Also, the situation being symmetrical for both conductors, $\overrightarrow{\mathbf{B}}_{AA'} = \overrightarrow{\mathbf{B}}_{BB'}$ and using (4.1), it can be obtained that

$$\overrightarrow{\mathbf{B}}_{P(a,0)} = \frac{\mu_0 i}{\pi a} \times \cos\alpha = \frac{\mu_0 i}{\pi a}\frac{L}{\sqrt{(L^2 + a^2)}} \tag{4.6}$$

This represents the vertical component of flux density when the point P is located at the midpoint of the perpendicular bisector of the two conductors.

4.2.2 Longitudinal Misalignment

Now, if the point P is located at one of the extremes but at perfect lateral alignment, the situation is shown in Fig. 4.3.

In this case, (4.4) can be rewritten with $\theta_1 = \alpha$ and $\theta_2 = \frac{\pi}{2}$ as

$$\overrightarrow{\mathbf{B}}_{AA'} = \frac{\mu_0 i}{4\pi a} \times (\cos\frac{\pi}{2} + \cos\alpha) = \frac{\mu_0 i}{4\pi a} \times \frac{2L}{\sqrt{(2L)^2 + a^2}} \tag{4.7}$$
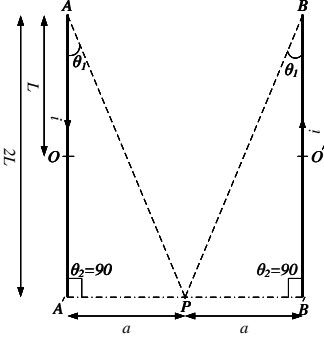
Figure 4.3: Calculating the vertical flux density at a point P which is at the edge of the symmetrical conductors of length $2L$ and located symmetrically at the mid-point of the lateral displacement of $2a$ between the conductors.

Thus, following the course of (4.1)

$$\overrightarrow{\mathbf{B}} = \frac{\mu_0 i}{2\pi a} \times \frac{2L}{\sqrt{(2L)^2 + a^2}} \tag{4.8}$$

Now, since length of the conductor is large $(2L >> a)$

$$\overrightarrow{\mathbf{B}} \approx \frac{\mu_0 i}{2\pi a} \tag{4.9}$$

Comparing (4.9) and (4.6), it can be obtained that

$$\overrightarrow{\mathbf{B}}_{P(a,-L)} = \frac{\overrightarrow{\mathbf{B}}_{mid}}{2} \times \frac{L}{\sqrt{(L^2 + a^2)}} \tag{4.10}$$

Thus, it can be inferred that the flux density at the laterally aligned state of the pick-up at the ends of the primary is lower than in the middle. This can be reasoned out by the fact that when the pick-up moves longitudinally away from the middle of the primary loop, it has minimal flux contributions from the current elements of that extreme end of the primary from where it is far away and as it reaches the extreme end, it has negligible contributions from the other end. This effect is essential to be considered for distributed systems as it can play a major role in determining the optimal length so as to transfer constant power.

Now, for the system of N_1 parallel conductors carrying current i_1 with the condition that (small angle $< \theta_2 < \frac{\pi}{2}$) and ($\frac{\pi}{2} < \theta_1 <$ small angle), the flux density at longitudinal points along the perfectly aligned lateral state is

$$\overrightarrow{\mathbf{B}}_{AA'} = \frac{\mu_0 N_1 i_1}{2\pi a} \times (\cos\theta_2 + \cos\theta_1) \tag{4.11}$$

If ϕ_{21} represents the mutual flux, A is the area of cross-section of that part of the core that houses the pick-up windings, in terms of mutual inductance

$$M = \frac{N_2 \phi_{21}}{i_1} = \frac{N_2}{i_1} \iint\limits_{S} \overrightarrow{\mathbf{B}}.d\overrightarrow{\mathbf{A}} = \frac{\mu_0 N_1 N_2 A}{2\pi a}(\cos\theta_2 + \cos\theta_1) = M_0(\cos\theta_2 + \cos\theta_1) \tag{4.12}$$

The result of (4.12) has been simulated in Fig. 4.4 with angular bounds with small angle defined as $0°$ and this yields the fact that if we consider a finitely long track, at perfect lateral alignment, the flux density and hence the mutual inductance will vary as a sinusoidal-like distribution as the pick-up moves longitudinally.
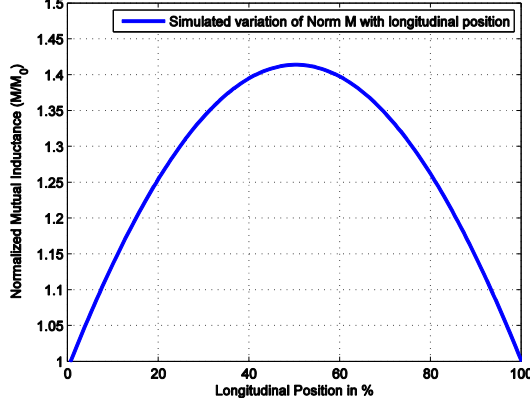
Figure 4.4: Simulation of longitudinal misalignment assuming $(0 < \theta_2 < \frac{\pi}{2})$ and $(\frac{\pi}{2} < \theta_1 < 0)$.

4.2.3 Lateral Misalignment

Consider the case of lateral misalignment taking place along the perpendicular bisector OO' as shown in Fig. 4.5.

In this case, (4.4) can be rewritten for AA' and BB' as

$$\overrightarrow{\mathbf{B}}_{AA'} = \frac{\mu_0 i}{4\pi a}(\cos(\theta_2 - \sigma) + \cos(\theta_1 - \sigma)) \quad (4.13)$$

Also for the conductor BB',

$$\overrightarrow{\mathbf{B}}_{BB'} = \frac{\mu_0 i}{4\pi a}(\cos(\theta_2 + \sigma) + \cos(\theta_1 + \sigma)) \quad (4.14)$$

Now, due to the symmetry of the perpendicular bisector, the angles $(\theta_1 - \sigma) = (\theta_2 - \sigma) = \beta$ and $(\theta_1 + \sigma) = (\theta_2 + \sigma) = \gamma$ and hence by the principle of superposition

$$\overrightarrow{\mathbf{B}} = \frac{\mu_0 i}{4\pi a}(\cos \beta + \cos \alpha) \quad (4.15)$$
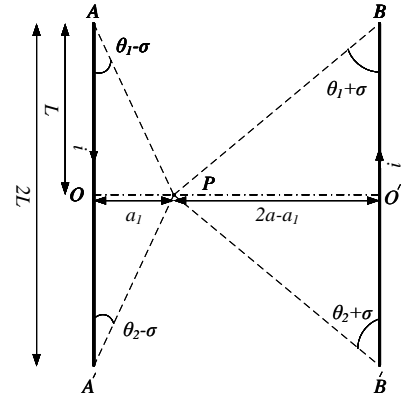
Figure 4.5: Calculating the vertical flux density at a point P which is located at a lateral distance of a_1 from O.

A special case of this condition is when the point P coincides with the point O on the Y axis. Then, $\beta = 0$ and $\cos \gamma = \frac{L}{\sqrt{L^2 + (2a)^2}} < 1$

$$\overrightarrow{\mathbf{B}}_{P(0,0)} = \frac{\mu_0 i}{2\pi a}\left(1 + \frac{L}{\sqrt{L^2 + (2a)^2}}\right) \tag{4.16}$$

Comparing (4.16) and (4.6), it is obvious that the flux density increases laterally from the extremes to the middle, where it peaks and it then again decays to a lower value on moving further away. Also, in terms of mutual inductance, (4.16) may be written as

$$M = \frac{\mu_0 N_1 N_2 A}{2\pi a}(\cos \beta + \cos \gamma) = M_0(\cos \beta + \cos \gamma) \tag{4.17}$$

Now, it is possible to move the pick-up beyond the lateral spacing between the conductors, in such a case, $\overrightarrow{\mathbf{B}}_{AA'}$ and $\overrightarrow{\mathbf{B}}_{BB'}$ components oppose each other and the mutual inductance for all the possibilities is represented by

$$M = \begin{cases} M_0(\cos \beta - \cos \gamma), P_x < 0 \\ M_0(\cos \beta + \cos \gamma), 0 < P_x < 2a \\ M_0(\cos \gamma - \cos \beta), P_x > 2a \end{cases} \tag{4.18}$$

Also, the two angles are related as

$$\tan \beta + \tan \gamma = \frac{2a}{L} \tag{4.19}$$

The simulation of (4.18) yields the Gaussian curve of lateral misalignment as shown in Fig. 4.6 with mutual inductance dying down to zero at both ends when displaced further away from the two conductors on either side.
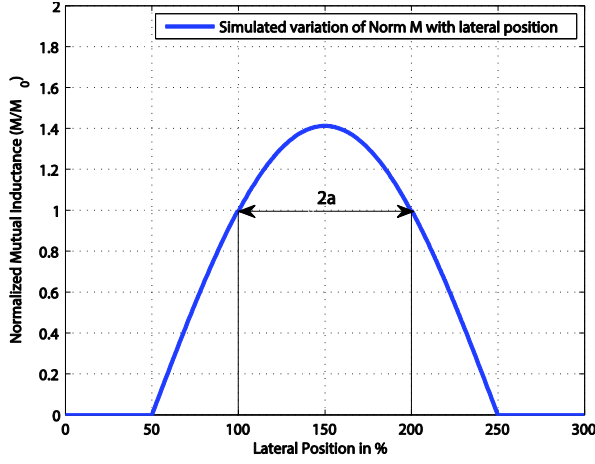
Figure 4.6: Simulation of lateral misalignment assuming $(0 < \gamma < \frac{\pi}{2})$ and $(\frac{\pi}{2} < \beta < 0)$ and setting the negative values of mutual inductances at the extremes to zero as higher angles are unrealistic.

4.3   System Description of the Experimental Setup

Before the actual experimentation procedure of the study on misalignment is dealt with, it is useful to consider a number of design choices which will be explained in the following subsections.

4.3.1   Choice of the Core and the Pick-up

In studies at the University of Auckland [145], in order to decouple the effect of the length of the distributed IPT systems and size of the pick-up, a new concept of magnetic efficiency (k_ϕ) was introduced and it was measured as a constant for different ferrite shapes with E pick-ups $(k_\phi \approx 0.65)$ having higher magnetic efficiency compared to flat pick-ups $(k_\phi \approx 0.35)$. It was therefore considered to utilize the E core. Such cores are commercially available in various sizes. For ease of laboratory experimentation and availability, a scaled down model of the IPT system based on Ferroxcube E80/38/20 core of the grade $3C90$ was used. This core has a distance between the center of the two C sections as 4 cm. Thus, the primary loops designed for this displacement, sits in perfect alignment below this.

Table 4.1: Physical properties of the track that forms the primary

S/No.	Property of tracks	Specification of the property
1.	Selected type of wire	*litz* wire – 600 (Strnd. No.) × 0.071mm (Dia of each strand)
2.	Length of rectangular loop (m)	1
3.	Width of rectangular loop (cm)	4

4.3.2   Consideration of Tracks and Pick-up

In this study, single phase primary systems were considered. In order to create an extensive study of the effect of the primary on the power transferred via IPT, four different configurations of the primary were constructed with a single turn, double turn, four turns and five turns. The physical properties of the tracks are tabulated in Table 4.1. The resistances and inductances of the primary as measured with the precision impedance analyser Agilent 4294 A (at 100 kHz) is tabulated in Table 4.2.
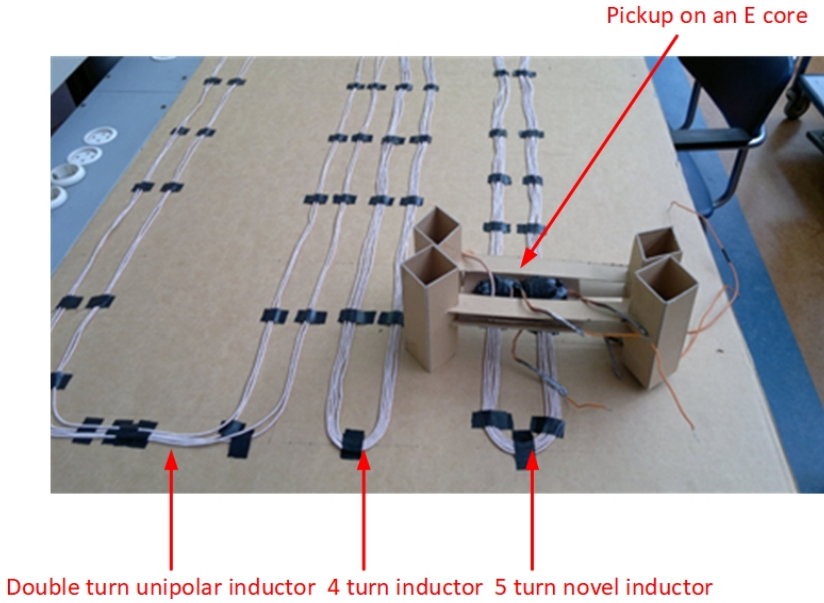
Figure 4.7: Unipolar inductor with double turn, four turn conventional inductor and five turn conventional inductor for dynamic powering.

One of the constructed inductors is shown in Fig. 4.7. In conventional primary inductor loops, the longitudinal sections of the loops carry currents in opposite directions. The unipolar inductors are a design in which currents were forced in the same direction with the

pick-up over such a configuration. This would lead to a better core utilization. The unipolar design is not considered further in this thesis.

Table 4.2: Physical properties of the track that forms the primary

S/No.	No. of turns	$L_1(\mu H)$	$R_1(m\Omega)$
1.	Single turn	2.1	19.7
2.	Double turn	5.6	35
3.	Four turn	18.9	66
4.	Five turn	27.5	81

The pick-up based on E core consisted of windings along the vertical axis used in the central limb. This winding referred to as the horizontal winding can capture the flux that is perpendicular to it, the vertical flux. The pick-up was composed of a double layer of windings of the same $litz$ wire with an inductance $L_2 = 52.5\mu$H.

4.3.3 Experimental Study of Misalignment

In case of lateral misalignment, the mutual inductance between the primary and the pick-up are noted at several displaced positions of the pick-up w.r.t the primary. In order to calculate the mutual inductance, the primary loop inductor was connected serially with the pick-up and the equivalent inductance for both constructive flux superposition, $L_{eq,c}$ and destructive flux superposition, $L_{eq,d}$ was noted. The following equations were used to calculate the same:

$$L_{(eq+c,-d)} = L_p + L_s \pm 2M$$
$$M = \left(\frac{L_{(eq,c)} - L_{(eq,d)}}{4} \right) \tag{4.20}$$

Measurements were made in the laboratory by using RLC meter. The parameters that represent the various dimensions of the IPT system are presented in Table 4.3.

Table 4.3: Physical properties of the track that forms the primary

S/No.	Parameter	Value
1.	Height (h, cm)	5
2.	Points along lateral displacement (cm)	2
3.	Points in the longitudinal direction (m)	0, 0.25, 0.5, 0.75, 1

4.3.4 Pick-up with Horizontal Coil and Study of Lateral Misalignment

The pick-up was displaced 2cm from its reference position to two new points along the left as well as the right of the x-axis and the variation in the mutual inductance was measured. The results are shown in Fig. 4.8 such that the points indicate the actual measured data and the dotted lines, the fitted curve obtained by a Gaussian fitting function that computes the average of various data points for the best fit.
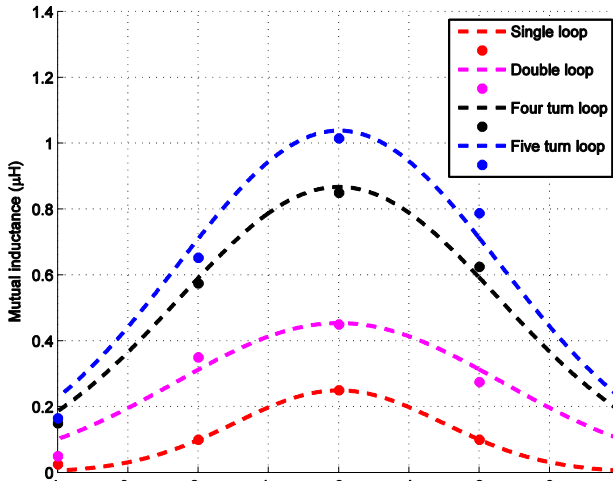
Figure 4.8: Variation of mutual inductance at several positions laterally.

The mismatch between the experimental results and the averaged fit is because of errors introduced in the measurements due to additional wires needed to measure misalignment particularly at points away from the extremes. These wires are needed to connect the serially combined primary track and pick-up coil to the RLC meter so as to measure M. The effect of these additional wires are minimized by using equal lengths of wires that introduce equal inductances which are then cancelled by making a differential measurement as in (4.20). Also, these wires were twisted so as to reduce the loop area enclosed and hence additional inductance.

The results of Fig. 4.8 indicate that the variation in mutual inductance and hence the variation in power transferred over the air gap will be in such a manner that the most perfectly aligned point would be at the middle with maximum power transferred at that point. Also, if the primary loop with maximum number of turns is selected, it would have much better mutual inductance at all possible points of observation and hence higher power transfer. This trend shows a very good agreement with the analytical results as simulated in Fig. 4.6.

4.3.5 Pickup with Horizontal Coil and Study of Longitudinal Misalignment
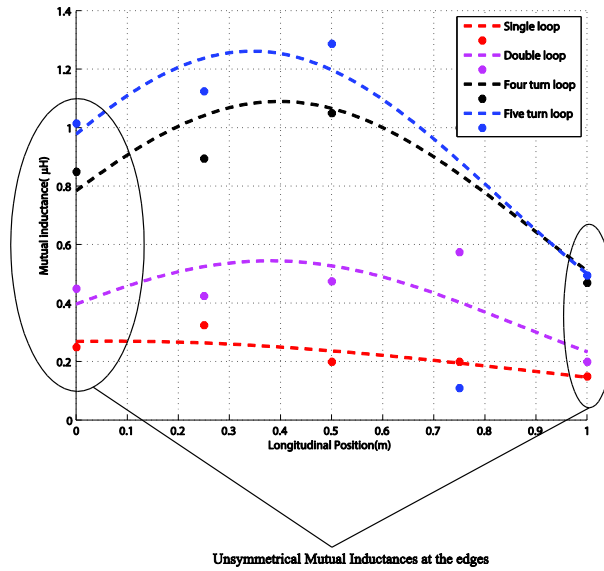
Figure 4.9: Variation of mutual inductance at several positions laterally.

In order to study longitudinal misalignment, various points were selected in the primary loop at variable distances from the reference and mutual inductance was plotted as a function of longitudinal distance for the point of perfect alignment laterally and is shown in Fig. 4.9.

In case of longitudinal misalignment, it was observed that there is a variation in mutual inductance even for the perfectly aligned state of the pick-up. This variation is sinusoidal as expected from Fig. 4.4 and the peak mutual inductance occurs when the pick-up is in the center of the loop. This can be explained as in the center, the pick-up is coupled to flux from current elements from both ends of the conductors. However, as the pick-up moves away from the center, it picks up flux minimally from the end that is farther away. What was surprising, however was that the mutual inductance at the sending end of the inductor is not symmetric with the value at the terminal end. This behavior is not as expected and it can result in detuning of system when the pick-up has to traverse from one section to another.

4.3.6   Edge Effects

In order to explain the unsymmetrical nature of mutual inductance as observed at the sending end and the terminal end of the inductor due to longitudinal misalignment, it is useful to consider the orientation of the magnetic fields particularly at the two ends. This is shown in Fig. 4.10.
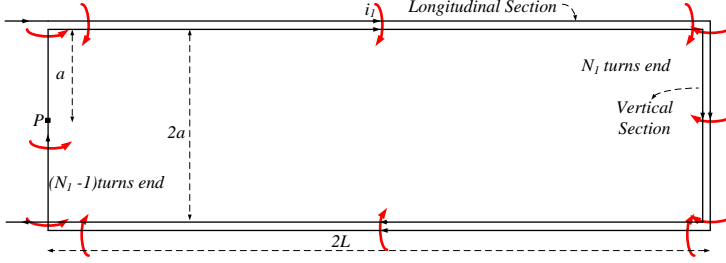
Figure 4.10: Orientation of the magnetic fields at the various sections of the inductor.

$$\overrightarrow{\mathbf{B}}_P = \overrightarrow{\mathbf{B}}_{P,L} + \overrightarrow{\mathbf{B}}_{P,V} \qquad (4.21)$$

It is safe to assume that the effect of vertical sections would not play a major role for longitudinal distances beyond 2a from the edges. Using (12) and for the condition of P on the midpoint of the vertical section, the resultant flux density

$$\overrightarrow{\mathbf{B}} = \frac{\mu_0 N_1 i_1}{2\pi a} + \frac{\mu_0 (N_1 - 1) i_1}{2\pi a} \qquad (4.22)$$

The second term in the previous expression is the flux density due to the vertical section. The mutual inductance combining the contributions of longitudinal and vertical sections, if a_1 and a_2 are the pick-up clearance w.r.t the horizontal and vertical sections respectively, can be written as

$$M_P = \frac{N_2 \phi_{21}}{i_1} = \frac{\mu_0 N_1 N_2 A}{2\pi a_1} + \frac{\mu_0 (N_1 - 1) N_2 A}{2\pi a_2} \qquad (4.23)$$

However, if the pick-up were at the other extreme end,

$$M_P = \frac{N_2 \phi_{21}}{i_1} = \frac{\mu_0 N_1 N_2 A}{2\pi a_1} + \frac{\mu_0 N_1 N_2 A}{2\pi a_2} \qquad (4.24)$$

Thus, the magnetic fields that are caused due to the vertical sections of the rectangle super-impose with the field due to the longitudinal sections which creates additive components at

either end but by different magnitude. This difference in magnitude is created due to the fact that conventional inductors have unequal number of vertical sections as shown in Fig. 4.10.
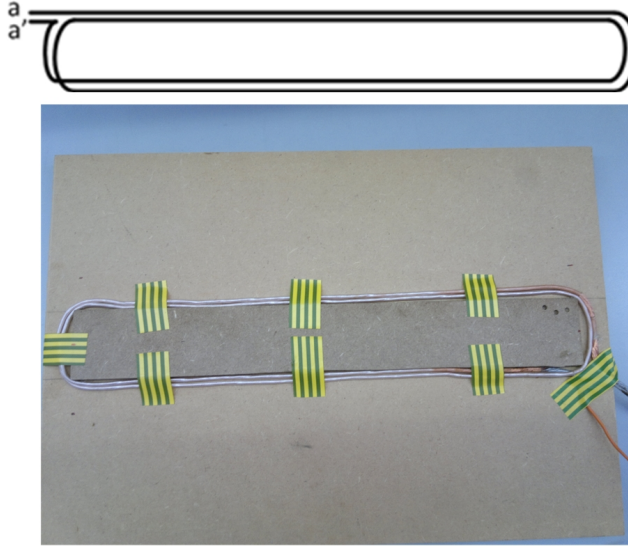
Figure 4.11: Orientation of the magnetic fields at the various sections of the inductor.

Hence, the mutual inductance at one end of the inductor will be higher than that of the other. Since the cause of edge effect was the difference in number of the vertical sections, a new primary, called as symmetrically ended inductor was constructed as shown in Fig. 4.11. It was observed that this design resulted in a symmetrical distribution of mutual inductance at either ends. The results are similar to Fig. 4.9, with a sinusoidal-like distribution but with the edges having similar values of mutual inductance.

4.4   Discussion

In this chapter, analytical expressions for both lateral and longitudinal misalignment for RPEVs were derived from Biot-Savart law. The new concept of longitudinal misalignment for finitely long tracks yielded the result that the mutual inductance at the middle of the primary loop for a well-aligned pick-up is much higher than that at the extremes. However, this effect was ignored in studies thus far assuming conductors to be infinitely long with 2D FEM results also assuming the same. This derivation, however did not take into account the effect of vertical sections.

Experimental studies matched the trends as observed analytically. However, in case of longitudinal misalignment, the edges created unsymmetrical coupling at the two extremes. This was referred to as "Edge Effect" and was due to the unequal number of vertical sections at either ends. This effect was mathematically considered and a new inductor called symmetrically ended inductor was proposed and it showed similar values of mutual inductance at the ends.

The edges of sectional tracks can result in detuning when the pick-up is moving between sections and hence while designing sectional tracks, care is required to make a smooth transition of power transfer between the neighboring tracks.

Multi-Objective Optimisation and Experimental Analysis of a DR IPT System for Light EVs

Inductive power transfer (IPT) systems for charging of electric vehicles (EVs) must employ charge-pads with minimal copper and ferrite core material for improving coupling and field shaping without sacrificing power transfer efficiency across the air gap. This chapter details the multi-objective optimisation of IPT coil systems with respect to efficiency of power transfer (η), material weight or cost (w), and area-power density (α) as required in EV applications. A combination of detailed analytical calculations and experimentally verified 3D finite element models is used to analyse performance of IPT systems with double rectangular pads (DR), I-shaped ferrite cores for field shaping and aluminium plates to reduce stray or leakage magnetic fields. A multi-objective pareto optimisation using Particle Swarm algorithm of a scaled 1kW prototype system with a 15 cm air-gap is presented. Experimental analysis of the system with SiC inverter with bridge angle control and operate at all switching modes.

Based on

- S. Bandyopadhyay, V. Prasanth, P. Bauer, and J. A. Ferreira, "Multi-objective optimisation of a 1-kW wireless IPT systems for charging of electric vehicles,"in *IEEE Transportation Electrification Conference and Expo (ITEC)*, 2016, Dearborn, MI, pp. 1-7; and

- P. Venugopal, P. Bauer, J.A. Ferreira and H.Polinder, "Analytical and Semi-Analytical Techniques for Modelling the Magnetics of Air-Cored IPT Systems,"*IEEE Transactions on Industry Applications* (Submitted).

5.1 Introduction

Designing a lumped IPT system for the use in an EV/HEV, a number of constraints like space of the pick-up coil in the underfloor of the vehicle and the allowable weight and cost of the components used in both the primary and the secondary exists. The power transfer efficiency should be high as possible for simple thermal management of the system. In addition to that, another design constraint arises from the limitation of the magnetic stray field in the vicinity of the IPT coils by well-defined International Commission on Non-Ionizing Radiation Protection (ICNIRP) standards [119].

The magnetic design of the transmission coils is of paramount importance in order to satisfy the mutually conflicting targets like efficiency, area-related power density and weight of copper and ferrite materials. In literature, it is shown that a Figure of Merit (FOM) = kQ given by the product of the magnetic coupling of the IPT coils and the inductor quality factor limits the maximum efficiency of power transfer [146]. To achieve high power transfer efficiency, large coils can be used at the cost of power density and charge pad weight. A high power density and light charge pad can be similarly designed at the cost of low power transfer efficiency and possibly thermal problems. In this chapter, it is shown how the three performance indices efficiency (η), power density (α) and material weight (w) are related and that a trade-off is encountered in the design optimisation of charge pad design in IPT systems, similar to other power electronic systems and in design of electric machines [147].

Nowadays, with higher computational resources, accurate Finite Element (FE) charge-pad models combined with multi-objective evolutionary algorithms are be used to design high performance IPT systems. The goal of this chapter is to present a systematic multi-objective framework for design optimisation of 1kW, 85 kHz IPT systems to realise the trade off between targets and to draw general design guidelines based on that. A multi-objective PSO algorithm combined with 3D FE charge-pad models is used to optimise the IPT system to generate pareto optimal fronts [148], [149]. The coil topology used in design of the IPT systems is the multi-coil polarized DR charge-pad, mainly due to its high tolerance to misalignment which is necessary for dynamic charging of EVs. To improve coupling and proper field shaping I-shaped ferrite bars are used. To reduce stray or leakage fields around the IPT pads, aluminium sheets in both primary and secondary charge-pads are used.

The trade-offs in the optimization is realized with the help of pareto fronts which is a physical performance boundary consisting of a set of system designs for which an increase of the performance indices result in the decrease in another [150].

Finally, in this chapter experimental demonstration of a 1 kW light EV IPT system is carried out. A 85 kHz SiC inverter is constructed to deliver power to a DR IPT system that is series compensated.
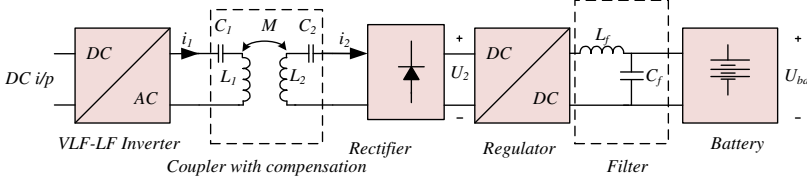
Figure 5.1: Schematic representation of a 1-kW Prototype Light EV IPT system

5.2 Light EV IPT charging System

The specifications of an IPT system typically includes the output power P_2 needed to charge the battery of the traction motor, the frequency of operation, the air gap, (l_g) across which the output power must be transferred and maximum dimensions of the pads. The air-gap and the maximum coil dimensions are dependent on the geometrical constraints and cannot be altered during the design process. Based on this an example prototype of an IPT system based is shown in Table 5.1. To incorporate the size constraint, maximum dimensions of width and length of the coils are fixed at 200 mm and 220 mm respectively. These constraints are carefully selected considering the air gap of 150 mm to highlight the tradeoffs encountered during charge pad design.

Table 5.1: Specifications of the Prototype Light EV IPT system

Parameters	Value	Description
f	85 kHz	Frequency of operation
P_2	1000 W	Power output
l_g	0.15 m	Air-gap
U_{bat}	40 V	Battery voltage
U_2	100 V	Receiver side dc-link voltage
W_{coil}	0.2 m	Maximum coil width
L_{coil}	0.22 m	Maximum coil length

A generic lumped IPT system is comprised of three components: a power supply, charge-pads and a pick up circuit. A block diagram of the system is shown in Fig. 5.1. A rectified dc power supply is followed by a single-phase square wave inverter operating at 85 kHz. The IPT system consists of resonant compensation networks for the transmitter and receiver coils along with a rectifier followed by a buck converter in the pick up side. A series-series compensation [146] is considered in this chapter. The choice is motivated mainly by the main advantages of series-series compensation technique, for example, independence of the compensation capacitors from the magnetic coupling of the coils and consequently, high tolerance of the system to coil misalignment. A rectifier followed by a dc-dc buck converter

is used in the pick-up circuitry to charge the traction battery.
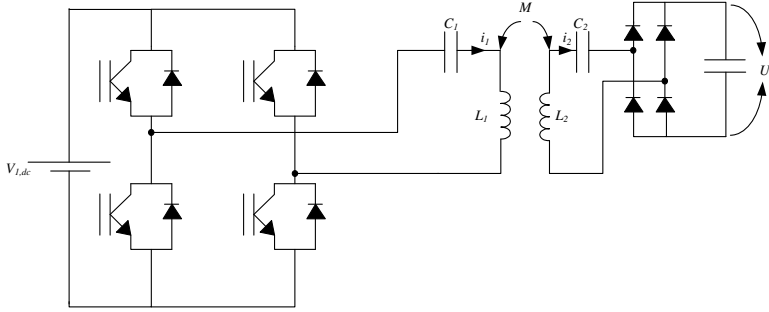
Figure 5.2: Equivalent circuit diagrams of a series-series compensated IPT system with a capacitive output filter

Before proceeding to modelling and optimisation, as the next step to design and analysis of IPT system performance the equivalent circuit and modelling the pick up circuit with the load and rectifier.

5.2.1 Equivalent Circuit & Load Modelling

Fig. 5.3 shows the equivalent circuit of the magnetically coupled IPT coils which is similar to the equivalent circuit of a transformer model. M denotes the mutual inductance between the two IPT coils and is defined as $M = k\sqrt{L_1 L_2}$, where k is the magnetic coupling coefficient of the IPT coils and L_1, L_2 are the self-inductances. The value of C_1 and C_2 are chosen to according to series-series compensation topology [146] in order to achieve maximum transmission efficiency.
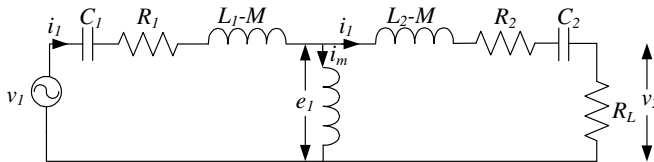
Figure 5.3: Transformer equivalent circuit of an IPT system with series-compensated capacitors on the primary and the pick up. The series resistances of the coils are R_1 and R_2.

Based on the analysis presented in [151], the load circuit of the pick-up or receiver side is modelled as an equivalent load resistance of a series-series compensated IPT system as shown in Fig. 5.4. The equivalent load resistance is calculated in the following equations.
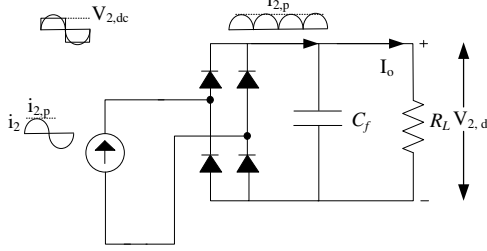
Figure 5.4: Equivalent resistance modelling of the rectifier and the load. The load resistance is modelled as $R_L = \frac{V_{2,dc}^2}{P_2}$. The input of the rectifier for series-series compensation is modelled as a current source. i_2 is the ac-current induced in the compensated pick up coil. I_o is the rectified output of the sinusoidal current i_2.

First, the pick-up current, i_2 is related to the rectified current, I_o as:

$$i_2 = \frac{i_{2,p}}{\sqrt{2}} = \frac{\pi}{2\sqrt{2}} I_o \tag{5.1}$$

Next, the pick-up voltage v_2 is related to output voltage of dc-link after rectification, E_o as

$$v_2 = \frac{2\sqrt{2}}{\pi} E_o \tag{5.2}$$

Finally, the equivalent load resistance is obtained in terms of the rectifier efficiency η as

$$R_{ac} = \frac{v_2}{\eta i_2} = \frac{8}{\pi^2 \eta} R_L \tag{5.3}$$

5.2.2 Charge-pad Layout

The coil layout used in this chapter as shown in Fig. 5.5 is a polarized single sided charge pad also known as DR coil topology. The main motivation of choosing this coil design is their relatively higher tolerance to misalignment and high fundamental flux path compared to conventional circular pads [152]. To improve magnetic coupling and shaping of the I-shaped field ferrite bars are used below the charge pads. The aluminium (Al) sheet is used to provide structural rigidity to the pad and shields any leakage stray fields generated to satisfy the ICNIRP guidelines of maximum leakage magnetic fields in IPT systems.
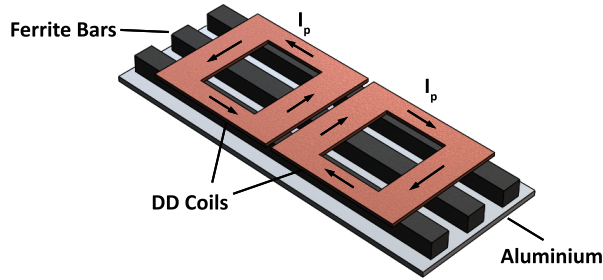
Figure 5.5: Layout of primary and secondary DR charge pads. Ferroxcube I-shaped ferrite bars 3C-90 are used to improve magnetic coupling. Aluminium plates are used behind both primary and pick up charge pads (not shown in figure) for shielding purposes.

5.3 FE Modelling of IPT Coils

In this section, the theoretical design considerations are taken into account and are extended to detailed 3D FE models for frequency domain analysis. The calculations of the copper losses, core losses and the aluminium losses are discussed here. The FE model built in this section is used for the subsequent $\eta - \alpha - w$ optimisation discussed in Section 5.4.

5.3.1 3D Finite Element Modelling

A 3D FE model is developed in this section for calculation of the IPT system parameters. Fig. 5.6 shows the sectional 2D plot of the simulation model using commercially available software COMSOL. The *litz* wire DR winding is modelled as a rectangular multi-turn coil domain in the model with uniform current density in the cross section. This reduces the computational load since the it will not compute the eddy current losses in the winding. This approximations are valid in this model since the *litz* wire strand diameter is chosen lower than the skin depth of copper at the operating frequency 85 kHz.

To increase the magnetic coupling of the coils, ferrite bars are added to the design as already shown in Fig. 5.6. The core is modelled with a linear or constant relative permeability of $\mu_r = 2400$ to resemble that of material 3C-90. The conductivity of the core material is low ($\sigma = 0.2\,\text{S/m}$) and therefore eddy currents in the core are neglected unlike the aluminium shields.

The unbounded space around the coils is bounded by a sphere with radius equal to five times the length of the charge pads, so that the accuracy of the simulations is independent of the size of the sphere. Magnetic shielding boundary condition is applied to the bordering
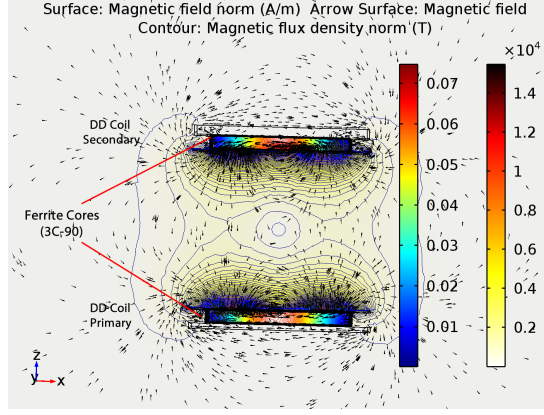
Figure 5.6: Plot of magnetic flux density in the simulated model. For better visualization, a section 2D plot of the 3D model is presented here.

surfaces of the sphere. Physics based automated meshing techniques are used to mesh the entire geometry. For accurate computation of the eddy currents and the stray fields, dense meshing is used in the aluminium shields with a maximum mesh size of one-third of thickness of the aluminium shield.

5.3.2 Computation of Losses

The type of losses incurred in the above IPT system are mainly: a) dc copper losses, b) ac losses in *litz* wire (skin and proximity losses), c) core losses in ferrite bars and d) Aluminium eddy current losses. Detailed analysis of ac-losses of *litz* wire winding is not considered in this chapter. Therefore, only the dc copper losses are considered.

The core losses are calculated by integrating the core loss density according to the Steinmetz equation:

$$p_{core} = \kappa f_0^\alpha \hat{\mathbf{B}}^\beta \tag{5.4}$$

over the volume of the ferrite cores. The Steinmetz parameters of the core material 3C-90 are $\kappa = 3.2 \times 10^{-3}$, $\alpha = 1.46$ and $\beta = 2.75$.

The skin depth of aluminium at an operating frequency of 85 kHz is 0.28 mm which is quite small compared to the dimensions of the aluminium shields. An Impedance Boundary condition is used in the FE model which essentially sets the skin depth to zero, making all induced currents flow on the surface of the conductors. Mathematically, the relation between the magnetic ($\overrightarrow{\mathbf{H}}$) and electric field ($\overrightarrow{\mathbf{E}}$) at the boundary reads:

$$\hat{\mathbf{n}} \times \overrightarrow{\mathbf{H}} + \sqrt{\frac{\epsilon - j\sigma/\omega}{\mu}} \hat{\mathbf{n}} \times (\overrightarrow{\mathbf{E}} \times \hat{\mathbf{n}}) = 0 \tag{5.5}$$

The distribution of the dissipated power, P_d (SI unit: W/m^2) can be calculated from:

$$P_d = \frac{1}{2}(\overrightarrow{\mathbf{J}}_S.\overrightarrow{\mathbf{E}}^*) \tag{5.6}$$

where $\overrightarrow{\mathbf{J}}_S$ is the induced surface current density, and the asterisk (*) denotes the complex conjugate. The overall aluminium eddy losses (P_{al}) are computed by an area integral of the dissipated power (P_d) over the surface of the aluminium shield.

5.3.3 IPT System Analysis

The numerical analysis of IPT is performed by a combination of MATLAB to create and postprocess the FE models and COMSOL to solve the FE models. To save time a minimum number of preferably static simulations is executed and IPT system characteristics are obtained by post-processing the results. The analysis of a single IPT design is comprised of the following steps:

- Simulation of primary and secondary DR coils to determine L_p, R_p and L_s, R_s.

- Simulation of total IPT system with primary excited and secondary open circuited. The open circuit voltage (v_{oc}) is used to compute the mutual inductance $M = \frac{v_{oc}}{j\omega i_p}$ where i_p is the primary current.

- Computation of coupling coefficient k using the formula $k = \frac{M}{\sqrt{L_p L_s}}$.

- Circuit simulation using $L_p, R_p, L_s, R_s, M, Z_{load}$ to extract primary current based on a fixed load or secondary current.

- Calculation of overall transfer efficiency of the IPT system in terms of losses in core (P_{core}), winding (P_{cu}) and shield (P_{al}), $\eta = \frac{P_{out}}{P_{out}+P_{core}+P_{cu}+P_{al}}$.

5.4 $\eta - \alpha - w$ Optimisation

A comparison between IPT design types is only fair if the designs under consideration are designed optimally for the requirements, so an optimisation approach is required. Any engineering related optimisation approach consists of two parts: models to describe the problem and an algorithm to control the optimisation. The models used here are all based on 3D FE computations, which allows a simple comparison of completely different IPT system designs. Non-linearity of ferrite cores can also be taken into account, however the flux levels seen from preliminary investigation shows the operating values are well below the saturation limit of the ferrite material used.

5.4.1 Particle Swarm Optimisation

The optimisation algorithm used is particle swarm algorithm, an evolutionary gradient free method based on the movement of birds or insects in a swarm. This algorithm was selected because it is gradient free and potentially requires very few function calls [153].

1) Multi-Objective PSO: A modified version of the original algorithm is used here to work with multiple targets simultaneously, which allows the pareto optimal fronts [148] to be computed. This is accomplished by storing all pareto optimal solutions in a repository and picking the global best target randomly from this repository.

2) Solution Space and Constraint handling: To prevent unnecessary exploration of uninteresting design regions and save computing time, the global targets are confined to more promising parts of the solution space, such as high efficiency or low weight designs. To ensure variable values within constraints, velocity reduction techniques on particles are used.

5.4.2 Optimisation Targets, Variables, Constraints
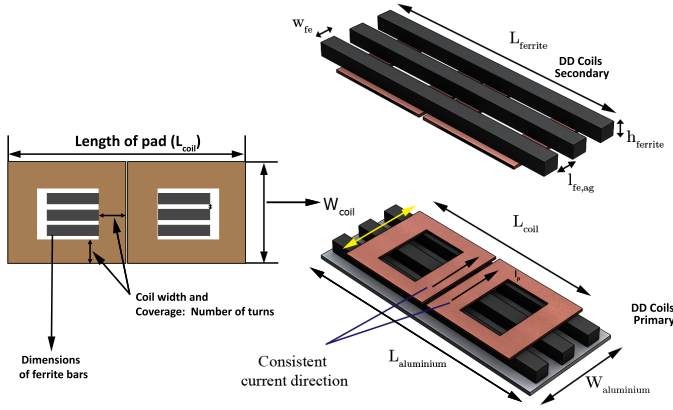
Figure 5.7: Graphical representation of optimisation variables. Inter-ferrite relative airgap is defined as $p_{ag} = \frac{l_{fe,ag}}{(W_{coil}/2 - w_{fe})}$. Relative length of ferrites is defined as $p_{fe} = \frac{L_{fe}}{L_{coil}}$. Number of turns in the coil layout determines the coil coverage or the coil width as shown in the figure.

The setup of the optimisation consists of specifying variables, constants, constraints and targets. Considering a theoretical 1-kW, 15 cm air-gap lumped IPT system for dynamic charging of EVs, the following global optimisation targets are chosen:

- Maximize power transfer efficiency
- Maximize area-power density of EV pick up

- Minimize active weight of the IPT charge pads

Fig. 5.7 shows the major design variables. The optimisation variables are all geometrical in nature and their ranges are presented in Table 5.2. The effect of the chosen variables on the magnetic properties of the IPT systems are briefly discussed here.

Table 5.2: Range of optimisation variables

Variables	Expression	Range
Number of turns	N	$15 \leq N \leq 40$
Number of ferrites	n	3
Width of ferrites (mm)	w_{fe}	$10 \leq w_{fe} \leq 25$
Thickness of ferrites (mm)	h_{fe}	$5 \leq h_{fe} \leq 12$
Inter-ferrite relative air-gap (%)	p_{ag}	$0 \leq p_{ag} \leq 60$
Relative length of ferrites (%)	p_{fe}	$50 \leq p_{ag} \leq 100$
Thickness of aluminium (mm)	t_{al}	$5 \leq t_{al} \leq 10$
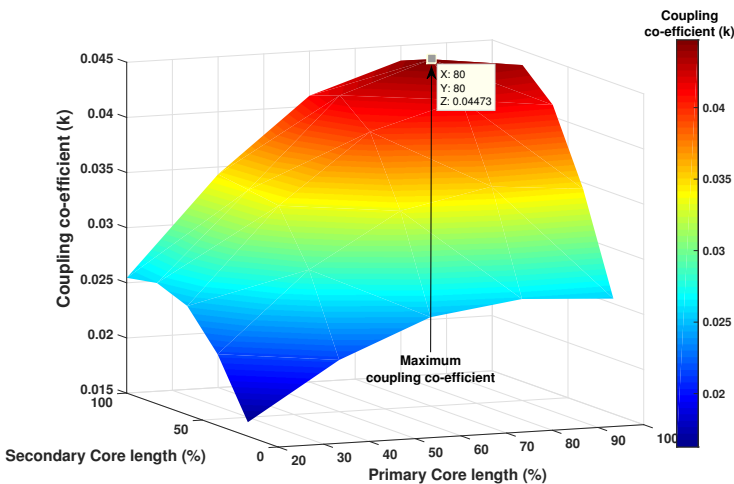
Figure 5.8: Placement strategy based variation of coupling coefficient with length of ferrite bars.

The number of turns (N) of the coils is an important design variable since the resistance, inductance and coil coverage is dependent on that. The choice of ferrite dimensions and optimal placement strategy is an interesting study undertaken in this research. A review of literature indicates that there is not sufficient work on the effect of ferrite dimensions and placement on IPT performance. Fig. 5.8 presents the results of the variation of coupling coefficient with ferrite length and Fig. 5.9 that of airgap between the bars. Stray or leakage
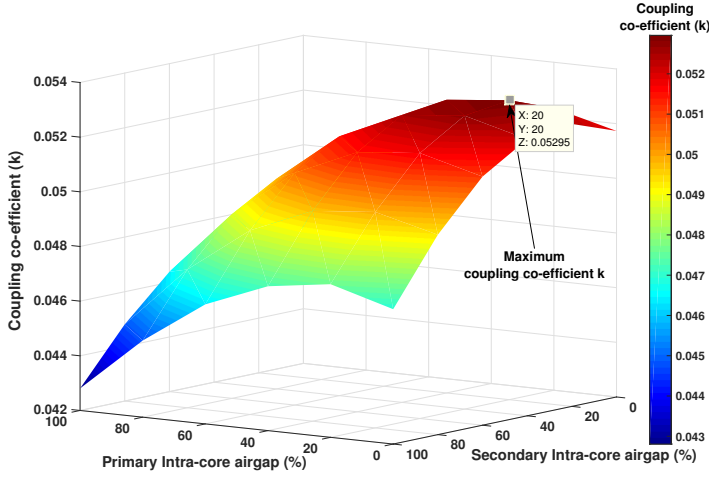
Figure 5.9: Placement strategy based variation of coupling coefficient with air-gap between ferrite bars.

fluxes around the coil region are dependent on the thickness of the aluminium used and also on the positioning of the ferrite cores as shown in Fig. 5.10.

To ensure that the optimisation does not lead to unrealistic designs in terms of thermal management, there are limits put on the primary current (25 A) and the flux density in the cores ($\leq B_{sat} = 0.45T$). To abide by the ICNIRP guidelines, an upper limit on the stray field (27 μT at a radial distance of 300 mm from back-end of the charge pads) is imposed.

5.4.3 Results of Optimisation

The results obtained from optimization should be carefully analysed before drawing scientific conclusions based on it. The optimization procedure generates a lot of data and a significant time must be devoted into post-processing those results to investigate possibilities of errors. Fig. 5.11 and Fig. 5.12 shows the 2D pareto fronts of the global optimisation targets. To gain more insight into the optimization process some secondary plots derived from the main pareto fronts are presented in Fig 5.13. After careful consideration of the results the following observations are made:

- Fig. 5.11 shows the plot of maximum power transfer efficiency of the optimal IPT designs with the active weight of the design. The trend shows increasing efficiency with heavier designs. It can be explained by increased weight of copper (higher number of turns) and ferrite bars leading to higher coupling coefficient (k) and quality
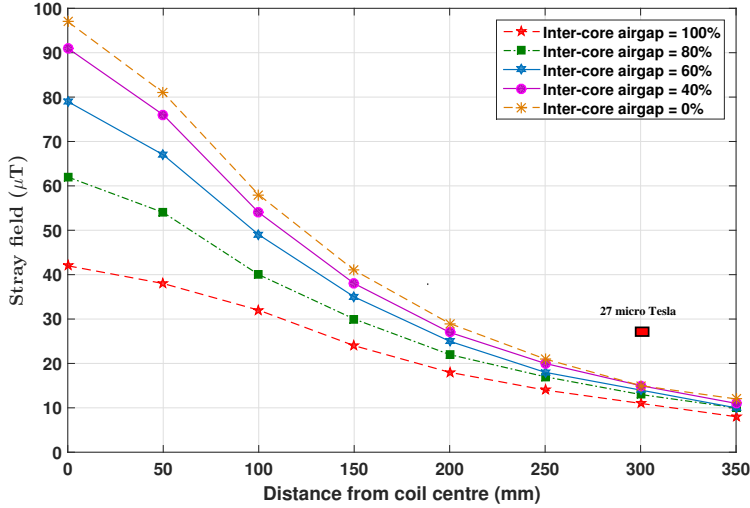
Figure 5.10: Graphical representation of the decay of the stray field (μT) from the charge pads at different placement strategies of the ferrite core. Thickness of aluminium shield (t_{al}) is 3 mm.

factor (Q) of the coils. This can be verified with plot of FOM (kQ) with weight in Fig. 5.13.

- Fig. 5.12 shows the pareto plot of the power transfer efficiency with area-related power density of the pick up charge-pad. With higher power density or with lower area coverage of the coils, mutual inductance between the coils decreases leading to lower coupling factors leading to low efficiencies.
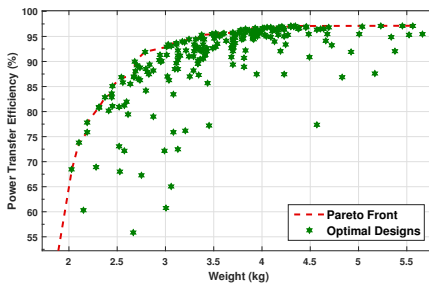
Figure 5.11: Plot of maximum efficiency versus system weight of the IPT system.
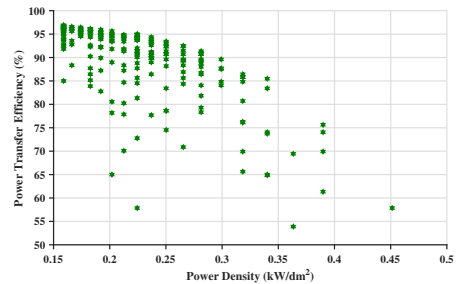
Figure 5.12: $\eta - \alpha$ Pareto front of optimal efficiencies with increasing area-power density of the designs.
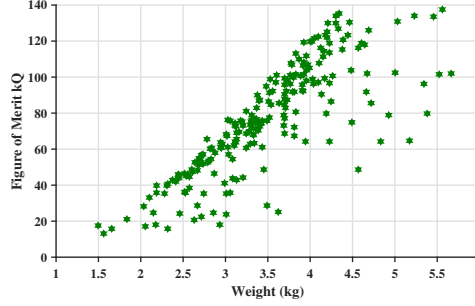
Figure 5.13: Plot of FOM of optimal IPT designs versus weight of IPT system. With heavier designs the coupling coefficient and quality factor of the coils increase leading to higher FOM (kQ). This leads to higher efficiencies in heavier designs.

5.5 Experimental Analysis

5.5.1 Experimental Validation of FEM Modelling

In this section, the 3D modelling procedure discussed in Section 5.3 will be validated using experimental results. In this chapter, a co-planar DR coil configuration is considered for FE modelling and further optimisation. However, for experimental validation instead of a DR configuration, a square coil shape with core as both primary and secondary pick up is used. The geometrical layout remains the same as that of DR coil configuration. Details of the coils are presented in Table 5.3. The self-inductance of the coils as measured by an LCR

Table 5.3: Design details of the experimental setup

Variables	Value	Description
N_p	26	Primary number of turns
N_s	16	Secondary number of turns
r_w	1.2 mm	Radius of *litz* wire
$L_p \times W_p$	20 cm×20 cm	Dimensions of primary coil
$L_s \times W_s$	10 cm×10 cm	Dimensions of secondary coil
w_{core}	3 mm	Width of core
h_{core}	2.75 mm	Height or thickness of core
l_{ag}	20 mm	Airgap between coils

meter are 117 μH and 16 μH respectively, which are quite close to the FE results, 111 μH and 15.2 μH. The comparative results of coupling of the two coils with presence or absence of cores and placement strategy of the ferrite bars are shown in Fig. 5.14 and Fig. 5.15.

The above graphs show good agreement between them with percentage error ranging from
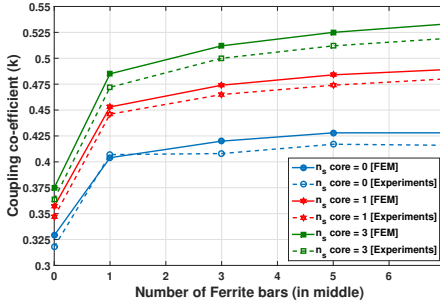
Figure 5.14: Placement strategy based variation of coupling coefficient with number of ferrite bars used in the charge pads.
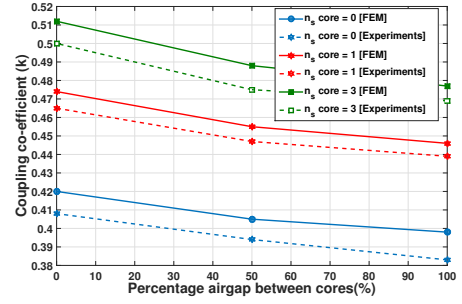
Figure 5.15: Placement strategy based variation of coupling coefficient with air-gap between ferrite bars ($n_{fe} = 3$).

1-4 % approximately, thus validating the model.

5.5.2 DR Charge-pad Design

Following the optimization, a particle (solution) was chosen at the knee point of the pareto front of the efficiency and weight. The particle was used to construct an optimized DR pad with dimensions as tabulated in Table 5.4. The measured inductances of the charge-pads are 199.8 μH and 198.6 μH respectively of the primary and pick-up (Agilent 4294A Precision Impedance Analyzer). The charge-pads that are constructed in the lab are shown in Fig. 5.16.

The strand diameter of the $litz$ wire is calculated by calculating the skin depth at the resonant frequency - 85 kHz for copper. The skin depth is related to the angular frequency of the imposing electromagnetic field ω, permeability μ of the media and conductivity of the material σ as

$$\delta = \sqrt{\frac{2}{\omega\mu\sigma}} \tag{5.7}$$

The skin depth of copper at 85 kHz corresponds to 223.62 μm and that of aluminium is 281.27μm. The $litz$ wire therefore chosen is from a 600 × 0.071 mm spool with a strand diameter less than the skin depth to utilize the copper completely for conduction. The ac-resistance of the primary and pick-up at 85 kHz is measured as 454 mΩ and 412 mΩ respectively.

The coupling coefficient variation with z-gap between the charge-pads is shown in Fig. 5.17. The coupling is between 19% and 7% in the variation of z-gap between 10 cm to 15 cm.

Table 5.4: Mechanical dimensions of DR charge-pad

Description	Value
Litz wire diameter	2 mm
Inner width of D half-pad	5 mm
Inner length of D half-pad	15 mm
Number of turns (N)	29
Length of ferrite core	242 mm
Width of ferrite core	22 mm
Thickness of ferrite core	8 mm
Width of Al plate	211 mm
Length of Al plate	362 mm
Thickness of Al plate	50 mm
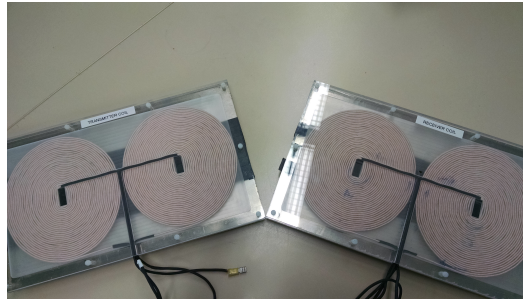
Figure 5.16: Constructed 1kW optimized DR-IPT charge-pads.

5.5.3 Reflected Reactance

Modelling magnetics becomes more challenging in IPT systems particularly in the presence of magnetic and conductive materials. In such a case, flux modifications due to a charge-pad in the vicinity influences magnetic parameters of the other charge-pad. Consider the example of a secondary charge-pad that moves close to a primary, the primary inductance gets enhanced due to the high permeability offered by the ferrite in the secondary and vice-versa. This further means that the magnetic parameters are not fixed for 3D movement of the charge-pads, further influencing the resonant behaviour. Fig. 5.18 shows the effect that a charge-pad of free space self-inductance 198.6 μH has due to the effect of a 199.8 μH charge-pad (with 5mm Al and ferrites of P material of Magnetics). The second charge-pad was considered without Al and then without ferrite to observe the individual material effects. As observed from Fig. 5.18, the effect of addition of ferrite results in enhanced self-inductance, the effect of which is reduced slightly due to eddy currents in Al shield. However, the result of inductance variations in air-cored coils is in comparison negligible. Therefore, in situations of flux modifying materials, it becomes imperative to have 3D
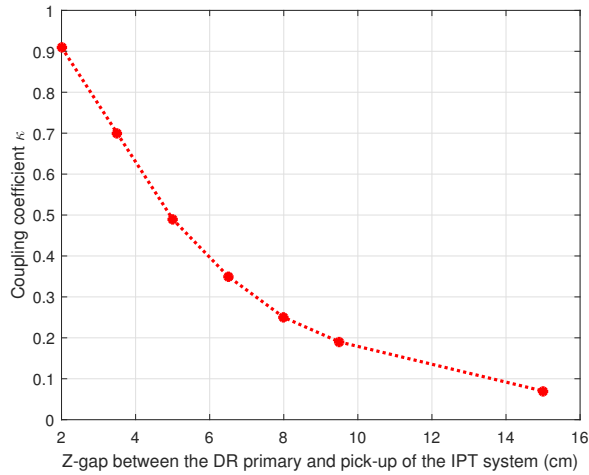
Figure 5.17: Variation of coupling coefficient of DR charge-pads with varying z-gaps.

inductance and coupling variation charts that use adaptive electric and magnetic circuits to accurately model misalignment behaviour.

Another challenge in modelling IPT systems is the reflected reactive impedance of all additional components in the system. Traditional modelling methods where resonant capacitors are selected to compensate the inductive reactance of magnetic coils alone results in detuning considering real-life systems. A situation being detuning caused by the filter capacitors of the rectifier in the pick-up power supply. Fig. 5.19 considers the differences in resonant behaviour (bifurcation) caused due to the addition of parallel filter capacitor (27.2 μF) in the rectifier network. The parameters of the IPT system is primary inductance $L_1 = 199.8$ μH, secondary inductance $L_2 = 198.6$ μH, resonant at 85 kHz. The measurements were made with Agilent 4294A impedance analyzer. The reactive loading in the primary supply caused due to the filter capacitor increases the order of the network, thereby creating an additional pole and zero. Similar results with the frequency shifting of the resonant points were observed when z-gap was varied. In a variable frequency system, the parallel resonant point for a system designed for SS compensation can lead to unstable behaviour. It is also important to note that the reflected reactive impedance from various elements connected to the secondary also depends on the compensation type and misalignment. In conclusion, a circuit model that analyses the system in entirety (with 3D inductance variations) is important to calculate system parameters and resonant condition to quantify real life-effects including misalignment and secondary reactive reflections.
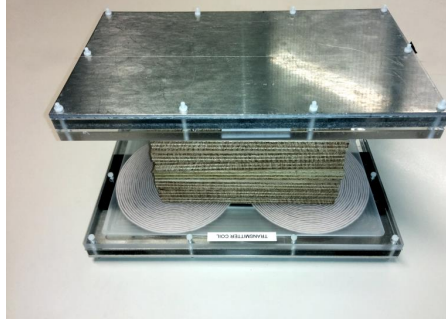
a)
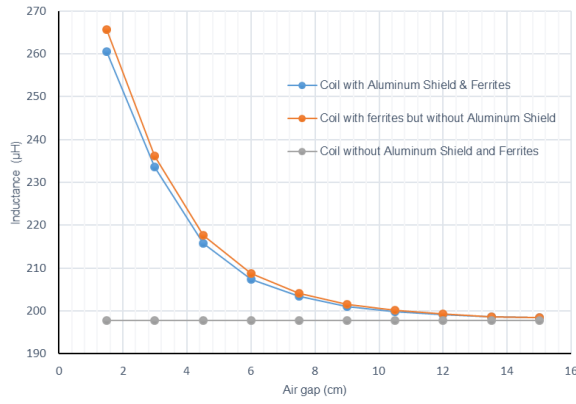
b)

Figure 5.18: a) A constructed DR charge-pad (362 mm $\times$211 mm) based IPT system with ferrite and Al. b) Experimental variation in self-inductance when another charge-pad with different material properties is positioned at varying z-gaps.

5.5.4 Inverter and Rectifier

A h-bridge inverter as a part of a larger project for supplying 11 kW processing solar PV power is the back ground of this section. The project also detailed a harmonic filter based IPT system for EMI reduction [154]. For the sake of brevity, only relevant details related to the experimentation for the light EV is mentioned in the following paragraphs.

The inverter that feeds power to the primary pad is based on a full bridge topology based on SiC power MOSFETs - 1200V, 80mΩ Cree C2M0080120D. The anti-parallel diodes are SiC Schottky diodes - Cree C4D40120D. The constructed rectifier and inverter is shown in Fig. 5.21 and Fig. 5.22.
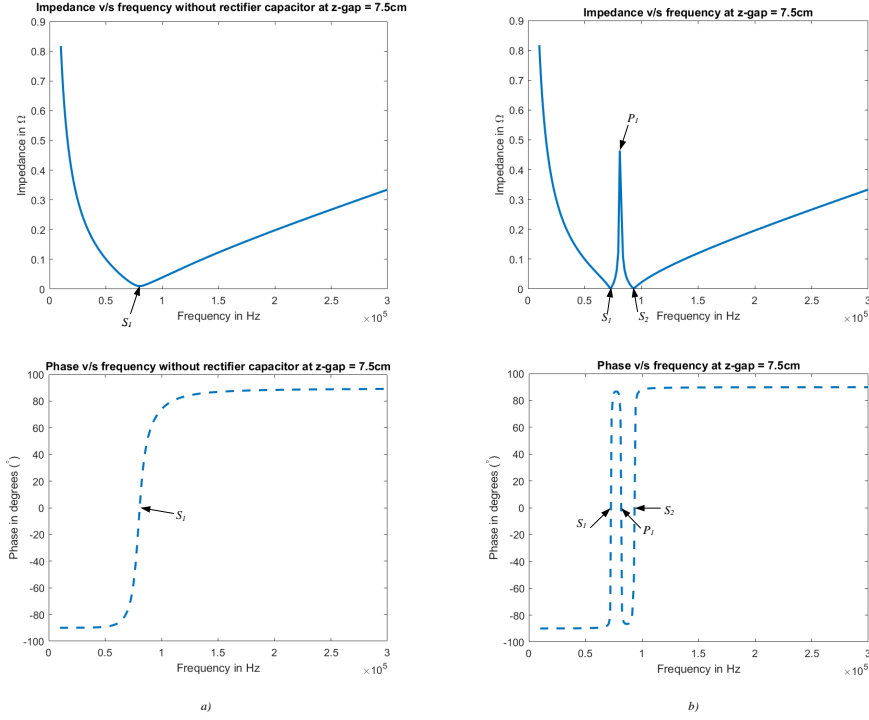
Figure 5.19: a) Measured impedance and phase plot of a series compensated IPT system based on DR charge-pads of Fig. 5.18 with SS compensation without considering the influence of a parallel filter capacitor of rectifier. b) Measured impedance also considering filter capacitor. $S_{1,2}$ = series resonance (72.57 and 81.65 kHz) and P_1 = parallel resonance (93.45 kHz).
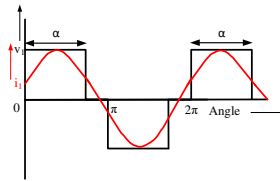
Figure 5.20: Defining the bridge angle α in a voltage cancellation/ phase-shifted control of a full bridge inverter.

The control of the bridge is performed using phase-shift control/ magnitude cancellation [155]. In this technique, the switching pattern of the two inverter legs are shifted by a time
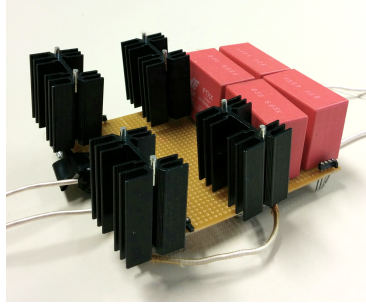
Figure 5.21: Constructed rectifier for folding the 85 kHz pick-up power and delivering it to charge the battery.

period, so as to create zero voltage periods that controls the power flow out of the bridge. The bridge conduction angle is α and the voltage waveform is represented in Fig. 5.20. The voltage output of this converter, performed using fourier series expansion of the signal and is obtained as [155].

$$v_1 = \frac{2\sqrt{2}}{\pi} V_{1,dc} \sin \frac{\alpha}{2} \tag{5.8}$$

Similarly, the secondary voltage when rectified and directly charging the EV battery U_{bat} is

$$v_2 = \frac{2\sqrt{2}}{\pi} U_{bat} \tag{5.9}$$

Using (1.2) and (1.1), the currents can be obtained from the voltages. Power output of secondary of IPT system is obtained interms of a function of duty cycle $f(D)$ as

$$P_2 = \Re\{v_2 \times i_2\} = f(D) \frac{8}{\pi^2} \frac{V_{1,dc} U_{bat}}{\omega M} \sin \frac{\alpha}{2} \tag{5.10}$$

5.5.5 Experimental Set-up

The experimental set-up consists of the 85 kHz power inverter feeding power to a SS compensated DR charge-pad system. The output power of the system is rectified and supplied to a load modelled as a resistor. The system is shown in Fig. 5.23. This load modelling is as per the industrial case study and is selected as battery internal resistance at 50% SoC. The system parameters is tabulated in Table 5.5.
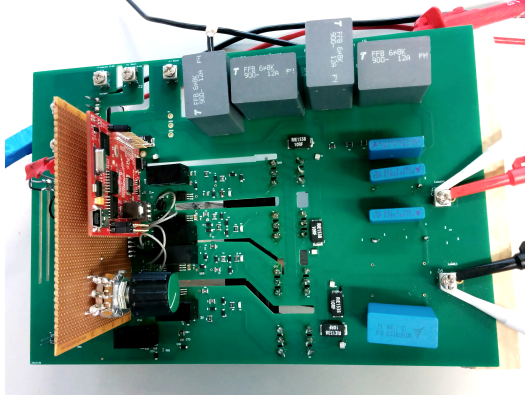
Figure 5.22: Constructed inverter for powering the SS compensated 1kW IPT system.
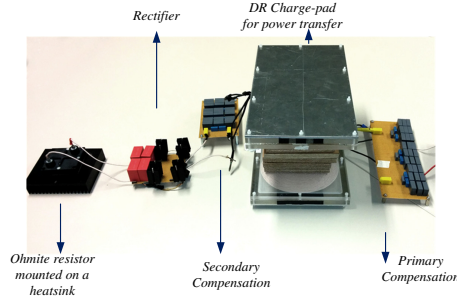
Figure 5.23: Experimental setup for light EV DR IPT system.

Table 5.5: Experimental parameters of DR IPT system

Description	Value
Frequency of operation f	85 kHz
Primary inductance L_1	199.8 μH
Primary ac-resistance R_1	454 mΩ
Secondary inductance L_2	198.6 μH
Secondary ac-resistance R_2	412 mΩ
Primary compensation C_1 (experimental)	19.3 nF
Secondary compensation C_2 (experimental)	19.3 nF
Rectifier filter capacitor C_f	27.2 μF
Equivalent load resistance R_L	30 Ω, 1 kW

The experimental performance is considered using both variable frequency and phase shift control. The three modes of load - resonant, inductive and capacitive operation of the

SS resonant system is experimentally verified by variable frequency operation. In case of a series resonant converter, ZVS is possible by controlling it at a slightly inductive load (super-resonant operation). This corresponds to the best overall efficiency point of operation due to optimal switching losses, even though the bridge is delivering reactive power due to the slightly lagging power factor. On the other hand, the resonant operation of the bridge delivers only real power, but the hard switching of the switches affects the overall operation and this point is not considered fruitful. The details of experimentation, with the load resistor current $I_{o,dc}$, load voltage $V_{o,dc}$ and efficiencies of the inverter η_{inv} and dc-dc efficiency η_{total} is considered in Table 5.6. The waveform showing the inductive mode of operation with switching frequency set to 88.3 kHz is shown in Fig. 5.24. The total system efficiency as obtained in the various operating points is compared in Fig. 5.25.
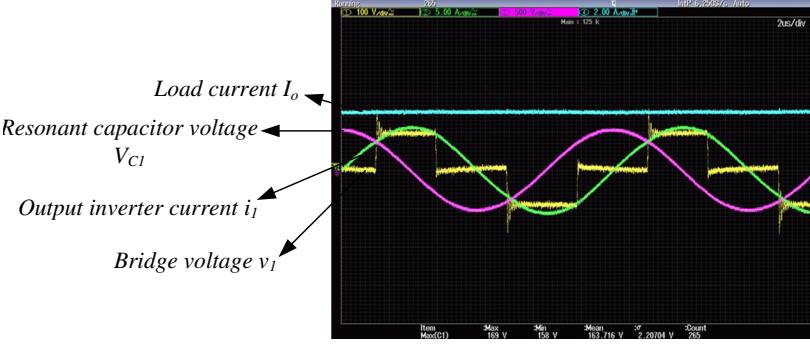
Figure 5.24: Inductive operation of inverter feeding power to a DR IPT system. The bridge angle is set as $\frac{\pi}{2}$.
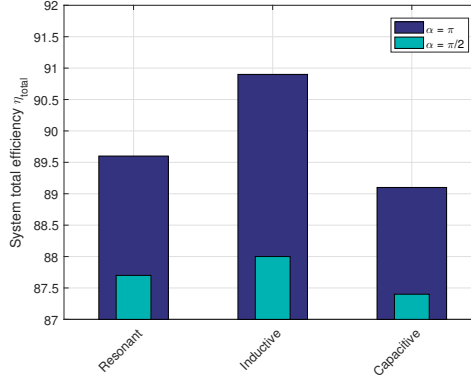
Figure 5.25: Comparison of system efficiency η_{sys} at various bridge angles ($\alpha = \pi$, $\frac{\pi}{2}$) and loads - resistive(resonant), inductive and capacitive.

Table 5.6: Experimental results of the DR IPT System

Input settings			Inverter i/o						Total system i/o						
Load	α (rad)	f (kHz)	$V_{1,dc}$ (V)	$I_{1,dc}$ (A)	$P_{1,dc}$ (W)	v_1 (V)	i_1 (A)	ϕ_1 (°)	p_1 (W)	η_{inv}(%)	$V_{o,dc}$ (V)	$I_{o,dc}$ (V)	$P_{o,dc}$ (W)	η_{total}(%)
Capacitive	π	85.3 k	100	3.72	372	86.7	4.3	15	360.2	96.8	87.44	3.79	331.4	89.1
Capacitive	$\frac{\pi}{2}$	85.3 k	100	1.64	164	60.7	2.6	19	149.2	90.98	57.58	2.49	143.3	87.4
Resonant	π	87.3 k	100	4.74	474	86.7	5.2	2	450.7	95.1	98.52	4.31	424.6	89.6
Resonant	$\frac{\pi}{2}$	87.3 k	100	2.18	218	60.7	3.47	3	210.37	96.5	66.64	2.68	178.6	81.9
Inductive	π	88.3 k	97.5	4.9	477.8	86	5.72	19	469.1	98.2	99.61	4.36	434.4	90.9
Inductive	$\frac{\pi}{2}$	88.3 k	97.5	2.36	230.1	60	3.99	22	224.6	97.6	68.39	2.96	202.4	88.0

Table 5.7: Higher power testing at resonant mode of DR IPT system

$V_{1,dc}$ (V)	$I_{1,dc}$ (A)	v_1 (V)	i_1 (A)	f (Hz)	i_2 (A)	R_L (Ω)	$P_{1,dc}$ (W)	p_1 (W)	p_2 (W)	p_{loss} (W)	η_{mag}(%)	η_{dc-ac}(%)
172	13	154.14	14.44	85.7	11.04	16.78	2236	2225.78	2047.0	178.8	91.97	91.55
158	11.9	141.2	13.2	85.7	10.13	16.78	1880.2	1865.2	1721.9	143.2	92.3	91.6
136	10.3	121.85	11.38	85.7	8.71	16.78	1400.8	1387.4	1273	114.4	91.75	90.9
110	8.3	99.05	9.18	85.7	7.06	16.78	913	909.28	835.4	73.9	91.9	91.50
92	6.9	82.76	7.7	85.7	5.92	16.78	634.8	636.42	588.1	48.3	92.40	92.64
79	6	70.75	6.59	85.7	5.06	16.78	474	466.24	430.1	36.1	92.26	90.75
66	5	59.08	5.5	85.7	4.21	16.78	330	324.58	297.8	26.8	91.76	90.25
53	4	47.6	4.42	85.7	3.4	16.78	212	210.4	194.0	16.4	92.20	91.50

Table 5.8: Loss distribution in resonant mode operation of DR IPT system

Copper loss dc (W)		Copper loss ac (W)		Core loss (W)		Capacitor (W)		Aluminium (W)		Total Losses (W)			
Primary	Pick-up	Primary	Pick-up	Primary	Pick-up	Primary	Pick-up	Primary	Pick-up	Primary	Pick-up	Sum	Error %
21.72	12.7	10.81	6.32	35.55	12.25	43.38	25.38	2.66	1.62	114.12	58.28	172.4	3.6
18.18	10.69	9.05	5.32	27.53	9.59	36.3	21.35	2.23	1.36	93.29	48.31	141.6	1.1
13.52	7.9	6.73	3.93	18.04	6.21	26.99	15.78	1.66	1	66.94	34.82	101.76	11.0
8.78	5.19	4.37	2.58	9.71	3.42	17.53	10.37	1	0.73	41.39	22.29	63.68	13.8
6.16	3.65	3.06	1.82	5.85	2.07	12.3	7.29	0.8	0.4	28.17	15.23	43.4	10.2
4.52	2.67	2.25	1.33	3.76	1.32	9.03	5.33	0.6	0.3	20.17	10.95	31.12	13.8
3.15	1.84	1.57	0.91	2.25	0.77	6.29	3.66	0.25	0.25	13.51	7.43	20.94	21.7

5.5.6 Validation of Magnetic Losses
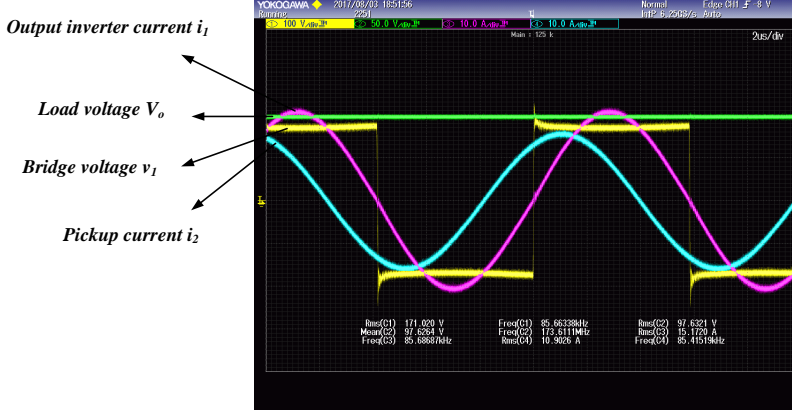
Figure 5.26: Resonant operation of inverter feeding power to a DR IPT system. The bridge angle is set as π.

Further system testing is performed by pushing the IPT system to higher power 2 kW (this is within the tolerance of design). The testing is performed at a z-gap of 10 cm, with the bridge angle set at the highest (π), performed at resonant conditions with a load of 16.78 Ω. This study is motivated to validate losses in the magnetic system with experiments directly connecting the load to IPT system, without rectification. The experimental results are tabulated in Table 5.7. The highest power efficiency from dc-link to the secondary of IPT system is $\eta_{dc-ac} = 92.6\%$. This despite resonant mode operation (one of the worst cases), where soft-switching is not guaranteed. One of the operating point experimental waveform is shown in Fig. 5.26.

The magnetic losses are further divided as: a) copper losses in *litz* wire (dc,ac), b) ferrite core losses, c) Al shield eddy losses and d) Dielectric losses in resonant capacitors. Loss models for ferrite core loss and shield loss have been introduced in Section 5.3.2. A semi-analytical combination of FEM and equations are used to estimate all these different losses. In the 3D FEM model developed previously, *litz* wire strands are not individually modelled to reduce computation time. However, this modelling technique is still fairly accurate since the *litz* wire diameter is chosen much lower than the skin depth of copper at 85 kHz frequency. Skin and proximity effects of a *litz* wire winding carrying peak sinusoidal current, $\hat{i}$ can be

calculated for a $'n'$ strand winding of length l, diameter d_i using [141]:

$$P_s = n \times R_{dc} \times F_s(f) \times \left(\frac{\hat{i}}{n}\right)^2 \tag{5.11}$$

$$P_p = n \times R_{dc} \times F_p(f) \times \left[H_e^2 + \left(\frac{\hat{i}}{\sqrt{2}\pi d_i}\right)^2\right] \tag{5.12}$$

The *litz* wire dc strand resistance can be calculated as $R_{dc} = \frac{4 \times l}{\sigma \pi d_i^2}$. The external proximity field H_e needs computation of the fields due to all sources in the neighbourhood. For accurate loss estimation, H_e is extracted from a 2D FE simulation separately for each turn and summed over for all the N number of turns. The skin and proximity effect factors can be computed in terms of a simplifying variable $q = \frac{d_i}{\sqrt{2}\delta} = \frac{\sqrt{\omega\mu\sigma}d_i}{2}$ as

$$F_s(f) = \frac{q}{4\sqrt{2}} \left(\frac{ber_0(q)bei_1(q) - ber_0(q)ber_1(q)}{ber_1(q)^2 + bei_1(q)^2} - \frac{bei_0(q)ber_1(q) + bei_0(q)bei_1(q)}{ber_1(q)^2 + bei_1(q)^2}\right) \tag{5.13}$$

$$F_p(f) = -\frac{q\pi^2 d_i^2}{2\sqrt{2}} \left(\frac{ber_2(q)ber_1(q) + ber_2(q)bei_1(q)}{ber_0(q)^2 + bei_0(q)^2} + \frac{bei_2(q)bei_1(q) - bei_2(q)ber_1(q)}{ber_0(q)^2 + bei_0(q)^2}\right) \tag{5.14}$$

The equations - (5.13) and (5.14) rely on Bessel functions and an alternative simpler approximate solution for low frequency is presented in [142]. It is important to note that the Bessel function solution doesn't consider the fields of the induced eddy currents in the conductor and hence is not accurate. For high-frequency magnetic problems, a more accurate solution considering the transverse, hyperbolic and own field (three field approximation) of the conductor is described in [142]. In addition, the resonating capacitors in the magnetic circuit undergo a frequency dependent power loss. This loss depends on the capacitance C, resonant angular frequency ω_0 and the dielectric $tan\delta$ (as indicated in the manufacturer's datasheet). For KEMET polypropylene capacitors, the dielectric loss factor $\tan\delta$ is chosen to be 0.1% at 100kHz.

$$P(f_0) = \frac{\hat{i}^2}{2C\omega_0} \times tan\delta(f_0) \tag{5.15}$$

The magnetic loss distribution is computed using the semi-analytical technique and is tabulated in Table 5.8. The losses calculated from the semi-analytical formulation and those obtained experimentally (Table 5.8) are compared and is graphically obtained in Fig 5.27.
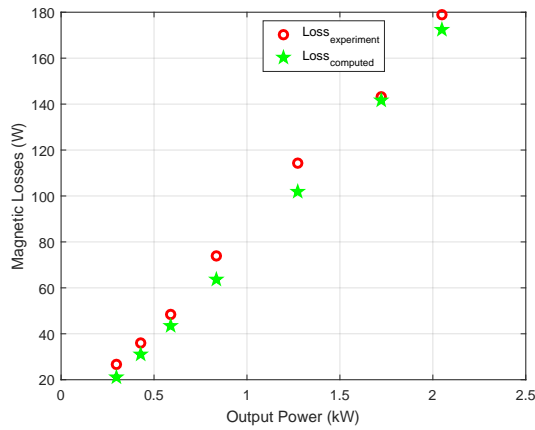
Figure 5.27: Comparison of loss in the charge-pads (magnetic) as a function of the power transferred.

The results indicate that there is in general good agreement between the semi-analytical computation of losses and their experimental measurements. Most observations are within 10% error bounds. However, the differences are worse at lower powers, limited by the modelling inaccuracies (*litz* wire assumptions, experimental inaccuries, proximity effect not modelled at a strand /bundle level) and experimental errors. The % loss in the magnetic system including the resonant capacitor is averaged for both the primary and pick-up and is represented in Fig. 5.28. It clearly shows that the resonant capacitors and the ferrite together contribute about 70% of the loss. Thus, improvements are important from the capacitor and ferrite distribution to minimize this loss in further iterations of the design.
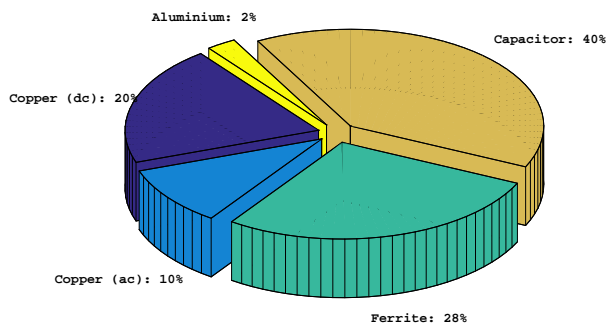
Figure 5.28: Pie-chart showing the percentage distribution of losses in an average charge-pad, capacitor resonant couple.

5.6   Conclusion

In this chapter, the framework for a multi-objective optimisation of a 1-kW, 15 cm airgap IPT system is presented. The FE modelling procedure is discussed in detail and experimentally verified. The optimisation targets, variables and constraints are chosen with detailed justification. From the results of the simulation it is seen that the dimensions, positioning of the ferrite cores with respect to each other influence the magnetic behaviour of the IPT system. From a parametric simulation, it is observed that the system achieves maximum coupling with ferrites that have dimensions, 80% of the respective dimension of coil. Also, having upto 20% of intra-core air-gap doesn't affect coupling.

It is seen that with decreasing air-gap between cores results in an increase of mutual inductance and coupling coefficient of the IPT coil systems at the cost of increasing stray fields. Trade-offs encountered in the $\eta - \alpha - w$ optimisation are discussed in detail with design guidelines showing the conditions to increase power transfer efficiency. Thermal management of IPT systems is not considered in this chapter. Future research, can, therefore address an optimisation of a system with detailed loss analysis coupled with integrated thermal model to determine the electro-thermal performance of high power IPT systems.

The shifting in resonance caused due to both the presence of flux modifying materials as well as due to reactive reflection of additional components to the pick-up has been discussed in this chapter. In a practical example, a charge-pad of self-inductance $198.6\ \mu H$ experiences an increase by 33.5% due to a pad of inductance $199.8\ \mu H$ at a 1.5 cm z-gap. Another example of bifurcation due to the effect of the rectifier parallel filter capacitor 27.2 nF in a series resonant IPT system, resulting in two zeroes and one pole, all frequency shifted is also explained. Holistic system level models considering 3D inductance variations, operating with a variable frequency IPT system is suggested to mitigate this problem.

Experimental analysis of the system is performed for various loads and bridge angles. The magnetic losses are validated by performing higher power testing and most observations have a maximum loss inaccuracy in the ballpark of 10%. The magnetic loss distribution is dominated by losses in the resonant capacitor bank and ferrite which contribute $\sim 70\%$ loss. The highest total system efficiency measured for the light EV charging is close to 91%.

Economic Analysis of IPT Systems - A case study

The economic viability of on-road wireless charging of electric vehicles (EVs) strongly depends on the choice of the inductive power transfer (IPT) system configuration (static or dynamic charging), charging power level and the percentage of road coverage of dynamic charging. In this chapter, a case study is carried out to determine the expected investment costs involved in installing the on-road charging infrastructure for an electric bus fleet. Firstly, a generic methodology is described to determine the driving range of any EV (including electric buses) with any gross mass and frontal area. Further, the impact of different IPT system parameters on driving range is incorporated. Economic implications of a combination of different IPT system parameters are explored for achieving the required driving range of 400 km, and the cost optimized solution is presented for the case study of an electric bus fleet. The cost break-up of various system components of the on-road charging scheme is estimated, and the final project cost and parameters are summarized.

Based on
- V. Prasanth and P. Bauer, "Study of misalignment for On Road Charging," in *IEEE Transportation Electrification Conference and Expo (ITEC)*, 2013, pp. 1-8.; and
- A. Shekhar, V. Prasanth, P. Bauer, and M. Bolech, "Economic Viability Study of an On-Road Wireless Charging System with a Generic Driving Range Estimation Method," in *Energies*, 2016.

6.1 Introduction

Transition from over-utilized fossil fuels to cleaner, environment-friendly and more efficient electrical energy has propelled the proliferation of electric vehicles (EVs) in the market. Plug-in vehicles that use electric motors as prime movers have seen rapid mass production since 2011 [156]. The implications of the evolution and integration of electric vehicular technology and its associated charging aspects with smart grids and distribution networks has garnered growing interest [157].

Bulk energy consumers, like the transportation sector, if electrified, can yield a more sustainable planet. The direct effect of such an effort in the form of a reduction in the emission of greenhouse gases and a reduction of the dependence on fossil fuels is motivated in [158], in which a battery swappable smart electric bus system is described that is currently in pilot operation. The performance study of electric buses in terms of actual measurements of range and energy consumption for some test city driving cycles is presented in [159]. A comparative economic analysis of different charging solutions for the range extension of systems, such as a trolley system, battery swapping and hybrid vehicles, is presented in [160], [161].

Because of volume and especially the weight considerations, the amount of battery capacity used in a vehicle, such as a public transport bus, is limited, and consequently, the autonomous driving range of the bus is also limited. On some bus lines with limited driving distance per day, specific buses may have adequate range. However, more often, some sort of recharging of the batteries is necessary during the day. For medium and heavy use, recharging at a bus stop or at the turning point of the line (so-called opportunistic charging) may help enough to enable day-long operation.

For energy-intensive bus lines, like bus rapid transit with relatively high speed and high passenger occupancy, there is simply too little time available for getting the required energy into the bus with stationary solutions. In such scenarios, dynamic charging or battery swapping mechanisms need to be employed. Presently, several solutions are available to circumvent this problem.

- Trolley systems [160], [161]: efficient energy transfer from overhead wires and a small, if any, energy buffer are needed. However, significant infrastructural costs are involved; mechanical contacts make the system inflexible and cause wear and tear, as well as cluttering of the landscape.

- Battery swapping [158], [160]: the on-board battery is replaced at regular intervals at battery charging stations. The infrastructural costs and required battery capacity are high. While the transport efficiency is more due to a small on-board battery, the increase in required driving range leads to the increase in the number of battery swapping operations.

- Hybrid vehicles [160]: a combination of two or more energy sources are used. The

design is complicated, and the vehicle cost is high. Transport efficiency decreases with the increase in on-board energy buffer weight.

An inductive power transfer (IPT) system for on-road EV charging is an upcoming option for driving range extension [162], [17]. Wireless on-road charging systems for EVs can address several disadvantages associated with plugged-in vehicles related to safety, aesthetics and operational versatility in harsh weather conditions. Companies, like Bombardier Primove, Conductix Wamfler and Qualcomm Halo, are involved in pilot projects looking into the implementation of this technology. For example, Primove has successfully developed an electric route served by 12 m and 18 m e-buses with opportunity charging in Braunschweig, Germany [163]. During market research, the authors requested information on economic aspects from such companies. However, only ballpark figures were offered that were insufficient to carry out an independent viability study. Hence, the need was felt to develop a generalized economic viability study based on the technical knowledge [164], [165].

The contribution of this chapter is the development of a generalized economic viability study of employing a wireless on-road charging system for driving range extension. It is essential to describe how such dynamic charging systems measure up in terms of economics to other available charging solutions. However, since this technology is still in its nascent stage, historical data pertaining to economic considerations of the system are scanty. A literature survey provides some ballpark figures, but these do not indicate the dependence on charging power level and road coverage. For example, the PATHteam [166] considers a baseline price assumption of 1.5 M€/km. The costs incurred for the on-line EV (OLEV) [167], [168], [169] for a 100 kW IPT system with four inverters/km and an I-type rail are estimated to be around 0.85 M$/km. Herein, the I-type rail refers to the structure of the magnetic core framework used in the rail at the primary side. A detailed analysis of the core structures used in the rails for shaping the magnetic fields is offered in [168]. In this, the cost estimate is given to be about 0.23 M$/km.

Economic viability, transport efficiency and initial infrastructural investment costs incurred are influenced by the charging power level of static and dynamic on-road charging, road coverage area and on-board battery capacity. This chapter presents a detailed case-study on the economic considerations concerning the on-road wireless charging system for an articulated electric bus fleet in the province of North Holland. The theory is structured in a way that it can be adapted in a generalized economic viability study. In particular, the chapter describes the choices designers must make in terms of static and dynamic charging power levels and the road coverage to develop the most economic on-road charging solution in order to achieve a given driving range and highlights the trends in incurred project cost by making specific choices. Further, the choice of on-board battery capacity based on the trade-off between savings due to efficient transport *versus* the extra incurred infrastructural costs for the IPT system is explored.

6.2 Generic Methodology for Driving Range Estimation

In order to account for the energy inflow and outflow, it is essential to develop a model for the dynamic power consumption of the EV. This consumption pattern is dependent on the vehicle's specifications and the velocity profile. The dynamic power consumption is simulated for a reference vehicle with parameters [170] listed in Table 6.1.

Several standard driving cycles [171],[172], like the standardised on-road test cycles (SORT 1, SORT 2 and SORT 3), the urban dynamometer driving schedule (UDDS), the Braunschweig cycle and the highway fuel economy driving schedule (HWFET), have been simulated to establish the methodology. The simulation results for the SORT 3 cycle are presented, and the "driving cycle constants"defined in the subsequent section are provided for all aforementioned driving cycles.

Table 6.1: Reference parameters for simulating the dynamical consumption model of the electric vehicle (EV).

Parameter	Value	Unit
Empty mass	13,300	kg
Gross mass	19,000	kg
Frontal area	8.568	m^2
Coefficient of drag (assumed)	0.7	-
Coefficient of rolling resistance (assumed)	0.01	-
Battery capacity	600 (200×3)	Ah
Energy capacity	324	kWh
Nominal voltage	540	V
Battery type	lithium ion	-
Initial state of charge (SoC) (assumed)	95%	-

The physics of the vehicle power consumption [173] is governed by the following forces:

- Aerodynamic drag ($P_{drag} = 0.5\rho C_d |v|^3 A_f$) is the load due to resistance offered by the air. ρ is the density of air in kg/m^{-3}; C_d is the coefficient of drag; vis the instantaneous velocity; and A_f is the frontal area of the vehicle.

- Rolling resistance ($P_{roll} = C_r gM \cos(\theta)|v|$) is the frictional resistance offered by the road due to the motion of wheels. C_r is the coefficient of rolling resistance; M is the mass of the vehicle; g is the acceleration due to gravity; and θ is the angle of inclination.

- Inertial load ($P_I = Ma|v|$) is the change in the stored energy of the vehicle due to dynamic motion (acceleration/braking). It is important to consider here that some energy is recoverable through the regenerative braking.

- Gravitational load ($P_\mathrm{g} = Mg\sin(\theta)|v|$) is due to the movement of the vehicle on an inclined road.

A dynamic power consumption model is developed based on the vehicle dynamics described by the above-mentioned equations depending on the power loss due to rolling resistance, power demand during acceleration, power lost during deceleration after, including regenerative braking, and power lost due to aerodynamic drag. The model involves the following assumptions:

- The overall average efficiency of the motor-drive system is assumed to be 80%. A corrective factor corresponding to the ratio of assumed average efficiency to actual average efficiency can be multiplied with the mass and area constant derived in the subsequent section to improve the accuracy of the model.

- Sixty percent of energy is recovered during regenerative braking.

- The angle of inclination of the road is zero.

- The auxiliary power P_aux will include heating, ventilation and air conditioning (HVAC), lighting, auxiliary services of vehicle, opening and closing of doors, route display screens, power steering and brakes. In the simulations to derive K_m and K_a, 0 kW is considered in order to eliminate the dependence of SoC on P_aux.

- Actual measurements were taken for the 12 m bus with a 324 kWh battery for SORT 1, 2 and 3 cycles. The specific consumption was measured to be 1.2 kWh/km for SORT 3 as compared to 1.3 kWh/km obtained from the simulation of our dynamic power consumption model under similar conditions. This increased the confidence on relying on the developed model for the economic viability study.

6.2.1 State of Charge Estimation of the Battery-Alone System

The impact of vehicle specifications, environmental factors and velocity profile on the SoC of the EV battery is simulated for a battery-alone system. Three Li-ion batteries are used in parallel (generic model available in matrix laboratory (MATLAB) software platform) with a nominal voltage of 540 V, a rated capacity of 200 Ah each and an initial SoC of 95%. Charge and discharge current flowing through this battery system are computed from the dynamic power flows and the nominal voltage of the system. The distance of 40 km is simulated to prove a linear dependence by regression analysis. A complete discharge of the battery up to the allowed depth of discharge (DoD) is not simulated for the regression analysis, implying that the dependence of internal battery resistance on the SoC is neglected in the derived constants of this section.

Mass Constant ($K_{\mathbf{m}}$) of the Driving Cycle

Fig. 6.1 and Fig. 6.2 shows the plots for SoC *versus* distance for different gross masses with the frontal area equal to zero and an ambient temperature of 20 °C for SORT 3 and the HWFET driving cycle. The auxiliary power demand of the EV is set to zero. The SoC, thus, in this case, depends only on the mass of the vehicle.
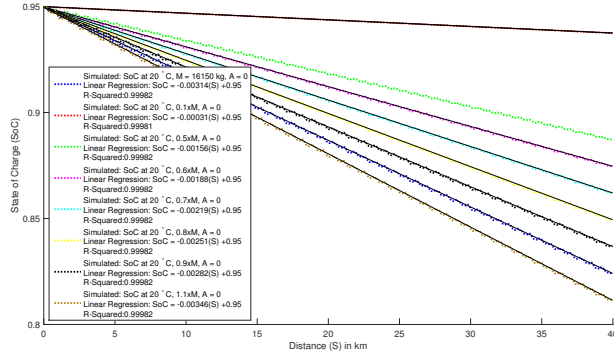
Figure 6.1: SoC versus distance for different gross masses of EV - SORT 3.
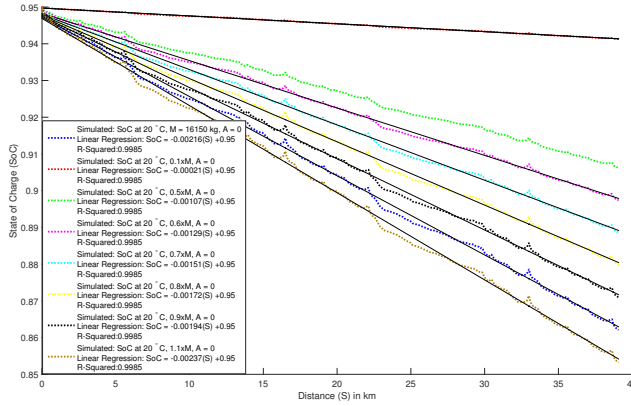
Figure 6.2: SoC versus distance for different gross masses of EV - HWFET.

The linear regression yields a coefficient of determination (R^2) > 0.99. An R^2 value close to one indicates a linear dependence of battery SoC on the distance traveled by the EV.

Fig. 6.3 and Fig. 6.4 shows the variation of the slope of the SoC *vs.* distance with respect to mass of the vehicle for the SORT 3 and HWFET driving cycles. Regression analysis yields $R^2 > 0.99$, which indicates a linear dependence of final state of the charge of the battery on

the vehicle mass. The slope, defined as the mass constant of the driving cycle K_m, is equal to 1.9464×10^{-7} for the SORT 3 driving cycle. In the case of the HWFET cycle, K_m is equal to 1.3371×10^{-7}.
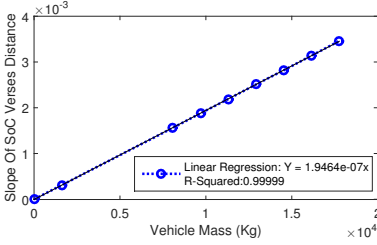
Figure 6.3: Slope of SoC versus distance w.r.t gross mass of vehicle - SORT 3.
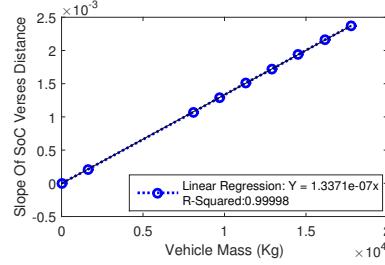
Figure 6.4: Slope of SoC versus distance w.r.t gross mass of vehicle - HWFET.

Area Constant (K_a) of the Driving Cycle

Fig. 6.5 and Fig. 6.6 shows the plots for SoC *versus* distance for different frontal areas with the gross mass equal to zero and an ambient temperature of 20 °C for the SORT 3 driving cycle. The auxiliary power demand of the EV is set to zero. The SoC, thus, in this case, depends only on the frontal area of the vehicle.
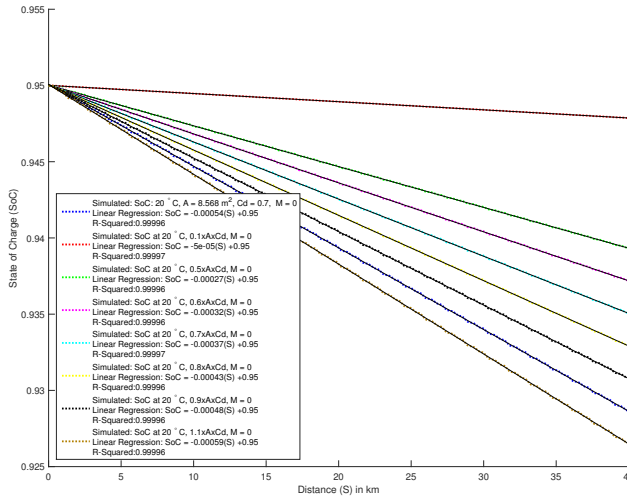
Figure 6.5: SoC versus distance for different frontal area of vehicle - SORT 3.
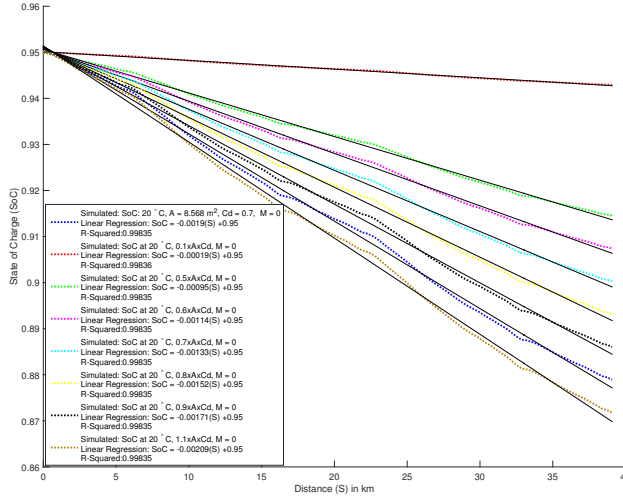
Figure 6.6: SoC versus distance for different frontal area of vehicle - HWFET.

Fig. 6.7 and Fig. 6.8 shows the variation of the slope of the SoC *vs.* distance with respect to the product of the frontal area and drag coefficient of the vehicle. The linear regression yields $R^2 > 0.99$, which indicates a linear dependence of the final battery SoC on the frontal area of the vehicle. The slope, defined as the area constant of the driving cycle, $K_a=8.9739\times10^{-5}$ for the SORT 3 driving cycle and 2.2176×10^{-4} for HWFET driving cycle.
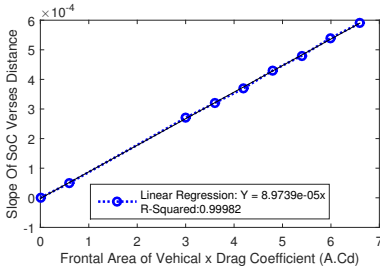
Figure 6.7: Slope of SoC Vs distance w.r.t frontal area x Cd of vehicle - SORT 3.
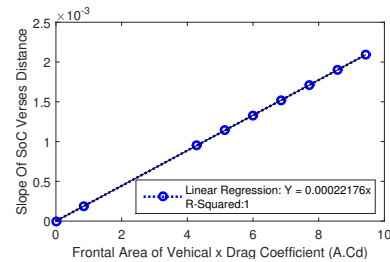
Figure 6.8: Slope of SoC Vs distance w.r.t frontal area x Cd of vehicle - HWFET.

Equation for State of Charge Estimation of the Battery-Only System

Hence, from the above theory, the expression for SoC of the on-board battery as a linear function of distance traveled can be derived. The SoC for the battery-alone EV system for any distance traveled can be estimated using (6.1):

$$SoC_{\mathrm{b}} = - \left(\frac{K_{\mathrm{m}}}{K_b} M + \frac{K_{\mathrm{a}}}{K_{\mathrm{b}}} A_{\mathrm{f}} C_{\mathrm{d}} + \frac{P_{\mathrm{aux}}}{U_{\mathrm{av}} \eta_{dis} E_{\mathrm{bat}}} \right) S + SoC(0) \tag{6.1}$$

A similar procedure was followed for different driving cycles to determine the velocity profile-dependent mass and area coefficients. Table 6.2 presents the mass and area constants of different driving cycles.

A clear increasing trend in area constant K_{a} with the average velocity of the driving cycle is observed, which is expected due to the increase in aerodynamic drag. On the other hand, the mass constant decreases despite increasing average velocity. This is because, while the mass-dependent vehicle power consumption is directly proportional to the instantaneous velocity, instantaneous power demand for acceleration is by far the dominant factor. Velocity profiles of driving cycles with a lower average velocity typically have higher acceleration and deceleration durations, resulting in a higher power consumption. Thus, K_{m} decreases with the increase in average velocity.

Table 6.2: Driving cycle constants. UDDS, Urban Dynamometer Driving Schedule.

Driving Cycle	K_{m} (kg^{-1}km^{-1})	K_a (m^{-2}km^{-1})	U_{av} (km/h)
SORT 1	2.09234×10^{-7}	2.4684×10^{-5}	12.1
SORT 2	1.9604×10^{-7}	4.9201×10^{-5}	18
Braunschweig	2.1225×10^{-7}	4.992×10^{-5}	22.9
SORT 3	1.9464×10^{-7}	8.9739×10^{-5}	25.3
UDDS	1.89×10^{-7}	9.3371×10^{-5}	31.53
HWFET	1.3371×10^{-7}	2.2176×10^{-4}	77.73
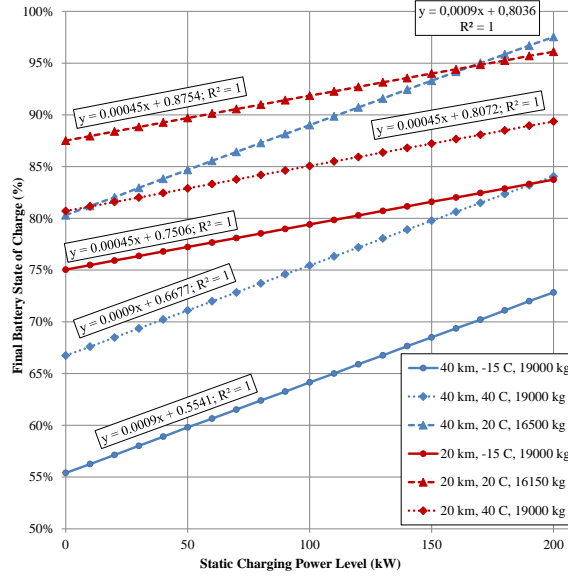
Figure 6.9: SoC of the battery for different charging powers of the static inductive power transfer (IPT) system.

6.2.2 Driving Range Extension with the Static Inductive Power Transfer System

Static IPT charging is employed at scheduled stoppages of the driving cycle. For the same energy transfer per vehicle, the infrastructure cost involved in the static is less than the dynamic IPT system. The system is simulated with different static IPT charging power levels at scheduled stoppages of the SORT 3 driving cycle. Fig. 6.9 shows the plots for the final battery SoC *versus* the power level for different scenarios for traveled distances of 40 km and 20 km.

The final SoC of the battery linearly varies with the charging power level. The regression analysis yields an R-squared value of one. The generic equation for estimating the SoC of the battery for different static charging power levels is described by (6.2):

$$SoC_{\text{static}} = \left(\frac{t_{\text{stop}} \times \eta_{\text{c}}}{E_{\text{bat}}} \right) P_{\text{stat}} + SoC_{\text{b}}(s_{\text{tot}}) \tag{6.2}$$

The initial point $SoC_{\text{b}}(s_{\text{tot}})$ is the SoC of the battery-alone system that can be estimated using (6.1).

6.2.3 Driving Range Extension with the Dynamic Inductive Power Transfer System

Fig. 6.10 shows the simulation plots for the final battery SoC *versus* the percentage of the road coverage area for different power levels of dynamic IPT charging for a traveled distance of 40 km with the SORT 3 driving cycle at an ambient temperature of $-15\,^{\circ}\mathrm{C}$ and 100% occupancy level. A static IPT system of 60 kW is considered to be installed in all cases.
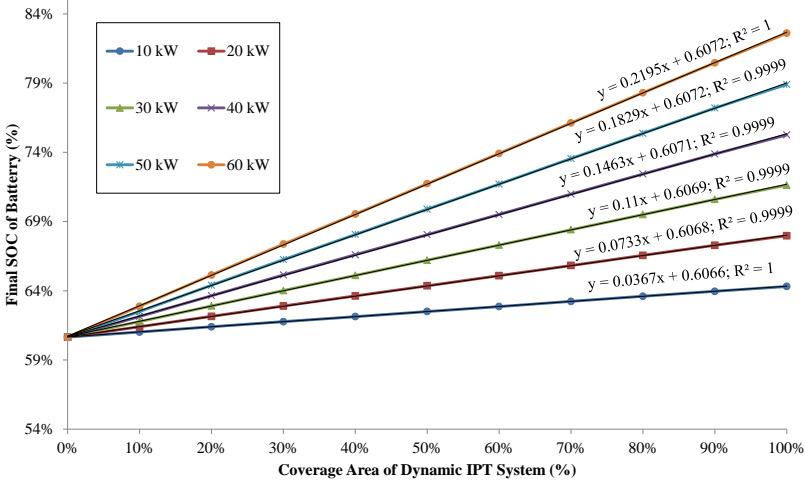
Figure 6.10: Final SoC *versus* road coverage area for different power levels of the dynamic IPT system.

The following observations can be made:

- The final SoC linearly increases with road coverage area despite the randomness in the velocity profile. This is because the IPT system is also randomly distributed on the road track. Regression analysis yields $R^2 > 0.99$, which indicates a strong correlation.
- The slope is directly proportional to the charging power level of the IPT system.
- SoC at the zero coverage area can be computed using (6.1) and (6.2) corresponding to the "static-only" charging system.

The battery SoC of the EV with dynamic on-road charging can be estimated using (6.3):

$$SoC_{\mathrm{dyn}} = SoC_{\mathrm{static}} + \underbrace{\left(\frac{(t_{\mathrm{total}} - t_{\mathrm{stop}})\eta_{\mathrm{c}} P_{\mathrm{dyn}}}{E_{\mathrm{bat}}} \right)}_{\text{Slope}} \frac{(C_{\mathrm{road}}(\%))}{100} \qquad (6.3)$$

The driving range of the vehicle can be calculated from the SoC of the battery using (6.4):

$$DR = \frac{(DoD_{\max} \times S)}{(SoC(0) - SoC_{\text{final}})} \tag{6.4}$$

6.2.4 Impact of Battery Weight

In the previous section, the impact of IPT systems on the driving range of the EV was studied. In order to achieve the same driving range with the battery-alone system, a greater energy capacity is needed and, hence, a greater battery weight and volume, which has implications on not only the transport efficiency [175], but also on the feasibility of installing such a system. This section describes the method to estimate the required energy capacity of the battery in order to achieve the desired driving range and the subsequent impact of increased weight on specific consumption of the electric bus.

Rearranging (6.4), the final SoC of the battery (SoC_{req}) for the required driving range at the end of travel distance is described by (6.5):

$$SoC_{\text{req}} = SoC(0) - \frac{DoD_{\max} \times S}{DR} \tag{6.5}$$

Here, DR is the required driving range in km. Now, (6.1) can be modified to compute the battery weight-dependent SoC at end of the total traveled distance, as shown in (6.6):

$$SoC_{\text{b}} = - \left(\frac{K_{\text{m}}}{K_{\text{b}}} (M_{\text{ref}} - W_{\text{bat,ref}}(1 - k_{\text{b}})) + \frac{K_{\text{a}}}{K_{\text{b}}} A_{\text{f}} C_{\text{d}} + \frac{P_{\text{aux}}}{U_{\text{av}} \eta_{\text{dis}} k_{\text{b}} E_{\text{bat,ref}}} \right) S + SoC(0) \tag{6.6}$$

where M_{ref} is the gross mass of the reference vehicle and $W_{\text{bat,ref}}$ is the weight of the reference vehicle battery in kg. The weight of the required battery is $K_{\text{b}} W_{\text{bat,ref}}$. Rearranging (6.6), it is possible to estimate the required battery capacity factor K_{b} as per (6.7), such that the SoC_{final} corresponding to the required driving range is equal to SoC_{b} for a battery-alone system.

$$K_{\text{b}} = \frac{K_{\text{m}}(M_{\text{ref}} - W_{\text{bat,ref}}) + K_{\text{a}} A_{\text{f}} C_{\text{d}} + \left(\frac{P_{\text{aux}}}{U_{\text{av}} \eta_{\text{dis}} E_{\text{bat,ref}}} \right)}{\left(\frac{SoC(0) - SoC_{\text{ref}}}{S} \right) - K_{\text{m}} W_{\text{bat,ref}}} \tag{6.7}$$

From the Ragone plot, the specific energy of a high-power Li-ion battery used in the reference e-bus is about 100 Wh/kg [176]. Hence, the weight of the reference vehicle ($W_{\text{bat,ref}}$) is $\left(\frac{1000 * E_{\text{bat,ref}}}{100} \right) = 3240$ kg. Fig. 6.11 shows the increase in the capacity factor and the specific consumption of the electric bus with the required driving range for different loading scenarios for the SORT 3 driving cycle for the battery-alone system with no on-road charging in

place. The simulated specific consumption of the reference electric bus used in this section is also marked.
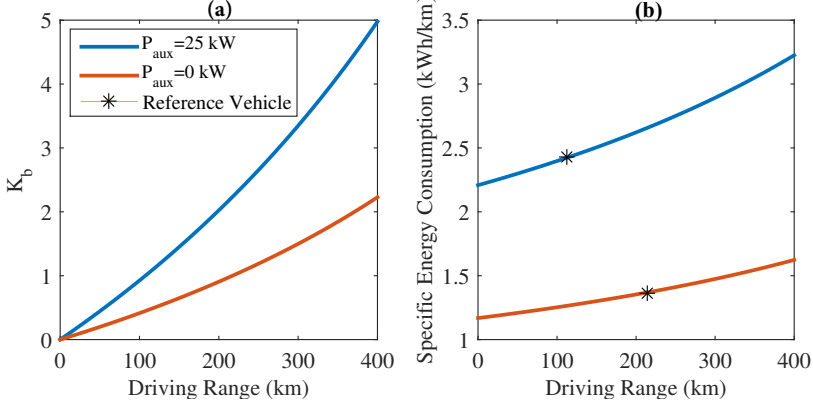
Figure 6.11: Impact of driving range of the vehicle for the SORT 3 driving cycle without any on-road charging on the (a) Capacity factor K_b (b) Specific consumption.

Finally, the impact of the increase in the battery weight on the specific consumption of the vehicle (E_{specific} in kWh/km) can be estimated from (6.8):

$$E_{\text{specific}} = E_{\text{bat}} * \left(K_{\text{m}}(M_{\text{ref}} - W_{\text{bat,ref}}(1 - K_{\text{b}})) + K_{\text{a}}A_{\text{f}}C_{\text{d}} + \frac{P_{\text{aux}}}{U_{\text{av}}\eta_{\text{dis}}E_{\text{bat,ref}}} \right) \tag{6.8}$$

6.2.5   Estimation Error

In Fig. 6.12, the percentage of absolute error between the estimated value obtained from the derived equations and the simulated value of the battery SoC of the reference vehicle obtained from the dynamic power consumption model of the vehicle developed on MATLAB for a 40 km traveled distance with 60 kW static + 60 kW dynamic on-road charging is presented for different driving cycles.
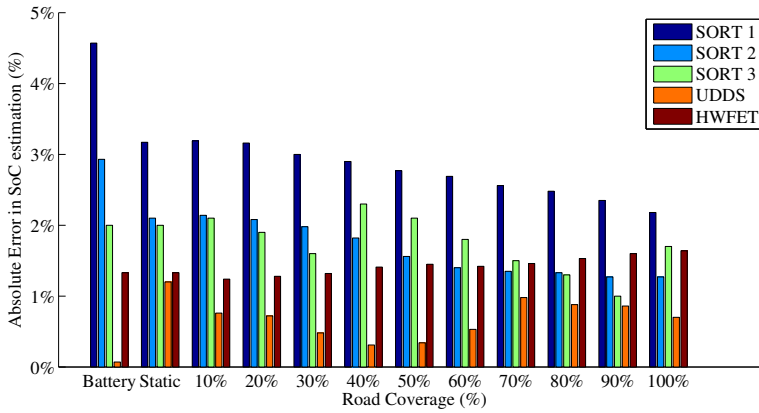
Figure 6.12: Percentage of the absolute error in SoC estimation for different driving cycles.

For a 30% road coverage with 60 kW charging power level of both the static and dynamic IPT system, the error in estimated SoC is 2% with the corresponding error in estimated driving range being 6.69%. Hence, the driving range of any EV in different scenarios can be estimated using simple linear equations with known parameters and vehicle specifications with reasonable accuracy.

6.3 Economic Analysis for the On-Road Inductive Power Transfer Charging System: Case Study

6.3.1 System Description

The economic aspects of on-road charging solution for a two-lane, 40 km-long bus line of Zuidtangent in the province of North Holland is explored. It should be noted that in this section, a larger articulated electric bus will be used for analysis with an empty weight of 20,000 kg and a 500 kWh on-board Li-ion battery pack with an additional weight of 5000 kg. The gross weight of the vehicle with 100% occupancy level is thus about 35,000 kg. The frontal area is 8.568 m^2; the coefficient of drag is taken as 0.7; and the rolling resistance is taken as 0.01. Twenty five articulated buses run per day on average. Each bus is expected to drive 400 km per day. Five buses are kept as spare. The design of the IPT system involves the following considerations:

- The battery is charged to its full capacity during night hours when the bus is stationary.

- There are 24 scheduled stoppages of 20 s each and a 6 min stoppage at the start of each run.

- The UDDS [172] is used to emulate the velocity profile of the e-bus.
  - ▷ The average velocity of the UDDS driving cycle is 31.53 km/h.
  - ▷ From Table 6.2, the mass constant is 1.89×10^{-7}, and the area constant is 9.337×10^{-5}.

- The required driving range is 400 km (10 trips of 40 km each) in the worst case scenario of $-15\,°C$, 100% occupancy.

- The climate model in [174] predicts that a normal bus would consume 167 kWh for HVAC in winter days for $-7\,°C$ in Netherlands for a 20 h operation. An articulated bus of almost double the length would consume double this (334 kWh). Correspondingly, 433 kWh will be consumed if the ambient temperature is $-15\,°C$.

  The total energy consumption of the auxiliary system, including HVAC, lighting, auxiliary services of the vehicle, opening and closing of doors, route display screens, power steering and brakes, during the worst winter condition is assumed to be 500 kWh for a 20 h operation. Therefore, the average P_{aux} is assumed to be 25 kW.

The SoC for the battery-alone system can be estimated from (6.1). With an initial SoC of 95% at the start of the day by considering overnight charging of the on-board battery of the electric bus, the SoC at the end of a 40 km travel distance without any on-road charging is 68.66%. At the end of the traveled distance ($S = 40$ km), the final SoC of the battery corresponding to the desired driving range ($DR = 400$ km) is given by (6.5) to be 87%. The deficit, $\Delta\text{SoC} = 18.34\%$, is removed using a combination of static and dynamic on-road charging.

P_{stat}, P_{dyn} and $C_{\text{road}}(\%)$ are varied, such that SoC_{dyn} at the end of traveled distance of 40 km is 87%. Several combinations can be used to achieve the required driving range, and the optimum values are chosen based on the minimum investment costs involved.

6.3.2 ΔSoC Deficit Removal with the Static Inductive Power Transfer Charging System

Static charging pads are installed at the scheduled stoppages. The charging time with each pad is 20 s. For a similar amount of charging time on a single dynamic IPT segment of 1.05 m, the e-bus must have a velocity of 0.19 kmph. Hence, for better infrastructural usage and lower investment costs, it is desirable that the static charging power be as high as possible.

The slope of (6.2) corresponding to the stop time in the winter worst case scenario is 0.000453. Fig. 6.13 shows the variation in final battery SoC and driving range achieved for different on-road static charging power levels for different starting and halt times. Note that with increasing halt time, the total daily operating time of the bus increases, thereby marginally increasing the energy consumption of the auxiliary bus system. This is reflected in decreasing SoC of (6.1) due to decreasing average velocity (U_{av}).
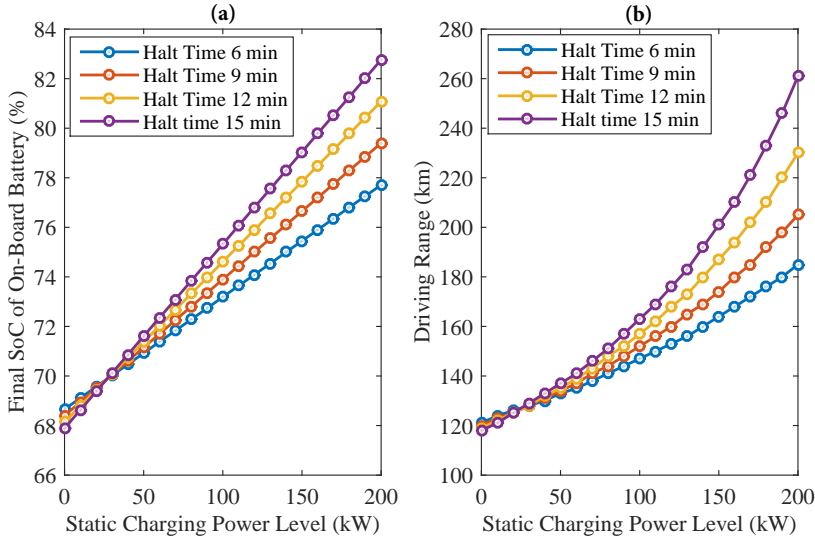
Figure 6.13: (a) On-board battery SoC (b) Driving range *versus* static charging power level for different starting and halt times.

With a 200 kW static charging power level, the driving range achieved is 185 km, and the battery SoC is 77.7%. The deficit has to be cleared by installing dynamic charging infrastructure.

6.3.3 △SoC Deficit Removal with the Dynamic Inductive Power Transfer Charging System

With increasing power level, the percentage of road coverage to achieve the required driving range of 400 km decreases; however, the investment costs per km of installed on-road charging infrastructure increases, as shown in Fig. 6.14.
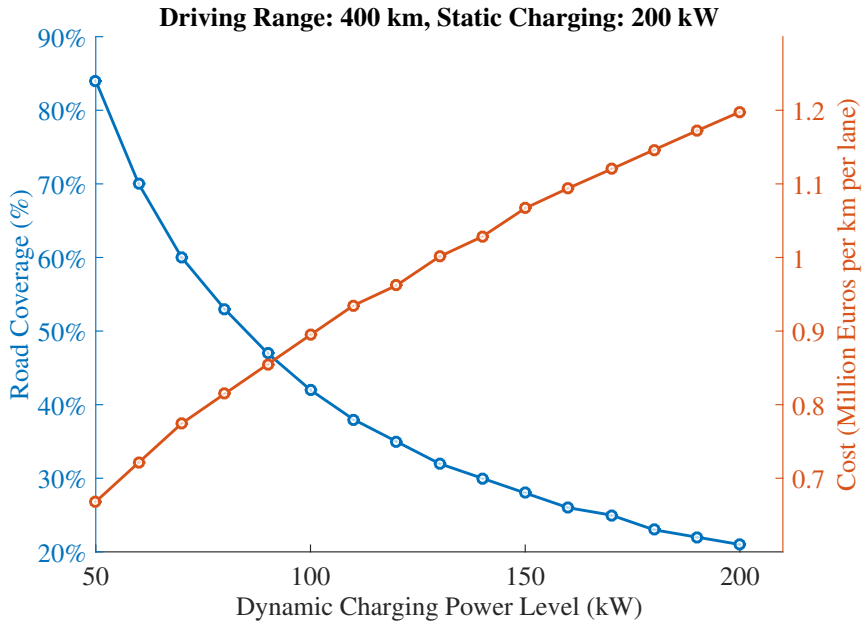
Figure 6.14: Percentage of road coverage for different dynamic charging power levels.

As shall be shown in the subsequent section, the investment costs incurred due to increasing the charging power level are outmatched by the decrease in infrastructural costs due to reducing road coverage. Hence, it is preferred to increase the charging power level from the economic point of view.

6.3.4 Bill of System Components - Costing

In this section, the investment costs incurred for different system components have been estimated. Since the technology is still in its nascent stage, market data are not available. Hence, the costs have been calculated from the design point of view. The following considerations have been observed to make the estimate:

- The total copper mass (in kg) in the air cored primary winding [177] based on the charging power level along with *litz* wire cost [8] of 35 €/kg are used to estimate the cost of a single IPT charging pad. An additional design cost of 50% is assumed.

- The cost of the power electronics [178] involved in the IPT supply system is considered to be 50 €/kW. Additional maintenance charges of 10% have been included.

- Corresponding to the operating frequency of 100 kHz, a minimum of 4 inverters per km are installed [179].

- The road construction (digging, labor, installation of IPT system) costs of 0.1 M€/km for IPT road coverage are assumed.

- Discrete charging pads of 1.05 m [177] in length each have been considered for dynamic on-road charging. The total number of dynamic charging pads have been estimated for total road coverage, and the corresponding cost of air cored primary winding is calculated. An illustration of the on-road dynamic charging system with discrete pads [180] is shown in Fig. 6.15.
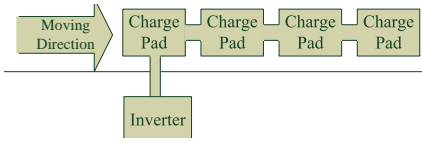
Figure 6.15: Illustration of the discrete IPT charging pads for on-road dynamic charging.

Fig. 6.16 shows the total cost of different IPT system components for achieving a driving range of 400 km with a 200 kW static IPT charging at scheduled stoppages and different dynamic charging power levels. The overall cost incurred decreases with increasing dynamic charging power level, because of the decrease in the percentage of road coverage. With a 200 kW dynamic charging, the total road coverage required is 21%, while the IPT system cost is 10.1 million Euros per lane of the Zuidtangent line. The specific cost is 1.2 M€/km/lane.
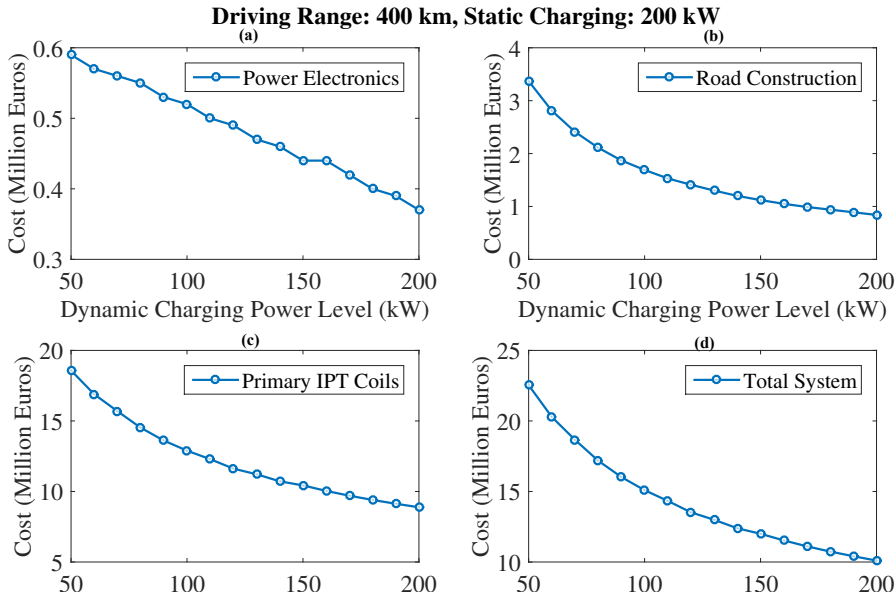
Figure 6.16: Cost estimation of the IPT charging system components (a) Power Electronics (b) Road Contruction (c) Primary IPT coils (d) Total System.

6.4 Second Order Economic Considerations

Several secondary factors influence the choice of system configuration. These include the following.

6.4.1 Running Schedule
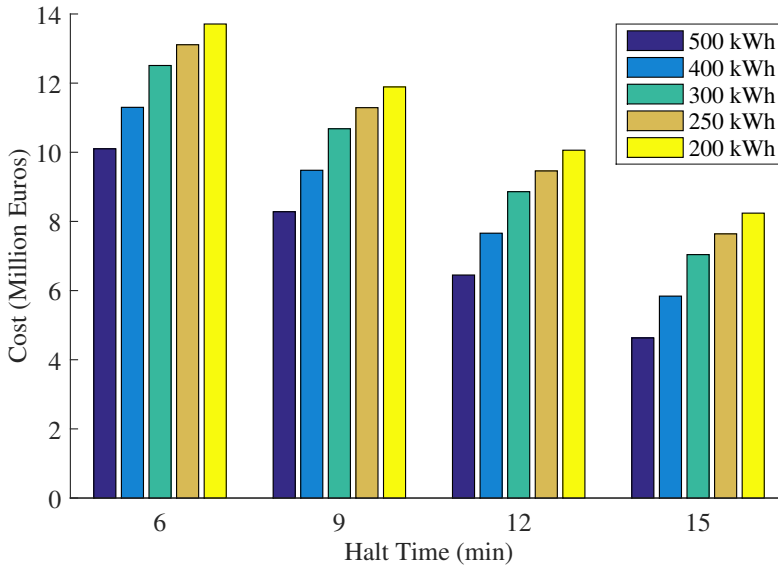
Figure 6.17: Incurred IPT infrastructure cost with changing halt time at the start of the 40 km run.

In the beginning of each 40 km run, there is a six min scheduled stop that provides an opportunity for static charging. During the worst loading scenario, which occurs only for a few predictable days of a year, increasing this stoppage time can lead to significant infrastructural cost reduction for meeting the driving range. Extra buses may be employed to run in these conditions for meeting the time deficit. Note that with increasing halt time, the total daily operating time of the bus increases, thereby marginally increasing the energy consumption of the auxiliary bus system. This is reflected in the decreasing SoC of (6.1) due to decreasing average velocity (U_{av}).

Fig. 6.17 shows the influence of scheduled stoppage time at the start of the 40 km run on the incurred investment cost of installing the IPT system for different battery capacities.

As observed, the incurred investment costs of installing on-road charging infrastructure significantly decreases by increasing the halt time. Hence, by choosing a halt time of 12 min during the worst loading scenario, the IPT system cost decreases from 10.1 M€/lane to 6.45 M€/lane, because the required road coverage of dynamic on-road charging decreases from 21% to 13%.

6.4.2   On-Board Battery Capacity

1. The transport efficiency increases with decreasing battery capacity corresponding to the weight reduction. The energy savings becomes significant with a high lifetime travel distance and the number of running buses.

2. IPT charging infrastructure cost increases with decreasing battery capacity due to the additional road coverage requirement of the dynamic IPT system. This is shown in Fig. 6.17.

3. The price of the installed on-board battery decreases with decreasing capacity. This can be a significant investment factor with increasing the number of e-buses.

Fig. 6.18 shows the IPT charging infrastructure cost, on-board battery cost and the total project cost for a 25 average running +5 spare all-electric bus system with decreasing battery size. Recall here that the charging power delivered to the on-board battery by the IPT system is 200 kW. Both static charging at scheduled stoppages, as well as dynamic charging with 13% road coverage are employed to obtain a driving range of 400 km.

The Li-ion battery price is considered to be 700 €/kWh and can last for about 12 years before needing replacement [160]. This relatively high price level is caused by high quality requirements and limited market size for buses so far. In five to 10 years, the cost is predicted to drop to approximately 250 €/kWh [181].

The total incurred project investment cost slightly increases with decreasing battery size as a net effect of the increase in IPT infrastructure cost balanced by the decrease in total battery cost. For attaining higher transport efficiency, it is desirable that the on-board battery capacity is lower. Hence there is a trade-off in selecting the on-board battery capacity, which is now explored.
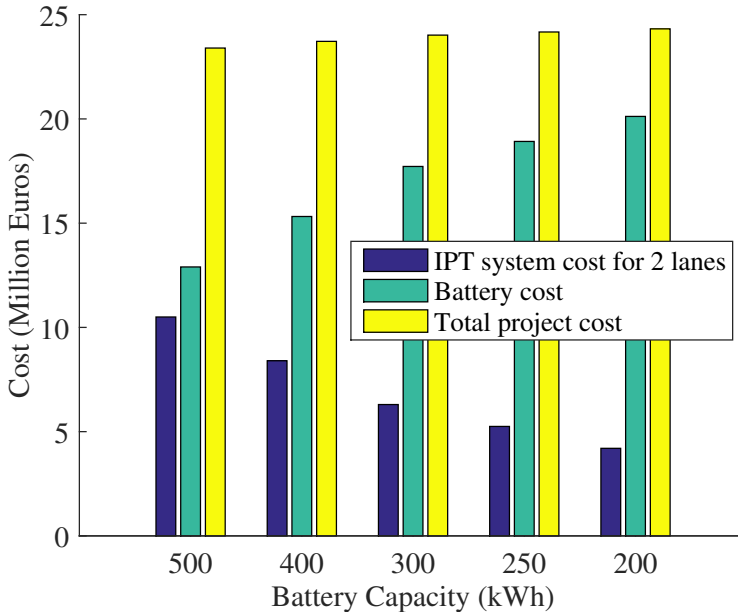
Figure 6.18: Battery size dependency of the incurred infrastructural costs.

The OLEV team looks into the trade-off between battery capacity, transport efficiency and charging infrastructural costs by defining the optimization problem [182] using particle swarm optimization based on the system dynamics. The solution involves allocating power transmitters to determine battery size by minimizing the vehicle power consumption while constrained by the battery energy level to be maintained.

In this chapter, the derived linear equations reduce the optimization problem to a solution of two linear equations with known constants without dynamic terms, as shown in Fig. 6.19, as against optimization techniques used in prior literature [183]. The optimum solution can be reached quickly by solving for the savings based on the specific energy consumption using (6.8) with the single variable "K_b" that describes the battery capacity against the incurred minimum infrastructural costs for the desired driving range for that K_b, as described in the above sections.
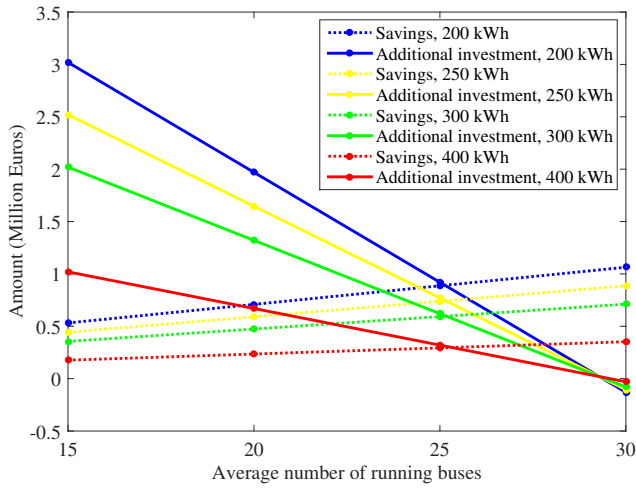
Figure 6.19: Savings and change in initial investment for different battery sizes with respect to a 500 kWh on-board battery system.

From (6.8), the specific consumption of the electric bus in the average loading scenario (25 kW of auxiliary power consumption and 100% occupancy level) is estimated to be 2.84 kWh/km with a 500 kWh on-board battery and 2.66 kWh/km with a 200 kWh on-board battery with a battery-specific weight of 10 kg/kWh.

Savings achieved in 12 years of operation due to efficient transport with varying kWh on-board batteries for different average numbers of running buses is shown in Fig. 6.19. Ten percent additional losses corresponding to the IPT system transfer efficiency are assumed. Energy cost is considered to be 0.1 €/kWh, and each bus runs for an average of 400 km per day. The change in investment corresponding to the net effect of the increase in the IPT infrastructure cost and the decrease in the total on-board battery cost ("x" running buses) is also depicted.

Fig. 6.19 shows that the reduction of the on-board battery size from 500 kWh to 200 kWh is only viable if an average of 30 buses are running daily. The point of intersection of the savings trend and the extra infrastructure trend (same colored lines) gives the average number of buses running per day above which a reduction in the on-board battery capacity becomes a viable option. In our system (25 buses running on average per day), the extra incurred costs cannot be recovered by efficient transport in a 12 year lifetime for even a 500 kWh to 400 kWh battery size reduction. Hence, we conclude that 500 kWh is cost-wise the most optimum choice.

6.5 Conclusions

Hence, the economic analysis of installing the IPT system to achieve a driving range of 400 km in the worst loading scenario on the Zuidtangent bus lanein the province of North Holland was carried out. Table 6.3 summarizes the IPT system parameters in terms of the charging power level (200 kW), road coverage percentage (13%), inverter rating (200 kW) and battery capacity (500 kWh) for the system described. The resulting specific cost is estimated to be 1.2 M€/km/lane for a lifetime of 12 years.

In order to develop a generalized theory towards this study, an analytical methodology has been presented to estimate the extension in driving range of any EV with on-road contactless charging. The SoC of the battery is described as a linear function of the distance traveled and can be estimated for an EV of any gross mass and frontal area. The energy consumption dependent on the velocity profile is estimated by defining mass and area constants for several driving cycles. The increase in the SoC of the battery depending on different power levels and road coverage of the static and dynamic IPT system is described mathematically.

The presented theory describes how to minimize the infrastructural costs based on the IPT design parameters. The chapter depicts how the infrastructural costs of dynamic wireless charging systems decrease with increasing power level due to the reduction in road coverage area and, hence, suggests to the designers to realize as high a charging power as possible. Further, the scheduled stoppage time is increased during the worst weather/load conditions to achieve a more economically-viable system. This solution brings down the cost from 10.1 M€/lane to 6.45 M€/lane due to a reduction in road coverage of dynamic charging from 21% to 13%.

Another major contribution of this chapter is the optimization of on-board battery capacity as a trade-off between the savings achieved due to the increase in transport efficiency and the extra investment costs incurred due to the battery weight reduction. The derived linear equations in this chapter reduce the optimization problem to a solution of two linear equations with known constants. It is also shown how a 500 kWh on-board battery capacity is chosen as the most optimized option. It is depicted how increasing the number of average running buses in the system can make the battery weight reduction a viable option.

The so-called lifetime impact (including fabrication, use and scrappage) of an EV in terms of CO_2 emission is dependent on the source of electric energy. If the electricity used is purely from coal-fired power plants, there is only a limited reduction in overall CO_2 emissions compared to a diesel-fueled vehicle of identical proportions. If more sustainable sources are added to the electricity generation mix (partly from renewables, partly natural gas, *etc.*, as is often the case), there is a clear reduction in lifetime CO_2 impact for the EV compared to the diesel-based vehicles [184].

Table 6.3: IPT system specifications.

Parameter	Value	Unit
On-board battery capacity	500	kWh
Driving range in worst loading scenario	400	km
Driving range without on-road charging	119	km
Scheduled stoppage at start of each run (worst case)	12	min
Scheduled stoppage at start of each run (normal)	6	min
Number of buses (average running + spare)	25+5	-
Static charging power level	200	kW
Dynamic charging power level	200	kW
Dynamic IPT road coverage	13%	-
Power rating of inverter	200	kW
Total number of inverters	22	-
Cost of primary winding	5.67	M€/lane
Cost of inverters	0.24	M€/lane
Total cost of IPT system	6.45	M€/lane
Specific cost	1.2	M€/km/lane
Battery cost for 30 buses	10.5	M€
Total project cost (M€/2 lanes/30 buses)	23.4	-

While IPT on-road charging of electric buses might offer an advantage over hybrid or completely diesel-based vehicles in terms of CO_2 emission reduction, another research objective was to utilize this cost analysis as a comparative tool to evaluate how IPT charging systems measure up to other solutions for extending the driving range of such electric buses in terms of economics [161]. At present, the specific cost of 1.2 M€/km/lane for this system is higher as compared to 0.75 M€/km/lane of a conventional trolley system. However, it must be noted that a conservative battery price of €700/km is taken, which is expected to decrease with the future evolution of market forces in favor of such technologies.

Challenges and Interdependencies of Future Sustainable Roads

A vision of future highways complementary to e-mobility is developed. Evolving technologies like (autonomous) electric vehicles (EVs), driving range enhancing contactless charging, lifetime time enhancing self-healing roads and in-situ energy generating elements are organically integrated. The infrastructure of inductive power transfer (IPT) and self-healing roads can be shared resulting in challenges. On the other hand, a sandwiched modular combination of energy generating solar roads and wireless EV charging maybe unfavourable. These technical implications of integrating different emerging on-road technologies are analytically and experimentally researched. Finally, case study of an integrated future highway is proposed for sizing of the required energy mix.

Based on

7.1 Introduction

The highway of the future is expected to perform three major operations so as to accommodate a transitory scenario to full electric mobility. These functions include energy generation, energy transport to the electric vehicles (EV) with a large fleet of autonomous vehicles and low maintenance self-healing roads based on inductive heating. Such a highway based on renewable energy is shown in Fig. 7.1.
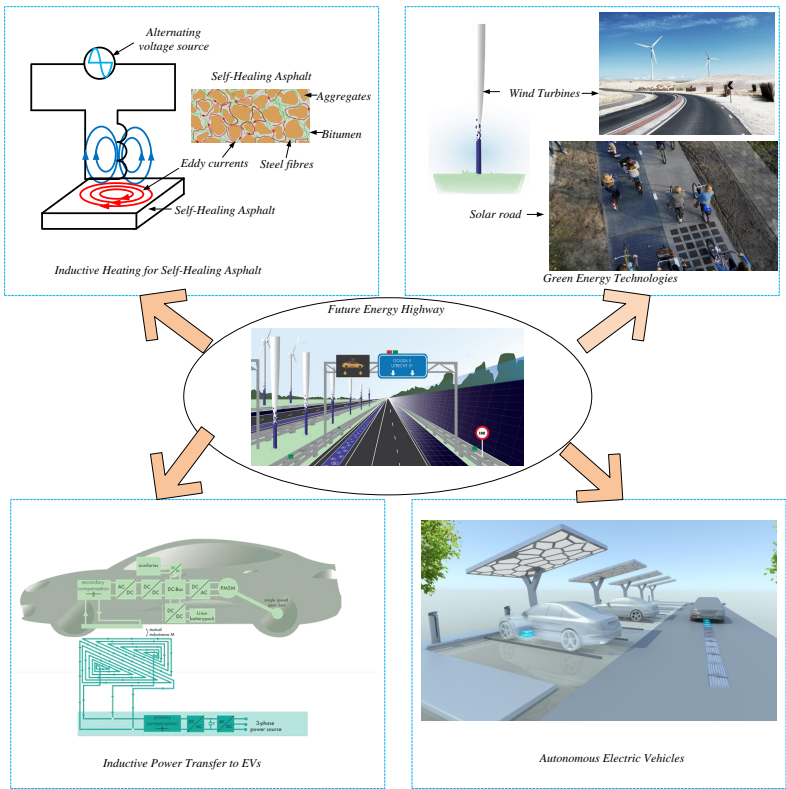
Figure 7.1: Future sustainable energy based highway integrating inductive coils for both inductive power transfer and induction heating, with green energy technologies for (autonomous) electric mobility

The four different technologies that can enable such a vision with power electronics, electromagnetic conversion and material sciences as the framework are:

- Electric Vehicle and More Autonomous Vehicles

- Wireless Inductive Power Transfer (IPT) for EVs
- Renewable Energy Technologies
- Self-Healing Material based low Maintenance Asphalt Roads

While these emerging on-road technologies individually enable a sustainable use of resources and energy towards the ease of introducing e-mobilitheir organic integration with each other presents technical challenges. The research objectives that are addressed in this chapter are:

- Develop a thermal model to estimate the power density required to heat IHA and that can be considered non-detrimental to performance.
- Identifying the possibility of combining IHA based roadway with IPT and determining the increase in operating losses such an infrastructure sharing would incur.
- Establishing the impact of performance in IPT system sandwiching a solar road element and recommending a solution for integrating the two technologies,
- Designing a self-healing highway integrated with on-road dynamic charging and attaining energy neutrality using green resources like solar road, wind turbine and vortex.

7.1.1 Electric Vehicles and More Autonomous Vehicles

Among EU countries, Norway and the Netherlands are front runners in terms of sales of EVs in 2014 [6]. A major goal for the Netherlands is to add a million EVs by 2025 [6]. Another technological progress is the innovation toward autonomy of vehicles. This technology with wireless charging enabled is expected to make full autonomy possible. A description of the autonomy level and its introduction in the market is depicted in Fig. 7.2.
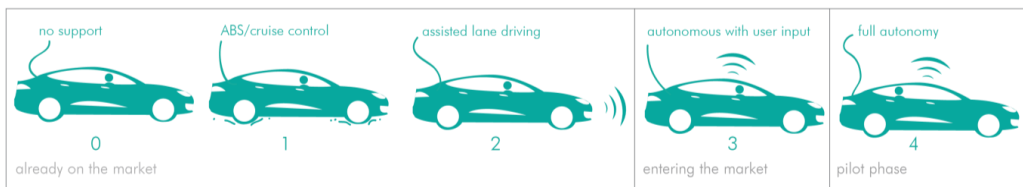
Figure 7.2: The different levels of automation. Level 1 to 3 are available for consumers. Level 4 is still in the test phase and the Dutch law does not allow consumers to drive around in this type of vehicle.

These different levels of autonomy to vehicles are defined by the NHTSA (National Highway Traffic Safety Administration) [15] as:

- Level 1 *Function-Specific Automation*, control function that are specific such as cruise control, lane guidance and automated parallel parking.

- Level 2 *Combined Function Automation*, where multiple function specific control integrated such as adaptive cruise control with lane centering.

- Level 3 *Limited Self-Driving Automation*, where all safety critical functions are automated (steering wheel, throttle, brake). In such an implementation, drivers are not expected to constantly monitor the roadway,

- Level 4 *Full Self-Driving Automation*, all safety critical driving functions are automated and monitoring of roadway is also automated. In such a case, occupants may/may not know driving.

Level 0 is when there exists no autonomy at all. The expectation of automation technology is that in the Netherlands, among various scenarios of technology improvement and policy scenario, the levels of automated vehicles will vary from a conservative and optimistic expectation of 1 and 11% in 2030 and between 7% and 61% in 2050 [16]. In the future, autonomous charging will feature as an important part of autonomy of EVs. This further highlights the role that wireless charging will play in future automotive technologies.

7.2 Combining Self-Healing Roads with IPT

Induction coils used in both self-healing roads and IPT systems is a shared infrastructure and can be utilized for both inductive power transfer and induction healing. However, the various challenges and advantages of such an integration need to be highlighted.

7.2.1 Thermal Modelling of Self-Healing Roads

If a homogeneous asphalt sample is required to be heated from 10 °C to 80 °C in 10 min then the desired heating rate is $\frac{dT}{dt} = 0.133$ K/s. The density of the asphalt is approximately $\rho = 1950$ kg/m^3 and the specific heat capacity is $C_p = 920$ J/(kg K). Therefore the required power density is

$$q = \rho C_p \frac{dT}{dt} = 1950 \times 920 \times 0.133 = 233 \text{ kW/m}^3. \tag{7.1}$$

This is a large power requirement but with limited utilization (once in 4-5 years). Thus, during healing, IPT system can transfer full/partial healing with the rest from external induction coils (currently only external heating is used).

A FEM analysis is performed to compare the estimated rise in temperature with the case when there are conduction and convection losses. The set-up used is shown in Fig. 7.3

and Fig. 7.4. The simulation is performed on a solid slab of asphalt that has a size of 1 m × 1 m × 0.05 m. The slab is surrounded by a concrete hemisphere with a radius of 2 m. The material parameters that are used are listed in Table 7.1. The initial temperature of the setup is 10 °C for all objects. On the spherical boundary of the hemisphere a constant temperature boundary condition of 10 °C is applied. On the entire flat surface a convective heat flux is specified. The convective heat transfer coefficient h_c is approximated with the formula

$$h_c = 7.4 + 6.39 \times W^{0.75}, \tag{7.2}$$

where W is the wind velocity at 2 m above the ground. For a wind velocity of 7 m/s the thermal convection coefficient is $h_c = 34.9$ W/(m² K). The heat source is defined to be homogeneously distributed trough the asphalt with a value of 233 kW/m³.

Material	Density	Specific heat capacity	Thermal conductivity
Asphalt	1950 kg/m³	920 J/(kg K)	1.8 W/(m K)
Concrete	2300 kg/m³	880 J/(kg K)	0.9 W/(m K)

Table 7.1: Material parameters used for the thermal simulation.
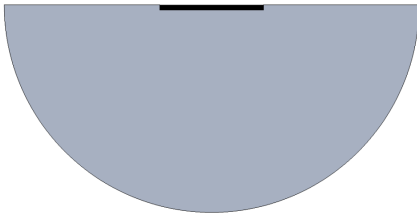
Figure 7.3: Cross section of the setup.
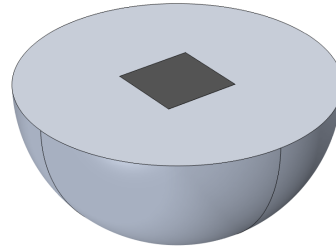
Figure 7.4: Overview of the setup.

The simulation is performed to calculate the temperature transient in the asphalt for the first 30 min of the heating. The temperature is evaluated at three points that are horizontally in the center of the asphalt. The vertical positions are the bottom, where the contact with the concrete is made, in the center and at the top, where the contact with the air is. The temperature transient of the three points is shown in the plot of Fig. 7.5. It can be seen that the center of the asphalt is heated to 80 °C in 620 s, which is very close to the expected 600 s. The top section is heated a bit slower, and takes 940 s to reach the desired temperature. This difference is due to the heat that is lost through the outgoing heat flux of the convection. The bottom part is heated the slowest, because of the conductive losses to the concrete surrounding the asphalt. It takes 1425 s for the bottom part to be heated to a temperature of 80 °C. In a real system the heat source will however not be distributed homogeneously through the whole material. The power dissipated in the asphalt will be higher at the

locations that are closer to the coils, because the flux densities will be higher in those regions. If the coils are located underneath the asphalt this would mean that the heat source near the bottom is higher, which will make the temperature distribution through the asphalt more constant. Inductive healing of the asphalt is expected to be necessary once every 4-5 years. This makes it possible to carefully plan the moment at which the induction heating is applied. In the summer, when the initial temperature is higher and the wind velocity is minimal a better temperature distribution can be achieved.
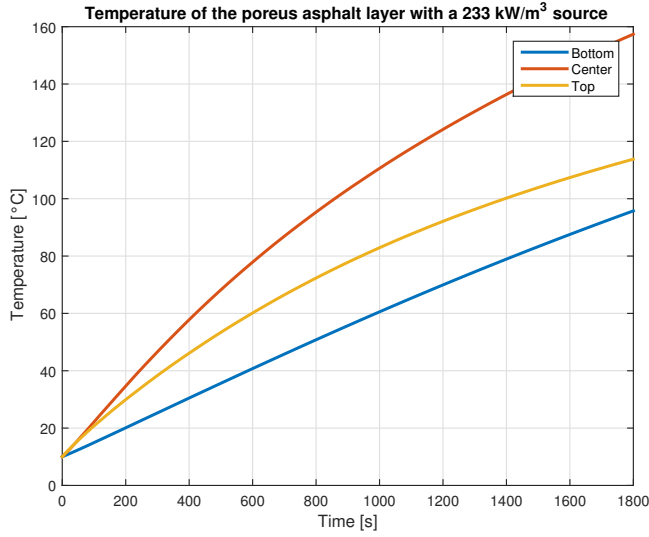
Figure 7.5: Plot of the temperatures of the asphalt.

However, repeated heating of IHA can lead to leakage of bitumen and ravelling of top layer. To estimate this, consider a piece of road of 1 m × 1 m. The thickness x_a of the IHA layer is 0.05 m and underneath the top layer there is a layer of concrete with a thickness x_c of 0.5 m. A heat source Q_{in} uniformly distributed in the IHA layer is considered. The steady state thermal behavior can be described using a thermal circuit as shown in Fig. 7.6. The thermal resistances of the asphalt and the concrete can be calculated using the respective thickness, the thermal conductivity $k_a = 1.8\,\mathrm{W/(m\,K)}$, $k_c = 0.9\,\mathrm{W/(m\,K)}$ and the area A as

$$R_a = \frac{x_a}{Ak_a}$$
$$R_c = \frac{x_c}{Ak_c} \tag{7.3}$$

The thermal resistance from asphalt to concrete is approximated to be one half of the total resistance of the asphalt, because the heat source is distributed uniformly. The bottom of

the concrete is assumed to have a constant temperature equal to the ambient temperature. There is also a thermal resistance R_{am} from the top of the asphalt to the ambient, related to the convection coefficient h_c and area A as

$$R_{am} = \frac{1}{Ah_c} \tag{7.4}$$
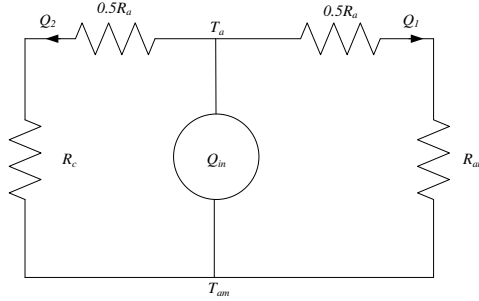
Figure 7.6: Thermal circuit describing the steady state temperatures of a highway that is considered to be combination of a top layer of IHA and bottom layer of concrete.

The expression for the temperature difference between the asphalt and the ambient based on the thermal circuit is

$$T_{asphalt} = \frac{\left(\frac{1}{2}R_a + R_c\right)\left(\frac{1}{2}R_a + R_{am}\right)}{R_a + R_c + R_{am}} Q_{in}. \tag{7.5}$$

This temperature difference is independent on the area A that is used. Therefore it is a useful characteristic for a highway where the thickness of the layers are defined. To set an upper limit for permissible heating of IHA, temperature difference between the ambient and the asphalt is set to be 5 °C then power density q_{in} in the IHA layer is

$$Q_{in,max} = \frac{R_a + R_c + R_{am}}{\left(\frac{1}{2}R_a + R_c\right)\left(\frac{1}{2}R_a + R_{am}\right)} T_{a,max} [\text{W}]$$

$$q_{in,max} = \frac{Q_{in,max}}{Ax_a} [\text{W/m}^3] \tag{7.6}$$

$$= 2.38 \text{ kW/m}^3$$

7.2.2 Transformer Loss Model

In case of an IPT system, to transfer a large amount of power efficiently, capacitive compensation is carried out in both the primary and secondary. This technique nullifies reactive

power and enhances power delivered to a load. Many combinations of capacitors in series and parallel yield several IPT compensation topologies. Due to a lack of standard coil definitions for EV IPT studies thus far, researchers build coils of various shapes and sizes that suite their requirements. Hence, to obtain specific results in all experimentation, the authors have considered coupling coefficient (dimensionless parameter) as the base metric and all derived parameters such as power and efficiency are valid for the coupling range considered in the respective experiments. The advantage of this choice is the fact that such a coupling range can be obtained for multiple charge-pads and the derived parameters are accurate for all such combinations. A combined IPT and IHA system will have additional losses inside the asphalt due to the alternating magnetic field, which is represented in the equivalent circuit as a series resistance as shown in Fig. 7.7.
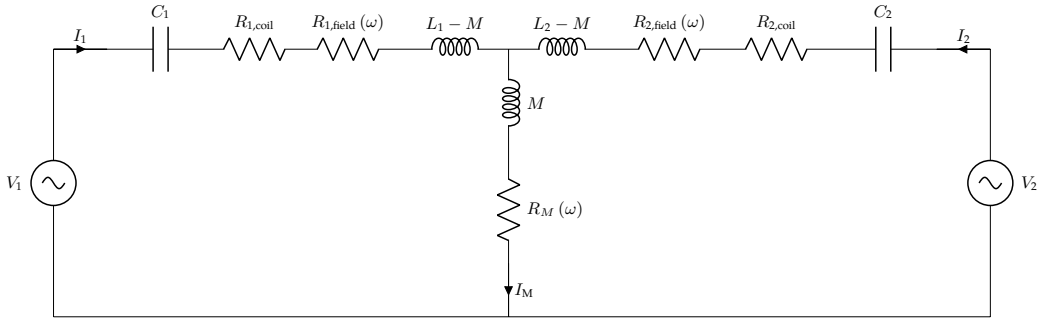
Figure 7.7: Equivalent circuit of an IPT system including associated IHA losses. Series capacitors are shown as an illustration of reactive power compensation.

Herein, the resistances $R_{1,\text{field}}(\omega)$ and $R_{2,\text{field}}(\omega)$ represent the frequency dependent induced losses inside the asphalt due to the fields created by the primary and secondary coils respectively, while resistance R_{M} represents the losses that are due to the combined field of the primary and secondary coils.

The linear system is mathematically represented by (7.7),

$$[v] = \begin{bmatrix} R_1(\omega) & R_{\text{M}}(\omega) \\ R_{\text{M}}(\omega) & R_2(\omega) \end{bmatrix} [i] + j\omega \begin{bmatrix} L_1 & M \\ M & L_2 \end{bmatrix} [i] \tag{7.7}$$

Where, L_1 and L_2 are self inductances of the primary and secondary coils, with M as mutual inductance respectively and the corresponding resistances R_1 and R_2, related to the dc coil resistances $(R_{1,\text{coil}}, R_{2,\text{coil}})$ and given by (7.8),

$$R_1(\omega) = R_{1,\text{coil}} + R_{1,\text{field}}(\omega)$$
$$R_2(\omega) = R_{2,coil} + R_{2,\text{field}}(\omega) \tag{7.8}$$

System Performance

In order to compare the IPT system performance with and without IHA, the maximum possible efficiency η_{max} and the coupling factor k are used. The uncompensated power transfer (without capacitors) is used in this chapter to decouple the power transfer from different types of compensation that can be used. Furthermore, the addition of compensation only scales the uncompensated power by the loaded quality factor of the secondary further justifying the use of uncompensated power as a system parameter. The η_{max} is derived from the maximum output apparent uncompensated power $S_{out,max}$ following the same logical evolution in [20] and is given by (7.9),

$$S_{out,max} = v_{out,oc} \times i_{out,sc}^* \tag{7.9}$$

where, $v_{out,oc}$ is the open circuit output voltage and $i_{out,sc}$ is the short circuit output current. Now, the expression for $S_{out,max}$ is derived and given by (7.10)

$$v_{out,oc} = (R_M + j\omega M)i_1$$
$$i_{out,sc} = \frac{(R_M + j\omega M)}{R_2}i_1 \tag{7.10}$$
$$S_{out,max} = \frac{R_M^2 + \omega^2 M^2}{R_2}i_1^2$$

The maximum output power is related to this uncompensated apparent power as, $P_{out,max} = S_{out,max}$. Also, the input power that drives this output is given by (7.11).

$$P_{in,min} = R_1 i_1^2 + P_{out,max} \tag{7.11}$$

From (7.10) and (7.11), maximum efficiency can be derived as (7.12),

$$\eta_{max} = \frac{R_M^2 + \omega^2 M^2}{R_1 R_2 + R_M^2 + \omega^2 M^2}. \tag{7.12}$$

7.2.3   Numerical Analysis

FEM analysis of a combined IPT and IHA system is performed 2D with axis-symmetry in Comsol Multiphysics 5.1 over a range of frequencies from 1 kHz to 1 MHz. The geometry that is used has a circular primary coil of 26 turns with a wire diameter of 2.24 mm, an inner radius of 37 mm and an outer radius of 105 mm. The secondary is a circular coil of 16 turns with a wire radius of 1.1 mm, an inner radius of 12 mm and an outer radius of 53 mm. These dimensions are chosen to make a scaled down laboratory experimental setup that can be used with the sample of IHA made available. The vertical offset between the primary and the asphalt layer is 5 mm, and the offset between the asphalt and the secondary is 20 mm. The radius of the asphalt layer is 250 mm and the layer is 45 mm thick. The numerical model developed is shown in Fig. 7.8.
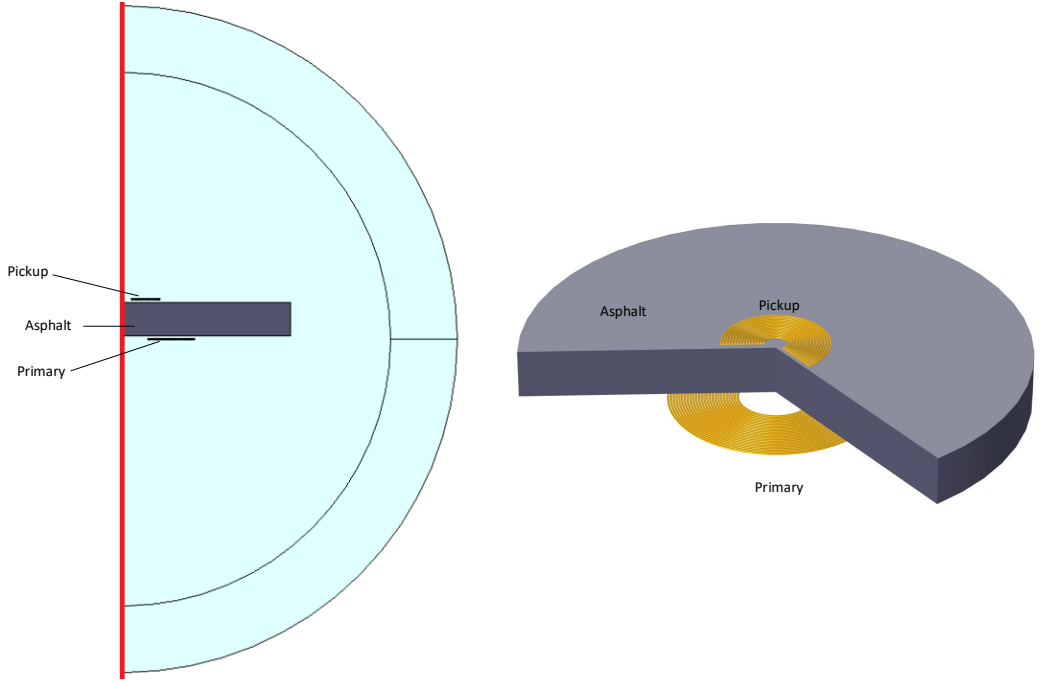
Figure 7.8: Developed 2D axis-symmetrical model and a 3D overview model of the combined IPT and IHA system.

Parameter Extraction

The parameters for the equivalent circuit of Fig. 7.7 are extracted from the results of the FEM analysis. For each coil the parameters are extracted using the coils emfs $[e]$, coil currents $[i]$ and power P from the simulations. The induced emf in the coils is given by

$$[e] = j\omega \begin{bmatrix} L_1 & M \\ M & L_2 \end{bmatrix} [i] \tag{7.13}$$

First, the self-inductance of the primary coil L_1 is calculated by exciting the coil while the secondary is simulated as an open circuit. The emf becomes

$$\begin{bmatrix} e_1 \\ e_2 \end{bmatrix} = j\omega \begin{bmatrix} L_1 & M \\ M & L_2 \end{bmatrix} \begin{bmatrix} i_1 \\ 0 \end{bmatrix}, \tag{7.14}$$

from this, L_1 can be calculated as

$$L_1 = \frac{e_1}{j\omega i_1}. \tag{7.15}$$

In the same way, the inductance of the secondary coil can be calculated. Now, to obtain the mutual inductance, the secondary coil is simulated as a short circuit while the primary is excited. Using the previously calculated self inductance L_1 and the current through secondary i_2, an expression for the mutual inductance $M = k\sqrt{(L_1 L_2)}$ can be derived as

$$e_1 = j\omega L_1 i_1 + j\omega M i_2$$
$$M = \frac{e_1 - j\omega L_1 i_1}{j\omega i_2}. \tag{7.16}$$

Also, the percent reduction in power transferred between the coils due to the addition of IHA to IPT system is obtained in terms of coupling with IHA k_{IHA} and without IHA, k as

$$\Delta P \% = \left[1 - \left(\frac{k_{IHA}}{k} \right)^2 \right] \tag{7.17}$$

Results

From the numerical analysis, the circuit parameters are extracted and the performance of the system is analyzed with maximum power transfer and the magnetic coupling factor. The combined IPT and IHA system is compared with an air core system in Fig. 7.9. The frequency of interest - 85 kHz which is earmarked in the upcoming standard SAE J2954 for roadway IPT EV systems. At 85 kHz, the maximum efficiency of the combined system drops to 93 %. It can also be seen that the coupling factor is lower than that of air-cored coils and start decreasing rapidly from 100 kHz. The coupling regime for the experimental IPT system is $k = 0.113$ and IHA sample volume is $8.84 \times 10^{-3} m^3$. The coupling is now reduced to $k_{IHA} = 0.107$. This results in a reduction of power transferred by 10.3% from (7.17).

7.2.4 Experimental Verification

The numerical results developed previously are verified with an experimental setup. The circuit parameters are measured with the Agilent 4294A Precision Impedance Analyzer. The geometry is the same as the system analyzed in the numerical evaluation, except that sample of asphalt that was used is a square with sides of 200 mm. Therefore the numerical analysis is performed again with an asphalt layer radius of 113 mm, such that the volume of the cylindrical slab from the numerical evaluation is conserved as that of the experimental square block.
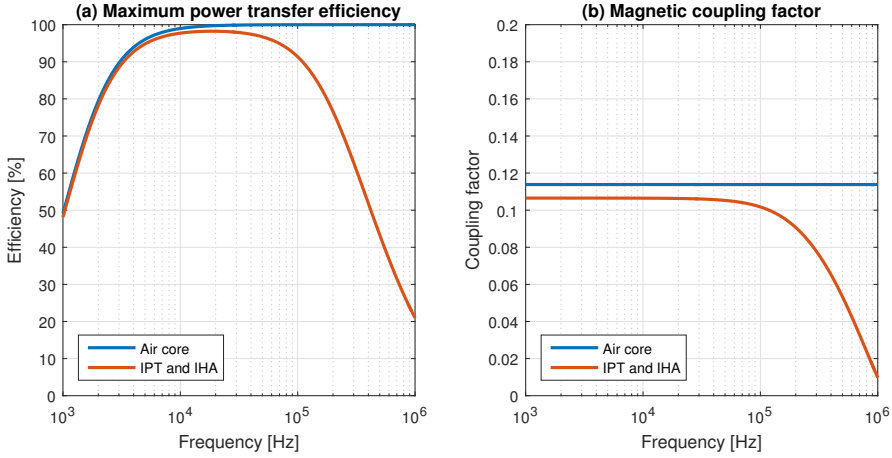
Figure 7.9: Performance of a combined IPT and IHA system compared with an air core system. (a) shows the maximum efficiency from the primary to the secondary and (b) shows the magnetic coupling factor between the primary and secondary.

Parameter Extraction

The circuit parameters are measured for a frequency range of 1 kHz to 1 MHz. For the mutual parameters, the primary and secondary coil are connected in series with a constructive flux addition (flux aiding). The measured impedance is then

$$Z_c = (R_1 + R_2 + 2R_M) + j\omega(L_1 + L_2 + 2M). \tag{7.18}$$

The measured impedance in destructive flux superposition is

$$Z_d = (R_1 + R_2 - 2R_M) + j\omega(L_1 + L_2 - 2M). \tag{7.19}$$

The mutual parameters can now be calculated as

$$Z_m = \frac{Z_c - Z_d}{4} = R_M + j\omega M. \tag{7.20}$$

Results

The measured circuit parameters are presented together with the numerical results in Fig. 7.11. The inductance values, and the simulations agree with the experimental results as shown in Fig. 7.11 (a). The small difference observed is due to interconnection wires leading to the impedance analyzer and minor differences between the real and the simulated coils.
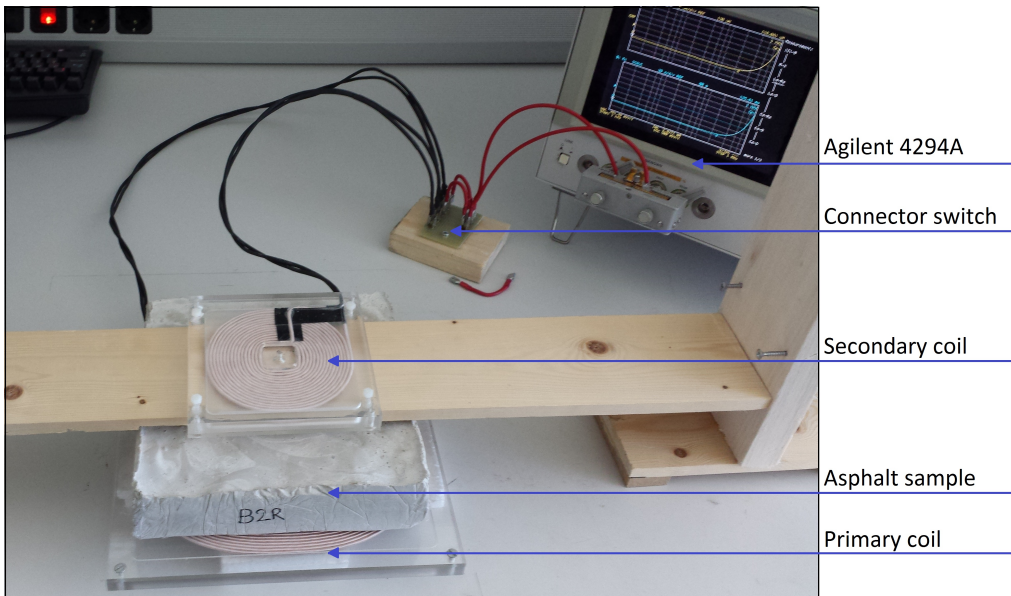
Figure 7.10: Overview of the setup of the measurement

The resistance values are presented in Fig. 7.11 (b). In the experimental system, the coil losses are higher and is variable with frequency. The frequency dependence is because of skin effect and proximity effect in the coils and due to stray fields (conductive parts below the table of the setup). The field losses due to the asphalt sample is calculated by subtracting the air core system resistances from the resistances measured with the asphalt sample in between. For the low frequency values, the expected losses are less than the accuracy (the limited resolution of the impedance analyzer), thus they do not match exactly with the simulations. From 20 kHz, the losses are accurately measured with the result that field losses are consistent with simulations. There is a minor offset noticeable, and this is due to the square geometry of experimental asphalt and cylindrical geometry of simulation.

Discussion

From the numerical analysis that was performed it is clear there will be a reduction in efficiency and power transferred when IPT is combined with IHA. The reduction in efficiency and power transferred by about 10 % in the coupling regime of $k = 0.113$ at 85 kHz can be a problem when the system operates at high power. This can lead to unintended asphalt heating. A further challenge is that the additional leakage in the system (due to IHA) can lead to variable tuning requirements for reactive power compensation. Further research is being carried out in material selection of IHA for asphalt roads wherein the healing process
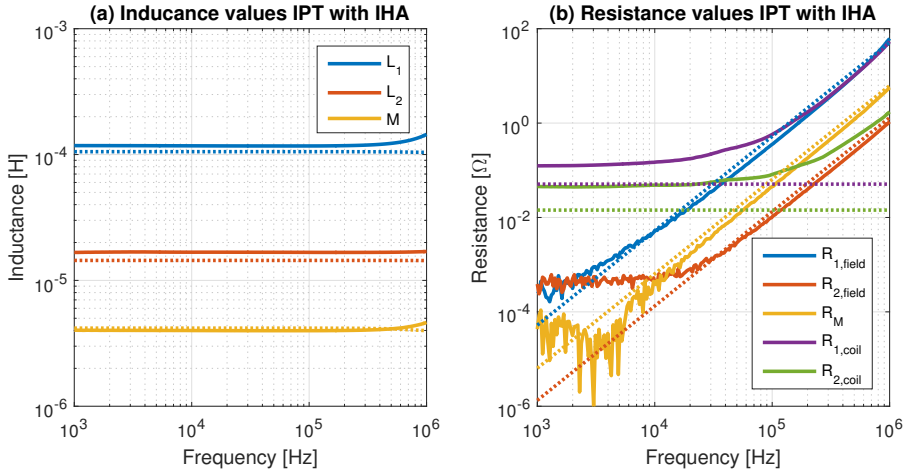
Figure 7.11: Measured circuit parameter values (solid line) plotted with respect to frequency and compared with the numerical results (dotted line).

doesn't impact IPT while it serves IHA when required. This decoupling is beyond the scope of this thesis. Importantly, accurate modelling of the system is carried out.

7.2.5 Renewable Energy Technologies

In the Netherlands, solar and wind energy are considered the major sources for highway based energy generation [9]. While conventional technologies can be installed, in this chapter, two revolutionary technologies that have vast untapped potential is considered:

- Bladeless Vortex [186]
- SolaRoads [187]

Bladeless Vortex

Bladeless vortex is a Spanish technology startup that produces turbines without blades that harness the *'vorticity'* of wind through the fibre glass and carbon fibre cylindrical structure [186]. Thus, the structure uses shear force of the wind that when falling onto the structure creates *eddies* [188]. This reciprocation is converted into electrical energy by cutting a magnetic field produced by magnets in the base. Due to the lack of blades, it has no friction and has no gears and hence reduced maintenance. Also, it is considerably cheaper. A figure showing a prototype of the same (Vortex Mini) and its performance characteristics is presented in Fig. 7.12 [186].
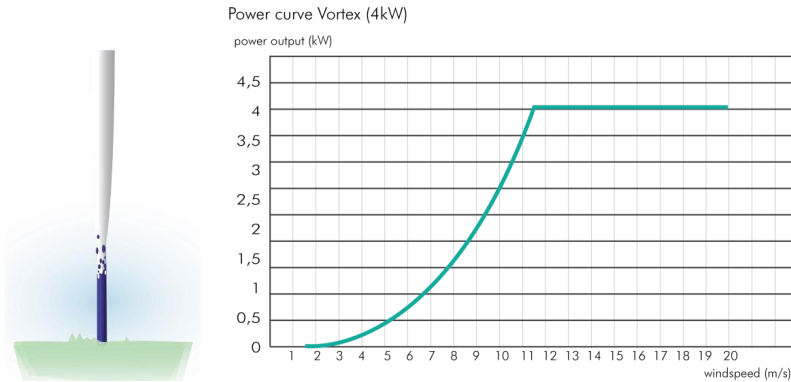
Figure 7.12: A 4-kW Vortex and its power-velocity profile, this turbine has a minimum safety distance of 13m from each other [186].

Some disadvantages of this technology include low efficiency, low power outputs thus far, viability for scaling up (stability of structure) and noise. However, the technology due to its cost-effective nature is a good solution for highways. This also considering places where land is limited for large sized classical propeller turbines due to existing infrastructure.

Solaroads

Solaroads is a Dutch innovation (TNO, Provence of Noord-Holland, Dynniq and Ooms Civiel) in which prefabricated concrete modules are laid on the ground [187]. On top of this, a layer of tempered glass that is translucent to light is used to absorb light and convert to electricity using crystalline silicon solar cells. A detailed analysis of Solaroads has been carried out in [189]. The maximum module efficiency attained from the study is 9.69%. Some important performance parameters are presented in Fig. 7.13.
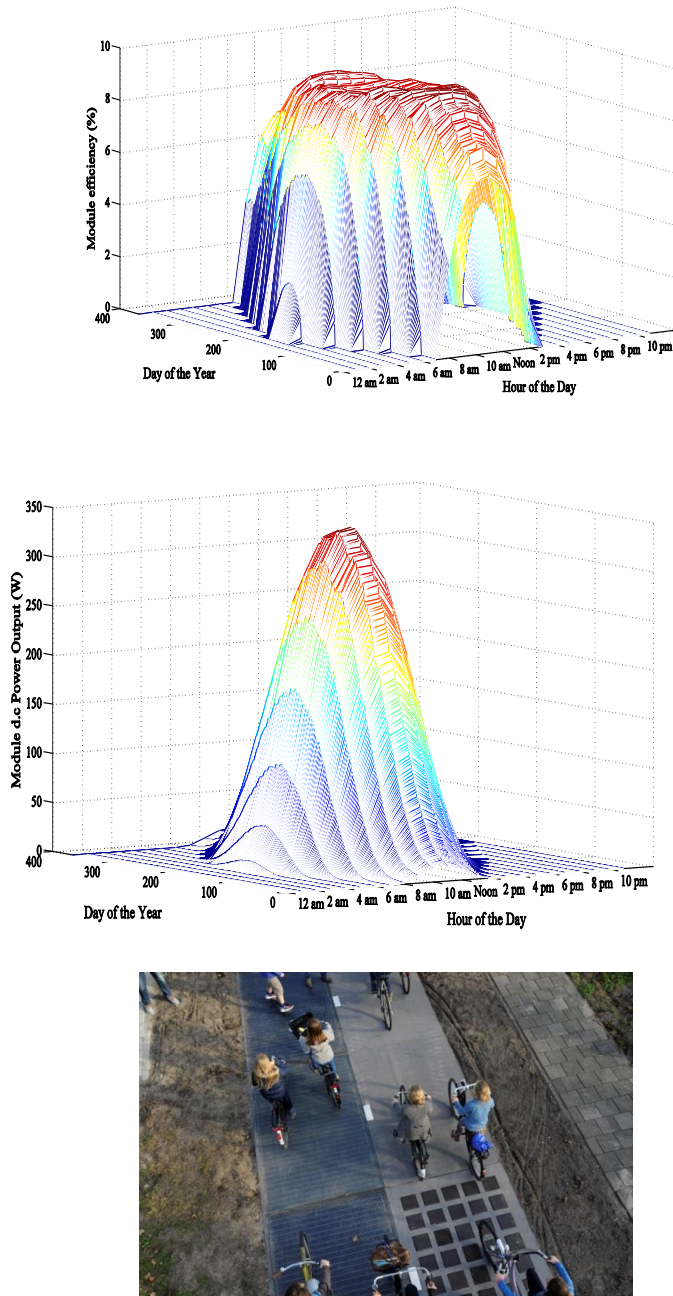
Figure 7.13: Estimated Operating Efficiency of the Solar Road in Year 2015, estimated dc power output in the same year and installed Solaroads in the bike lane in the village of Krommenie, North Holland [189].

7.3   Integration of Solar Roads with IPT Charging

The integrated system consists of an IPT system with solar road sand witched in between. In order to obtain empirical understanding of the magnetic coupling between IPT coils sandwiching a solar road element in between, a lab scale prototype is tested.
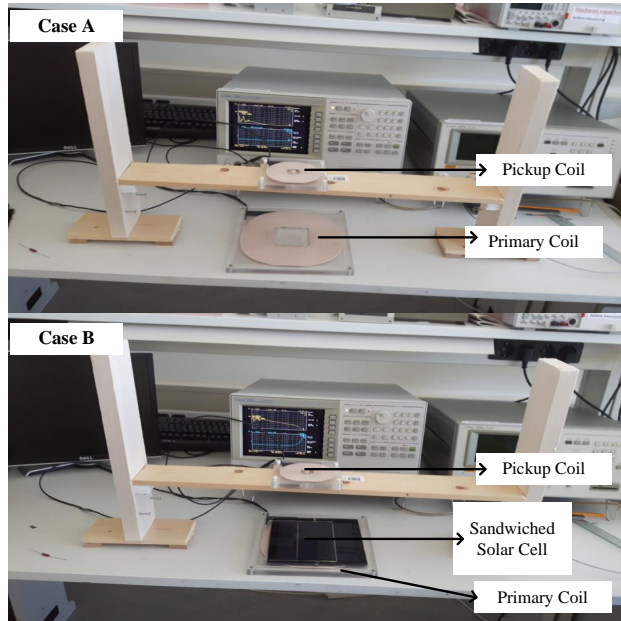
Figure 7.14: Experiemental setup for solar road element in combination with IPT charging coils

Fig. 7.14 shows the experimental setup of the IPT coils with 17 cm air gap, Case (a) without solar cell in between, Case (b) with SR in between. Measurements for mutual inductance are conducted on IPT coils, first without, then with the solar cell following the methodology presented in Section 7.2.4. The frequency dependant mutual inductance is calculated from the measured values using (7.20) and converted to coupling. Fig. 7.15 shows the measured coupling between the IPT coils for different operating frequencies for each case.

It is observed the coupling starts decreasing linearly after 10 kHz on a logarithmic frequency scale. Considering that the desired operating frequency of the IPT system would be around 85 kHz, this decrease in coupling of $\approx 50\%$ leads to reduction in efficiency as well as cost of charging infrastructure for the same power level. For frequencies higher than 10 kHz, the decrease in mutual inductance is hypothesized due to the eddy currents in the conductive parts of the solar road element. Specifically, in the frequency range of 85 kHz, the coupling
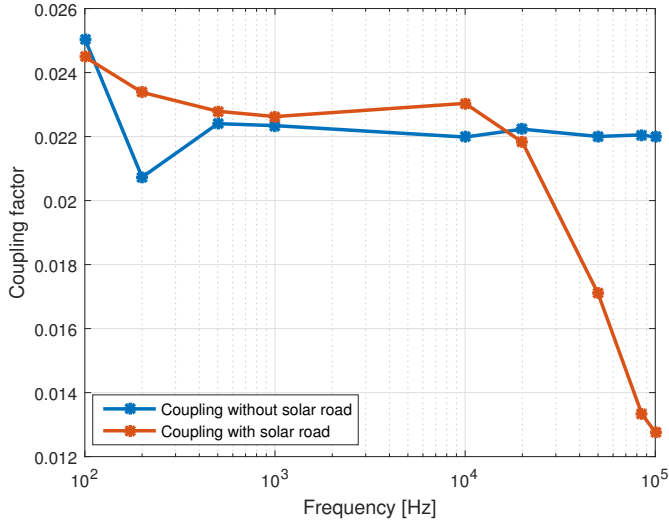
Figure 7.15: Measured coupling and frequency with the introduction of solar road element. As the frequency increases beyond 10 kHz, the eddy currents begin to dominate and coupling decays exponentially in case of solar road.

of the coils fall from $k = 0.022$ to $k = 0.0135$, this results in a reduction in power transfer by 62.3%. This translates to a large reduction in efficiency also.

To prove the validity of these inferences, numerical FEM analysis is carried out using COMSOL and the model developed is shown in Fig. 7.16. Both the coils are of 50 turns each with an air gap of 17 cm and radius of 0.5 m. The primary coil is energized with 1 A current for frequencies 1 Hz, 100 Hz, 1 kHz, 10 kHz and 100 kHz. In the simulations, a thicker 10 mm aluminium back surface is considered for the solar cell for adequate computational capability and removing the influence of skin effect, which come into effect at frequencies lower that 10 kHz. This frequency range is much lower than the operational regime of the IPT system.

Each solar cell is of 156x156 mm^2. A side view of the model is shown in Fig. 7.16 (b). The eddy currents will be generated mainly in the metallic back contact of the solar cell. 10 mm thick aluminium layer is defined while the semiconductor layers are neglected in the analysis (due to several order lower conductivity). The surface plot of induced eddy currents in the solar road when primary IPT coil is excited with 1 A current at 50 Hz is shown as an example in Fig. 7.17.

The red arrows depict the coil current direction while the black arrows show the direction of opposing induced currents. Apart from eddy current, a frequency dependant decrease
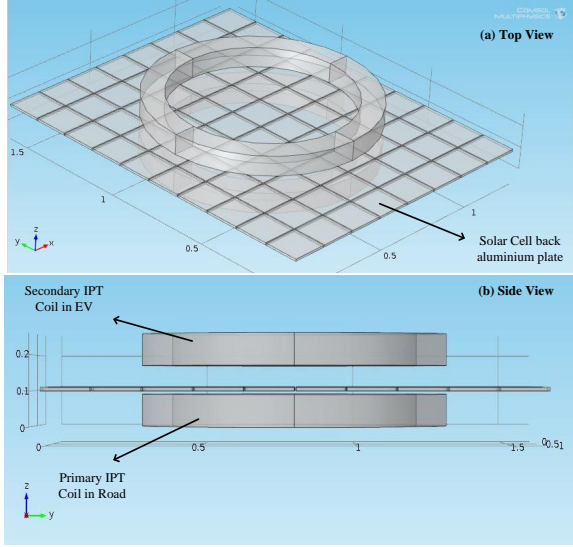
Figure 7.16: COMSOL model for validating the inferences of the experimental results.
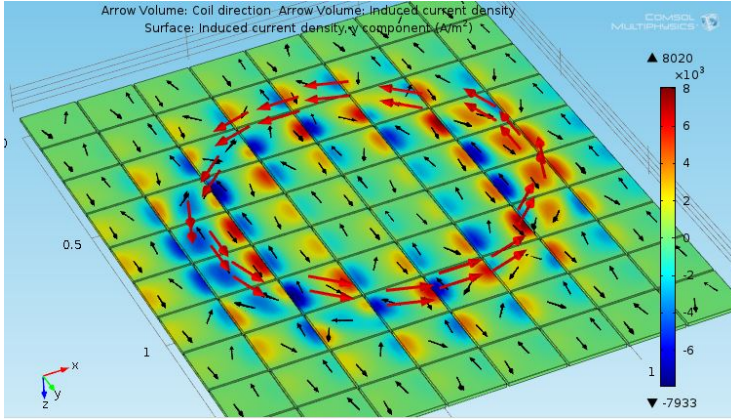
Figure 7.17: Eddy currents induced in the solar road at 50 Hz.

in the mutual inductance is observed. The mutual inductance between the IPT coils is calculated using (7.21).

$$M = \left(\frac{N_{\text{primary}}}{N_{\text{pickup}}} \right) \left(\frac{v_{\text{pickup}}}{j\omega i_{\text{primary}}} \right) \tag{7.21}$$

In the model, the primary and pick up turns are 50, while the induced voltage in the pickup

coil (v_{pickup}) is simulated for different frequencies. The mutual inductance for different operating frequencies of IPT system with and without solar cell in between is shown in Fig. 7.18.
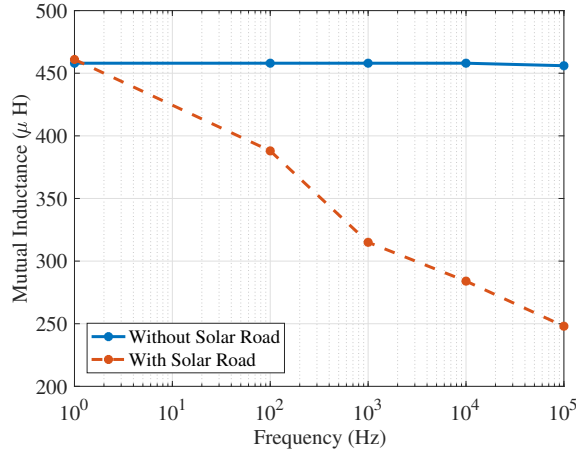
Figure 7.18: Decreasing mutual inductance between IPT coils as a function of operating frequency in the finite element model.

It can be observed that at the operating frequency increases, the mutual inductance decreases. The thickness of aluminium back contact is taken as 10 mm in this simulation. In actual practice, the solar road itself, and hence its back contact is a fraction of this thickness. Therefore, mutual inductance would start reducing only after 10 kHz due to skin effect, which plays a positive role in our application, as observed in experimental results of Fig. 7.15. Nevertheless, skin effect is not effective in limiting the eddy currents for IPT operating freqncies of 85-100 kHz. Therefore, the power transfer capability significantly reduces with lower mutual coupling. Further, the efficiency of IPT operation drops due to heating losses in the solar cell back contact due to these eddy currents.

7.3.1 Discussion

Based of the understanding derived from the theoretical and experimental study in this section, the following conclusions are drawn:

- It is recommended that the solar road be installed at the emergency lane of the highway. Not only will this avoid proximity with the on-road IPT charging, but also reduce dynamic shading of solar cell by passing vehicles. Also, emergency lanes usually have low occupancy and now, energy utilization is made feasible.

- If dynamic IPT charging is not required for complete highways coverage [191], a Mosaic on-road space sharing design instead of sandwiched structure can be used.
- From solar cell design point of view, an ultra-thin or meshed instead of sheet of metallic back contact could reduce the eddy current. Smaller unit cells could also be advantageous. However, these possibilities and their consequences on the solar road performance are beyond the scope of this chapter.

7.4 Case-study of a Future Highway

For the design and estimation of the economics of the future highway with IPT, green energy, solar road and self-healing properties, the A12 motorway in Netherlands is used as a test case, shown in Fig. 7.19. A12 highway is 165 km and connects the city of Hague and Arnhem in Netherlands. For the design, a Nissan Leaf EV with 24 kWh battery pack is used as a reference and is assumed that the battery has a 85 % efficiency. Such a EV represents a worst-case scenario for driving range due to its limited battery capacity as compared to EV with much larger battery pack like the Tesla Model S with 85 kWh.

Figure 7.19: A12 highway between Den Haag and Arnhem with IPT system installed over two sections - Part A for 20km and Part B for 30 km.

7.4.1 Design of IPT system for A12

Of the total 165 km, it is assumed that the EV drives 10 km each at the beginning and end of the highway in the urban areas at 60 km/h and the remaining 145 km at the speed limit

of 120 km/h. The dynamics of the EV driving are simulated based on the model in [190]. The power demanded by the EV for driving is dependent on the speed of the EV. This can be linearly estimated as 5.6 kW when driving at a speed of 60 km/h and goes upto 24.1 kW for 120 km/h speed. Based on this, it has been estimated that the required energy for the Leaf to cover 165 km is 31 kWh [185]. This value is higher than the 24 kWh capacity of the Leaf even if it is assumed that the EV begins at 100 % SOC and ends the journey at 0 % SOC, which never occurs practically.

In order to ensure that the EV is able to comfortably complete the journey without having to stop, the IPT system is used to charge it en-route. The motive of the IPT system is that if an EV begins the journey with 80 % SOC, it must complete the trip along A12 with at least a SOC of 20 %. This corresponds to using $24\,\text{kWh} \times (80\,\% - 20\,\%) \times 85\,\% = 12.2\,\text{kWh}$ of the EV battery at 85% round trip efficiency. The remaining (31-12.2)=18.8 kWh has to be supplied by the IPT. To achieve this, a 50 kW IPT system with 85 % efficiency is used. To meet the energy demand, the IPT system has to be installed over a length of 50 km[185]. This IPT is assumed to be installed in the busiest parts of the highway indicated as A and B in Fig. 7.19.

The SOC of battery along the highway as the EV drives from Hague to Arnhem is shown in Fig 7.20. Without an IPT system, the SOC reduces from 80 % and EV runs out of energy by the time it has crossed 96 km. With the IPT system, the EV is able to fulfill the full length of 165 km with an SOC of 20-25 % remaining. If the EV travels at an average speed lower than 120 km/h which happens most of the time in practice, then it finishes the journey with a higher SOC as shown in Fig 7.20 for speeds of 110 km/h and 100 km/h. This demonstrates the effectiveness of using IPT for on-road charging of EVs.

7.4.2 Powering the IPT System using Renewables

In 2030, 2.3 million EV are expected in the Netherlands which comprises about 40 % of all cars. For calculations on the power demand, it is assumed that 10 % of all EV will charge while driving using the IPT system. The combined power demand of the EV per hour for a round trip on A12 is shown in Fig. 7.21. The peak demand reaches 18 MW in the evening while the lowest demand is less than 1 MW in the early mornings.

To have a truly sustainable IPT system, this energy required by the EV must be powered from renewable sources. This can be achieved by the use of solar roads, wind turbines and vortex turbines along the A12 highway. Since there is variability in the renewable generation on a diurnal and seasonal basis, the motive here would be to supply the energy required by the IPT system on yearly basis an energy neutral manner. This means the grid is used as an energy buffer to manage the variability in generation.

The total length of these lanes on the A12 is 114 km. The surface of this lane on both sides of the road which can generate solar energy is $2 \times 114 km \times 3.5\text{m} = 0.798\,km^2$. The efficiency of the solar road is 9.69 % [189]. The energy that can be generated per day using the solar
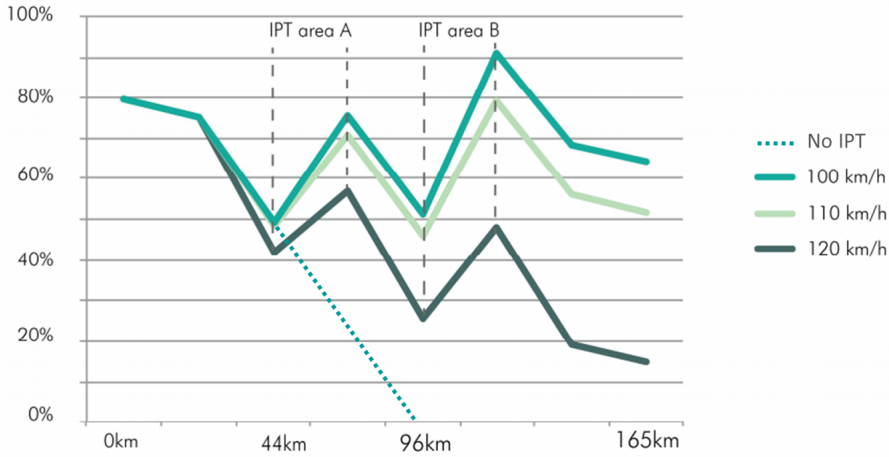
Figure 7.20: The SOC of the battery along the A12 highway for different driving speeds. The average speed for urban driving remained the same for all three situations. A driving speed of 100 km/h is more energy efficient.
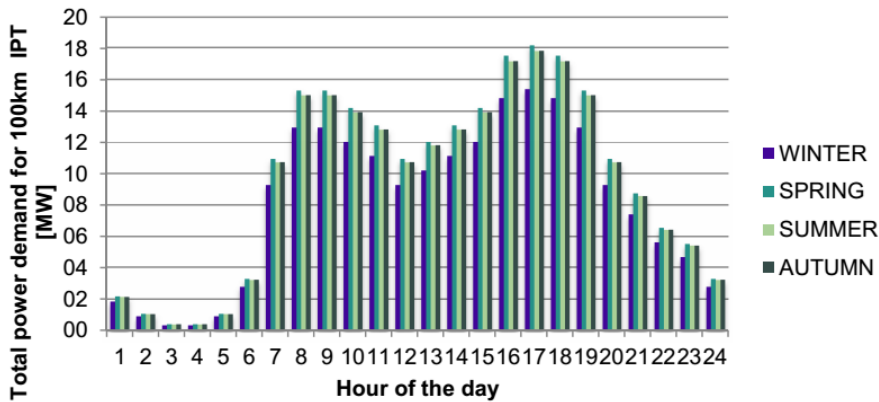
Figure 7.21: Seasonal dependence of power demand of IPT powered EVs per hour for a round trip on A12.

road for different months of the year has been estimated and shown in Fig. 7.22. It can be seen that the energy generation varies from 350 MWh in summer to 50 MWh in winter. The 114 km solar road can provide for 95 % of the energy requirements of the IPT over the year with a surface of $0.789\,km^2$.

For harnessing wind power, two types of wind turbines are considered. First is a 2 MW
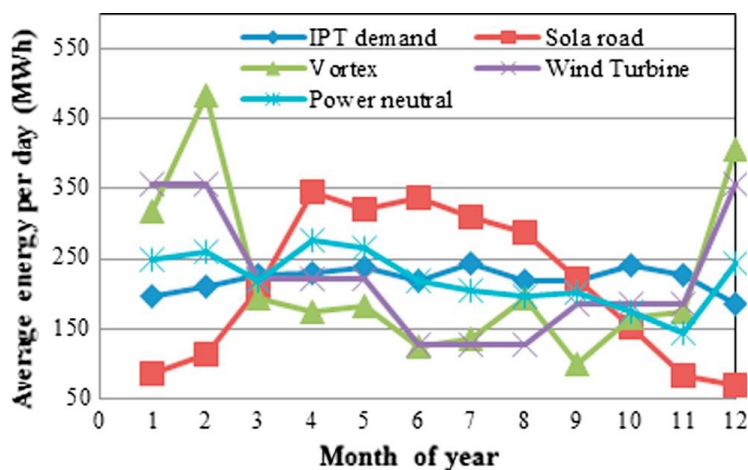
Figure 7.22: Calculated average energy generated per day by renewables to power the IPT system on A12. Both emergency lanes are replaced with a solar road and wind turbines and vortex are used to extract power from the wind.

Table 7.2: Energy Mix for Powering the IPT using Renewables

Case	Vortex	WT	SR	Energy Neut.
	4 kW	2 MW	%	%
SR	0	0	100	95.5
Vortex	14860	0	0	100
WT	0	107	0	100
SR+Vortex	7775	0	50	100
SR+WT	0	56	50	100
Power Neutral	0	64	42	100

conventional wind turbines with a minimum speed of 4 m/s. Second, a 4 kW Vortex mini wind turbines operating at a rated speed of 12 m/s and minimum speed of 2 m/s. The wind generation trend is opposite to solar road showing higher generation in winter and lesser in summer as shown in Fig 7.22. A more detailed modelling methodology is presented in [185].

Based on the operating characteristics of the two turbines and meteorological data from the KNMI, 14860 vortex or 107 wind turbines would be required to produce enough energy to 100 % match with the energy requirements of the IPT as shown in Fig 7.22 and Table 7.2. In [193], it is obtained that a 40 %-60 % combination of solar and wind is most ideal in achieving power neutral generation in Netherlands where the higher generation of solar in

summer and in the day is balanced by the higher generation of wind in the night and in winter. It can be seen in Fig. 7.22, that the combination of wind and solar gives a generation that closely follows the IPT demand for different months of the year. However, it is important to mention that vortex is an early stage innovation with little field testing.

7.5   Conclusion

In this chapter, functional integration of different elements of future highways has been analyzed, along with a system level study of a real-highway implementation in the Netherlands. A number of results were obtained from this study:

- Sharing of infrastructure for both IPT and IHA is important for future highways. A thermal model with power density for healing and maximum permissible limit to prevent ravelling is proposed. A loss model that integrates eddy current losses by utilizing frequency dependent resistances is included in this chapter. The challenge in this integration is that up to a frequency of 100 kHz, the magnetic efficiency and power transfer of IPT systems drops to 90% in the coupling regime of $k = 0.113$. Thus, direct integration can be lossy.

- Solar roads and IPT system, placed closeby would result in lower transmission losses due to in-situ energy generation and utilization. A sandwich approach couldn't work due to eddy currents induced in the backplates of the solar roads. The coupling declined to $k = 0.0135$, a reduction of 38.6% at operation close to 85 kHz. This results in a reduction in effective power transfer of 62.3%. It was therefore considered to use emergency lanes of roads for solaroads operation.

- It is possible for a Nissan LEAF to complete its trip 80% - 25% SOC along A12 by on-road IPT system. The total IPT coverage (IPT efficiency = 85%) in this highway is 30.3%. This corresponds to a distance of 50 km in a highway of total length 165 km.

- In the Netherlands, due to the complementary distribution of wind-solar profiles (peaks in winter and summer respectively), the choice of solar and wind technologies must match with the overall availability of renewable energy. While vortex is cost-effective, it is still an experimental technology and hence an optimal mix of technologies would be the best techno-economic scenario.

CHAPTER 8

Conclusion

The primary goal of this thesis was to analyze and apply magnetic fields for energy transfer and self-healing roads. The thesis is focused on IPT systems for EV applications as one of the backbone technology in the transition from polluting carbon based transportation to electric. Analytical modelling and FEM based optimization with experimental validation of IPT systems is carried out. Several infrastructure changes including highway based green energy technologies and maintenance-free inductive roads are considered as a complementary development for this transition. Finally, economical evaluation of IPT system by taking a real life case scenario of a highway in Netherlands with electric buses is performed. The research goals with which this work began is briefly restated here:

- To identify magnetic field analysis techniques that can be used to design charge-pads.
- Perform comprehensive comparison of charge-pad concepts with variable coupler shapes.
- Model and analyze the problem of misalignment in distributed IPT systems.
- Perform a multi-objective optimization and build a lab-scale demonstrator, with validation of power transfer and magnetic models.
- Study the economic implications of IPT based energy transfer systems.
- Model the concept of inductive healing asphalt and to study the trade-offs and interdependencies in a combined technology roadway.

In the next paragraphs, the important results obtained from the thesis are listed. Here, research goals as originally envisioned are revisited. This comparison is performed to analyze the results obtained also in conjecture with the original goals of the thesis. Constructive results obtained are highlighted along with some drawbacks which open room for improvement and they are further captured in future work recommendations.

In Chapter 2, the analytical and semi-analytical coil design techniques are reviewed. Several field modelling techniques have been described with several comparative features: ease of

implementation, ability to solve boundary problems, 2D/3D problem formulations, ability to handle boundary conditions, etc. In case of distributed IPT systems, simple rectangular tracks can be modelled with Biot-Savart's law and closed form expressions derived. For more complicated shapes, Biot-Savart's law becomes cumbersome and closed form expressions become arduous. Here, theory of partial-inductance can be applied by breaking down such a structure into simpler sections and summing up individual contributions. The assumptions of thin filamentary currents and its operation of the magnetic vector potential improves the computational efficiency. In case of problems with a boundary, the theory of images and conformal mapping can be applied. Important limitations being the requirement of infinite images at complex boundaries (method of images) and limitations of 2D problem (conformal mapping). A discussion of standards that limit magnetic and electric field exposure is important so as to design IPT systems that are safe. ICNIRP 2010 limits general public exposure for B-fields at $27\mu H$ and H-fields at 21 Am^{-1} for power transfer at 3 kHz - 10 MHz. Designing such systems taking in multiple objectives, multiple constraints with staged iterations respecting magnetics and power electronics is described. This design flow apart from respecting the IPT system design also sets a stage for a technology and economic impact assessment. All these steps together make a complete design of the energy transfer system.

Another important contribution of this thesis lies in the development of an analytical model of charge-pads using the theory of partial inductances (Chapter 3). A sectional matrix method that is generic and can be applied to a single coil coupler is developed. An extension of this theory using the principle of superposition is carried out to model multi-coil couplers. The charge-pad shapes (circular, square, rectangular) of air-cored couplers - single coil and multi-coil (DR, DCirc, DR+Quad) have been analytically computed and verified with both FEM analysis and experimentation. Comparisons are made keeping area of coupler/perimeter conserved and it is observed that the circular couplers have better coupling at the best aligned point than four sided couplers. On the other hand, the four sided shapes have better tolerance to misalignment as they extend the range of power tranfer. The power null point of multi-coil couplers can be eliminated by designing additional coils in quadrature. For constant power applications, DR Quad pads with optimized magnetics can deliver power but at the cost of more weight and complexity. In case of EV applications, odds of parking at the low power position (stationary charging)/ travelling along the power null point (dynamic powering) is negligible due to access to alignment information. Thus, DR (primary)-DR (pick-up) couplers are a good choice for both stationary and dynamic operations. This design choice is used to further develop a demonstrator in Chapter 5. Some limitations of this analytical tool as developed includes: inability to deal with non-linearities, high frequency effects and material interfaces.

Position tolerance of IPT systems is an important feature especially for applications involving movement (Chapter 4). 3D variations in coupling, mutual inductance etc. is not considered in traditional design. Also, variation in leakage inductances has implications on reactive power compensation. This problem is especially exacerbated in distributed IPT systems. An electromagnetic model of the fields created by the tracks is analytically derived using

Biot-Savart's law. During misalignment of rectangular shaped tracks over the dimension of the edge, it is observed that there is a reduction of upto 40% in mutual inductance (at 100% edge length misalignment). The edge effects further exacerbate the mutual inductances as observed in the ends of the inductor.

In Chapter 5, the DR charge-pad is used for performing a M.O.O by considering efficiency (η), power density (α), and material weight (w) as targets and by evolving a trade-off using these parameters. Before the optimization, a parametric study undertaken gave the result that the ferrite dimension need not cover the entire coil dimension to achieve maximum coupling (80% already yields maximum coupling). Also, a intra-core gap of upto 20% is acceptable for maximum coupling. A charge-pad of free space self-inductance of $198.6\ \mu H$ experiences an increase in self-inductance by 33.5% due to a pad of inductance $199.8\ \mu H$ at a 1.5 cm z-gap due to flux modifying materials in the other pad. Another example of bifurcation due to the effect of the rectifier parallel filter capacitor 27.2 nF in a series resonant IPT system, resulting in two zeroes and one pole, all frequency shifted is also explained. Holistic system level models considering 3D inductance variations, operating with a variable frequency IPT system is suggested to mitigate this problem. Experimental analysis of the system is performed using SiC MOSFETs for various loads and for various bridge angles. The highest total efficiency measured for the light EV charging is about 91%. The magnetic losses are validated by performing measurements upto 2kW. Simulations are made where a semi-analytical approach is used to estimate the losses. In comparison, most observations are quite accurate with $\leq 10\%$ inaccuracy between estimated and measured. A notable exception being at very low powers, were they are offset by larger margins. Overwhelming percent losses in the magnetics ($\sim 70\%$) are observed in the resonant capacitors and ferrite.

Next, economic analysis (Chapter 6) is performed by proposing a generic analytical methodology for driving range of any EV with energy supplied from on-road IPT system. For a bus fleet of charging power level (200 kW), road coverage percentage (13%), inverter rating (200 kW) and battery capacity (500 kWh), the resulting specific cost of installing IPT is estimated to be 1.2 M€/km/lane for a lifetime of 12 years. At this moment, the project cost is expensive as compared to 0.75 M €/km/lane for a conventional trolley system. However, it is expected that volume economics will further push prices of IPT technology and battery down and the technology could be applied to scenario specific cases.

Finally, in Chapter 7, a vision of an upgraded infrastructure for future roadway electrification is evolved. Several integration challenges of IHA, solar roads are highlighted, modelling and loss analysis performed and possibilities are evolved for a combined technology highway. A thermal model with power density for healing and maximum permissible limit to prevent ravelling is proposed. The challenge in the integration of IPT and IHA is that up to a frequency of 100 kHz, the magnetic efficiency and power transfer of IPT systems drops to 90% in the coupling regime of $k = 0.113$. Thus, direct integration can be lossy. Sandwiched solar roads and IPT system couldn't work due to eddy currents induced in the backplates of the solar roads. The coupling declined to $k = 0.0135$, a reduction of 38.6% at operation close to 85 kHz. In a case study of A12 highways, It was therefore considered to use emergency

lanes of roads for solar roads operation. It is possible for a Nissan LEAF to complete its trip (80 % - 25 %) SOC along A12 by on-road IPT system. The total IPT coverage (IPT efficiency = 85 %) in this highway is 30.3 %. This corresponds to a distance of 50 km in a highway of total length 165 km. In the Netherlands, due to the complementary distribution of wind-solar profiles (peaks in winter and summer respectively), the choice of solar and wind technologies must match with the overall availability of renewable energy. A technology mix for energy neutrality is established.

Recommendations

This thesis has presented a number of results that led to the successful development of a prototype IPT system. It also opened some research in the areas of self-healing roads and an integrated technology roadway. Several topics can trigger further research:

- The analytical matrix method based partial inductance model proposed in this thesis is currently applicable to air-cored couplers. The theory of images could be applied to model the effects of flux modifying materials such as ferrite and aluminium. An extended partial inductance based inductive parameter solver is a fast and relatively computational cheap alternative to FEM.

- Integrated magnetic and thermal model for IPT systems leads to better charge-pad designs especially considering the dual effect of large currents and heating which could lead to thermal runaway. Also, accurate computation of magnetic losses by improved loss models can lead to better optimization outputs and hence more efficient designs. This is especially important for high power IPT systems.

- Exposure to electromagnetic fields (fundamental and harmonic) in the vicinity of inductive power transfer systems present safety concerns for humans and animals. Foreign object and living object protection is an important feature for field implementation of these systems. Further work in the control of power transfer that can detect metal objects, animals in the vicinity is an important target for system safety. H-field and B-field measurements coupled with simulation must conform to standards before its release to general public use.

- Finally, the idea of integrating self-healing roads with IPT system presents a challenging area that needs to be tackled. Here, best practices and trade-offs also considering material properties and its optimization can yield a combined solution. An interdisciplinary team of electrical and material scientists can create a frequency selective magnetic switch that can result in unhindered powering of vehicles during IPT mode and healing when necessary.

Bibliography

[1] F. Fan and Y. Lei, "Decomposition analysis of energy-related carbon emissions from the transportation sector in Beijing," *Transportation Research Part D: Transport and Environment*, vol. 42, 2016.

[2] "Reducing Transport Greenhouse Gas Emissions Trends & Data," 2010. [Online]. Available: http://www.internationaltransportforum.org

[3] T. M. Fisher, K. B. Farley, Y. Gao, H. Bai, and Z. T. H. Tse, "Electric vehicle wireless charging technology: a state-of-the-art review of magnetic coupling systems," *Wireless Power Transfer*, vol. 1, no. 2, pp. 87–96, 2014.

[4] Conductix Wampfler Website. Available online: http://www.conductix.us/en/news/2013-05-29/charging-electric-buses-quickly-and-efficiently-bus-stops-fitted-modular-components-make-charge-g (accessed on 03 December 2017).

[5] Wave IPT Website. Available online: http://wave-ipt.com/wave-announces-wireless-charging-at-walnut-creek-bart-station/(accessed on 02 December 2017).

[6] N. Lutsey, "Global climate change mitigation potential from a transition to electric vehicles," 2015.

[7] A. Zaheer, G. A. Covic, "A comparative study of various magnetic design topologies for a semi-dynamic ev charging application," *IEEE Annual Southern Power Electronics Conference (SPEC)*, Auckland, 2016.

[8] S. Chopra, P. Bauer, "Driving Range Extension of EV with On-Road Contactless Power Transfer—A Case Study. *IEEE Trans. Ind. Electron.* 2013, *60*, 329–338.

[9] T. E. Stamati and P. Bauer, "On-road charging of electric vehicles," in *Transportation Electrification Conference and Expo (ITEC), 2013 IEEE*. IEEE, 2013, pp. 1–8.

[10] M. Fuller, "Wireless charging in california: Range, recharge, and vehicle electrification *Transportation Research Part C: Emerging Technologies 67 (Supplement C)*, 2016.

[11] J. M. Miller et al., "Demonstrating Dynamic Wireless Charging of an Electric Vehicle: The Benefit of Electrochemical Capacitor Smoothing," in *IEEE Power Electronics Magazine*. IEEE, March 2014, pp. 12-24.

[12] V. Cirimele, F. Freschi and M. Mitolo, "Inductive power transfer for automotive applications: State-of-the-art and future trends," in *IEEE Industry Applications Society Annual Meeting*. Portland, OR, 2016, pp. 1-8.

[13] Witricity Website. Available online: http://witricity.com/products/automotive/(accessed on 02 December 2017).

[14] Qualcomm Website. Available online: https://www.qualcomm.com/products/halo/(accessed on 03 December 2017).

[15] T. Litman, "Autonomous Vehicle Implementation Predictions: Implications for Transport Planning," *Transportation Research Board Annual Meeting*, vol. 42, no. January 2014, pp. 36–42, 2014.

[16] D. Milakis, M. Snelder, B. Van Arem, G. Van Wee, and G. Homem De Almeida Rodriguez Correia, "Exploring plausible futures of automated vehicles in the netherlands: results from a scenario analysis," 2015.

[17] V. Prasanth and P. Bauer, "Distributed ipt systems for dynamic powering: Misalignment analysis," *IEEE Transactions on Industrial Electronics*, vol. 61, no. 11, pp. 6013–6021, Nov 2014.

[18] J. T. Boys, G. A. Covic, and A. W. Green, "Stability and control of inductively coupled power transfer systems," *IEE Proceedings - Electric Power Applications*, vol. 147, no. 1, pp. 37–43, Jan 2000.

[19] K. Colak, E. Asa, M. Bojarski, D. Czarkowski, and O. C. Onar, "A novel phase-shift control of semibridgeless active rectifier for wireless power transfer," *IEEE Transactions on Power Electronics*, vol. 30, no. 11, pp. 6288–6297, Nov 2015.

[20] G. Covic and J. Boys, "Modern Trends in Inductive Power Transfer for Transportation Applications," *IEEE Journal of Emerging and Selected Topics in Power Electronics*, vol. 1, no. 1, pp. 28–41, 2013.

[21] Z. Pantic, S. Bai and S. M. Lukic, "ZCS *LCC*-Compensated Resonant Inverter for Inductive-Power-Transfer Application," *IEEE Transactions on Industrial Electronics*, vol. 58, no. 8, pp. 3500-3510, Aug. 2011.

[22] R. Bosshard, J. Mühlethaler, J. W. Kolar and I. Stevanović, "The n-α-Pareto front of inductive power transfer coils," *IECON 2012*, Montreal, QC, pp. 4270-4277, 2012.

[23] G. Ombach, D. Kurschner and S. Mathar, "Universal base coil solution for interoperable system for stationary wireless EV charging," *International Conference on Sustainable Mobility Applications, Renewables and Technology (SMART)*, Kuwait City, pp. 1-9, 2015.

[24] J. L. M. Voskuilen and P. N. W. Verhoef, "Cause of premature raveling failure of porous asphalt." *Sixth international RILEM symposium on performance testing and evaluation of bituminous materials*, 2003.

[25] "Induction heating of electrically conductive porous asphalt concrete," *Construction and Building Materials*, vol. 24, no. 7, 2010.

[26] B. Kim and R. Roque, "Evaluation of healing property of asphalt mixtures," *Transportation Research Record: Journal of the Transportation Research Board*, vol. 1970, pp. 84–91, 2006.

[27] Q. Liu, "Induction healing of porous asphalt concrete," Ph.D. dissertation, TU Delft, October 2012.

[28] Q. Liu et al., "Induction healing of asphalt mastic and porous asphalt concrete," *Construction and Building Materials*, vol. 25, pp. 3746–3752, 2011.

[29] M. Budhia, G. A. Covic, and J. T. Boys, "Design and optimization of circular magnetic structures for lumped inductive power transfer systems," *IEEE Transactions on Power Electronics*, vol. 26, no. 11, pp. 3096–3108, Nov 2011.

[30] A. P. Sample, D. T. Meyer, and J. R. Smith, "Analysis, experimental results, and range adaptation of magnetically coupled resonators for wireless power transfer," *IEEE Transactions on Industrial Electronics*, vol. 58, no. 2, pp. 544–554, Feb 2011.

[31] J. O. McSpadden and J. C. Mankins, "Space solar power programs and microwave wireless power transmission technology," *IEEE Microwave Magazine*, vol. 3, no. 4, pp. 46–57, Dec 2002.

[32] W. Zhong, C. K. Lee, and S. Y. R. Hui, "General analysis on the use of tesla's resonators in domino forms for wireless power transfer," *IEEE Transactions on Industrial Electronics*, vol. 60, no. 1, pp. 261–270, Jan 2013.

[33] V. Prasanth, P. Bauer, J. A. Ferreira, and H. Polinder, "Review of analytical methods to extract magnetic parameters of an inductively coupled circuit," in *Emerging Technologies: Wireless Power (WoW), 2015 IEEE PELS Workshop on*, June 2015, pp. 1–8.

[34] J. C. Maxwell, *A treatise on electricity and magnetism*. Clarendon press, 1881, vol. 1.

[35] M. T. Casey, "Nicholas callan - priest, professor and scientist," *Physics Education*, vol. 17, no. 5, p. 224, 1982. [Online]. Available: http://stacks.iop.org/0031-9120/17/i=5/a=307

[36] National Science Museum. [Online]. Available: https://www.radiomuseum.org/museum/irl/national-science-museum-maynooth/.html

[37] D. J. Allan, "Power transformers-the second century," *Power Engineering Journal*, vol. 5, no. 1, pp. 5–14, Jan 1991.

[38] J. Vujic, A. Marincic, M. Ercegovac, and B. Milovanovic, "Nikola tesla: 145 years of visionary ideas," in *Telecommunications in Modern Satellite, Cable and Broadcasting Service, 2001. TELSIKS 2001. 5th International Conference on*, vol. 1, 2001, pp. 323–326 vol.1.

[39] W. C. Brown, "The history of wireless power transmission," *Solar Energy*, vol. 56, no. 1, pp. 3 – 21, 1996, wireless Power Transmission. [Online]. Available: http://www.sciencedirect.com/science/article/pii/0038092X9500080B

[40] Campbell standard of mutual inductance poster, National Physical Laboratory-fine art america. [Online]. Available: http://fineartamerica.com/featured/campbell-standard-of-mutual-inductance-national-physical-laboratory-c-crown-copyright.html

[41] T. H. Fawzi and P. E. Burke, "The accurate computation of self and mutual inductances of circular coils," *IEEE Transactions on Power Apparatus and Systems*, vol. PAS-97, no. 2, pp. 464–468, March 1978.

[42] S. Butterworth, "Capacity and eddy current effects in inductometers," *Proceedings of the Physical Society of London*, vol. 33, no. 1, p. 312, 1920. [Online]. Available: http://stacks.iop.org/1478-7814/33/i=1/a=332

[43] S. B. M.Sc., "Lviii. on the coefficients of self and mutual induction of coaxial coils," *Philosophical Magazine Series 6*, vol. 29, no. 172, pp. 578–592, 1915. [Online]. Available: http://dx.doi.org/10.1080/14786440408635335

[44] F. W. Grover, *Inductance calculations: working formulas and tables*. Courier Corporation, 2004.

[45] H. A. Wheeler, "The spherical coil as an inductor, shield, or antenna," *Proceedings of the IRE*, vol. 46, no. 9, pp. 1595–1602, Sept 1958.

[46] E. R. Joy, A. Dalal, and P. Kumar, "Accurate computation of mutual inductance of two air core square coils with lateral and angular misalignments in a flat planar surface," *IEEE Transactions on Magnetics*, vol. 50, no. 1, pp. 1–9, Jan 2014.

[47] S. I. Babic and C. Akyel, "Calculating mutual inductance between circular coils with inclined axes in air," *IEEE Transactions on Magnetics*, vol. 44, no. 7, pp. 1743–1750, July 2008.

[48] N. Astbury, "A precision method for the measurement of the mutual conductance of thermionic valves," *Journal of Scientific Instruments*, vol. 16, no. 8, p. 269, 1939.

[49] A. Campbell, "On a standard of mutual inductance," *Proceedings of the Royal Society of London. Series A, Containing Papers of a Mathematical and Physical Character*, vol. 79, no. 532, pp. 428–435, 1907.

[50] Z. Li, Z. Zhang, Q. He, Y. Fu, J. Zhao, B. Han, S. Li, Y. Lu, and C. Li, "A compensation method to measure the mutual inductance at low frequency," in *CPEM 2010*, June 2010, pp. 547–548.

[51] P. Harrison and G. Rayner, "A primary standard of mutual inductance," *Metrologia*, vol. 3, no. 1, p. 1, 1967.

[52] M. K. Kazimierczuk, *High-frequency magnetic components*. John Wiley & Sons, 2009.

[53] R. A. Serway, R. J. Beichner, and J. W. Jewett, "Physics for scientists and engineers with modern physics," 2000.

[54] E. B. Rosa, *The self and mutual inductances of linear conductors*. US Department of Commerce and Labor, Bureau of Standards, 1908.

[55] W. A. Perkins and J. C. Brown, "Mafco—a magnetic field code for handling general current elements in three dimensions," *Journal of Applied Physics*, vol. 35, no. 11, 1964.

[56] L. Urankar, "Vector potential and magnetic field of current-carrying finite arc segment in analytical form, part iii: Exact computation for rectangular cross section," *IEEE Transactions on Magnetics*, vol. 18, no. 6, pp. 1860–1867, Nov 1982.

[57] H. Kofler and E. Reisinger, "Inductances of air gap generators," *IEEE Transactions on Magnetics*, vol. 24, no. 1, pp. 63–65, Jan 1988.

[58] B. Azzerboni, E. Cardelli, M. Raugi, A. Tellini, and G. Tina, "Analytic expressions for magnetic field from finite curved conductors," *IEEE Transactions on Magnetics*, vol. 27, no. 2, pp. 750–757, Mar 1991.

[59] B. Azzerboni, G. Tina, and E. Cardelli, "Three dimensional forces and energy computation software package 'feman' and its applications," *IEEE Transactions on Magnetics*, vol. 29, no. 1, pp. 728–732, Jan 1993.

[60] K. Fotopoulou and B. W. Flynn, "Wireless power transfer in loosely coupled links: Coil misalignment model," *Magnetics, IEEE Transactions on*, vol. 47, no. 2, pp. 416–430, 2011.

[61] C. R. Paul, *Inductance: loop and partial*. John Wiley & Sons, 2011.

[62] G. A. Campbell, "Mutual inductances of circuits composed of straight wires," *Phys. Rev.*, vol. 5, pp. 452–458, Jun 1915. [Online]. Available: http://link.aps.org/doi/10.1103/PhysRev.5.452

[63] H. Chan, K. Cheng, and D. Sutanto, "A simplified neumann's formula for calculation of inductance of spiral coil," in *Power Electronics and Variable Speed Drives, 2000. Eighth International Conference on (IEE Conf. Publ. No. 475)*. IET, 2000, pp. 69–73.

[64] A. Schramm and D. Gerling, "Analytical calculation of the end winding leakage inductance based on the solution of neumann integrals," in *Proceedings of the IEEE International Symposium on Industrial Electronics, 2005. ISIE 2005.*, vol. 2, June 2005, pp. 851–855 vol. 2.

[65] D. Ban, D. Zarko, and I. Mandic, "Turbogenerator end winding leakage inductance calculation using a 3-d analytical approach based on the solution of neumann integrals," in *Electric Machines and Drives Conference, 2003. IEMDC'03. IEEE International*, vol. 3, June 2003, pp. 1576–1582 vol.3.

[66] G. Zhong and C. K. Koh, "Exact closed form formula for partial mutual inductances of on-chip interconnects," in *Computer Design: VLSI in Computers and Processors, 2002. Proceedings. 2002 IEEE International Conference on*, 2002, pp. 428–433.

[67] C. L. W. Sonntag, E. A. Lomonova, and J. L. Duarte, "Implementation of the neumann formula for calculating the mutual inductance between planar pcb inductors," in *Electrical Machines, 2008. ICEM 2008. 18th International Conference on*, Sept 2008, pp. 1–6.

[68] T. Imura and Y. Hori, "Maximizing air gap and efficiency of magnetic resonant coupling for wireless power transfer using equivalent circuit and neumann formula," *IEEE Transactions on Industrial Electronics*, vol. 58, no. 10, pp. 4746–4752, Oct 2011.

[69] F. B. J. Leferink, "Inductance calculations; methods and equations," in *Electromagnetic Compatibility, 1995. Symposium Record., 1995 IEEE International Symposium on*, Aug 1995, pp. 16–22.

[70] A. E. Ruehli, "Inductance calculations in a complex integrated circuit environment," *IBM journal of research and development*, vol. 16, no. 5, pp. 470–481, 1972.

[71] V. Prasanth, P. Bauer, and J. Ferreira, "A sectional matrix method for ipt coil shape optimization," in *Power Electronics and ECCE Asia (ICPE-ECCE Asia), 2015 9th International Conference on*. IEEE, 2015, pp. 1684–1691.

[72] D. Hockanson, J. L. Drewniak, R. E. DuBroff, T. H. Hubing, and T. P. V. Doren, "Considerations for magnetic-field coupling resulting in radiated emi," in *Electromagnetic Compatibility, 1998. 1998 IEEE International Symposium on*, vol. 2, Aug 1998, pp. 808–813 vol.2.

[73] P. Scholz, W. Ackermann, T. Weiland, and C. Reinhold, "Antenna modeling for inductive rfid applications using the partial element equivalent circuit method," *IEEE Transactions on Magnetics*, vol. 46, no. 8, pp. 2967–2970, Aug 2010.

[74] R.-B. Wu, C.-N. Kuo, and K. K. Chang, "Inductance and resistance computations for three-dimensional multiconductor interconnection structures," *IEEE Transactions on Microwave Theory and Techniques*, vol. 40, no. 2, pp. 263–271, Feb 1992.

[75] T. A. Driscoll and L. N. Trefethen, *Schwarz-Christoffel Mapping*. Cambridge University Press, 2002, vol. 8.

[76] A. Balakrishnan, W. T. Joines, and T. G. Wilson, "Air-gap reluctance and inductance calculations for magnetic circuits using a schwarz-christoffel transformation," in *Power Electronics Specialists Conference, 1995. PESC '95 Record., 26th Annual IEEE*, vol. 2, Jun 1995, pp. 1050–1056 vol.2.

[77] T. C. O'Connell and P. T. Krein, "A schwarz–christoffel-based analytical method for electric machine field analysis," *Energy Conversion, IEEE Transactions on*, vol. 24, no. 3, pp. 565–577, 2009.

[78] J. Mühlethaler, J. Kolar, and A. Ecklebe, "A novel approach for 3d air gap reluctance calculations," in *Eighth International Conference on Power Electronics, ICPE, ECCE Asia*, 2011.

[79] M. Curti, J. J. H. Paulides, and E. A. Lomonova, "An overview of analytical methods for magnetic field computation," in *Ecological Vehicles and Renewable Energies (EVER), 2015 Tenth International Conference on*, March 2015, pp. 1–7.

[80] J. J. Thomson, *Notes on Recent Researches in Electricity and Magnetism: Intended as a Sequel to Professor Clerk-Maxwell's Treatise on Electricity and Magnetism*.   Cambridge University Press, 1893.

[81] D. Zarko, D. Ban, and T. A. Lipo, "Analytical calculation of magnetic field distribution in the slotted air gap of a surface permanent-magnet motor using complex relative air-gap permeance," *Magnetics, IEEE Transactions on*, vol. 42, no. 7, pp. 1828–1837, 2006.

[82] M. Markovic, M. Jufer, and Y. Perriard, "Analytical force determination in an electromagnetic actuator," *IEEE transactions on magnetics*, vol. 44, no. 9, pp. 2181–2185, 2008.

[83] B. Gysen, E. Lomonova, J. Paulides, and A. Vandenput, "Analytical and numerical techniques for solving laplace and poisson equations in a tubular permanent magnet actuator: part ii. schwarz–christoffel mapping," *Magnetics, IEEE Transactions on*, vol. 44, no. 7, pp. 1761–1767, 2008.

[84] K. Boughrara, D. Zarko, R. Ibtiouen, O. Touhami, and A. Rezzoug, "Magnetic field analysis of inset and surface-mounted permanent-magnet synchronous motors using schwarz-christoffel transformation," *IEEE Transactions on Magnetics*, vol. 45, no. 8, pp. 3166–3178, Aug 2009.

[85] E. Ilhan, E. T. Motoasca, J. J. Paulides, and E. A. Lomonova, "Conformal mapping: Schwarz-christoffel method for flux-switching pm machines," *Mathematical Sciences*, vol. 6, no. 1, pp. 1–9, 2012. [Online]. Available: http://dx.doi.org/10.1186/2251-7456-6-37

[86] W. Min, J. T. Chen, Z. Q. Zhu, Y. Zhu, M. Zhang, and G. H. Duan, "Optimization and comparison of novel e-core and c-core linear switched flux pm machines," *IEEE Transactions on Magnetics*, vol. 47, no. 8, pp. 2134–2141, Aug 2011.

[87] P. Hammond, "Electric and magnetic images," *Proc. IEE*, vol. 107, p. 306, 1960.

[88] B. Hague, *The principles of electromagnetism applied to electrical machines:(formerly titled: Electromagnetic problems in electrical engineering)*.   Dover Publications, 1962.

[89] A. Pramanik, *Electromagnetism: Theory and Applications*.   PHI Learning Pvt. Ltd., 2008.

[90] N. Mullineux and J. Reed, "Images of line charges and currents," *Electrical Engineers, Proceedings of the Institution of*, vol. 111, no. 7, pp. 1343–1346, 1964.

[91] C. Carpenter, "The application of the method of images to machine end-winding fields," *Proceedings of the IEE-Part A: Power Engineering*, vol. 107, no. 35, pp. 487–500, 1960.

[92] M. Lambert, F. Sirois, M. Martinez-Duro, and J. Mahseredjian, "Analytical calculation of leakage inductance for low-frequency transformer modeling," *Power Delivery, IEEE Transactions on*, vol. 28, no. 1, pp. 507–515, 2013.

[93] J. Janssen, "Extended analytical charge modeling for permanent-magnet based devices/practical application to the interactions in a vibration isolation system," 2011.

[94] R. H. Park, "Two-reaction theory of synchronous machines generalized method of analysis-part i," *American Institute of Electrical Engineers, Transactions of the*, vol. 48, no. 3, pp. 716–727, 1929.

[95] G. Kron, "Equivalent circuit of the field equations of maxwell-i," *Proceedings of the IRE*, vol. 32, no. 5, pp. 289–299, 1944.

[96] N. Marcuvitz and J. Schwinger, "On the representation of the electric and magnetic fields produced by currents and discontinuities in wave guides. i," *Journal of Applied Physics*, vol. 22, no. 6, pp. 806–819, 1951.

[97] J. R. Carson, "Electromagnetic theory and the foundations of electric circuit theory1," *Bell System Technical Journal*, vol. 6, no. 1, pp. 1–17, 1927.

[98] M. N. Sadiku, *Numerical techniques in electromagnetics with MATLAB*. CRC press, 2011.

[99] S.-A. El-Hamamsy and E. I. Chang, "Magnetics modeling for computer-aided design of power electronics circuits," in *Power Electronics Specialists Conference, 1989. PESC'89 Record., 20th Annual IEEE*. IEEE, 1989, pp. 635–645.

[100] E. C. Cherry, "The duality between interlinked electric and magnetic circuits and the formation of transformer equivalent circuits," *Proceedings of the Physical Society. Section B*, vol. 62, no. 2, p. 101, 1949.

[101] G. Slemon, "Equivalent circuits for transformers and machines including non-linear effects," *Proceedings of the IEE-Part IV: Institution Monographs*, vol. 100, no. 5, pp. 129–143, 1953.

[102] G. W. Ludwig and S.-A. El-Hamamsy, "Coupled inductance and reluctance models of magnetic components," *Power Electronics, IEEE Transactions on*, vol. 6, no. 2, pp. 240–250, 1991.

[103] B. RW, "Analogs between magnetic and electrical circuits," *ELECTRONIC PRODUCTS MAGA-ZINE*, vol. 12, no. 5, p. 108, 1969.

[104] D. C. Hamill, "Lumped equivalent circuits of magnetic components: the gyrator-capacitor approach," *IEEE transactions on power electronics*, vol. 8, no. 2, pp. 97–103, 1993.

[105] R. Buntenbach, "A generalized circuit model for multiwinding inductive devices," *Magnetics, IEEE Transactions on*, vol. 6, no. 1, pp. 65–65, 1970.

[106] P. Blanken and J. Van Vlerken, "Modeling of electromagnetic systems," *Magnetics, IEEE Transactions on*, vol. 27, no. 6, pp. 4509–4515, 1991.

[107] D. C. Hamill, "Gyrator-capacitor modeling: a better way of understanding magnetic components," in *Applied Power Electronics Conference and Exposition, 1994. APEC'94. Conference Proceedings 1994., Ninth Annual*. IEEE, 1994, pp. 326–332.

[108] M. Eaton, "Modeling magnetic devices using the gyrator re-cap core model," in *Northcon/94 Conference Record*. IEEE, 1994, pp. 60–66.

[109] M. E. Eaton, "Adding flux paths to spice's analytical capability improves the ease and accuracy of simulating power circuits," in *Applied Power Electronics Conference and Exposition, 1998. APEC'98. Conference Proceedings 1998., Thirteenth Annual*, vol. 1. IEEE, 1998, pp. 386–392.

[110] L. Dalessandro, W. Odendaal, and J. W. Kolar, "Hf characterization and non-linear modeling of a gapped toroidal magnetic structure," in *Power Electronics Specialists Conference, 2005. PESC'05. IEEE 36th*. IEEE, 2005, pp. 1520–1527.

[111] Q. Chen, L. Xu, X. Ruan, S. C. Wong, and C. K. Tse, "Gyrator-capacitor simulation model of nonlinear magnetic core," in *Applied Power Electronics Conference and Exposition, 2009. APEC 2009. Twenty-Fourth Annual IEEE*. IEEE, 2009, pp. 1740–1746.

[112] L. Yan and B. Lehman, "Better understanding and synthesis of integrated magnetics with simplified gyrator model method," in *Power Electronics Specialists Conference, 2001. PESC. 2001 IEEE 32nd Annual*, vol. 1. IEEE, 2001, pp. 433–438.

[113] L. Yan, D. Qu, and B. Lehman, "Integrated magnetic full wave converter with flexible output inductor," *Power Electronics, IEEE Transactions on*, vol. 18, no. 2, pp. 670–678, 2003.

[114] L. Yan and B. Lehman, "An integrated magnetic isolated two-inductor boost converter: analysis, design and experimentation," *Power Electronics, IEEE Transactions on*, vol. 20, no. 2, pp. 332–342, 2005.

[115] S. Roy and L. Umanand, "Magnetic arm-switch-based three-phase series-shunt compensated quality ac power supply," *Electric Power Applications, IET*, vol. 6, no. 2, pp. 91–100, 2012.

[116] G. Sen, Z. Ouyang, O. C. Thomsen, M. A. Andersen, and L. Moller, "Integrated current balancing transformer for primary parallel isolated boost converter," in *Power Electronics and Applications (EPE 2011), Proceedings of the 2011-14th European Conference on*. IEEE, 2011, pp. 1–7.

[117] K. A. Grajski, R. Tseng, and C. Wheatley, "Loosely-coupled wireless power transfer: Physics, circuits, standards," in *Microwave Workshop Series on Innovative Wireless Power Transmission: Technologies, Systems, and Applications (IMWS), 2012 IEEE MTT-S International*, May 2012, pp. 9–14.

[118] I. Guideline, "Guidelines for limiting exposure to time-varying electric, magnetic, and electromagnetic fields (up to 300 ghz)," *Health Phys*, vol. 74, no. 4, pp. 494–522, 1998.

[119] I. C. on Non-Ionizing Radiation Protection *et al.*, "Guidelines for limiting exposure to time-varying electric and magnetic fields (1 hz to 100 khz)," *Health Physics*, vol. 99, no. 6, pp. 818–836, 2010.

[120] "Ieee standard for safety levels with respect to human exposure to radio frequency electromagnetic fields, 3 khz to 300 ghz," *IEEE Std C95.1-2005 (Revision of IEEE Std C95.1-1991)*, pp. 1–238, April 2006.

[121] I. C. on Non-Ionizing Radiation Protection *et al.*, "Factsheet on the guidelines for limiting exposure to time-varying electric and magnetic fields (1 hz to 100 khz)," *Health Physics*, vol. 99, no. 6, pp. 818–836, 2010.

[122] J. Kim, J. Kim, S. Kong, H. Kim, I. S. Suh, N. P. Suh, D. H. Cho, J. Kim, and S. Ahn, "Coil design and shielding methods for a magnetic resonant wireless power transfer system," *Proceedings of the IEEE*, vol. 101, no. 6, pp. 1332–1342, June 2013.

[123] G. Lipworth, J. Ensworth, K. Seetharam, J. S. Lee, P. Schmalenberg, T. Nomura, M. S. Reynolds, D. R. Smith, and Y. Urzhumov, "Quasi-static magnetic field shielding using longitudinal mu-near-zero metamaterials," *Scientific reports*, vol. 5, 2015.

[124] F. Y. Lin, G. A. Covic, and J. T. Boys, "Evaluation of Magnetic Pad Sizes and Topologies for Electric Vehicle Charging," *IEEE Transactions on Power Electronics*, vol. 30, no. 11, pp. 6391–6407, nov 2015.

[125] D. J. Perreault, J. Hu, J. M. Rivas, Y. Han, O. Leitermann, R. C. N. Pilawa-Podgurski, A. Sagneri, and C. R. Sullivan, "Opportunities and Challenges in Very High Frequency Power Conversion," in *Applied Power Electronics Conference and Exposition, 2009. APEC 2009. Twenty-Fourth Annual IEEE*, feb 2009, pp. 1–14.

[126] M. Ibrahim, P. Lefranc, D. Frey, L. Gonnet, J. P. Ferrieux, and S. Am, "Design optimization of single-phase PFC rectifier using Pareto-Front analysis and including electro-thermal modelling," in *Industrial Electronics Society, IECON 2015 - 41st Annual Conference of the IEEE*, nov 2015, pp. 3253–3258.

[127] R. Bosshard, J. W. Kolar, J. Mühlethaler, I. Stevanović, B. Wunsch, and F. Canales, "Modeling and η - α -Pareto Optimization of Inductive Power Transfer Coils for Electric Vehicles, volume = 3, year = 2015," *IEEE Journal of Emerging and Selected Topics in Power Electronics*, no. 1, pp. 50–64.

[128] M. Budhia, G. a. Covic, and J. T. Boys, "Design and optimization of circular magnetic structures for lumped inductive power transfer systems," *IEEE Transactions on Power Electronics*, vol. 26, no. 11, pp. 3096–3108, 2011.

[129] E. Lanaras, V. Prasanth, and P. Bauer, "Comparative study of transformer topologies for distributed IPT systems," in *2014 IEEE Transportation Electrification Conference and Expo (ITEC)*. IEEE, Jun. 2014, pp. 1–8.

[130] J. Shin, S. Shin, Y. Kim, S. Ahn, S. Lee, G. Jung, S.-J. Jeon, and D. H. Cho, "Design and Implementation of Shaped Magnetic Resonance Based Wireless Power Transfer System for Roadway-Powered Moving Electric Vehicles," *IEEE Transactions on Industrial Electronics*, vol. 61, no. c, pp. 1–1, 2013.

[131] F. W. Grover, *Inductance Calculations: Working Formulas and Tables*. Dover Publications, 1946.

[132] J. T. Conway, "Inductance calculations for noncoaxial coils using bessel functions," *IEEE Transactions on Magnetics*, vol. 43, no. 3, pp. 1023–1034, 2007.

[133] J. C. Maxwell, *A Treatise on Electricity and Magnetism*. Cambridge: Cambridge University Press, 2010.

[134] T. S. Tran, G. Meunier, P. Labie, and J. Aime, "Comparison of FEM-PEEC coupled method and finite-element method," *IEEE Transactions on Magnetics*, vol. 46, no. 4, pp. 996–999, 2010.

[135] A. E. Ruehli, "Inductance Calculations in a Complex Integrated Circuit Environment," *IBM Journal of Research and Development*, vol. 16, no. 5, pp. 470–481, 1972.

[136] A. Ruehli, C. Paul, and J. Garrett, "Inductance calculations using partial inductances and macromodels," *Proceedings of International Symposium on Electromagnetic Compatibility*, pp. 7–12, 1995.

[137] A. Müsing, J. Ekman, and J. W. Kolar, "Efficient calculation of non-orthogonal partial elements for the peec method," *IEEE Transactions on Magnetics*, vol. 45, no. 3, pp. 1140–1143, 2009.

[138] T. V. D. Simon Ramo, John R. Whinnery, *Fields and Waves in Communication Electronics*, 3rd ed. John Wiley, 2012.

[139] H. Takanashi, Y. Sato, Y. Kaneko, S. Abe, and T. Yasuda, "A large air gap 3 kw wireless power transfer system for electric vehicles," in *2012 IEEE Energy Conversion Congress and Exposition (ECCE)*, Sept 2012, pp. 269–274.

[140] F. E. Terman *et al.*, "Radio engineer's handbook," 1943.

[141] J. Muhlethaler, *Modeling and Multi-Objective Optimization of Inductive Power Components*. ETH Zurich PhD. Thesis, 2012.

[142] A.V.D. Bossche and V.C. Valchev, *Inductors and Transformers for Power Electronics*, CRC Press, pp.2005.

[143] S. Bandyopadhyay, V. Prasanth, P. Bauer, and J. A. Ferreira, "Multi-objective optimisation of a 1-kw wireless ipt systems for charging of electric vehicles," in *2016 IEEE Transportation Electrification Conference and Expo (ITEC)*, June 2016, pp. 1–7.

[144] S. Raabe, *Inductive Power Transfer Pickups for High Demand Applications*. The University of Auckland, 2011.

[145] J.T. Boys, G.A.J. Elliot, and G.A. Covic, "An appropriate magnetic coupling co-efficient for the design and comparison of ICPT pickups," *IEEE Transactions on Power Electronics*, vol. 22, no. 1, pp. 333–335, 2007.

[146] E. Waffenschmidt and T. Staring, "Limitation of inductive power transfer for consumer applications," in *3th European Conference on Power Electronics and Applications*, Barcelona, 2009, pp. 1-10.

[147] M. van der Geest, H. Polinder, J. A. Ferreira and D. Zeilstra, "Optimization and comparison of electrical machines using particle swarm optimization," in *XXth International Conference on Electrical Machines*, 2012, pp. 1380-1386.

[148] C. A. C. Coello, G. T. Pulido and M. S. Lechuga, "Handling multiple objectives with particle swarm optimization," *IEEE Transactions on Evolutionary Computation*, vol. 8, no. 3, pp. 256-279, June 2004.

[149] R. Bosshard, J. W. Kolar, J. Muhlethaler, I. Stevanovic, B. Wunsch and F. Canales, "Modeling and eta-$alpha$-Pareto Optimization of Inductive Power Transfer Coils for Electric Vehicles," *IEEE Journal of Emerging and Selected Topics in Power Electronics*, vol. 3, no. 1, pp. 50-64, March 2015.

[150] M. v. d. Geest, *An Integral Approach to Design High Performance Permanent Magnet Synchronous Machines*. TU Delft PhD Thesis, 2015.

[151] R. L. Steigerwald, "A comparison of half-bridge resonant converter topologies," *IEEE Transactions on Power Electronics*, vol. 3, no. 2, pp. 174-182, Apr 1988.

[152] M. Budhia, J. T. Boys, G. A. Covic and C. Y. Huang, "Development of a Single-Sided Flux Magnetic Coupler for Electric Vehicle IPT Charging Systems," *IEEE Transactions on Industrial Electronics*, vol. 60, no. 1, pp. 318-328, Jan. 2013.

[153] Y. Duan and R. G. Harley, "A Novel Method for Multiobjective Design and Optimization of Three Phase Induction Machines," *IEEE Transactions on Industry Applications*, vol. 47, no. 4, pp. 1707-1715, July-Aug. 2011.

[154] G. Channoullis, *Wireless Charging of Electric Vehicle with 11kW Induction Charger*. TU Delft MSc. Thesis, 2016.

[155] T. Diekhans and R. W. De Doncker"A Dual-Side Controlled Inductive Power Transfer System Optimized for Large Coupling Factor Variations and Partial Load," *IEEE Transactions on Industrial Electronics*, vol. 30, no. 11, pp. 6320-6328, Nov. 2015.

Fox, G.H., "Electric Vehicle Charging Stations: Are We Prepared?,"*Ind. Appl. Mag.* 2013, *19*, 32–38.

[156] Maheshwari, P., Tambawala, Y., Nunna, H.S., Doolla, S., "A review on plug-in electric vehicles charging: Standards and impact on distribution system, "In Proceedings of the 2014 IEEE International Conference on Power Electronics, Drives and Energy Systems (PEDES), Mumbai, India, 16–19 December 2014, pp. 1–6.

[157] Mwasilu, F., Justo, J.J., Kim, E.-K., Do, T.D., Jung, J.-W. Electric vehicles and smart grid interaction: A review on vehicle to grid and renewable energy sources integration. *Renew. Sustain. Energy Rev.* 2014, *34*, 501–516.

[158] Choi, W., Kim, J. Electrification of public transportation: Battery swappable smart electric bus with battery swapping station. In Proceedings of the 2014 IEEE Conference and Expo, Transportation Electrification Asia-Pacific (ITEC Asia-Pacific), Beijing, China, 31 August–3 September 2014, pp. 1–8.

[159] *Performance of Electric Buses in Practice: Energy Consumption and Range*, TNO Report 2013 R10212, TNO: Delft, The Netherlands, 2013.

[160] *E-Buses for SolaRoad*, *TNO Report for the Province of North Holland*, TNO: Delft, The Netherlands, 2014.

[161] *Electric Buses for SolaRoad II, Internal TNO Document 2015 R10055*, TNO: Delft, The Netherlands, 2015.

[162] Wu, H.H., Gilchrist, A., Sealy, K., Israelsen, P., Muhs, J. A review on inductive charging for electric vehicles. In Proceedings of the 2011 IEEE International Electric Machines & Drives Conference (IEMDC), Niagara Falls, ON, Canada, 15–18 May 2011, pp. 143–147.

[163] Bombardier PRIMOVE Website. Available online: http://primove.bombardier.com/media/news/ (accessed on 15 October 2015).

[164] Shekhar, A., Prasanth, V., Bauer, P., Bolech, M. Generic methodology for driving range estimation of electric vehicle with on-road charging. In Proceedings of the 2015 IEEE Transportation Electrification Conference and Expo (ITEC), Dearborn, MI, USA, 14–17 June 2015, pp. 1–8.

[165] Shekhar, A., Bolech, M., Prasanth, V., Bauer, P. Economic considerations for on-road wireless charging systems—A case study. In Proceedings of the 2015 IEEE PELS Workshop on Emerging Technologies: Wireless Power (WoW), Daejeon, Korea, 5–6 June 2015, pp. 1–5.

[166] *Roadway Powered Electric Vehicle Project Parametric Studies: Phase 3D Final Report*, *California Partners for Advanced Transit and Highways Research Report*, University of California: Berkeley, CA, USA, 1996.

[167] Jang, Y.J., Suh, E.S., Kim, J.W. System Architecture and Mathematical Models of Electric Transit Bus System Utilizing Wireless Power Transfer Technology. *IEEE Syst. J.* 2015, doi:10.1109/JSYST.2014.2369485.

[168] Shin, J., Shin, S., Kim, Y., Ahn, S., Lee, S., Jung, G., Jeon, S.-J., Cho, D.-H. Design and Implementation of Shaped Magnetic-Resonance-Based Wireless Power Transfer System for Roadway-Powered Moving Electric Vehicles. *IEEE Trans. Ind. Electron.* 2014, *61*, 1179–1192.

[169] Rim, C. T. The Development and Deployment of On-Line Electric Vehicle (OLEV). In Proceedings of the IEEE Energy Conversion Congress and Exposition (ECCE), Denver, CO, USA, 15-19 September 2013.

[170] Build Your Dreams (BYD) E-Bus. 2014. Available online: http://www.byd.com/la/auto/ebus.html (accessed on 13 September 2014).

[171] *Standardised On-Road Test Cycles*, International Association of Public Transport (UITP): Belgium, Brussels, 2009.

[172] United States Environmental Protection Agency. Dynamometer Drive Schedules. Available online: http://www.epa.gov (accessed on 13 September 2014).

[173] Van Assen, V. Physics of City Buses and Their Environment. Master Thesis, University of Groningen, Groningen, The Netherlands, 2013.

[174] *Inzetbaarheid Van Zero Emissie Bussen In Nederland*, Ministerie van Infrastructuur en Milieu, TNO, R10315, TNO: Den Hague, The Netherlands, 2015. (In Dutch)

[175] Wolterink, S., Bauer, P. High range on-line electric vehicles powered by Inductive Power Transfer. In Proceedings of the 2014 IEEE Transportation Electrification Conference and Expo (ITEC), Dearborn, MI, USA, 15–18 June 2014, pp. 1–7.

[176] Jager, K., Isabella, O., Smets, A.H.M, Van Swaaij, R.A.C.M.M., Zeman, M. A Student Introduction to Solar Energy. Available online: https://courses.edx.org (accessed on 25 September 2014).

[177] Sallan, J., Villa, J.L., Llombart, A, Sanz, J.F. Optimal Design of ICPT Systems Applied to Electric Vehicle Battery Charge. *IEEE Trans. Ind. Electron.* 2009, *56*, 2140–2149.

[178] De Doncker, R.W. Power electronic technologies for flexible DC distribution grids. In Proceedings of the 2014 International Power Electronics Conference (IPEC-Hiroshima 2014—ECCE-ASIA), Hiroshima, Japan, 18–21 May 2014, pp. 736–743.

[179] Stamati, T.-E., Bauer, P. On-road charging of electric vehicles. In Proceedings of the 2013 IEEE Transportation Electrification Conference and Expo (ITEC), Detroit, MI, USA, 16–19 June 2013, pp. 1–8.

[180] Covic, G.A., Boys, J.T. Modern Trends in Inductive Power Transfer for Transportation Applications. *IEEE J. Emerg. Sel. Top. Power Electron.* 2013, *1*, 28–41.

[181] Schlick, T., Hagemann, B.,Kramer, M., Garrelfs, J., Rassmann, A. *Zukunftsfeld Energiespeicher*, Roland Berger: Munich, Germany, 2012. (In German)

[182] Ko, Y.D., Jang, Y.J. The Optimal System Design of the Online Electric Vehicle Utilizing Wireless Power Transmission Technology. *IEEE Trans. Intell. Transp. Syst.* 2013, *14*, 1255–1265.

[183] Pantic, Z., Bai, S., Lukic, S.M. Inductively coupled power transfer for continuously powered electric vehicles. In Proceedings of the Vehicle Power and Propulsion Conference, VPPC '09, Dearborn, MI, USA, 7–10 September 2009, pp. 1271–1278.

[184] Verbeek, I.R.P., Bolech, M., Van Gijlswijk, R.N., Spreen, I.J. TNO 2015 R10386. Energie en Milieu Aspecten Van Elektrische Personenvoertuigen. Available online: http://www.rvo.nl/actueel/nieuws/tno-elektri sch-rijden-tot-70-zuiniger (accessed on 15 October 2015). (In Dutch)

[185] V. Prasanth, N. Scheele, E. Visser et al., "Green energy based inductive Self-Healing highways of the future," *IEEE Transportation Electrification Conference and Expo (ITEC)*, pp. 1–8, June 2016.

[186] Bladeless vortex. [Online]. Available: http://www.vortexbladeless.com/

[187] Solaroad. [Online]. Available: http://en.solaroad.nl/

[188] Bladeless wind turbines may offer more form than function. [Online]. Available: https://www.technologyreview.com

[189] A. Shekhar, S. Klerks, P. Bauer, and V. Prasanth, "Solar road operating efficiency and energy yield – an integrated approach towards inductive power transfer," in *European Photovoltaic Solar Energy Conference and Exhibition (EU-PVSEC)*, 2015, pp. 2614–2619.

[190] A. Shekhar, V. Prasanth, P. Bauer and M. Bolech, "Generic methodology for driving range estimation of electric vehicle with on-road charging," *IEEE Transportation Electrification Conference and Expo (ITEC)*, pp. 1-8, 2015.

[191] A. Shekhar, V. Prasanth, P. Bauer and M. Bolech, "Economic Viability Study of an On-Road Wireless Charging System with a Generic Driving Range Estimation Method," *Energies* 9, no. 2: 76, 2016.

[192] "Renewable energy technology: cost analysis of wind power," *Int. Renew. energy agency,* 2012.

[193] T. E. Stamati and P. Bauer, "Green energy for on-road charging of electric vehicles," *MECHATRONIKA* 2012.

List of publications

Main papers:

- V. Prasanth and P. Bauer, "Distributed IPT Systems for Dynamic Powering: Misalignment Analysis,"*IEEE Transactions on Industrial Electronics* vol. 61, no. 11, pp. 6013-6021, Nov. 2014.

- P. Venugopal, S. Bandyopadhyay, P. Bauer and Jan Abraham Ferreira, "A Generic Matrix Method to Model the Magnetics of Multi-Coil Air-Cored Inductive Power Transfer Systems "*Energies* vol. 10, no. 6, June 2017 *(Cover/Feature Paper)*.

- A. Shekhar, V. Prasanth, P. Bauer and M. Bolech, "Economic viability study of an on-road wireless charging system with a generic driving range estimation method "*Energies* vol. 9, no. 2, Jan. 2016.

- V. Prasanth et al., "Modelling Challenges and Interdependencies of Future Green Highways with Integrated IPT Self-Healing, Solar Road and EVs,"*Applied energy*.

- P. Venugopal, P. Bauer, J.A. Ferreira and H.Polinder, "Analytical and Semi-Analytical Techniques for Modelling the Magnetics of Air-Cored IPT Systems,"*IEEE Transactions on Industry Applications* (Submitted).

Co-author:

- A. Shekhar et al., "Harvesting Roadway Solar Energy - Performance of the Installed Infrastructure Integrated PV Bike Path,"*IEEE Journal of Photovoltaics*, 2018.

Conferences (Not exhaustive):

- V. Prasanth and P. Bauer, "Study of misalignment for On Road Charging," in *IEEE Transportation Electrification Conference and Expo (ITEC)*, 2013, pp. 1-8.

- V. Prasanth, P. Bauer, J. A. Ferreira, and H. Polinder, "Review of analytical methods to extract magnetic parameters of an inductively coupled circuit," in *IEEE PELS Emerging Technologies: Wireless Power (WoW)*, 2015, pp. 1–8.

- V. Prasanth, P. Bauer and J. A. Ferreira, "A sectional matrix method for IPT coil shape optimization," in *International Conference on Power Electronics and ECCE Asia (ICPE-ECCE Asia)*, 2015, pp. 1684–1691.

- V. Prasanth, S. Bandyopadhyay, P. Bauer and J. A. Ferreira, "Analysis and comparison of multi-coil inductive power transfer systems," in *Power Electronics and Motion Control Conference (PEMC) Varna*, 2016, pp. 993–999.

- S. Bandyopadhyay, V. Prasanth, P. Bauer and J. A. Ferreira, "Multi-objective optimisation of a 1-kW wireless IPT systems for charging of electric vehicles,"in *IEEE Transportation Electrification Conference and Expo (ITEC), Dearborn, MI*, 2016, pp. 1-7.

- V. Prasanth et al., "Green energy based inductive Self-Healing highways of the future," in *IEEE Transportation Electrification Conference and Expo (ITEC)*, 2016, , Dearborn, MI, pp. 1-8.

- E. Lanaras, V. Prasanth, and P. Bauer, "Comparative study of transformer topologies for distributed IPT systems," in *2014 IEEE Transportation Electrification Conference and Expo (ITEC)*. IEEE, Jun. 2014, pp. 1–8.

- D. Voglitsis, V. Prasanth, T. Todorcevic and P. Bauer, "Theoretical analysis and experimental investigation of high frequency bidirectional CPT system," in *2014 IEEE Transportation Electrification Conference and Expo (ITEC)*, Jun. 2014, pp. 1–8.

- A. Shekhar, M. Bolech, V. Prasanth and P. Bauer, "Economic considerations for on-road wireless charging systems - A case study," in *IEEE PELS Emerging Technologies: Wireless Power (WoW)*, 2015, pp. 1–8.

Patents:

- P. Bauer, V. Prasanth and J.R.E.G. Prazeres, "An inductive power transfer system, a method and a computer program product," N.L. Patent NL1041080 (B1), 2016.

- V. Prasanth, S. Bandyopadhyay, and P. Bauer, "A Multi-Frequency IPT System with a Single Pickup Stage," Application: OCT-16-079, July 2017 (In process).

- G. Channoullis, V. Prasanth, and P. Bauer, "Inductive Power Transfer system with an inherent EMI elimination technique," Application: OCT-16-067, July 2017 (In process).